Design and thermal analysis of high-pressure gas turbine blade internal swirl cooling chambers

Ramesh Devaramani

Submitted in accordance with the requirements for the degree of

Doctor of Philosophy

The University of Leeds, UK

School of Mechanical Engineering

September 2025

Acknowledgements

This research studies were carried out at the School of Mechanical Engineering at the University of Leeds, UK. I would like to express my sincere gratitude to my primary supervisor Dr. Gregory de Boer, whose vision, guidance and unwavering support have been involved, these all through this doctoral journey. His knowledge and mentorship have been valuable, shaping not only the path of my research but also these my growth as a research scholar.

I would like to equivalently thankful to my secondary supervisors, Dr. Carl Gilkeson and Professor Harvey Thompson, as my advisor. Their productive feedback, insights and inspiration this was significantly enriched the depth of my research.

I would like to special thanks to the Graduate School Office (GSO) team for their continued support in offering their administrative support for this entire research. In specific, I would like to thanks to Mrs Victoria masters and Miss Joanne Sah for their special support, which greatly contributed to the progress of my academic journey.

I would like to thank to the Government of India for its continuous funding support for this research.

To my parents, I express my sincere gratitude for your unwavering love and support throughout my academic journey, and their belief in me since childhood has been a constant source of motivation. I would like to thank to Captain Dr Rajendra (IAS) for, support and motivation during this academic journey.

Ramesh Devaramani

Declarations

I affirm that the work provided in this thesis has not been submitted for any other degree or professional qualification and is the product of my individual work.

Full name: Ramesh Devaramani

Date: 29/09/2025

Abstract

The numerical simulation of swirl cooling is one of the promising and latest internal cooling approaches for gas turbines. Thermal and isentropic efficiencies with the best-designed chambers were investigated, considering a flow through internal swirl cooling channels for heat transfer and flow behaviour in single-stage and multi-stage (two– to three–stage) swirl cooling channels. These rectangular nozzles to round shapes nozzles are used for each three-stage designs to find the best design chambers. However, this investigation on the multi-stage swirl cooling with changing the different types of round shape nozzles concluded. The generally employed k -ω turbulent model, with varying types of wall treatment, and 20,000 to 40,000 Reynolds numbers. In this simulation work, a single-stage internal cooling was used and considered the baseline geometry for further studies of multi-stage configurations. This work investigated the pressure drop, heat transfer, and total thermal performance of each cooling chambers. Following the multi-stage cooling chambers, there are additional pressure drops that occur, and the cooling performance is observed. This research aims to improve pressure drops and enhance the cooling performance for multi-stage cooling chambers. The rectangular-shaped nozzles were modified to round nozzles, resulting in a significant improvement: 60% higher heat transfer and reduced pressure drop. These three stages of swirl-cooling configurations can result in an average surface temperature along the entire leading edge that is around 40K lower than in the single-stage cooling chamber configuration. However, significant improvements in heat transfer during the multi-stage swirl cooling analysis increased overall pressure losses.

Nevertheless, if the bends linking the adjacent angles of the nozzle stages are new and rounded, the rounded shape will gradually reduce pressure loss. Following this, the thermal efficiency of the multi-stage swirl cooling configurations was higher than that of the single-stage configurations.

Furthermore, the design features three-stage swirl cooling chambers, transitioning from a rectangular shape to a round shape nozzles, with three types of round shapes used, 2 mm, 4 mm, and 6mm. In these three models, different types of boundary conditions are applied, changing the temperature distribution in each design. This investigation indicates that the 4 mm designs are the best design, with better pressure drop and heat transfer overall, across all variables.

Key words – MT-1 gas turbine blade, heat transfer, pressure drop, swirl cooling chambers, and best design.

Nomenclature

Symbol	Description	Units
α_1	Inlet angle	rad
α_2	Outlet angle	rad
P	Pitch length	mm
H	Blade height	mm
D_L	Leading edge diameter	mm
C	Chord length	mm
L	Length of the coolant chambers	mm
W	Width of coolant chambers	mm
l	Length of nozzles	mm
β	Blade angles	rad
ρ	Density	kg/m^3
p	Pressure	Pa
T	Temperature	K (Kelvin)
$\dot{m}$	Mass flow rate	kg/s
U	Blade tangential velocity	m/s
V	Absolute velocity	m/s
V_r	Relative velocity	m/s
V_m	Meridional velocity	m/s
V_u	Tangential velocity	m/s
Δh	Change in specific enthalpy rise/drop	J/kg
n	Rotational speed	rpm
D	Diameter	m
ω	Angular velocity	rad/s
η_{cool}	Cooling effectiveness–related efficiency	--
T	Time	s
$U^'$	Instantaneous velocity	m/s
U_t	Tangential velocity	m/s
ε	Viscous dissipation distance	--
Y^+	Dimensionless wall distance	--
θ	Closeness of fit	--

τ_w	Wall shear of the fluid	--
μ_t	Turbulent viscosity	Pa·s
T_{ref}	Temperature reference	^{O}C
nx	Normal x wall components	--
ny	Normal y wall components	--
tx	Tangential x wall components	--
ty	Tangential y wall components	--
x, y and z	Cartesian coordinates	--
k	Turbulent kinetic energy	m^2 / s^3

Abbreviations/ Acronyms

N	Number of cooling stages
MSC	Multistage Swirl Cooling
CFD	Computation Fluid Dynamic
RPM	Revolution Per Minutes
SI	Internal System of Units
CAD	Computer – Aided – Design
HPT	High Pressure Turbine
MT-1	Name Code of the Turbine Blade
MFR	Mass Flow ratio
TR	Temperature ratio

Subscripts

c	Coolant
s	Mainstream
j	Coolant jet
iw, and ow	Inner and outer wall
f	fluid
in	Stage inlet
exit	Exit vortex chamber

Table of contents

List of Figures

List of Tables

Chapter 1: Introduction to the gas turbine operation and cooling

1.1 Introduction

1.1.1 General overview

High-pressure gas turbine (HPT) producers must overcome challenging technological difficulties in the 21st century to remain competitive in the aviation propulsion industry. A gas turbine engine's performance must be enhanced to remain competitive, and new components must be developed for brand-new aircraft types. Moreover, the number of people travelling by air is increasing, and different types of planes are being made to meet the needs of airlines and travelers

The basic gas turbine cycle configuration discussed in this section highlights the key temperature stations used throughout this thesis (as shown in Fig. 1.1). It shows overall engine improvement, followed by an increase in the turbine inlet temperature. Theoretically, an increase in Turbine Entrance Temperature (TET) could enhance the power output of a given engine, increasing the thrust-to-weight ratio. However, raising TET alone cannot increase engine efficiency when blade metal temperature and coolant mass flow are also considered. This will be covered in more detail, with the number increasing as noted in [1].

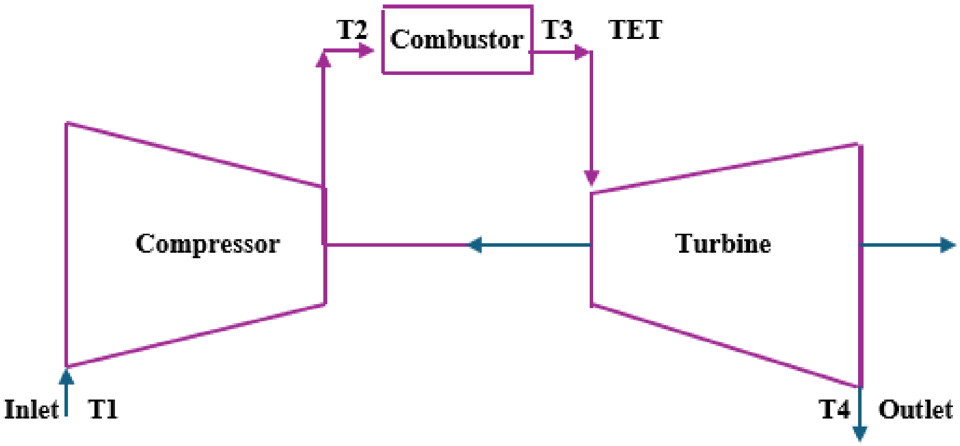

Figure 1-1: Basic gas turbine cycle adopted from [1]

1.1.2 Basic turbine operation

In 1903, the first gas turbine was investigated, and it contained a three-cylinder, multi-stage reciprocating compressor, a combustion chamber, and an impulse turbine. Liquid fuel was burned in the combustion chamber, which was fed air by the compressor. Air is the working fluid of gas turbines and is operated by the Brayton cycle. Brayton engines had a piston compressor and a piston expander.

Modern gas turbine engines that use air as fuel are also based on the Brayton cycle as reported in [2]. In the gas turbine combustion chamber, liquid is burned, which is feed air by the compressor. However, presently, gas turbine industries address strict requirements regarding pollutant emissions and decreased fuel consumption. Therefore, thermal efficiency must be increased to fulfil this essential requirement for aircraft engines and industrial gas turbines in [3]. A gas turbine involves a compressor, combustion chambers, and a turbine, as shown in Fig 1.2. The compressor increases the air pressure; fuel has been supplied and ignited, and a high-temperature flow is generated in the combustion chamber.

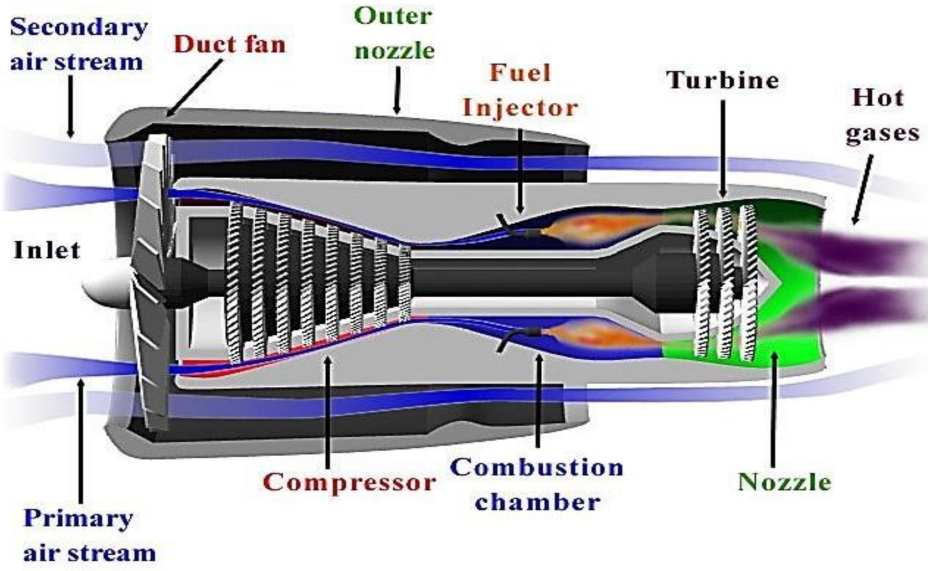

Figure 1-2: Basic schematic for gas turbines: Reprinted from the modern gas turbine systems [10] with their permission from Elsevier. Copyright © 2013

However, the input of high pressure and temperature of the gas turbine develops more output power. Higher thermal efficiency of the gas turbine is achieved by increasing the turbine entry temperature and the speed pressure ratio across the turbine, expanding the combustion chamber temperature and consequently increasing the turbine inlet temperature and pressure. The first-stage turbine blades consist of an internal air-cooling system based on these high thermal loads, as shown in Fig 1.2. Here a cross-section of a turbine blade is shown with an internal serpentine cooling channel with ribs in [3]. Furthermore, blades contain film cooling holes which generates an air film on the outer surface of the blade to protect the material from hot gases. The cooling air for the blade cooling system is derived from an upstream compressor stage, improving air loss for the combustion and, thus, the entire engine cycle. A more effective cooling method would require less cooling air from the compressor stage with higher pressure and temperature.

Further air is heated in the combustion chamber by burning this air-fuel mixture in a jet of airflow. Gases and combustion by-products expand in the turbine near atmospheric pressure (engines producing mechanical or electrical energy) or the pressure required by the jet engines, and the open Brayton cycle means the gases are discharged directly into the atmosphere.

A civil gas turbine engine's performance is also assessed using additional parameters, including:

a) **Reliability**: Gas Turbine engine manufacturers are under constant pressure to increase the time between overhauls. The modern civil gas turbine design prioritises component durability and thermal management, which directly increase the engine's working hours, minimise maintenance, and lower the life cycle cost. Rolls–Royce and other aero-engine manufacturers have prioritised design.

b) **Emission:** Environmental concern has led to legislation to control the jet engine's emission stages in the pollution NO_x, CO and CO_2. Fig 1.3 shows how much the pollutant stage in NOx and CO_2 has changed over a particular time. Furthermore, Fig 1.3 (i) illustrates the NOx emission stage for Rolls-Royce's Trent series engine since 1998.

The NOx emitted has reduced by 40 % since the Trent 895 and is prediced to continue to drop. Fig 1.3(ii) shows the CO_2 emission stage, which has been reduced by 60% since the 1960s, while the TET and pressure ratio has significantly increased.

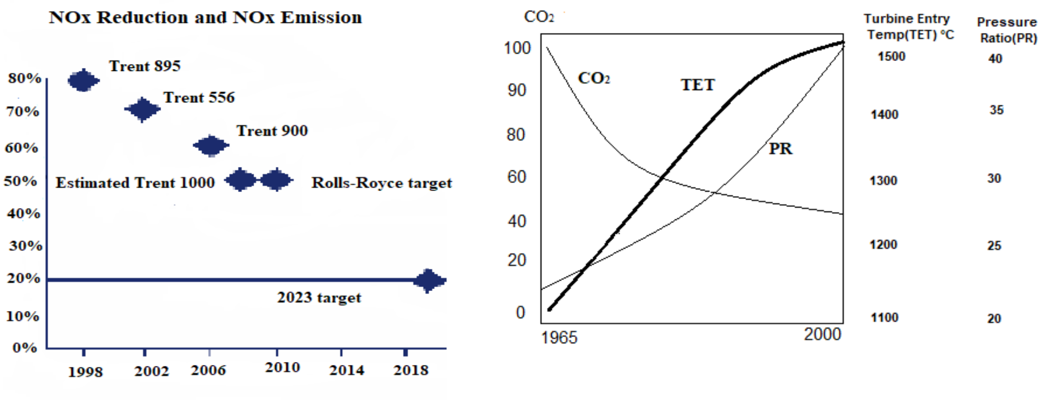

(i) (ii)

Figure 1-3: Level of NOx, CO2 with TET, pressure compression: Reprinted [4] permission from Elsevier License copyright © 2013

The gas turbine (GT) operates by drawing in air, mixing it with fuel, and compressing it, producing high pressure and temperature through the combustion mixture. These gases expand around the turbine blades, which causes them to spin [4]. Up to 20% of all the air is used to cool the hot stage sections, involving the nozzle guide vanes, turbine blades, and discs.

When cooling air is used, the total pressure drops due to irreversible mixing and flow through internal passages, resulting in less work being done. This in turn lowers the mean temperature of the coolant entering the turbine and the engine's overall efficiency. From the gas turbine engine has been hotter at a higher range of temperatures, so it can work more efficiently, however the hotter with high temperature is required the sustainable with longer life materials for handle these heat and temperature. Meanwhile Fig 1.4 shows that operating temperatures are increasing with advances in different types of metal alloys. Specific solidified metals and single crystal alloys are the most effective at temperature distributions.

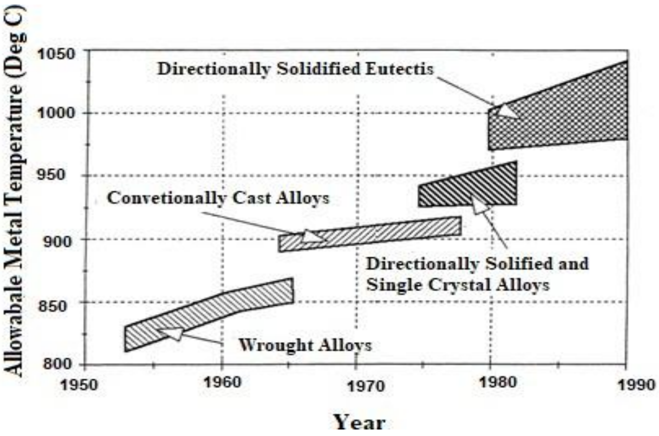

Figure 1-4: Advance in allowable metal temperature: Reprinted [4] permission from Elsevier License copyright © 2013

Furthermore, Watson et al. [5] also states that the gains in cycle efficiency due to an increase in TET can become negligible when significant quantities of cooling air are necessary. The TET must increase at a constant mass flow of cooling air and metal temperature to increase engine efficiency and thrust-to-weight ratio while meeting service life requirements.

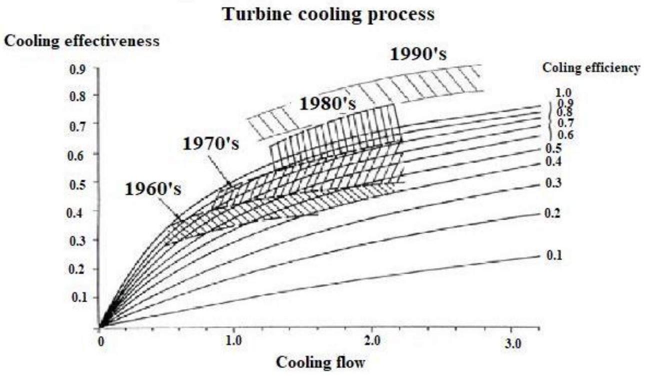

Figure 1-5: Chronological advances in cooling effective versus non-dimensional coolant mass flow: Reprinted [6] permission from Elsevier License copyright © 2013

Therefore, continuous efforts are made to enhance various cooling techniques to accomplish greater cooling efficiency with a reduced coolant flow.
Fig 1.5 [6] shows the efficiency of coolants versus non-dimensional coolant mass flow has changed over time. From the 1960s to the 1990s, the turbine cooling technology improved significantly, with each year seeing enhanced cooling performance and efficiency. Since the 1990s a primary cooling flow was achieved through the use of cooling systems, such swirl cooling methods, which is considered one of the best internal cooling strategies. This technology has the potential to be improved offering better. The internal cooling technology demonstrates good performance, which is a key motivation for this research.

1.1.3 Importance of internal swirl cooling mechanisms in gas turbine engines

This section briefly summarises the history and evolution of multi-stage swirl cooling, a form of internal swirl cooling that is widely used to improve thermal efficiency, heat transfer, and pressure drop of high-pressure gas turbine blades. Internal swirl cooling techniques induce rotational coolant flow within multi-stage internal chambers, improving heat transfer while controlling pressure drop and thereby enhancing overall cooling performance. Meanwhile, a wide range of research has been conducted on single-stage swirl cooling configurations, examining their performance. Consequently, a multistage swirl cooling configuration is being researched, which involves relatively underexplored and sequential applications for the swirl cooling chambers. This is specific area of research in this thesis through investigating the performance and optimal design of multi-stage swirl cooling chambers with a focus on the interaction between fluid dynamics, pressure drop, and heat transfer. This will be investigated for multiple stages including design.

In recent decades, the significance of internal cooling air systems has grown in modern high-bypass aero engines [7]. This is gradually increasing the turbine entry temperature (TET) of the hot gas exiting from the combustion chamber in the primary annulus gas path. This enhances efficiency and the specific fuel consumption (SFC) decreases. Nowadays, these air temperatures are higher than the thermal material limits of the directly exposed blades and vanes and indirectly exposed engine cavities, which makes them hazardous in [8].

Internal cooling systems are made to keep these parts from breaking due to an extreme thermal environment.

In 1962, the Rolls-Royce Conway was the first aeroengine manufactured with a specific internal cooling air system by utilising 2% of the compressor's output as cooling air, the TET could exceed the blade material's melting point by approximately 120K while extending the blade's lifespan. Nowadays, TET can operate at 200K or above the thermal material limits without affecting the life cycle or safety margins [9].

In order to maximise the overall cycle performance, it is desirable to minimise the quantity of cooling air while still ensuring optimal component life. There are primarily two arguments in favour of reducing the quantity of cooling air: first, as the amount of cooling air increases, the thermodynamic cycle performance of the turbine deteriorates as reported in [10]. Second, stage efficiency decreases as the quantity of cooling air re-enter. In another stage efficiency is decreased

1.2 Research Motivation

In engineering design, numerical simulations for predicting structural, fluid, and heat transfer have become increasingly important as computer power has grown over the past few decades. This is applied to the market of aerospace manufacturers, where experiments with a full-size engine are costly, and it is hard to put all the necessary instruments into the engine. Therefore, numerical simulations are preferable, especially from an industrial point of view, because they are cheaper and easier to set up. In the aerospace sector, the effectiveness of thermal management is a critical issue, where the high temperature of gas turbine engines poses a challenge. Due to this high temperature, the convective cooling technique was developed to balance improvements in efficiency and thermal activities, based on a compact design. A major fact to consider is internal swirl cooling, one of the key factors for improving the efficiency of the gas turbine. Swirl cooling is currently underutilised and under investigation by the aerospace engineering sector. There clear a opportunity for swirl cooling innovation and obtain lighter and more efficient design improving the efficiency of the gas turbine blade.

Internal swirl cooling enhances internal heat transfer efficiency in turbines, reducing the mass flow rate of cooling air and blade wall thicknesses to ensure lighter components and greater turbine performance. Therefore, though expensive, full-scale engine tests are essential to validate numerical models and create realistic boundary conditions for complex cooling flows.

Optimisation of swirl cooling technology essential for advancing new technology as mentioned in Xiao et a. [3].

CFD is a powerful tool that helps researchers and designers understand aerodynamic and thermal problems, which means that they do not have to do as many expensive experiments, at least in the early stages of the design process. The numerical investigation for the aerothermal characteristics, interaction between the first stage and combustion chamber of a high-pressure turbine, is presented in this thesis.

1.3 Aim and objectives

The purpose of this research is to use CFD analysis to improve the performance of a generic high-pressure gas turbine blade. The main aim is to enhance leading edge thermal performance by developing the design of internal swirl cooling chambers, within the blade itself.

In order to achieve these aims the following objectives were identified:

1. Using literature, to get the important characteristics of turbine blade operation, cooling methods and approaches to modelling and simulating fluid dynamics and heat transfer.
2. To develop and validate a CFD modeling approach to accurately and reliably simulate the aerodynamic flow around a generic high-pressure blade, the MT-1 design, including the effects of rotor–stator interaction, using experimental data.
3. To develop a separate CFD approach to accurately model internal flow and heat transfer through a swirl cooling chamber by validating with available experimental data.
4. Combine the results from objectives (2) and (3) to simulate conjugate heat transfer within a generic high–pressure turbine blade. This will involve the design of internal swirl cooling channels, including validations in the number of cooling stages.
5. Investigation of the impact of parametric changes, such as critical channel radii, on the design of swirl cooling channels within the turbine blades.

1.4 Contribution

The main contributions of this thesis are:

1. The main contribution is the evaluation of a new swirl cooling concept which is embedded within a generic MT-1 blade. This analysis provides new knowledge about the relation between aerodynamic and thermal interactions for this particular design, something that has not been addressed previously in this way.
2. A detailed CFD comparison is made between single, two-stage, and three-stage swirl cooling chamber studies, including detailed analyses of pressure drop, thermal behaviour and isentropic efficiencies.
3. The proposed single, two-stage, and three-stage configurations are systematically studied with CFD and compared against experimental configurations. The results show clear advantages in both pressure drop and thermal behaviour.
4. Detailed design changes to cooling chambers in the form of varying radii (2mm,4mm and 6mm) are explored and, this is not fully addressed in previous swirl cooling studies, where multi-stage swirl cooling geometry rounding is typically neglected.

1.5 Thesis Structure

The first chapter provided basic background information and theory about high-pressure gas turbine blades, and advanced cooling strategies with a particular focus on swirl cooling.

The second chapter covers relevant literature including a review of existing cooling methods and identifying the research gap, particularly in relation to multistage swirl cooling geometry. Such designs and their cooling principles are explored.

Following the literature review, the third chapter describes the methodology for accurately simulating the flow around a generic high-pressure turbine blade specifically, the MT-1 design. CFD simulations are run in both 2D and 3D the effect of the mixing plane between rotor and stator is accounted for. The approach is validated and based on available experimental data.

The fourth chapter explains the approach for a purely internal flow analysis of a generic swirl cooling geometry. As with Chapter 3, CFD results are compared to experimental data to demonstrate the accuracy of heat transfer modelling.

In Chapter 5, the main elements from chapters 3 and 4 are combined to enable full conjugate heat problems to be defined, including flow around the turbine blade and the separate internal swirl cooling flows. Thermal performance is evaluated for chambers within the cooling passage.

Chapter 6 provides a more in-depth design study for a unique three-stage swirl cooling arrangement. A parametric design study is described which includes a new technique for adjusting nozzles sizes and transitioning from rectangular to round shapes. Candidates for enhanced thermal performance are identified and analysed.

The seventh chapter discusses the outcome and the conclusion of this research study including a summary of the findings of the research work, highlighting the novel contributions, discussion of the results, and suggested future work for this research.

Chapter 2: Literature review of gas turbine blade swirl cooling chambers

2.1 Gas turbine blade cooling

This literature review includes numerical and theoretical analyses, and this present study investigates key concepts in computational fluid dynamics (CFD) and thermodynamics, including turbulence modelling, heat transfer, and wall-treatment methods. All of these areas are essential for accurately predicting the aerodynamic and thermodynamic behavior of high-pressure turbine (HPT) blades and their leading-edge cooling performance. Which is the main focus on this thesis.

Previously, studies have shown that reliable modelling of blade cooling requires an integrated understanding of heat transfer, fluid flow, and gas turbine operating theories. It has been investigated in CFD–based turbine cooling analyses, which highlight the importance of appropriate thermal boundary conditions and turbulence models for capturing fluid flow and heat transfer distributions within these swirl cooling passages.

Therefore, this chapter focuses on a literature review of gas turbine blade cooling, with emphasis on fundamental strategies in single and multi-stage cooling chambers and their parametric studies. By synthesising these established approaches, this literature review justifies the modelling and analysis framework adopted in this thesis, which is directly supported by the research objectives and links prior work to the selected simulation methods and analysis technique.

Working principle of a gas turbine blade

The combustion process is producing a high-pressure gas that expands through the turbine, which produces mechanical work [13]. This combustion generates a high temperature, and flow at this high temperature, and pressure gas enters a turbine, producing this shaft work for the process output to drive the compressors in [14]. The gas turbine is most required split of energy between the shaft work and thrust is enhanced. The gas turbine operation has 4 main processes which is following: (a) isentropic compression (b) Isobaric combustion (constant pressure), (c) isotropic expansion, and (d) while this process heat was rejected. Mechanical energy is irreversibly expressed into pressure and heat energy in an ideal gas turbine when the gas is compressed, as shown in Fig 2.1 [15]. The thermal efficiency of the Brayton cycle, which includes the compressor exit temperature and atmospheric temperature, is the same as that of Carnot efficiency which is the wet steam mixture in the compressor. This is related to the Brayton cycle's considerable temperature, and the heat is added in a combustion chamber and increases the specific volume, along with less loss.

In an the gas turbine engine a irreversible energy is transitions which is reoccurs with an the rotational of a intel new atmospheric air, leading an substitute to heat exits in [16]. When an adiabatic turbine undergoes a steady-flow process, both the pressure at the entrance and the pressure at the exit are constant.

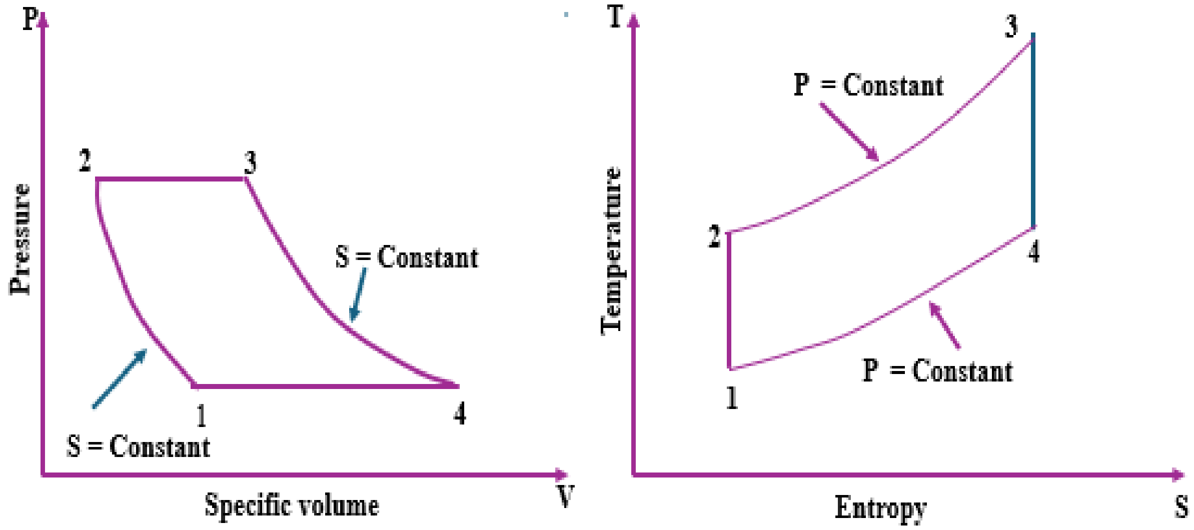

Figure 2-1: Basic ideal gas turbine cycle with P-V and T-S diagram by [13]

So, the ideal process for a turbine is one in which the pressures at the entrance and exit are the same in [17]. The work output comes from the turbine. So, the isentropic efficiency of a turbine is the ratio of the turbine work, and the turbine works through an isentropic process between the same pressures at the entrance and exit, as shown in Fig. 2.1[13].

2.1.1 Turbulence model on heat transfer

The substantial study of this internal multistage swirl-cooling gas turbine blade leading edge is understudied. In this particular case, the combined effects of the swirl cooling geometry, Turbine intensity, pressure loss, and heat transfer performance are unclear. This study fills the gap by using CFD to simulate the thermal behaviour of the leading edge of the internal swirl-cooling high-pressure gas turbine blade.

The correlation between turbulent models and fluid dynamics, and the relatively limited availability of heat transfer models, make temperature behaviour more difficult to estimate precisely [25].

2.1.2 Pressure forces fluid elements

A pressure gradient is a topographical force exerted on the any others surfaces of an element. In addition, a body force could exist because of gravitational potentials, which act on the whole mass of the element [43]. However, this phenomenon can be observed by analysing the pressure exerted on the two x faces, as shown in Fig 2.2 [44]. A shear stress due to viscous forces enters the momentum equation separately from the pressure term.

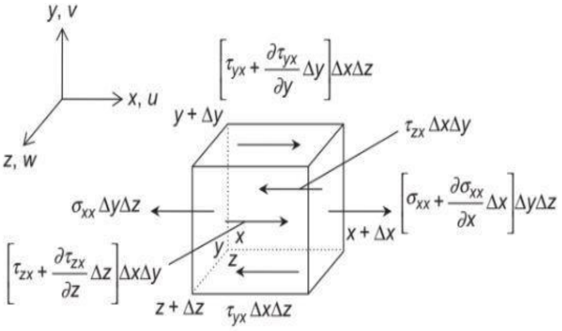

Figure 2-2 Net x force acting on an element as a result of fluid pressure fluctuations, reprinted with the permission from Elsevier Licence [44]

According Ding et al. [44], where the Cartesian frame (coordinates), which is the x, y, and z-axis coordinates, invoked the fundamental law can be:

$$dV = dxdydz \tag{2.1}$$

The x-direction net force acting on the element in Fig 2.2 is obtained as:

$$dF_x = -\frac{\partial p}{\partial x}dV \quad dF_y = -\frac{\partial p}{\partial y}dV \quad dF_z = -\frac{\partial p}{\partial z}dV \tag{2.2}$$

From Eq 2.2 rewrite the vector from;

$$d\mathrm{F}_{press} = -\nabla p dV \tag{2.3}$$

2.1.3 The acceleration of the Fluid flow

Eq 2.3 mentions the Cartesian vector form of a velocity field that exhibits spatial and temporal variation that was re-determined:

$$\mathrm{V(r,t)} = u(x,y,z,t)\mathrm{i} + v(x,y,z,t)\mathrm{j} + \mathrm{w}(x,y,z,t)\mathrm{k} \tag{2.4}$$

This is the most significant variable in fluid mechanics: understanding the velocity vector field is virtually identical to solving a fluid-flow problem in [45]. Furthermore, Georgiou et al. [46] state that a wind tunnel is used to fix the coordinates to watch the fluid passing through a glass window.

The formulation of Newton's second law of the fluid system concerns the computation of the acceleration vector field generated the flow. Therefore, calculate the cumulative time derivative of the velocity vector:

$$\mathrm{a} = \frac{d\,\mathrm{V}}{dt} = \mathrm{i}\frac{du}{dt} + \mathrm{j}\frac{dv}{dt} + \mathrm{k}\frac{dw}{dt} \tag{2.5}$$

2.1.4 Turbulent boundary layer profile

An no-slip condition are states that the solid boundary of the fluid velocity is an equal to the stationary zero velocity boundary wall. This turbulent flow no-slip wall condition is necessary because the tangential velocity fluctuations are reduced by viscous dampening near the flat plate surface in [48].

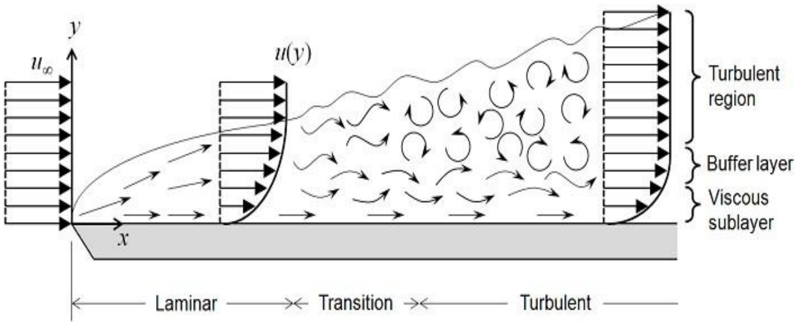

Figure 2-3: Comprehension of the foundation of the boundary layer on a flat plate [50]

As the turbulent kinetic energy flows along with the wall, the amount of gradients in a mean velocity rapidly rises in turbulence in [49]. Fig 2.3 [50] presents the velocity profile throughout the length of a flat plate.

The no-slip condition at the wall creates a boundary layer with large velocity gradients that average to the surface when a uniform free-stream flow meets a flat plate. As mentioned above, the fluid's velocity increases in the viscous sublayer above a flat plate since zero at its surface. Nearby the viscous sublayer, the buffer layer appears while turbulent flow dominates throughout viscous stresses. In that region, the standard flow speed relates to the long distance to the surface.

The log-law area is this charting in semi-log coordinates shown in Fig 2.3 [50]. In the semi coordinates, the regions is plotted with dimensional wall distance y^+ on the horizontal axis vertical axis and dimensionless velocity u^+ on the vertical axies:

$$y^+ = \left| \frac{y u_\tau \rho}{\mu} \right. \tag{2.6}$$

$$u^+ = \frac{u}{u_\tau} \tag{2.7}$$

$$u_\tau = \sqrt{\frac{\tau_w}{\rho}} \tag{2.8}$$

Therefore, u_τ is denoted as the frictional velocity, and the τ_w. is the turbulence fluid wall stress. The primary velocity profilte is divided into outer and inner layers. The near wall (inner) layers comprises sublayers $5<y^+$, buffer layer $5<y^+ < 30$ and a logarithmic regions ($y^+ >30$). However, the upper axes' limit depends on the Reynolds number flow as mentioned in Fig 2.4 [51].

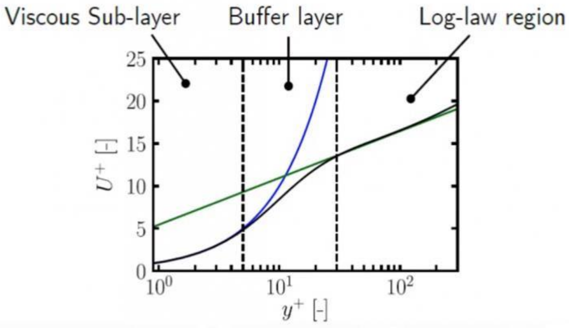

Figure 2-4: Divisions of near–wall regions in a channel [51]

The laminar-turbulent transition and the potential development of laminar separation bubbles in the presence of unfavourable pressure gradients, as depicted schematically in Fig. 2.5 [52]. Qualitatively, the shear stress is shown for turbulence and laminar boundary layers, with natural transition, on a flat plate and in its complete separation bubble. Increasing the boundary layer thickness diminishes shear stress downstream; a considerable increase in shear stress occurs in the transition regions. However, the heat transfer coefficient profile resembles a step in the turbulent transition, with rapid decreases in heat transfer.

Meanwhile, in the presence of flow separation, shear stress is zero, and even the wall shear stress is zero when the velocity gradient is perpendicular to the reattachment points. In the Reynolds analogy, heat transfer at the separation point is very low, and it reaches its maximum in the local thermal boundary layer.

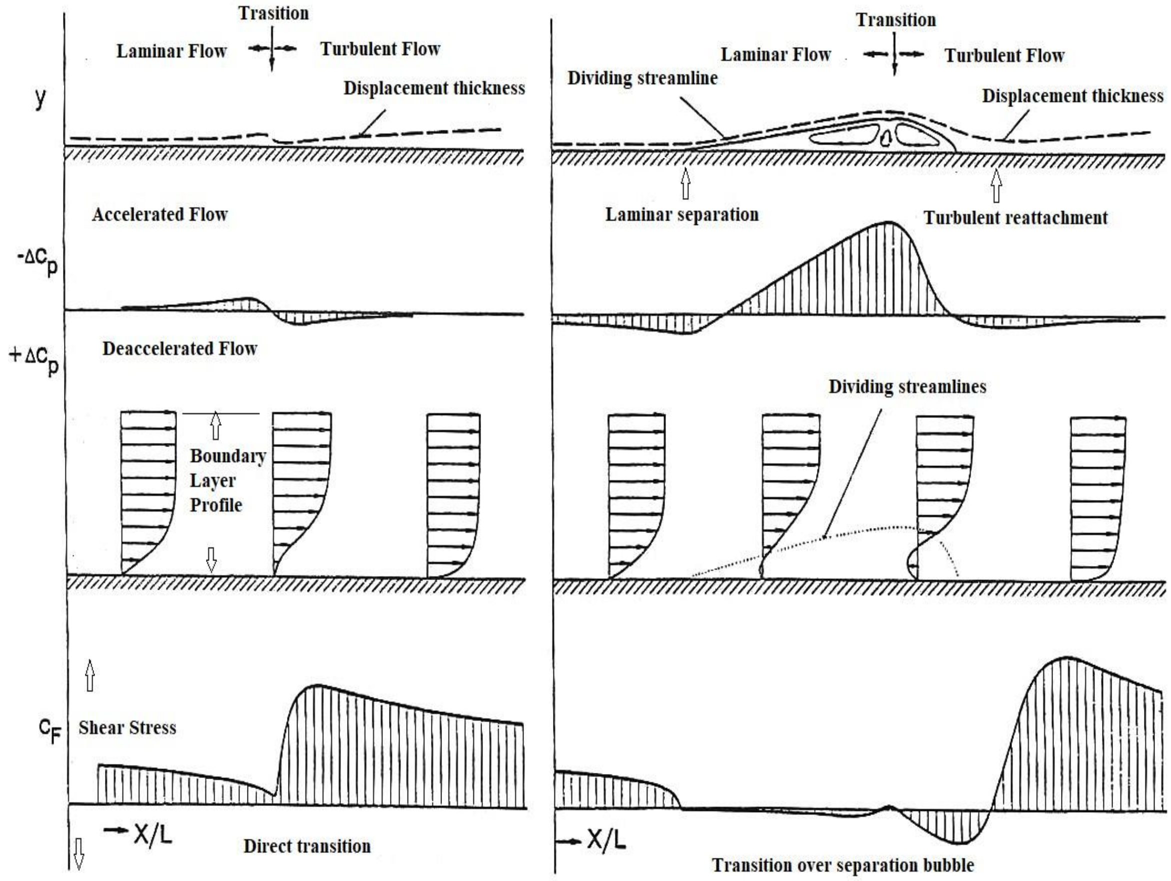

Figure 2-5: Shear stress qualitative distribution along a flat plat, from [52]

2.2 Computational Fluid Dynamics

2.2.1 Introduction

Computational Fluid Dynamics (CFD) is a subdivision of fluid mechanics that use computing resources to solve the governing equations of fluid flow. Utilising numerical analysis and algorithms, it addresses issues related to fluid dynamics. The derived solution comprises a set of pointwise field solutions at various spatial and temporal levels. CFD combines the subjects of computer science, fluid mechanics, and mathematics. CFD approximates a solution for the governing equations when an analytical or theoretical solution is impossible. A typical approach involves experimental or analytical validation to aid with research challenges in heat transfer and fluid dynamics. Nonetheless, CFD appears to be a reliable consideration for several engineers when the fluid flows are very complex in [53]. Furthermore, major CFD challenges involve discretisation error and turbulence modelling [54].

2.2.2 CFD Overview

CFD is used in many engineering applications to model fluid-flow. Fig 2.6 [55] illustrates the three main steps used to generate a CFD model. Initially, in the pre-processing stage, the computational domain includes geometry details (e, g, a high-pressure turbine (HPT) blade). Next the domain is discretised, usually into millions of cells, to create a mesh from which to compute the flow regions, and pre-processing is complete.

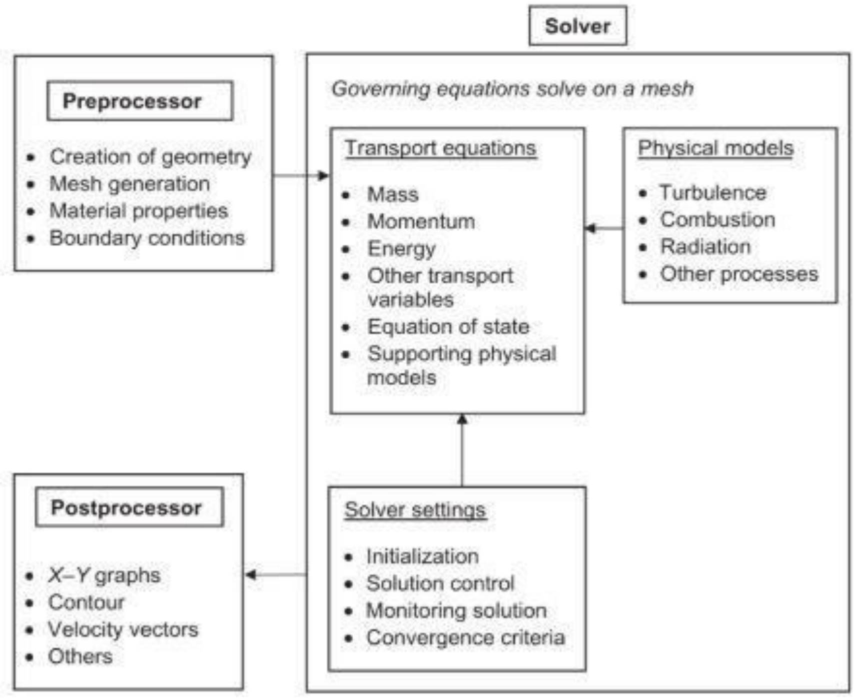

Figure 2-6: CFD Analysis Framework [55]

Once proper boundary conditions have been assigned, these steps involved choosing suitable physical models to represent numerous flow phenomena, such as heat transfer, temperature, and turbulence.

Next, key solution algorithms and solver settings are selected based on critical assumptions (e.g., compressible vs incompressible, unsteady vs steady state, etc.). The governing equations are solved to generate the solution and finally, post-processing completes the process.

2.2.3 Conservation of Laws and the Navier-Stokes Equations

Fluid flow problems can be explained mathematically with the three conservation laws, specifically, the momentum and conservation of mass, and energy [55]. The conservation of mass equation is given below:

$$\frac{\partial \rho}{\partial t} + \nabla \cdot (\rho V) = 0 \qquad (2.9)$$

where ρ, t and V is the fluid density, time and velocity, which is defined as $\vec{V}$ = ui + vj +wk where u, v and w are three-dimensional coordinate directions. The three-dimensional momentum equations are given as:

$$\frac{\partial \rho u}{\partial t} + \nabla \cdot \rho u \vec{V} = \rho g_x + \frac{\partial \sigma_{xx}}{\partial x} + \frac{\partial \tau_{yx}}{\partial y} + \frac{\partial \tau_{zx}}{\partial z} \tag{2.10}$$

$$\frac{\partial \rho v}{\partial t} + \nabla \cdot \rho v \vec{V} = \rho g_y + \frac{\partial \tau_{xy}}{\partial x} + \frac{\partial \sigma_{yy}}{\partial y} + \frac{\partial \tau_{zy}}{\partial z} \tag{2.11}$$

$$\frac{\partial \rho \mathrm{w}}{\partial \mathrm{t}} + \nabla \cdot \rho \mathrm{w} \vec{V} = \rho \mathrm{g}_{\mathrm{z}} + \frac{\partial \tau_{\mathrm{xz}}}{\partial \mathrm{x}} + \frac{\partial \tau_{\mathrm{yz}}}{\partial \mathrm{y}} + \frac{\partial \sigma_{\mathrm{zz}}}{\partial \mathrm{z}} \tag{2.12}$$

where σ_{xx}, τ_{yx} and τ_{zx} characterise stresses in the viscous stress sensor. The stresses acting in the x,y and z directions are represented by $(\sigma_{xx}, \tau_{yx}, \tau_{zx})$, $(\sigma_{yy}, \tau_{xy}, \tau_{zy})$, and $(\sigma_{zz}, \tau_{xz}, \tau_{yz})$, respectively. The body force components g_x, g_y, and g_z are the negligible and are therefore excluded from the momentum equations. The expressions for the individual viscous stress tensors are below.

$$\tau_{\mathrm{xy}} = \tau_{\mathrm{yz}} = \mu \left(\frac{\partial \mathrm{v}}{\partial \mathrm{x}} + \frac{\partial \mathrm{u}}{\partial \mathrm{y}} \right) \tag{2.13}$$

$$\tau_{\mathrm{yz}} = \tau_{\mathrm{zy}} = \mu \left(\frac{\partial \mathrm{w}}{\partial \mathrm{y}} + \frac{\partial \mathrm{v}}{\partial \mathrm{z}} \right) \tag{2.14}$$

$$\tau_{\mathrm{xz}} = \tau_{\mathrm{zx}} = \mu \left(\frac{\partial \mathrm{w}}{\partial \mathrm{z}} + \frac{\partial \mathrm{v}}{\partial \mathrm{x}} \right) \tag{2.15}$$

$$\sigma_{\mathrm{xx}} = -\mathrm{p} + \frac{2}{3} \mu \nabla \cdot \vec{V} + 2\mu \frac{\partial \mathrm{u}}{\partial \mathrm{x}} \tag{2.16}$$

$$\sigma_{yy} = -p - \frac{2}{3} \mu \nabla \cdot \vec{V} + 2\mu \frac{\partial v}{\partial y} \tag{2.17}$$

$$\sigma_{\mathrm{zz}} = -\mathrm{p} - \frac{2}{3} \mu \nabla \cdot \vec{V} + 2\mu \frac{\partial \mathrm{w}}{\partial \mathrm{z}} \tag{2.18}$$

where p is the static pressure and μ is the dynamic viscosity. A combination of these equations (2.13)-(2.18) with equations (2.19)-(2.21) results in a modified constructs a various form of the momentum equations:

$$\frac{\partial \rho u}{\partial t} + \nabla \cdot \rho u \vec{V} = \rho g_x - \frac{\partial p}{\partial x} + \mu \left(\frac{\partial^2 u}{\partial x^2} + \frac{\partial^2 u}{\partial y^2} + \frac{\partial^2 u}{\partial z^2} \right) \tag{2.19}$$

$$\frac{\partial \rho v}{\partial t} + \nabla \cdot \rho v \vec{V} = \rho g_y - \frac{\partial p}{\partial y} + \mu \left(\frac{\partial^2 v}{\partial x^2} + \frac{\partial^2 v}{\partial y^2} + \frac{\partial^2 v}{\partial z^2} \right) \tag{2.20}$$

$$\frac{\partial \rho w}{\partial t} + \nabla \cdot \rho w \vec{V} = \rho g_z - \frac{\partial p}{\partial z} + \mu \left(\frac{\partial^2 w}{\partial x^2} + \frac{\partial^2 w}{\partial y^2} + \frac{\partial^2 w}{\partial z^2} \right) \tag{2.21}$$

These unknown four variables' equations are u, v, w and p. In simple flow cases, they can be resolved numerically without further approximations;

2.2.4 Discretisation and pressure–velocity coupling schemes

Finding an analytical solution to the governing equations is impossible in practical fluid-dynamics problems. This procedure is known as discretisation. There are various discretisation methods, such as Finite Difference, Finite Volume, and Finite Element analysis methods. This study utilises the finite volume method, a prevalent discretisation technique in commercial CFD solvers, to guarantee rigorous conservation of mass, momentum, and energy.

Finite Element Method

The finite element method (FEM) is the primary method used to solve complex simulation engineering problems and is divided into two parts: breaking larger problems into smaller ones. The two simpler parts are elements, which are interconnected through nodes, forming the mesh mentioned by Ryan [38] and Dryden et al.[39]. This polynomial is used to interpolate and characterise the value of the dependent variable at a constant point in the computational domain, as a function of the distance from the constant point to an element's nodes. This polynomial represents any point in the domain of the dependent variable, which involves the distance from the point to the nodes of the element. This method is used for discretisation problems, which create equations for each element, and is applied in various fields, including heat transfer, fluid flow, and structural analysis.

Finite Volume Method

In the finite volume method the domain is divided into small parts control volume where independent variables are characterised by algebraic equations. This finite volume method (FVM) ensures conservation of energy, momentum, and mass, and it is implemented in Ansys Fluent (Version 2022 R2, which was used in this research.

2.2.5 Pressure–velocity coupling schemes

After FVM-based discretisation is used for a computational simulation domain, it is significant to link the pressure and velocity regions by a pressure-velocity coupling scheme. A method of algebraic equations representing the governing PDE's is taken (in terms of independent variable quantities such as velocity, pressure and temperature) there are two common approaches a coupled and segregated. A coupled solver will resolve the algebraic equations for pressure and velocity instantaneously.

This method is often utilised for compressible flow cases. Instead, segregated solvers retain a sequential approach to resolve momentum equations, with the continuity equation (correction of pressure). The semi- implicit method for the pressure linked equations (SIMPLE) method is the most common example of a pressure–velocity algorithm which is utilised a the correct and guess technique in [57]. This couple pressure and velocity equations, where the is pressure region starting with momentum equations are solved some of which acquire intermediate velocities. Further, the velocity regions are corrected accordingly, and the correlations established between the continuity and momentum equations.

However when the SIMPLE method is applied to compressible flow, and it has fluctuations for density. As a couple with between the energy and momentum equations to ensure thermodynamic behaviour.

The pressure region is predicted and represented by p^*. Next this is applied in the momentum equation to resolve for velocities, specifically: u^*, v^* and w^*. These velocities are established with a prediction, the continuity equation used afterwards to determine a new and more correct values of pressure, P_{new} i.e. correction of the pressure. The newly modified pressure quantities ensure that the velocity field relates more intimately to the continuity equation [58]. The SIMPLE technique is exposed to divergence as with any another iterative technique, so the under-relaxation factor, α is elaborated in the correction of the pressure equation.

$$P_{new} = p^* + \alpha p' \tag{2.22}$$

wherever $0 \leq \alpha \leq 1$. If the solver experiences divergence, decreasing the α is recommended to reduce in the difference in pressure per reiterative step encourage convergence. For the definite value of $\alpha=1$, the method decreases to a conventional method.

2.2.6 RANS Models

As previously explained RANS is a common approach for resolving turbulence in aerodynamic analysis in [65]. The computational widely available, and the computational method accurately solves numerical problems. Nowadays, industries require solving fluid flow problems; RANS is very popular for these sectors in [66].

Particularly, there are two significant problems in this RANS model: the first one is that the choice of the turbulence model is strongly dependent on results, and the secondly.

The RANS cannot resolve unsteady flow problems, e.g. if massive flow separation occurs. Moreover, this is more suitable for wind tunnel tests and other aerodynamic applications, and this will conclude the promising output in [66]. This is divided into fluctuating and mean parts:

$$\phi = \phi^{-} + \phi' \tag{2.23}$$

where the time average is a specific time parameter, the mean part, compared to the small, turbulent model, is a bit longer. The Navier-Stokes equations are a set of equivalent equations after applying the Reynolds decomposition and the Reynolds-averaged Navier-Stokes equations[1]. The RANS equations primarily involve qualities based on the Reynolds-averaged approach, which is used in the current solving and the original RANS. Additionally, the producer of time averaging, Reynolds stresses:

$$\tau_{ij} = \overline{u_i' u_j'} \tag{2.24}$$

This mainly describes Reynolds averaging Reynolds closure problems.

2.2.7 Reynolds averaged Navier -stokes equations

The sheer computational power needed for the direct resolution of time dependent Navier-Stokes in turbulent flow problems is totally out of reach. The properties of the time-averaging flow, such as mean pressure and velocities make it impossible model the lifetime of every eddy. For engineering applications, the concept of the average flow captures mean flow properties as shown by Kjishima et al. [67]. A variant of the Navier-Stokes equations is the RANS approach which uses the averaging method without considering turbulent fluctuations. Hence, these RANS equations are essential since they permit flow solutions to be attained more easily. To obtain the RANS equations, it is essential to substitute the standard form of the flow property varying equation from Eq 2.23 obsessed by the momentum equations and the time-dependent Eq are (2.16) and (2.25)-(2.27). As a result:

$$\frac{\partial \rho}{\partial \mathrm{t}} + \nabla \cdot (\rho \nabla) = 0 \tag{2.25}$$

$$\frac{\partial (\rho u)}{\partial t} + \nabla \cdot (\rho u \mathbf{V}) \tag{2.26}$$

$$\rho g_x - \frac{\partial p}{\partial x} + (\mu + \mu_t)\nabla^2 u \tag{2.27}$$

---

[1] Visit the additional approaches and compressive analysis (E,g Favre averaging) [184].

$$\frac{\partial\rho\overline{\mathrm{v}}}{\partial \mathrm{t}} + \nabla\cdot\rho\mathrm{v}\overline{\mathrm{V}} = \rho \mathrm{g}_{\mathrm{y}} - \frac{\partial\overline{\mathrm{p}}}{\partial \mathrm{y}} + (\mu+\mu\mathrm{t})\left(\frac{\partial^2\overline{\mathrm{v}}}{\partial \mathrm{x}^2} + \frac{\partial^2\overline{\mathrm{v}}}{\partial \mathrm{y}^2} + \frac{\partial^2\overline{\mathrm{v}}}{\partial \mathrm{z}^2}\right) + \left[-\frac{\partial(\rho\overline{\mathrm{uv}})}{\partial \mathrm{x}} - \frac{\partial\left(\rho\overline{\mathrm{v}}^2\right)}{\partial \mathrm{y}} - \frac{\partial(\rho\overline{\mathrm{v}}\hat{\mathrm{w}})}{\partial \mathrm{z}}\right] \tag{2.28}$$

$$\frac{\partial\rho\bar{w}}{\partial t} + \nabla\cdot\rho\bar{w}V = \rho g_z - \frac{\partial\bar{p}}{\partial z} + (\mu+\mu t)\left(\frac{\partial^2\bar{w}}{\partial x^2} + \frac{\partial^2\bar{w}}{\partial y^2} + \frac{\partial^2\bar{w}}{\partial z^2}\right) + \left[-\frac{\partial(\rho\bar{u}\bar{w})}{\partial x} - \frac{\partial(\rho\bar{v}\dot{w})}{\partial y} - \frac{\partial\left(\rho\overline{w^2}\right)}{\partial z}\right] \tag{2.29}$$

2.2.8 Turbulence modelling

The Navier–Stokes equations can fully explain flow behaviour in laminar flow approaches. In such problems, these equations can be solved numerically without added approximations, and they can also be resolved analytically in some examples. Conversely, in turbulent flow systems, different flow variables (e.g., pressure, velocity, etc.) needs additional assumptions and approximation to solve the flow properties, which is described in [60]. To refer the characteristics of the stochastic turbulent flow, fluid characteristics are coupled as the combination of two components: (i) these mean values are ($\bar{u}$, $\bar{v}$, $\bar{w}$, and $\bar{p}$) and (ii) are the fluctuations (u\`, $v$\`, w\`, and $p$\`). These all are mathematically characterised as below:

$$\mathrm{u} = \mathrm{u}^{-} + \mathrm{u}` \tag{2.30}$$

$$\mathrm{v} = \mathrm{v}^{-} + \mathrm{v}` \tag{2.31}$$

$$\mathrm{w} = \bar{\mathrm{w}} + \grave{\mathrm{w}} \tag{2.32}$$

$$\mathrm{p} = \mathrm{p}^{-} + \mathrm{p}` \tag{2.33}$$

$$\vec{\mathrm{V}}{\rightarrow} = \bar{\mathrm{V}} + \grave{\mathrm{V}} \tag{2.34}$$

From the equations (2.30) (2.34) a compressible form of the RANS equations is obtained and these are commonly used in commercial CFD solvers such as Ansys Fluent which is used in this. Where, u, $v$and z of the velocity of the fluid $x, y,$ and z directions, meanwhile the static pressure is the p and the velocity vector is the $\vec{\mathrm{V}}{\rightarrow}$, additionally, the descriptions of mean $\bar{\varphi}$ of time-averaged property, however, the variation of the temperature $\varphi(\mathrm{t})$ is known as:

$$\varphi^{-} = \frac{1}{\Delta t}\int_0^{\Delta t}\varphi(t)dt \tag{2.35}$$

2.2.9 Mesh methods

The mesh module was discretization on domain, with these module dimensions and classification of grid components can influence the quality of CFD outcomes. High-quality cartesian meshes may be readily generated in straightforward flow via cooling channels.

The 3D challenges, attaining high-quality meshes necessitate increased work and time. Numerous techniques exist for addressing complicated geometries, with three prevalent approaches being:

1. Body- filled.
2. Structured block.
3. Unstructured mesh.

In body-fitted approaches, the flow region is changed onto a simple shape and then edge spacing are used to make the mesh structure. Fig. 2.7 [55] shows body fitted mesh in a computational domain. The body-fitted methodology has a main drawback in a substantially complex domain, it can repeatedly construct reduced cells in the grid, leading to unpredictable behavior.

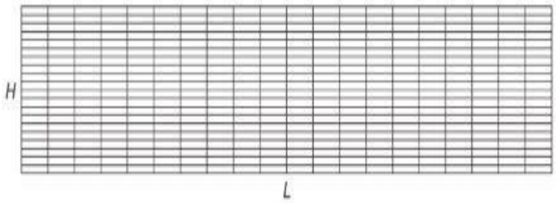

Figure 2-7: Computational structure mesh by [55]

Consequently, it is only suitable for simple geometries. Alternately, block-structured meshes depend on the computational domain being decomposed and split into other sub-blocks, each meshed discretely. This technique permits the mesh density to be dominated to be enhanced around the region of interest (e.g., in the bluff wake body). An alternative ordinary meshing method is the unstructured technique, which has flexibility that is specific for complicated geometries. Cell sizes are adjusted to change and deal with complicated shapes, including large and small regions. Fig. 2.8 [59] illustrates an unstructured mesh with refinement near a 2D cylinder. This method commonly requires less computational resource requirements and time to execute than the abovementioned methods.

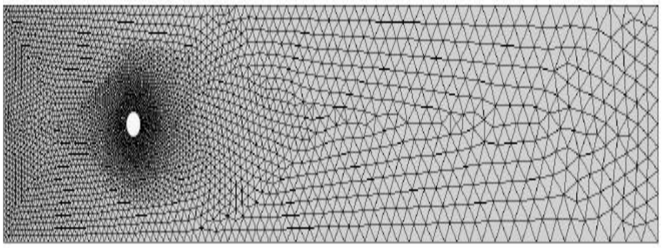

Figure 2-8: Representative of an unstructured triangular mesh [59]

2.2.10 Mesh quality

The mesh quality in each cell of the domain is essential for the suitable convergence of CFD solutions; higher quality improves the probability of convergence. Numerous cell quality metrics are retained in commercial CFD including ANSYS.

Common metrics includes:

- Ratio of aspect – the ration of the minimum and maximum length of an edge, per cell.
- Equiangular of the skew – the internal angles of the cell measure distortion.
- Equitize of the skew – the cell edge lengths measure distortions.
- Volume – the cell volumes aspect ratio.

The pronounced "skewness" of mesh components extensively affects accuracy and solution stability, making the evaluation of skewness necessary. Cell skewness is the variation of a selected cell's form from that of an ideal symmetrical cell. The Equiangular skew criterion is an established metric for assessing skewness, defined as follows:

$$\mathrm{Q_{SK}} = \max\left(\frac{\theta_{\mathrm{max}}-\theta_{\mathrm{eq}}}{180-\theta_{\mathrm{eq}}}, \frac{\theta_{\mathrm{eq}}-\theta_{\mathrm{min}}}{\theta_{\mathrm{eq}}}\right) \tag{2.36}$$

where θ_{max} and θ_{min} characterise the maximum and minimum internal angles of a given cell, respectively, and θ_{eq} signifies the angle corresponding to an ideal cell devoid of alteration, where $\theta_{\mathrm{eq}} = 60^{\mathrm{o}}$ for tetrahedral and triangular elements, and $\theta_{\mathrm{eq}} = 90^{\mathrm{o}}$ for hexahedral and quadrilateral elements. Maximum skewness estimates should not surpass 0.95 (ANSYS). When the maximum skewness reaches 0.95 or higher, the solver may encounter convergence concerns. Sometimes, these challenges can be relieved by modifying the solver settings, such as reducing under-relaxation factors; however, it is commonly necessary to improve the mesh quality. Table 2.1 explains the different cell quality categories matching the skewness criteria.

Table 2-1: Cell quality classification (Ansys, 2023).

Quality	Classification
$QSK = 0.00$	Perfect
$0.00 < QSK < 0.25$	Excellent
$0.25 < QSK < 0.50$	Good
$0.50 < QSK < 0.75$	Fair
$0.75 < QSK < 0.90$	Poor
$0.90 < QSK < 1.00$	Very Poor
$QSK = 1.00$	Degenerate

Another essential quality standard is the cell aspect ratio, which measures the degree of deformation of mesh cells. Usually, inside boundary layers, the aspect ratios of hexahedral and quadrilateral or wedge cells should not surpass 10:1. Equally, in areas distant from walls where flow gradients are less, the aspect ratios must not surpass 5:1.

2.3 Boundary condition of flow phenomena

Boundary conditions are essential since they define the flow conditions and they are an important part of the CFD calculation method. Many categories of boundary conditions accessible in commercial CFD software such as ANSYS Fluent.

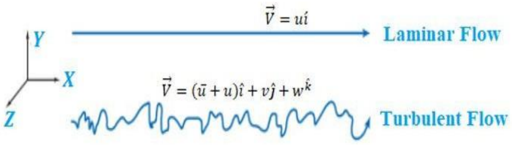

Figure 2-9: Particle path lines - 3D turbulent and 1D laminar flows [61]

The walls are one of the most general boundary categories. Every wall in a solution domain can be appointed as a no-slip condition or full-slip and can be described as moving or stationary. Here, in the case of stationary no-slip walls, the cells at the wall surface are allocated a zero velocity. On the other hand, for the case of zero-slip and full-slip conditions these are related to a surface in the moving walls. The inlet and outlet these boundaries should indicate the pressure, free-stream velocity, or mass flow rate. As their names suggest velocity inlets need the velocity of the free stream to be proposed, and for outlet pressure, the set of static pressure (atmospheric pressure) needs to be suggested. The location of inlet and outlet boundaries is considerable within free-air or wind tunnel simulations. Generally, the inlet must be located suitably upstream of the object (e.g., aerofoil) to accept the flow to be fully developed. Also, the outlet must be placed downstream of it, and this allows turbulent wakes to be fully acquired, specifically in the case of direct aerodynamics. Fig. 2.9 [61] presents an average time description of the velocity of a fluid calculated at the detail for together laminar and turbulent flow.

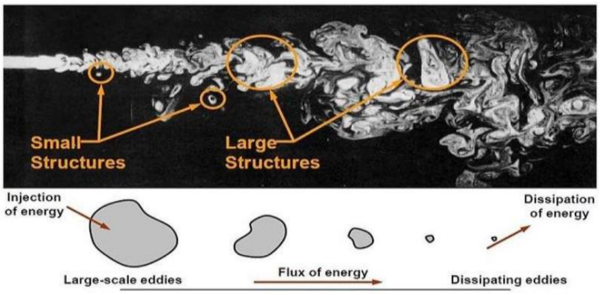

Figure 2-10: Top: The image appears the presence of the different structures size in the different types of flow [62]

In a real fluid, turbulent fluctuations vary in all directions. In the turbulent flow problems, rotational flow (turbulent eddies) are caused by mixing, and these turbulent eddies have a wide range of sizes, from large eddies spanning meters in scale to small eddies.

By interfering with the main flow, the largest eddies may drain energy from it. The large eddies stretch and generate smaller eddies, making additional smaller eddies. As shown in Fig. 2.10 [62] the energy cascade is movement of kinetic energy from large to smaller and smaller eddies.

For the smallest turbulent eddies, scattering kinetic energy is transformed into thermal internal energy. The kinetic energy dominates the flow, and turbulent exchanges dissipate in this energy initiating the losses. The Navier-Stoke equations have been used for solving the flow and simulation problems, such as steady state-related problems. However, this direct numerical simulation (DNS) and large eddy simulations (LES) for near wall simulation problems RANS equations [45]. The shared computational requirement to complete the external aerodynamics DNS models means that this methodology is completely out of scope and will be for periods as reported by Tsubokura et al. [66]. LES has a high computational order but is not as effective as DNS. There are studies of LES near the body of the bluff as described by Sandreh at el. [47] and Cantrak et al.[48] which provide insights into the aerodynamics.

2.3.1 Eddy viscosity

The method of RANS itself computes the average and time-average of flow variable quantities. The turbulence model's effect considers the implied flow by determining the Reynolds stresses in Eq (2.33) -(2.25). There are some different types of turbulence models, including the mixing length models, two- equations *k-ε*, and *k-ω* models and Reynolds Stress Model [63]. The primary variation involving these models is how to calculate the model of the Reynolds stresses. This has been upfront on the replacement of the Reynolds stress relations by the mean flow of the viscous stresses, and significantly, these substitutions are stated in conditions of mean quantities, and not instantaneous ones. In the 1877 Boussinesq proposed that the Reynolds stress to the main deformation rates as mathematically described in the equations below;

$$\tau_{xy} = \tau_{yx} = -\rho\bar{\bar{u}}\bar{v} = \mu_t\left(\frac{\partial\bar{v}}{\partial x} + \frac{\partial\bar{u}}{\partial y}\right) \tag{2.37}$$

$$\tau_{xz} = \tau_{xy} = -\rho\bar{u}\grave{w} = \mu_t\left(\frac{\partial\bar{w}}{\partial x} + \frac{\partial\bar{u}}{\partial z}\right) \tag{2.38}$$

$$\sigma_{xx} = -\rho\overline{u^2} = 2\mu_t\left(\frac{\partial\bar{u}}{\partial x}\right) \tag{2.39}$$

$$\sigma_{yy} = -\rho\bar{v}^2 = 2\mu_t\left(\frac{\partial\bar{v}}{\partial y}\right) \tag{2.40}$$

$$\sigma_{zz} = -\rho\overline{\grave{w}^2} = 2\mu_t\left(\frac{\partial\overline{w}}{\partial z}\right) \tag{2.41}$$

where eddy viscosity or μt is turbulent

The mixing length, which is a zero equation models, represents a solution to the problem. It approaches an eddy viscosity that describes momentum transfer in a fluid flow under the turbulent Reynolds stresses. A consequence of diffusion convection of turbulent descriptions in the fluid flow permits one to characterise the impact of turbulence models on average flow in basic algebraic equations for eddy viscosity as a function of location. Nevertheless, experimental explanations show that turbulence generally changes itself to limited conditions. Hence, additional models, such as the k-ε model, consider the impacts of convection and diffusion in other turbulent measures, such as the turbulent kinetic energy or the dissipation rate. This is completed by solving other transport equations in [64].

2.3.2 *k-ε* Models

This *k-ε* model is a RANS type turbulence model where two additional transport equations are invoked: the *k-ε* model is one of the oldest turbulence models. The standard *k-ε* model account for diffusion and convection properties of two transport equations, for '*k*' the turbulence kinetic energy, and *'ε'* the rate of dissipation of turbulence of flow, as given by:

$$k = \frac{1}{2}(\overline{u'^2} + \overline{v'^2} + \overline{w'^2}) \tag{2.42}$$

The *k-ε* transport equations defined as:

$$\frac{\partial(\rho k)}{\partial t} + \nabla \cdot (\rho k \mathrm{V}) = \nabla \cdot \left[\left(\mu + \frac{\mu_t}{\sigma_k}\right)\nabla k\right] + P_k - \rho\epsilon \tag{2.43}$$

$$\frac{\partial(\rho\varepsilon)}{\partial t} + \nabla \cdot (\rho\varepsilon\mathbf{V}) = \nabla \cdot \left[\left(\mu + \frac{\mu_t}{\sigma_\varepsilon}\right)\nabla\varepsilon\right] + C_{1\varepsilon}\frac{\varepsilon}{k}P_k - C_{2\varepsilon}\rho\frac{\varepsilon^2}{k} \tag{2.44}$$

where, P_k is the turbulent kinetic energy production, ϵ is the turbulent dissipation rate and σk is turbulent Prandtl number for *k* [68].

2.3.3 *k-ω* model

The *k-ω* is another RANS type turbulence model; this invokes two transport equations, for *'k'* and *'ω'* which is the specific dissipation rate [69] where:

$$\omega = \frac{\varepsilon}{k} \tag{2.45}$$

The *k-ω* transport equations are presented below:

$$\frac{\partial(\rho k)}{\partial t} + \nabla \cdot (\rho k\mathbf{V}) = \nabla \cdot \left[\left(\mu + \frac{\mu_t}{\sigma_k}\right)\nabla k\right] + P_k - \beta^*\rho k$$

$$P_k = 2\mu_t S_{ij} S_{ij} - \frac{2}{3}\rho k \nabla \cdot V, S_{ij} = \frac{1}{2}\left(\frac{\partial U_i}{\partial x_j} + \frac{\partial U_j}{\partial x_i}\right), \mu_t = \rho \frac{k}{\omega}. \tag{2.46}$$

where, V is the velocity mean vector, ρ is an density, μ is the molecular viscosity, μ_t is turbulent viscosity, k turbulent kinetic energy, ω is the specific dissipation rate, and S_{ij} is the mean strain-rate tensor. Following a change to the standard *k-ω,* model a change was implemented by linking both *k-ω* and *k-ε* models to create another turbulence model, the Shear Stress Transport (SST) *k-ω* model as reported by Mentor et al.[70]. By dealing with the *k-ε* turbulence model in the free-stream and the near- wall regions where development pressure gradients generally ensue, the SST *k-ω* provides a useful turbulence model as described in [64].

Spalart Allmaras Model

The Spalart -Allmaras (SA) model is an one- equation eddy viscosity model which computes modified turbulent kinetic viscosity. This transport equation is;

$$\frac{\partial \tilde{v}}{\partial t} + U_j \frac{\partial \tilde{v}}{\partial x_j} = C_{b1}(1 - f_{t2})\tilde{S}\tilde{v} + \frac{1}{\sigma}[(v + \tilde{v})\nabla^2 \tilde{v} + C_{b2}|\nabla \tilde{v}|^2] - \left(C_{w1} f_w - \frac{C_{b1}}{\kappa^2} f_{t2}\right)\left(\frac{\tilde{v}}{d}\right) \tag{2.47}$$

where, ν is an molecular velocity, *d* is an wall distance and $S^{\tilde{}}$ is vorticity modified magnitude. The SA models are give good performance for attached boundary layer flows, however is it less precise in separated or free shear flow cases.

2.4 Mixing plane

The mixing plane is one of the key elements of turbomachinery simuation**;** the basic principle of the mixing plane concept is that each fluid zone is treated as a steady-state problem and handled separately. Flow measurements at the mixing plane interface are averaged in the circumferential direction on the stator outlet and the rotor inlet borders at some predetermined iteration interval, as studied by Chen et al. [71]**.** The stator blade is a stationary part that guides the flow in a particular direction, and the rotor blade is a dynamic (rotational) part that extracts energy from the flow past the stator blade.

2.4.1 High-pressure gas turbine blade (HPT) mixing plane

This section on mixing plane methodology includes 2D and 3D stator and rotor mixing plane, which consists of the pressure drop and heat transfer in each stator and rotor blade. Nonetheless, the stator remains in a steady state, and while the rotor is in a dynamic state, the heat transfer through the stator and rotor blades is critical for evaluating the thermal performance and efficiency of the turbomachinery.

In the application of CFD for turbomachinery rotor–stator interactions are modelled at lower computational cost using the stable mixing-plane technique, which has been widely used in compressor and turbine-stage research. Instead of transient sliding-mesh simulations, the mixing-plane method circumferentially averages flow quantities at the rotor–stator interface to eliminate blade-passing effects and maintain the mean flow. A robust, computationally efficient model of stage-averaged flow behaviour, suitable for parametric analysis, was used in this work (Fig. 2.11 [72]).

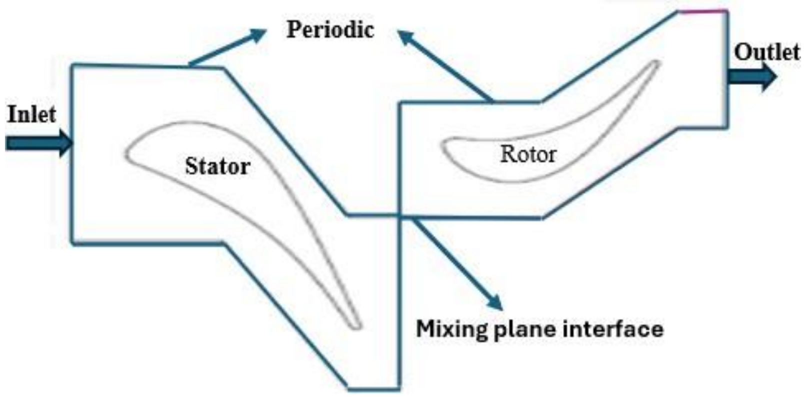

Figure 2-11: Mixing plane stator and rotor blades [72]

A circumferential averaging operation must be done on the rotor-stator interface to pass flow information through it, and it is referred to as the mixing plane approach, where a rotor and stator interaction is accomplished by exchanging circumferentially averaged flow volumes. This mixing plane means that the blade wake or separation phenomena during the blade passage are combined before entering the downstream component. As a result, velocity and pressure components are uniform in the circumferential direction as the rotating speed increases. The mixing plane interface flow variables are:

$$\bar{\phi}(r) = \frac{1}{2\pi}\int_{0}^{2\pi} \phi(r,\theta)d\theta \tag{2.48}$$

where, r is a radius distance from the axial rotation, θ is the circumferential angle around, ϕ is an parameter variables, and ϕ^{-} is an flow variable. Meanwhile the mixing plane continuity condition is:

$$\int_{A} \rho V \cdot ndA = \int_{A} \rho \overline{V} \cdot ndA \tag{2.49}$$

Here, A is the area of the mixing plane (which is the interface between stator and rotor blades), ρ is a surrounding fluid density, $\overline{V}$ is a velocity vector for the instantaneous interface, V adjacent domain average velocity vector. n is the number of sections at surface area of mixing plane blades, and dA is an element area of the surface of in both blades.

The mixing plane technique is the most popular rotor/stator modelling approach in turbomachinery industries as described by Buckers et al. [73]. This method supposes that boundary condition types have been established at the mixing plane interface.

The “mixing plane pair” is the union of an upstream outlet boundary zone and a downstream inlet boundary zone; these border zones must be of the following types to produce mixing plane pairs ANSYS Fluent, as described in Table 2.2.

Table 2-2: Stator and rotor blade mixing plane study by [74]

Upstream	Downstream
Pressure outlet	Pressure inlet
Pressure outlet	Velocity inlet
Pressure outlet	Mass flow inlet

These mixing plane boundary condition types are particular to the solver implementations, which is facilitating information across the flow domain of the mixing plane. However, there are no particular mathematical definition for this mixing plane instead there is numerical implementations of the averaging process**.**

2.5 CFD analysis of gas turbine leading edges

The CFD represents a powerful instrument that supports researchers and designers in understanding aerodynamic and thermal issues, reducing the need for expensive experimental activities. These activities are dedicated to developing the validation and application of a methodology for an integral CFD simulation of the turbine and combustor. Yao et al.[75] state complete that a steady-state three-dimensional numerical simulations of single-stage and multi-stage swirl cooling with the configurations shown in Fig 2.12 [75]**.**

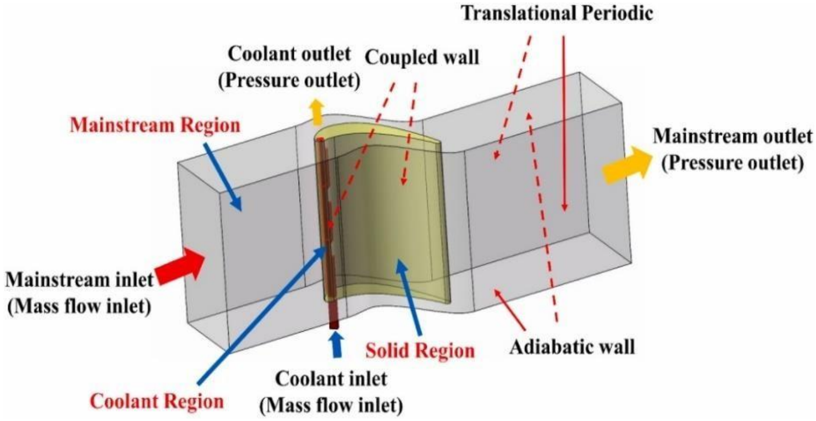

Figure 2-12: Computational domain and boundary condition in the multi-stage chamber (MSW) [75]

A coolant and mainstream are set as ideal gas air, and fluid dynamics numerical simulation has been used to find the stagnation temperature of the leading edge of a gas turbine blade. This temperature is then compared to a reference wall temperature.

2.5.1 Swirl cooling gas turbine blade leading edge

The leading-edge swirl cooling system was achieved by a thorough experimental, numerical, and optimisation study to observe the complex flow field and heat transfer.

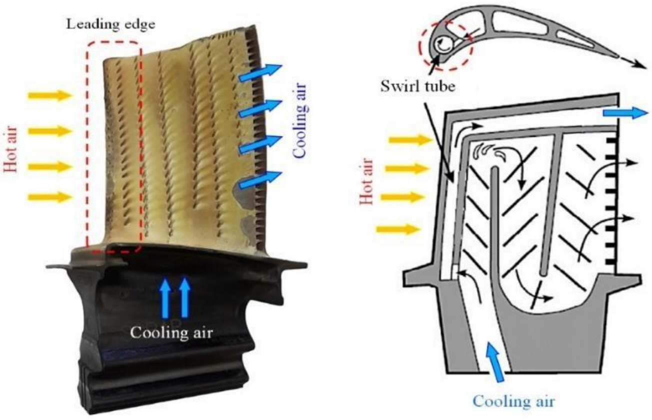

Figure 2-13: Turbine blade model and cross-sectional with leading-edge swirl tube [76]

According to the Yao et al. [76] air is cooled by going through these holes from the hub to the blade's tip. A machine called an air compressor makes this cool air. In a gas turbine, the fluid on the outside is usually a very hot around 1500 K was reported in [76]. Leading-edge swirl cooling generates secondary vortical motion in the internal cooling flow by adding tangential momentum, which improves near-wall mixing and local heat transfer coefficient in high-load places. Heat transfer, pressure loss, and coolant mass flow vary with impingement cooling, serpentine ribbed channels, and film cooling for turbine blade cooling. Swirl cooling is desirable near the leading edge because it enhances heat transfer with a compact passage geometry, but pressure losses and manufacturing complexity make it less popular than other cooling methods (Fig. 2 .13 [76]).

2.5.2 Swirl cooling

The tangential inlet ports in the cooling route in this shape generate swirl by imposing a circumferential velocity component that directly influences the swirl number in Eq. (2.54). i_ϕ and dividing from the radial tube R to the axial momentum i_z the flow is expressed as follows:

$$S = \frac{i_\phi}{R i_z} = \frac{\int_{r=0}^{R} \rho U_z U_\phi 2\pi r^2 \,\mathrm{d}r}{R \int_{r=0}^{R} \rho U_z^2 2\pi r \,\mathrm{d}r} = \frac{\int_A \rho U_z U_\phi r \,\mathrm{d}A}{R \int_A \rho U_z^2 \,\mathrm{d}A} \qquad (2.50)$$

Here U_z and U_ϕ are the axial and circumferential velocity components, respectively. The swirl number depends on the local conditions and decreases as the circumferential velocity changes downstream over the length of the tube. The downstream velocity field establishes the local swirl number, which cannot be predicted.

Moreover, based on the conditions at the inlet, a geometrical swirl number can be used to distinguish between the different shapes of the swirl tubes that have been studied. Considering the axial, and tangential velocities a continuity equation can be defined as follows terms:

$$\rho U_\phi A_{\text{inlet}} = \rho U_z A_{\text{tube}} \tag{2.51}$$

Assuming the constant velocity over the cross-sectional, the swirl number yields that it can be expressed as follows:

$$S \approx \frac{\rho U_Z U_\phi \int_A l \, \mathrm{d}A}{R\rho U_Z^2 \int_A \, \mathrm{d}A} \approx \frac{\rho l U_Z U_\phi}{R\rho U_Z^2} = \frac{l U_Z^2 A_{\text{tube}} / A_{\text{inlet}}}{R U_Z^2} = \frac{l A_{\text{tube}}}{R A_{\text{inlet}}} \tag{2.52}$$

Where l is the lower angular moment is, the geometrical swirl cooling only depends on the inlet and tube cross section and not on the velocity. The tube of single and multi-inlet configurations has been studied in different types of swirl cooling numbers, *S*, and various Reynolds numbers as reported in [77].

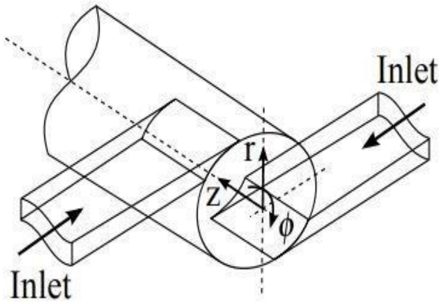

Figure 2-14: Baseline swirl tube geometry and the user coordinate system by [78]

However, there are three various ways to specify the flow rate while configuration have a multiple inlet chamber. Meanwhile this tube has two tangential inlets in the experimental and numerically studied swirl cooling range of the Reynolds number and both swirl cooling outlet geometries, as shown in Fig 2.14 [78]**.** The relatively simple geometry is designed to assist in understanding more about the complex physical mechanisms in swirl cooling chambers. The geometry has several inlet nozzles and the additional inlet nozzle further down the length of the chambers enhances the swirling flow and make the heat transfer more evenly along the length of the chambers, as shown in Fig 2.11 [78].

In addition, the air flow is dispersed throughout the intake, which minimises the maximum jet velocity at the inlet and, consequently, the pressure loss in the tube for this investigation.

Therefore, tube radius R, this channel height is H and weight is W, and the inlet nozzle is number N. The geometrical swirl chambers are presented in Fig 2.15 [78]. In this module swirl chamber configuration was defined by the geometric swirl number, $Sgeo$, is defined as:

$$S_{\text{geo}} = \frac{(R-h/2)\pi R^2}{Rhwn} \tag{2.53}$$

where R is a radius, h is an height w is an width, and n is the number of blades.

The swirl cooling gas turbine blade has been widely utilised in modern gas turbine blades design. Since swirl cooling is a promising alternative to internal cooling techniques at the leading edge of the blade due to its significantly enhanced heat transfer, it is crucial to comprehend the fundamental flow and heat transfer behaviour of swirling flows to guide improved swirl cooling design in today's advanced turbine blades. Swirl cooling flows have a net positive effect on the performance of gas turbines, however, because turbine cooling flows bypass the combustor, some work is lost.

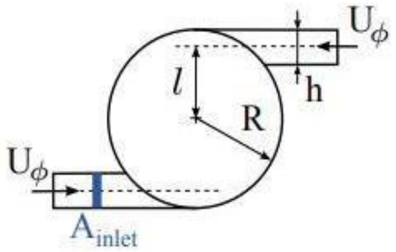

Figure 2-15: Swirl tube tangential inlet [78]

Swirl cooling flows permit a more significant temperature, resulting in a net increase in gas turbine power production and improved efficiency. There are two solution approaches for both inside and outside of the axial and circumferential: (1) main mass flow dominated, and the next one is (2) main swirl tube dominated. The high discharge coefficient is present at the low swirl main mass flow, which was selected as the first solution. The main swirl tube (considered the second one) is present at extensive (high) pressure loss regions with reverse velocities as reported in [79]**.** This research work was further continued Mager et al. [80], who determine that the analytical and pressure distribution are reasonable.

In addition Kobiela et al. [81] examined further this swirl cooling in terms of pressure distribution and analytics, finding that the swirl tube centre has a backflow axial direction for the pressure gradient. The pressure and centrifugal forces decrease due to the length of the swirl cooling tube. The low swirl of the axial pressure loss is responsible primarily for the axial direct flow in the whole tube using a negative axial pressure gradient $\partial p/\partial z$. The swirl reduction leads to a vortex core, a positive axial pressure gradient develops and makes a reversal flow. To maximise backflow, the pressure gradient by the tube axis must be zero: $\partial p/\partial z = 0$.

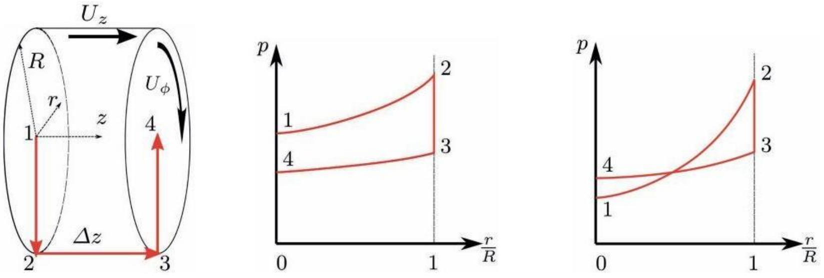

(a) **(b)** **(c)**

Figure 2-16: The pressure distribution in a swirl tube: (a) The tube segment for pressure drop is considered, (b) the low swirl number, and (c) the high-pressure number by [81]

Fig 2.16 [81] shows the short segment of the pressure distributions as stated by Kobiela et al. [81]. The pressure distribution along the discussed path from 1 to 4 appeared low, as shown in Fig 2.16 (b) and (c) in the high-pressure number. Position 1 is located in the tube centre, and this path directs to the tube wall (2), followed by pressure increases in centrifugal force. Linking 2 and 3, the tube length Δz in this section causes more pressure drops due to more friction between points. At point 3 to 4, pressure will decrease due to the centrifugal force. As the swirl has reduced, the pressure drop is less substantial than the increase between 1 and 2. In the case of a sufficiently robust swirl, the pressure at point 4 is above that at point 1; similarly, for a weak swirl, the pressure at point 1 is more significant than at point 4. With this consideration, Kobiela et al. [81] analytically estimated that the swirl cooling number S_{limit} for the swirl tube centre pressure axial gradient disappears. However, due to this, presumptions of a solid body rotation in the swirl tube disregarded the narrow band potential vortex in the outer tube. Therefore, the circumferential velocity may be expressed as:

$$U_\phi = \omega r \tag{2.54}$$

where ω is the angular velocity which is around the radius r. The yield radial pressure distribution is as follows:

$$p(r) = p_{\text{center}} + \int_0^r \rho\omega^2 \tilde{r}\, \mathrm{d}\tilde{r} = p_{\text{center}} + \frac{1}{2}\rho\omega^2 r^2 \tag{2.55}$$

Based on these constrained cases, the tube centre axial velocity is zero and an axial velocity increase near the wall $U_{z,w}$:

$$U_z(r) = \frac{U_{z,w}}{R} r \tag{2.56}$$

The axial velocity is presumed to be constant in the axial direction. Considering an angular and axial momentum balance throughout the tube section, which includes swirl tube and pressure loss owing to wall friction, the axial velocity near the wall is determined as reported in [81].

$$U_{z,w} = R\omega. \tag{2.57}$$

For information about the momentum balance and the direct computation, the viewer is directed to the original study as mentioned in [81]. Ultimately, the velocity components are included into the swirl number as per Eq (2.62), and Uz, w is substituted with Eq (2.56):

$$S = \frac{\int_{r=0}^{R} \rho \frac{U_{Z,w}}{R} r\omega r 2\pi r^2 \, \mathrm{d}r}{R\int_{r=0}^{R} \rho \left(\frac{U_{Z,w}}{R} r\right)^2 2\pi r \, \mathrm{d}r} = \frac{\int_{r=0}^{R} \rho 2\pi \omega^2 r^4 \, \mathrm{d}r}{R\int_{r=0}^{R} \rho 2\pi \omega^2 r^3 \, \mathrm{d}r} \tag{2.58}$$

2.6 Geometrical model of the single-stage and multi-stage swirl cooling

The swirl cooling structure used in this work is integrated into the leading edge of a high-pressure turbine (HPT) blade with a linear cascade as reported in [82]. The chord length of the high-pressure turbine blade, *C,* the pitch of the blade, *P,* the height of the blade, *H,* and the diameter of the blade leading edge, D_L, are important parameters. The typical single-stage swirl cooling model is made up of a cuboid coolant chamber, a cylindrical vortex chamber, and six tangential nozzles. First, coolant goes into the coolant chamber. Then, it goes to the vortex chamber through the six tangential nozzles, with the chamber length, *L*, and width, *W*, respectively, as shown in Fig 2.17 [75] (a). The nozzles have length and width, the vortex chamber has a diameter, and an angle between the tangential direction and the *x*-axis. The places where the centre of the single-stage swirl cooling with six nozzles (N=1) are shown in Fig 2.17 (b).

The multi-stage swirl cooling models have two configurations including two and three stages (N=2 and N=3), respectively. The specifications of these in terms of nozzles, coolant chamber, and vortex chamber are identical to those of the single-stage model (N = 1). Moreover, the vortex chamber has two or three stages, each with the same number of nozzles (three or two), as shown in Fig 2.17 (c). The coolant enters the subsequent stage after passing through one, two, or three of the first stage's six nozzles rather than all six simultaneously.

Other important parameter includes, the conjunction section between two adjacent stages, *e*, the stage-entrance displacement, *h,* and the length, *l,* respectively. The most significant improvement in heat transfer characteristics that multi-stage swirl cooling provides comes at the expense of a more significant overall pressure loss. However, the pressure loss can be significantly reduced by making the bends between the adjacent stages round, which raises the thermal performance of the multi-stage swirl cooling models over that of the single- stage model.

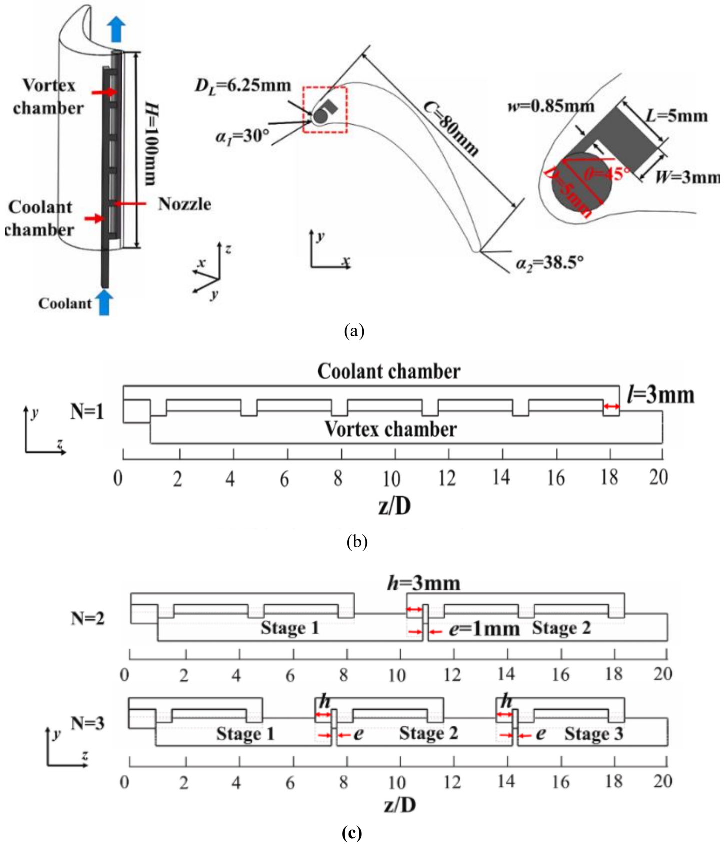

Figure 2-17: Geometry specification (a) Blade model, (b) single stage, and (c) multi -stage swirl cooling. Adapted from [75].

2.6.1 Experimental investigation for swirl cooling tube

Over the last 60 years there have been many scientists who have experimentally studied swirl cooling flow through tubes, and an overview of key a literature is shown in the Table 2.3. The first person who proposed this was in [83] where convective heat transfer enhancement was to used through the swirl cooling flow in swirl tubes. There are four suggested methods for swirl cooling flow: (1) vortex ramp, which is followed by the first and second ones; (2) tangential injection nozzle; (3) strip insert twisted; and (4) twisted tube. The heat transfer coefficient for axial flow in swirl cooling is four times larger, which was observed in those methods (as mentioned above, serial numbers (1 to 4) [83]. Later, other scientists studied the swirl cooling tube used as water flow or air flow as the working fluid, these were researched by Mentor et al. [70, 64, 71].

However five nozzles for a single stage chamber were studied by Nakajima et al. [72,73,74] and Cheputech et al.[76]-[82]. During the 1980s turbine blade cooling as investigated, and inlet and outlet tangential injection in a turbine blade was reported in [91]. Meanwhile, Khalatov et al.[92,93] studied swirl cooling in a gas turbine blade leading edge by using conical nozzles. Kitoh et al.[94] investigated the potential turbulence stresses of the vortex-type velocity for the circumferential profile at the swirl tube entrance. Dhir et al.[95]-[97] researched two different types S= 2.78 and 5.23 of swirl cooling flow tangential injections (nozzles) with straight outlets. It has been concluded that the heat transfer enhancement for two types of mechanisms include [63], (1) Elevated maximum axial velocity adjacent to the wall which enhances the heat flow from the wall and (2) enhanced turbulence levels are found by improving the mixing in particular region of the swirl cooling tube flow region. Furthermore Glezer et al.[98,99] researched turbine blade swirl cooling flow in a like test case of the engine, and it was investigated experimentally to monitor heat transfer in the rotating swirl cooling channels at a 20,000 Reynolds number, as shown in Fig 2.18.

The implications of rotation values ranging from 0 to 0.023 determined that they significantly improve internal heat transfer. Further investigation Lingrani et al.[100,101,102] Connell et al. [103], and Lingrani et al.[104] found that the tangential jet wall flow with a different Reynolds number outlet radial introduces a local heat transfer swirl cooling structure. Infrared thermography was used for heat transfer, thermocouple measurements, and boundary conditions.
Nozzle flow visualisation identified interaction in different sizes as shown through Gortler vortex pairs Fig 2.18 [99]. With ranges from 1,200 to 7,200 the Reynolds number was investigated. Larger Reynolds numbers decreased the size of the Gortler vortex pair as they become more unsteady. Lingrani et al.[105]-[91] mainly considered different types of Reynolds numbers in swirl cooling chamber techniques.

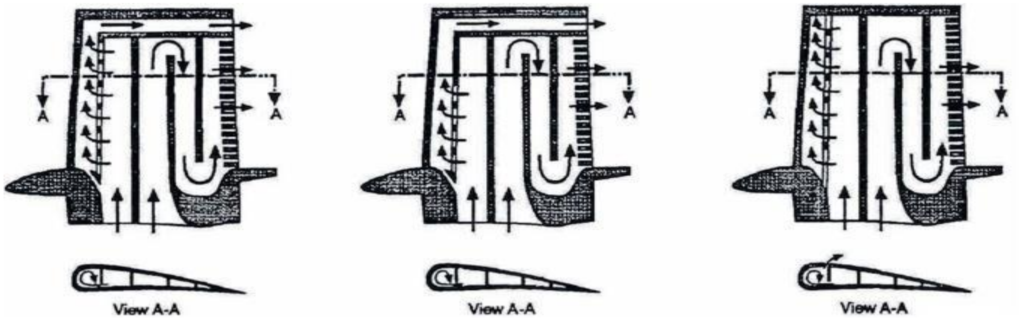

Figure 2-18: Representation view of swirl cooling configuration by [99]

Choi et al.[106] reviewed a technology for aerothermal swirl cooling applied to aerospace engineering. They calculated the hydraulic and thermal performance based on the pressure losses and heat transfer in the swirl cooling chambers as shown on the Eq 2.58.

$$(\overline{Nu}/Nu_0)/(f/f_0)^{1/3} \tag{2.59}$$

This Nusselt number correlation was provided and linked with literature data from Glezer et al.[98] and Lingrani et al.[102] which involved further investigation of the same swirl cooling chamber geometry but with a variation in heat transfer. The same swirl cooling geometry has two axial displacements: a tangential flow inlet and a radial outlet and retained the tube inlet temperature as the reference temperature and determined the heat transfer using thermochromic liquid crystals with a transient approach.

Further, the experiment used hot wire by using the Colburn analogy to find heat transfer in the curved surface of the near-wall. Schiffer et al.[107] investigated the rotation effect on the swirl cooling chamber. However, they observed that the critical flow is in swirl cooling chambers, and pressure is developed by using the side section for rotation flow.

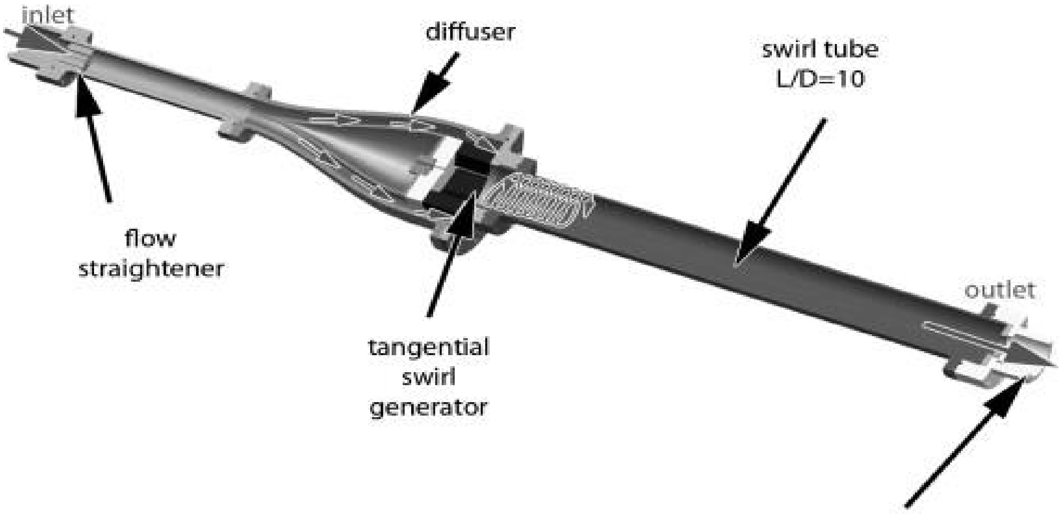

Figure 2-19: CAD – Model of the swirl tube complete set up and visualization of the flow [109]

Following Schiffer et al.[107] further research Grudmann et al.[108, 109, 110] used 3D high-resolution measured water flow regions by using magnetic resonance velocimetry (MRV); this was a novel contribution. Meanwhile, they researched the range between 1 and 5 for the swirl cooling chamber; this complete measurement was provided for the swirl cooling chamber inlet and outlet flow region; however, the outlet and bend of this swirl cooling chamber's flow field are round, which is 180°.

The final output for this research indicated that a stable flow region structure characterised the swirl cooling chamber. This indicates that the swirl cooling chamber can also accommodate complex geometry, as depicted in the Fig 2.19 [109].

Further, researched by Kobiela et al.[81] utilised the transient liquid crystal technique was used experimentally with a PIV method to measure the flow regions on the same experimental swirl cooling tube (ring). Meanwhile, the Reynolds number ranged from 10,000 to 40,000 and 2.36 to 5.89 for single stage swirl cooling chamber numbers was investigated. The axial outlet consisted of a swirl cooling ring/ chamber. The researcher detected the heat transfer scattering visible in the secondary swirl structure, and they estimated the 'Gortler vortex pairs' appearance.

The researcher presumed that no 'Gortler vortex pairs' appear at turbulent flow, as investigated at the high Reynolds numbers, as shown in Fig 2.20. Further investigation by Quian et al.[111] and Harvey et al.[112] concentrated on these swirl and impermanent cooling channels with constant mass flow. In particular Quian et al.[111] investigated the Reynolds number range between 33,000 to 80,000 (here will Re_{jet} = 125,000-300,00), and the 'sublimation naphthalene method' was used to find out the measurement of heat transfer with different cooling Reynolds numbers. Impingement cooling on the leading edge shows maximum higher heat transfer with same baseline geometry, however the averaged Nusselt number is more (20% increases) in swirl cooling chamber and higher (20% increases) heat transfer activities as compared to baseline and impingement cooling geometry with constant pressure drop for all cases. Ling et al.[113] researched decreasing the taper to reduce the size in the outlet region of the swirl cooling chamber tube diameter with this new, and reduced model with the swirl tube baseline model and this baseline model constant diameter.

The tapered and reduced diameter module has an outlet of 2/3, and the inlet is 1/3; the researcher took the outlet to inlet reduce the diameter. These modules compared with Reynolds number (*Re* =10,000), which is constant for both cases; the researcher has observed the downstream region heat transfer is (*x/R* =7-8) and concluded the tapered model (with an inlet ratio of 1/3, and outlet ratio of 2/3) both demonstrated that heat transfer was enhanced by 23% and 17 % respectively compared to the baseline.

Ekkada et al.[114] Investigated the merge between two cooling systems in a geometry containing impingement and swirl cooling channels with internal injection (nozzles) connected between two cooling systems. This is a complete U–bend size design for cooling; based on this merging technique, a pressure drop occurs with heat transfer through cooling with the constant mass flow in each region for injection nozzle, as shown in Fig 2.20 [114].

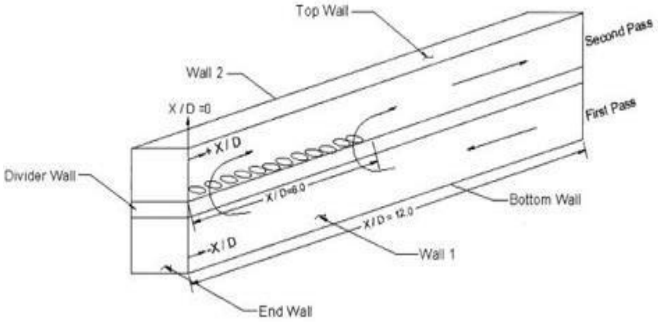

Figure 2-20: Schematic diagram for the combination of swirl and impingement cooling duct [114]

Few experimental studies have been conducted on swirl cooling of gas turbine blade leading edges. Over the last 60 years, numerous scientists have experimentally investigated the swirl cooling flow gas turbine leading edge in [80] and the enhancement of convective heat transfer through swirl cooling flow tube [78].

The suggest four different methods involving the swirl cooling flow, such (1) vortex cooling, (2) tangential injection, (3) twisted strip insert, and (4) twisted tube, the swirl cooling in the vertical cylindrical as shown in Fig 2.21.

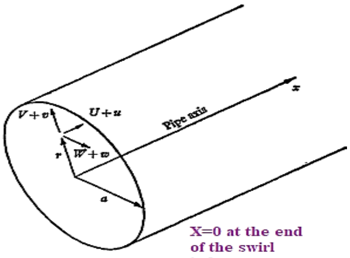

Figure 2-21: Schematic geometry of co-ordinates of swirl cooling tube by [85]

Further swirl cooling by Nissan et al.[85] were studied with three factors considered including (1) tangential, (2) wall pressure drop, and (3) boundary layers. This experimental study showed the pressure drop behaviors in a tube of two diameters with a four-length pipe.

Grudmann et al.[108] Conducted experimental studies on two–dimensional slot jets and single-stage round jets, focusing on the maximum heat transfer in cylindrical heat transfer tubes. These studies modified these configurations to reduce both heat transfer and pressure drop.

Experimental apparatus

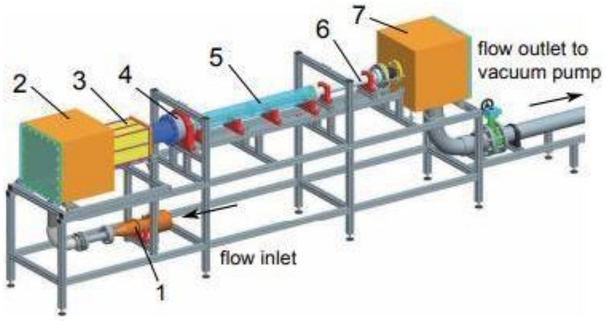

Figure 2-22: Experimental apparatuses (CAD) with (1) Laminar flow,(2) Inlet plenum,(3) mesh heater/seeding chamber,(4) Swirl generator,(5) swirl tub,(6)outlet tube, by [115]

An example of experimental measurement equipment to study is swirl tube apparatus, as shown in Fig 2.22 [115]. The open-loop facility is driven by a central vacuum pump not shown in Fig 2.22, and the air enters a laminar flow element. The effects of a three-dimensional flow field on heat transfer and film cooling on an end wall, suction, and pressure surface as reported in [116]. A blade utilises low-speed vortex, secondary flow, and nozzle wake to enhance heat transfer, thereby improving film cooling on the suction vane surface. The heat transmission and film cooling processes on the annular vane passage surface are studied. Salcudean et al.[117] found that the effectiveness of the film cooling by measurements from a flame ionisation detector technique. The first study of film cooling in this geometry differs from that of Mack and Moyle. They utilised three rows of 15 to 44-degree holes, and as expected, the ratio of the two experiments. This simulation work has been compared with experimental data, decreasing the different types of film cooling sizes by changing the direction of film cooling flow and the inlet and outlet angles. The *k-ω* turbulent model was used throughout these simulations to improve gas turbine blade pressure drop and thermal efficiency. The cylindrical cyclone and the design of the cylindrical swirl cooling region of a three-dimensional stream are suggested in [118]. The method of the three-dimensional flow utilised two immiscible liquids and investigated the design and parameters of the three-dimensional turbulent flow cylinder. Further Foster et al. [119] internal cooling gas turbine blades that are centrally balanced with high external heat loads and the studied tip section of the gas turbine blade. To improve the inlet temperature of the gas turbine blade and suggest a non-traditional film cooling technique based on the application of this swirl-dominated flow in the internal channel of the blade leading edge, an experimental study was conducted. The *k-ω* turbulent model was employed throughout these simulations, with a circular swirl cooling tube. A constant Reynolds number was maintained throughout the simulations improving the isothermal efficiency and pressure drop of these models.

Table 2-3: Experimental investigations for swirl cooling chambers (tube) – highlighting the researchers ' work

Author	Year	$Re_D \times 10^{-3}$	Highlighting research work
Kreith and Margolis [83]	1959	10-140	The Main research focuses on the swirl cooling tube on the flow surface heat transfer (Twisted strip, coiled wire, axial outlet water)
Nissan et al.[85]	1961	5-25	Experimentally, pressure drops were measured using three or four types of factor swirl decay to investigate the behaviour of pressure drop and heat transfer.
Kreith and Sonju [78]	1965	10-100	In the study, both experimentally and numerically, twisted tape and swirl decay were used to investigate the pressure drop across a range of Reynolds numbers, from lower to higher.
King et al. [84]	1969	$10 - 25$	The leading research focused on the swirl cooling tube used as water flow or airflow as the working fluid in this water swirl decay.
Weske et al. [116]	1974	10- 30	This experimental research focused on the rotating tube, which was made up of Plexiglas with a straight pipe tube, using a guide vane angle 60, 45, 30, 5 and 0 degrees as concluded based on the angle and tube diameter to find the velocity behaviours.
Hay et al. [120]	1975	10-49	This research was experimentally studied using the constant swirl cooling tube to measure the variation swirling motion on downstream and the constant 90-degree angle of the swirl tube S= 6.65-3.0. The axial outlet concludes this swirl tube's final pressure drop and heat transfer behaviour.
Akiyama and Ikeda [121]	1986	$30 - 100$	This research experimentally carried out, particularly in swirl cooling pipe flow section is made of eight nozzle inlets, which was tangentially connected between each nozzle energy and pressure loss were studied.
Kitoh [94]	1991	$40 - 80$	The experimental research was carried out during the entire work, and this analysis observed the velocity variations to use lower to higher Reynolds numbers for $S = 1.0$ swirl cooling tube flow turbulent stresses, axial outlet.
Dhir et al. [95]	1992	$10 - 53$	This research was focused on improving the efficiency of the heat transfer for swirl cooling flow S= 2.78, 5.23 tangential inlet.
Kumar and Conover [118]	1993	$15 - 60$	Cylinder type of swirl cooling flow with used inlet and outlet tangential as aspect ratio was 2 and 4 researched on visualization in water with variation of the Reynolds number.

Author	**Year**	$\boldsymbol{Re_D}$ $\boldsymbol{\times 10^{-3}}$	**Highlighting research work**
Reader-Harris [87]	1994	$10-10^4$	Using the Navier – Stroke equations, swirl cooling analytical swirl decay was solved; however, this was fit with the swirl cooling downstream tube to find the heat transfer behaviour.
Chang et al.[96]	1994	12.5	In this experimental research, different types of injections (nozzles), which are sized between 88.09 in the side tube and outside the 1.5 m cylinder tube or the S = 2.67, 7.84 axial outlet, conclude the heat transfer activities in this model.
Chang and Dhir [97]	1995	12.5	As following the in [96], further research was carried out; this was the same tube and specification(S= 2.67,7.84 axial outlet) was used in this experiment, but there mentioned two main activities of heat transfer were observed: first was higher heat transfer was produced near the wall, and next one the middled region more turbulence activities for swirl cooling tube.
Qian et al. [111]	1997	$32-77$	In experimental studies, researchers used Goertler vortices, which are part of a thermal boundary layer, to compare impingement and vortex cooling; they found that using impingement as a baseline and validating with vortex cooling led to a 20% higher Nusselt number and a steady pressure drop.
Glezer et al. [122]	1998	20	Experimentally studied the swirl cooling flow with the rotating channel, 90° bend outlet, and this research concluded the heat transfer and pressure drop by using the swirl tube rotating for injection (nozzle).
Ligrani et al. [102]	1998	1-18.5	This research was done on the experimentally one/two inlet/s, tangential outlet; however, in this swirl, cooling the “Goetker vortices (embedded term boundary)” to find the heat transfer and pressure drop.
Moon et al. [103]	1998	0.24-1.9	This research investigated the swirl cooling tube lengthwise tangential injections. The initial (inlet) injection (nozzle) was higher (the jet slot height, which includes the channel diameter and length) than the outlet tube with constant Reynolds, concluding the behaviour of the heat transfer in the swirl tube.
Steenbergen and Voskamp [89]	1998	50,300	This experiment research was done in the ample swirl cooling pipe S = 0.1 water, swirl decay, and with different types of two Reynolds numbers. A researcher concluded the behaviour of the friction in the two Reynolds numbers.

2.6.2 Numerical study of gas turbine blade design

Additionally, the overview of the numerical swirl cooling chambers literature review is mentioned in Table 2.4. Biegger et al.[115] numerically studied the behaviour between the turbulent stress transport *k-ε* eddy viscosity model; the finite volume method has been used to perform a contrast of the closured Reynolds-stress transports module (RSM) with the *k-ε* eddy viscosity model in the fluid flow region; moreover, the researcher has observed in the swirl tube that by using the Reynolds-stress transport module (RSM), the downstairs sublayer of fluid was returning. This is the velocity predicted in the turbulent field.

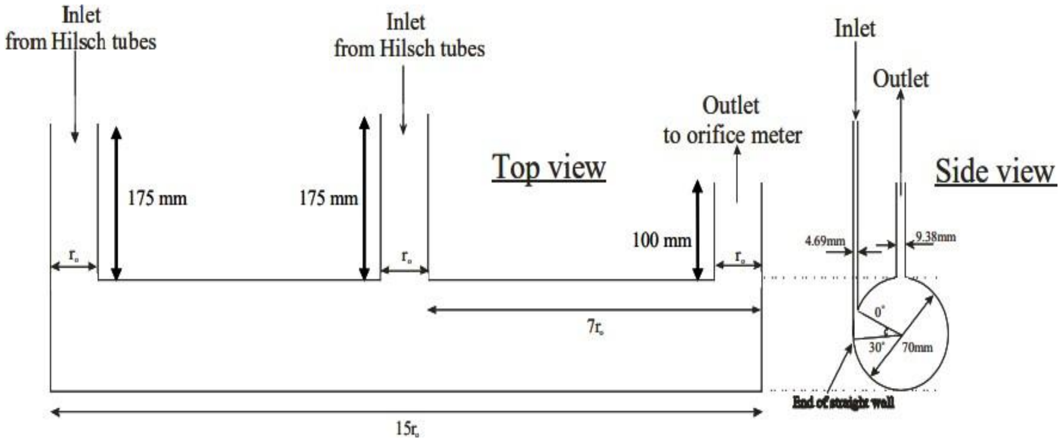

Figure 2-23: Representation of the vortex chamber tube diagram [112]

These are all stable agreements for both module measurements. Sydem et al.[123] also confirmed the explicit 'algebraic Reynolds-stress model (EARSM) using the 'standard *k-ε* eddy viscosity model'. In the turbulent swirling flow, a vortex breaks down the RSM simulation. The researcher found that a *k-ε* fails to predict the occurrence of breakdown; however, vortex breakdown is reasonable to expect in the RSM. Additionally, this extra work combines the cooling flow tube studies with the RSM and eddy viscosity mentioned by Jakirlic et al. [124], and Chen et al.[125] such as following this, Varna et al.[88] Counted the same swirl cooling chamber geometry for the heat transfer behaviour, which has been investigated and considered as one radial and two axial inlets, tangential and outlet. Researchers have found that the heat transfers from the numerical and experimental results matched well; however, close to the wall, the flow does not separate well when using *k-ε* turbulent model, as shown in Fig 2.23 [112]. Paik et al.[126] looked at the swirl cooling flow utilising a Detached Eddy Simulation (DES) method for modelling turbulence for abrupt expansion. The Reynolds number and swirl numbers ranged from 30,000 (3.0 x 10^4) to 100,000 (1.0 x 10 ^5) and from 0.17 to 1.23, respectively. The turbulent flow field reasonably satisfies numerical and experimental results Liu et al.[127] in further internal swirl cooling simulation investigations.

There are two rectangular sections in the inlet, which produces tangential flow in the swirl pipe. The Reynolds number is constant for all three cases of injections (nozzles) to investigate the pressure drop and heat transfer for this swirl cooling tube, using this same geometry as Hay et al.[120]. They proposed the schematic swirl cooling chamber geometry specification as shown in Fig 2.24 [127].

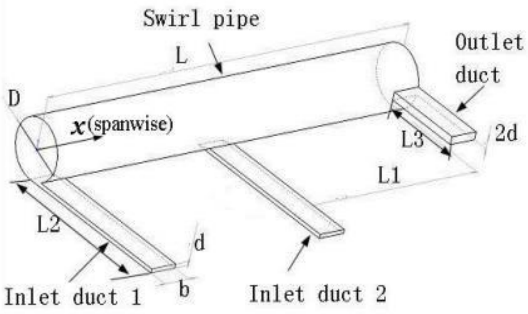

Figure 2-24: Schematic geometry for the swirl cooling chamber specifications [127]

Numerical studies the swirl cooling tube using the Reynolds number range 10,000 to 40,000 with swirl number of 2.36 to 5.3 is mentioned in [128]. Furthermore, Kobiela et al.[81] found that numerical investigation of the temperature behaviour is more in the swirl cooling chamber tube flow. Choi et al.[106] investigated the same geometry specifications, and the same swirl cooling geometry. Further research by Speziale et al. [129] studied that the eccentric opening and centred outlet orifices shape variable, concluding that both numerical and experimental data presented good validation. Furthermore another types of double swirl cooling chamber tube (DSC) is a another different type of swirl cooling technique proposed by Kusterer et al. [130] where the double swirl cooling (DSC) was merged between two swirl cooling tubes (two vortex tube). Validated with CFD results for thermal performance found a link between heat transfer and pressure drop with the single stage swirl cooling chamber tube. Caretto et al.[131] found that the three-dimensional boundary layer flow mainly depends on (1) the variable of the velocity and pressure, (2) the condition of the number of staggered, interlacing grids, each of which is associated with (3) the main upwind difference and (4) the solution of the algorithms implicit steady state. Bunker et al.[132] did numerical calculations to examine various techniques for minimising tip leakage flow and heat transfer on the GE-E high-pressure turbine (HPT) rotor blade. This simulation work maximises the leakage flow and heat transfer distribution in the swirl cooling blade. This CFD results were compared with experimental results with. Liu et al.[133] showing that a numerical study that made it possible to predict the swirl cooling of a model of the cooling passage.

The simulation of the swirl cooling tangential inlet jets in a circular pipe was compared with available experimental data. However, the circular pipe features a single rectangular tangential inlet jet or two rectangular tangential jets, which are used for pressure drop and heat transfer. Grundmann et al.[109 a] studied the comparison of three different internal cooling configurations of the leading edge of a turbine blade through**,** impingement cooling, swirl cooling, and double swirl cooling. Their numerical investigation considered, various nozzle directions for better pressure drop and thermal efficiency and these CFD results were validated with experimental results.

Lin et al. [111] introduced the double swirl cooling system (DSC) cooling technology, and based on the model, they attempted to increase the gas turbine inlet temperature and improve the thermal efficiency of the gas turbine leading edge. Instead of the single cooling chamber, the double cooling chamber system is better for higher heat transfer and lower pressure drop; the swirl cooling DSC cooling configuration specification is shown in Fig 2.25 [135].

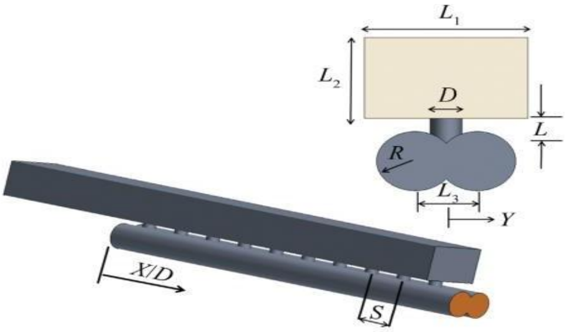

Figure 2-25: Schematic double swirl cooling (DSC) configurations [135]

Karsten et al.[109 b] conducted a numerical study on the three types of film holes to investigate the effect of coolant swirling motion on film cooling efficiency. This film's cooling effectiveness and heat transfer coefficients for injection was beneficial. In additional Bunker et al. [132] investigated the double swirl cooling mechanism technology, which involves the flow of the gas turbine system's vortex cooling mechanism, leading-edge analysis, and its impact on heat transfer and friction. Based on this double swirl cooling model, it decreased the pressure drop and improved thermal efficiency, and these CFD Results were validated with experimental results.

Table 2-4: Numerical investigations for swirl cooling chambers (tube) – highlighting the (researchers) work

Author	Year	$Re_D \times 10^{-3}$	Highlighting their research
Hogg and Leschziner [136]	1989	-	Finite volume method was used in this simulation $k - \epsilon$, RSM was major part to find the thermal performance and heat transfer
Spall et al., [137]	1995	10	It has been showed the ‘sampling – based dynamic process’ by using this $k - \epsilon$, EARSM by increasing the numerical results on discretization method, and Richardson extrapolation technic were used for the 2D model at constant Reynolds number.
Spall and Ashby [123]	1999	130	Used the flat duct to find out the swirl flow pressure drops and heat transfer by suing this RSM $k - \epsilon$, turbulent models
Chen and Lin [125]	1999	$Re_{in} = 125$	Two different types such as 2.25m and 0.85 were investigation by using this RSM, $k - \epsilon$, quadratic pressure-strain model, and conclude the 0.85 is the good for validation for both pressure distribution.
Jakirlić et al. [115]	2002	50	Validation between the experimental and numerical data from using this Eddy-Viscosity Models (ESM) and RSM on single swirl cooling tube rotational flow. To observe the behaviour of the pressure distribution on the tube
Kazantseva et al. [138]	2005	–	The numerical results were validated with the experimental data by using this turbulent models SST $k - \epsilon$, and flow visualization on swirl cooling tube flow pattern can be observed.
Ling et al. [112]	2006	1.8-72	Numerical investigation to find the heat transfer on swirl cooing tube and the FLUENT $k - \epsilon$ turbulent model were used, and by hot wire anemometry to find vortex fluid flow activities.
Gupta and Kumar [139]	2007	9-18	Numerical studied the swirl cooling inlet and outlet exist tangential tube by using the velocimetry (PVT) for this simulation and FLUENT $k - \epsilon$ turbulent model used for the pressure drop of the tube.
Paik and Sotiropoulos[126]	2010	30-100	Numerical investigation of the swirl cooling tube used the different types of Reynolds number and swirl number ($S = 0.17 - 1.23$) using the DES model to find the heat transfer.
Liu et al. [133]	2011	$5.4 - 24.6$	Numerical investigation of the swirl cooling chamber (tube), and SST, $k - \epsilon, k\ \omega$, RNG these turbulent modules were used for to find the heat transfer behaviours.
Liu et al. [127]	2013	$5.4 - 10$	In additional, as reported in [133] used the same geometry was used for further numerical investigation.
Kusterer et al. [130]	2013	10.5	Numerical researched for Double swirl chamber (DSC), Star CCM +, SST, V2F, $k - \epsilon$ turbulent model use for the heat transfer.
Lin et al. [140]	2014	$Re_{jet} = 15$	[133] same geometry was used for this heat transfer by using the DSC, Star CCM + with SST, V2F, $k - \epsilon$, Spalart-Allmaras turbulent models.
Foroutan et al., [141]	2014	-	The numerical investigation for Partially averaged Navier-Stokes (PANS) model compared to DDES and SST and conclude the pressure drop and heat transfer behaviours.

2.7 Scientific research gaps (from experimental and numerical analysis for swirl cooling).

Several researcher have conducted experimental and numerical analyses and optimisations of vortex cooling within a gas turbine blade's leading edge. Researchers mainly focus on pressure loss, heat transfer, and cooling efficiency.

Lin et al.[142] used the SSTk -ω model as part of a numerical investigation of the heat transfers, pressure loss, and cooling effect with two swirl chambers and single swirl and double swirl chambers. They merged two chambers with a merge ratio of 20%, and heat transfer was measured. The findings of Yang et al.[143] showed that single swirl cooling pressure drop, and static pressure were quite different; they increased the merging ratio by from 20% to 30% of the thermal performance of both models, as presented in Fig 2.26 [142].

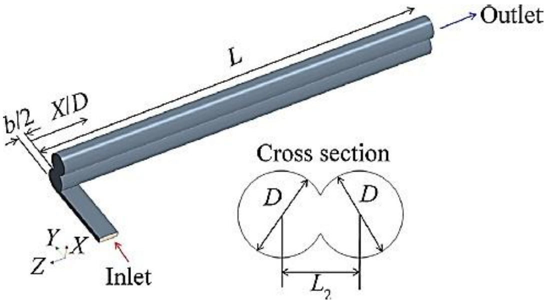

Figure 2-26: Schematic swirl cooling gas turbine blade leading edge by [142]

According to this research, validation with various turbulence models, including the SSTk -ω, realisable k-ε, and V2F, is necessary to investigate the merging between double swirl cooling chambers (DSC). Double join shaped double swirl cooling is developed with proper fluid mixing in a double swirl cooling chamber; researchers have found that it is 7.5 times larger than standard swirl cooling chamber turbulent flow as noted in [133]. The Nusselt number of this model is 41% larger than that of the standard swirl cooling chamber, however which indicates enhanced cooling performance, and it helps remove heat from the blade surface. This means it maintains a lower blade temperature with the same operation conditions. This blade remains cooler for this double cooling chamber (DSC), and an improvement was based on the single-stage design. The present research work merging the double-swirl cooling chamber does not reduce the pressure drop and improve cooling efficiency as reported in [144]. However, further modification is needed for the double-swirl cooling chambers (DSC) with a nozzle to reduce the pressure drop and improve cooling efficiency. Fan et al. [145] numerically studied pressure loss and heat transfer for swirl, film, and no-film cooling configurations. The diameter of the film cooling increased the mass flow and the temperature ratio.

In all cases, the mass flow rate is constant in every film cooling hole and increased by 5.2% due to heat intensity. Consequently, pressure fluctuations were observed in all cases in [146]. Further, increasing the diameter of the film cooling holes from 0.1% to a larger value increases the velocity upstream, and the downstream velocity decreases due to this increase, as shown in Fig 2.27 [145]**.**

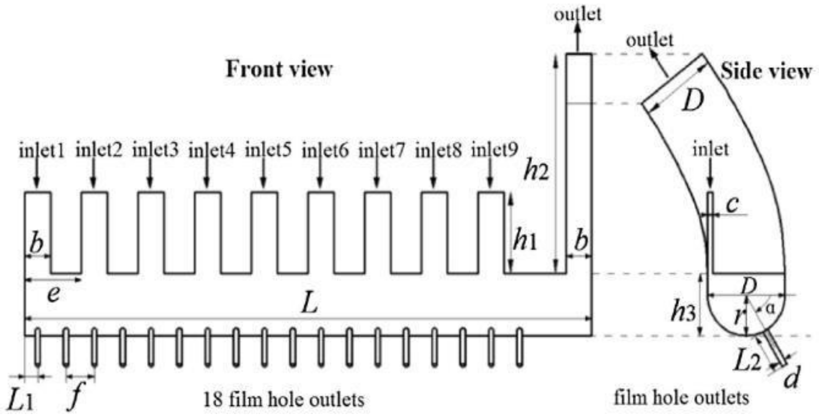

Figure 2-27: Details of the vortex cooling chamber according to [145]

In all cases, the mass flow rate is constant in every film cooling hole and increased by 5.2%, resulting in pressure fluctuations in all cases as noted in [147]. Moreover, they used 0.1 sizing of film cooling holes, and between these holes, there is not much distance between these film cooling holes. Finally, they compared this model with single-stage vortex cooling using nine fixed continuous nozzles, and specifically, they utilised nozzles 1,5, and 9 for constant flow in [148]. However, modifying (reducing) the vortex nozzle size and film cooling hole sizes on the double vortex cooling chambers makes it possible to get a 0.25% reasonable pressure drop. Ran Yao et al. [75] studied pressure loss, cooling efficiency and heat transfer in single and multi-swirl cooling chambers. Numerical data from this multi-stage vortex cooling system simulation determined the relevant heat transfer of multi-stage vortex cooling. For a Reynolds number of 40,000, the average Nusselt number in the three-stage swirl cooling structure is improved by 75 % over the single-stage swirl cooling. These higher heat transfers from the blade surface are more effective; this output is that the blade surface is significantly cooled.

The researcher found that a single-stage swirl cooling gas turbine blade leading edge structure can be nearly 100 K lower than a multi-stage one. Nevertheless, the heat transfer is higher in multi-stage systems, and the pressure loss is in the higher range between 5 -8% as mentioned in [149].

Bend connected with the adjacent stages were modified into a round shape; therefore, heat transfer and pressure loss are less [150]. However, further modification of the multi-stage cooling chambers' size, including nozzle thickness, can enable a better pressure to drop and improved cooling efficiency for the swirl cooling gas turbine blade leading edge.

In additionally, Fawzy et al.[151] stated that the optimisation of the compound unit of swirl cooling and impingement cooling technique involves using a multi-conical nozzle on a gas turbine blade, which achieves a 97.7% ratio at constant temperature and increased efficiency. The Nusselt number is 11% if the temperature ratio is 0.65 to 0.95, with an identical nozzle Reynolds number of 10,000 to 15,000. They compared the experiment and optimised results for better temperature distribution and heat transfer in the compound cooling gas turbine blade leading edge as mentioned in [152].

The flow and heat transfer behavior, and they used a single-stage circular-shaped chamber with ten nozzles for swirl and nine nozzles for impingement cooling. The researcher achieved cooling 47.0% to 49.5% with each conical nozzle and optimised a high Reynolds number and Temperature ratio (TR) of this model. Unfortunately, there is no such gap between this nozzle, for better flow distribution, and conical nozzles are not suitable for better flow distribution: this always flows will hammering. However, further modification of nozzles to change the conical nozzle to an angle can make it possible to get better flow and less pressure drop. Du et al.[154] improved gas turbine blade leading heat transfer, pressure loss, and cooling efficiency under the rotation condition of the swirl cooling channel with nine attached nozzles. This was done by solving, 3D steady RANS equations and grid independence used for numerical analysis. In this analysis, velocity and streamlining are not sensitive to rotating directions. In this work, researchers utilised a single–stage vortex cooling chamber equipped with nine vertical 5mm nozzles, employing rotation number mechanisms to solve the RANS and the standard k-ω turbulence model. This is an effect of the heat transfer distribution of all nozzles, and hence, constant rotational number Ro, of 0.384 for increasing the vortex air velocity cooling, pressure drop, and heat transfer intensity of this model as reported in [155].

However, further modification of a multi–stage cooling (MSC) chamber (10.11) with nozzle size (5mm) and constant rotation number (Ro). It can increase velocity by streamlining in very sensitive directions with a little higher possibility of reducing the backflow (Newton's law 2^{nd} of motion) will decrease the pressure loss and improve the cooling efficiency.

According to Fawzy et al.[156] pressure loss, cooling efficiency and heat transfer in multi- swirl cooling chambers. Numerical data from this multi-stage spiral cooling system simulation determined the relevant heat transfer of the multi-stage vortex cooling. They used six conical nozzles with different angles set up in the nozzle area RANS simulation coupled with the SST k-ω were used, as mentioned in Fig 2.28 [156].

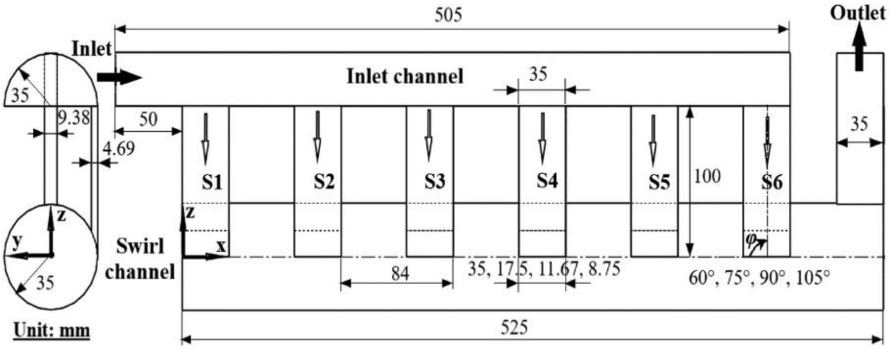

Figure 2-28: Swirl cooling dimensional specifications [156]

The researcher compared CFD with experimental data in this model. A multi-stage swirl cooling chamber with six conical nozzles was set up with 60, 70, 90, and 105 degrees at nozzle inlets area as reference in [157]. With a constant Reynolds number in each nozzle the researchers studied which nozzle is best for heat transfer distribution and thermal efficiency of the cooling blade.

Outcome from this research showed that slightly increasing the angle of each of four nozzle, set up a 105- degree angle, improving 29.9% of heat transfer with a constant Reynolds number [158]. However further modification is necessary because of the conical-shaped nozzle is unsuitable for reducing pressure drop and improving cooling efficiency this research outcome is an increased frictional loss. Additional investigation by Xiaojun et al.[162] studied pressure loss, cooling efficiency and heat transfer to evaluate an effectiveness of different cooling methods.

In this research different configurations swirl cooling chambers have been used, and based on this research work outcome vortex cooling method has more pressure loss and heat transfer intensity, and double multi-vortex cooling makes more pressure loss and is best for heat transfer performance.

This work is compared with different cooling configuration methods, such as impingement cooling and double vortex cooling of the turbine blade leading edge. RANS equation coupled with standard k-ω is used, and the mass flow of each nozzle is increased from upstream to downstream, the cooling method is significant to heat transfer performance Zhang et al.[160] investigated middle double vortex cooling suitable for better heat transfer performance. However, further modification of mismatched cooling nozzles (4 mm) and coolant chamber (9.903 mm) of the gas turbine blade leading edge can make it possible to improve the cooling efficiency and decrease the pressure drop.

Biegger et al.[161] reported improvements in heat transfer and pressure drop comparing the Detached Eddy Simulation (DES) and their own experimental data. This model was validated with double-swirl cooling (DSC). This work is compared with the own experimental data and DSC literature review, and the behaviours of heat transfer performance, pressure drop, and axial velocity were investigated. The complex 3D problem used RANS equations, and a Spalart–Allmaras (SA) turbulence model used. The axial velocity of the near-inlet wall chamber is a high heat transfer performance of more than eight times of a smooth cooling chamber in [162]. The swirl cooling chamber has a 1.0 % tolerance and a 4.5 mm nozzle size. However, further modification of the clearance between the edges should be (0.6-0.8%) with increases in the partition’s stages in a swirl tube. It is possible to improve the backflow with a decrease in the pressure loss and get better cooling efficiency.

2.8 The important points of these research gaps are from this chapter

1. Modification is needed for the double-swirl cooling chambers (DSC) with a nozzle to reduce the pressure drop and improve cooling efficiency.
2. Reducing the vortex nozzle size on the double vortex cooling chambers makes it possible to achieve both cooling efficiency and pressure drop.
3. This modification can make it possible to obtain a better pressure drop and improve the cooling efficiency of the swirl cooling gas turbine blade leading edge.
4. Further modification of nozzles to change the conical nozzle to an angle can make it possible to get better flow and less pressure drop.

5. A further modification is needed because the conical-shaped nozzle is unsuitable for decreasing the pressure drop and cooling efficiency, and there are more frictional losses.
6. Further modification of mismatched cooling nozzles (4mm) and coolant chamber (9.903mm) of the gas turbine blade leading edge can make it possible to improve the cooling efficiency and decrease the pressure drop.
7. Further modification of the clearance between the edges should be (0.6-0.8%) with increases in the partition's stages in a swirl tube. It is possible to improve a Backflow with a decrease in the pressure loss.

Research gap

The methods covered in this literature review for internal swirl cooling of gas turbine blade leading edge mainly focus on the fluid flow and thermal activities of internal cooling behaviour; based on this, several studies have been obtained the desired improvement in cooling similar finding were absorbed by Rao et al.[75], Bunker et al.[163], and Yang et al. [144]. A aerospace and aviation industries are looking to improve their productivity and the quality of work. These are the major difficulties for industries; they require improvement and addressing these issues, and running complex analysis for these improvements to a reasonable series of values is essential for conducting these simulation models several times; however, given the enormous time and energy required, such an endeavour is not practical. To improve this CFD extensively used are outlined in this literature review. CFD is useful for solving complex analysis, improving the thermal and cooling efficiency of the blade.

The swirl cooling chamber geometry configuration with three-stage rounding plays a critical role in establishing both pressure drop and heat transfer performance. Further modification for the three-stage swirl cooling chamber feature, such as rounding each parameter (such as 2mm, 4mm, and 6mm), directly influences the effective pressure drop, thermal performance, heat transfer, and flow distributions. However, three-stage swirl cooling channels with a rounded shape improve the internal behaviour characteristics, such as convection mixing of heat transfer and fluid flow distribution, which were found from further parametric studies. Each rounded swirl cooling channel reduces the pressure drop and improves the thermal behaviour. These rounded geometry adaptations improve efficiency and pressure drop simultaneously.

Finally, it was validated with experimental data, and CFD output improvement and values from past simulation and experimental work on this internal swirl cooling of a gas turbine blade leading edge.

2.9 Summary

This Literature review (Chapter 2) chapter altogether provides the theory of the background information for heat transfer and fluid flow; this outline of the literature review is related to the cooling of the gas turbine blade leading edge and CFD software used for the cooling of the turbine blade leading edge. The present cooling technique is available in this literature review. Based on the assumptions highlighted in these models, it was discussed that prediction reliability is required in this model. Related to this model, one of the vital issues, which is used for the correlation of empirical of turbulent diffusivities (for internal cooling) and sublayer viscous thickness (for internal cooling), was complex and finding the cooling thermal efficiency due to the flow is challenging to understand. However, for this issue CFD is very useful for solving these problems. By using the CFD technique, accurate predictions with pressure drop and heat transfer for enhancement on internal cooling of the gas turbine blade leading edge can be achieved.

This current research focuses on the swirl cooling of the gas turbine blade's leading edge. This blade is called the MT-1 gas turbine blade, and created several swirl cooling channels design based on the MT- blade investigated the uses of these swirl cooling channels to find the thermal activities such as thermal performance of each model, pressure drop, and heat transfer with based of this further investigated the CFD parametric study of the multi-stage cooling channels to find the best cooling model to sustain thermal and pressure drop activities. The present study were investigated convective heat transfer inside the cooling configurations, and conduction within the solid blade.

A review of the design of the MT-1 blade is provided in next chapter which is the basic for the methodology in this thesis.

Chapter 3: Validation for MT-1 blade mixing plane

3.1 Introduction

This chapter is the first step of the methodology. It shows the work done to accurately simulate the flow past a generic turbine blade. This involves comparison between CFD simulation and experimental for the flow around a turbine blade. It gives confidence that pressure can be well predicted around the blade's perimeter. It focuses on the flow characteristics around a generic high-pressure turbine blade including the implementation of a mixing plane to separate stator and rotor. A thorough numerical analysis is made to allow comparison with experimental data of pressure distributions and heat transfer results. This validation is carried out to assess the reliability and accuracy of the numerical method which will be used in later chapters in this thesis.

3.1.1 Rolls–Royce high-pressure gas turbine blade

The mixing plane design was done in SolidWorks software [164], and is based on a Rolls-Royce High- pressure gas turbine blades which is provide complete geometry in STL format. Fig 3.1 as shown the full 3D geometry. For 2D cases, the SolidWorks slicing tool was used to extract shape of the fluid as shown in Fig 3.2.

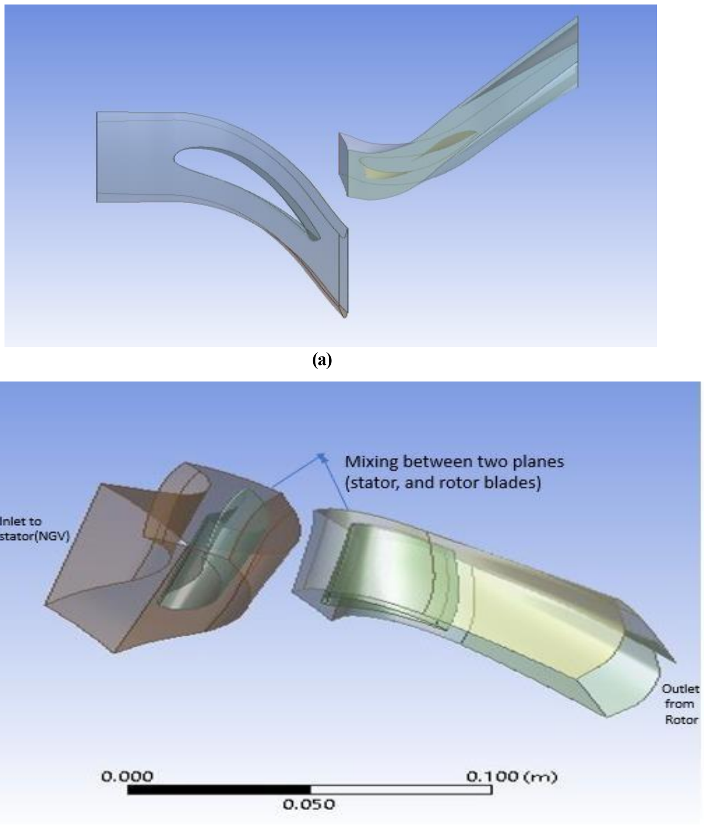

(a)

(b)

Figure 3-1: (a) and (b)- Rolls–Royce MT-1 3D blade

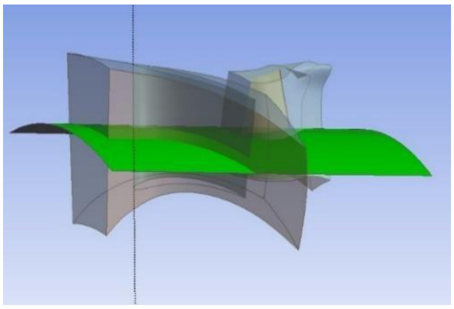

Figure 3-2: 2D gas turbine blade solid works model

However, there are several stator and rotor sections in this 2D gas turbine blade. The stator and rotor blade for this mixing plane are taken here, as shown in Fig 3.2. The stator (NGV) and rotor blade specifications are illustrated in Table 3.1.

Table 3-1: 2D gas turbine blade stator (NGV), and rotor specification

S.L. No	Parameters for NGV (stator).	Values	Parameters for rotor	Values
01	Chord (C)	69.82 [mm]	Chord (C)	37.5 [mm]
02	Max Thickness (t)	14.52 [mm]	Max Thickness (t)	2 [mm]
03	No of blades	32	No of blades	60
04	Blade angle inlet(α_1)	42°	Blade Angle inlet (β_1)	37.2°
05	Blade angle outlet(α_2)	67°	Blade Angle outlet (β_2)	60°

The 2D SolidWorks stator and rotor blade model is imported into ANSYS 2022 R1 design modeller to create a fluid flow domain of the stator and rotor blade, as illustrated in Fig 3.3.

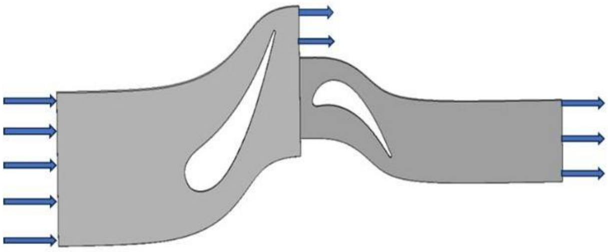

Figure 3-3: 2D gas turbine blade Ansys design modeller

The main external domain has been created for this 2D gas turbine blade and this complete wall. The inlet stator and outlet rotor's periodic boundary condition are based on gas turbine high-pressure turbine (HPT) on of the stator and rotor blade. However, these sizes are based on the literature review in [165].

Moreover, the inlet and outlet periodic of the 2D stator (NGV) and rotor blade are 54.4 mm for the stator, which is called as H1, and 29.3mm for the rotor, this is called as H2, which is taken based on the calculations.

3.2 High-pressure gas turbine (HPT) blade 2D Mesh design

A structured hexahedra mesh block was used in this fluid flow 2D gas turbine blade stator (NGV), and rotor for simulation geometry parameters are described in Table 3.1.

Table 3-2: 2D gas turbine blade stator (NGV) and rotor blade mesh specifications

S.l no	Parameters for NGV (stator).	Values	Parameters for rotor	Values
01	Number of elements	9082	Number of elements	6414
02	Nodes	14121	Nodes	10074
03	Size factor	1	Size factor	0.88
05	Expansion rate	1.3	Expansion rate	1.3
06	Spanwise elements	2	Spanwise elements	2
07	Edge Length ratio	13.6	Edge Length ratio	24.2
08	Minimum face angle (θ)	57.792 [deg]	Minimum face angle (θ)	57.640 [deg]
09	Maximum face angle (θ)	112.366 [deg]	Maximum face angle (θ)	115.014 [deg]
10	Maximum skewness	0.50786	Maximum skewness	0.50955

This main domain uses structured mesh and it has complete specifications, as shown in Table 3.2. The name selection for this domain, includes such as pressure boundaries, wall, and periodic ones, and inlet-outlet of this stator and rotor blades, has been given, as illustrated in Fig 3.4.

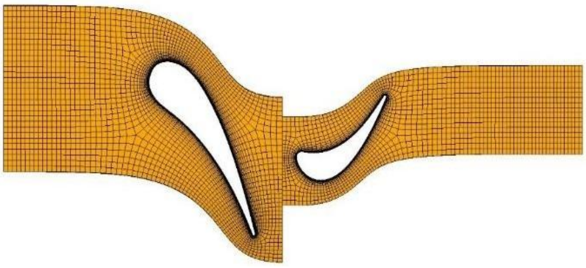

Figure 3-4: 2D gas turbine blade ANSYS Turbo gird mesh

For better flow distribution, smooth inflation layers have to be used in the near-surface turbine blade, and the ten layers have to be used [74].

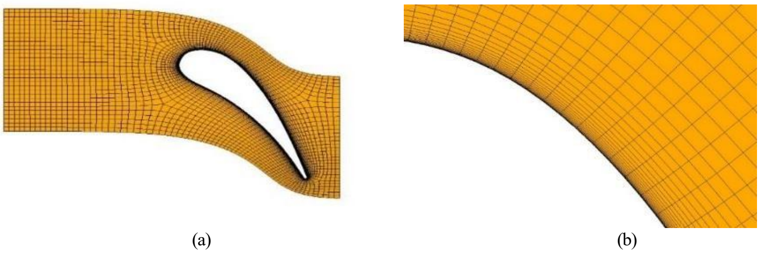

(a) (b)

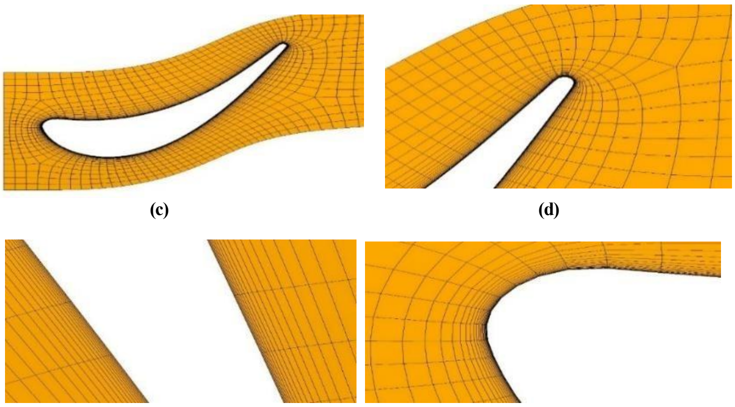

(c) (d)

(e) (f)

Figure 3-5 (a) to (f): 2D gas turbine blade ANSYS turbo grid mesh

Fig 3.5(a) illustrates that the turbo grid mesh is utilised across the whole stator (NGV) structured mesh, including a full periodic boundary, such as an inlet to an outlet. Fig 3. 6 (b, c and d) reveals, that the 2D gas turbine blade stator (NGV), which is located near the blade, uses a structured block mesh. The 2D gas turbine blade rotor is a block mesh with a specific structure that allows for complete periodic boundaries from the intake to the outlet. The mesh is designed to closely surround the rotor blade, as seen in Fig 3.5 (e,f). In this 2D mixing plane, different types of grids were used, such as the mesh factor between 0.5, 2, and 3, as shown in Fig 3.6.

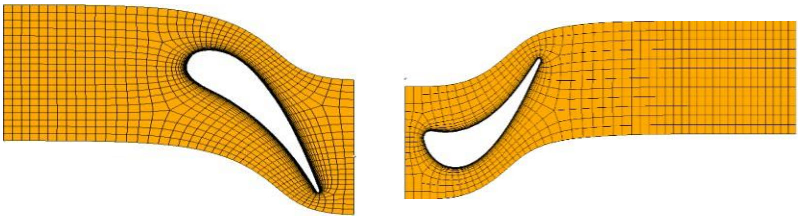

(a):2D Stator 0.5x mesh **(d): 2D Rotor 0.5x mesh**

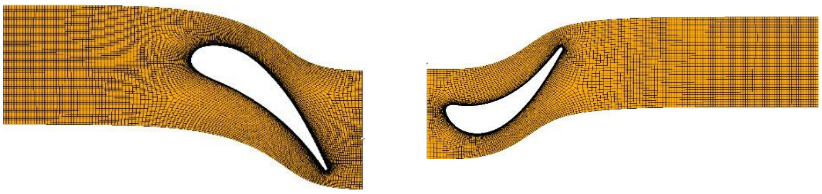

(c): 2D Stator 2x mesh **(d): 2D Rotor 2x mesh**

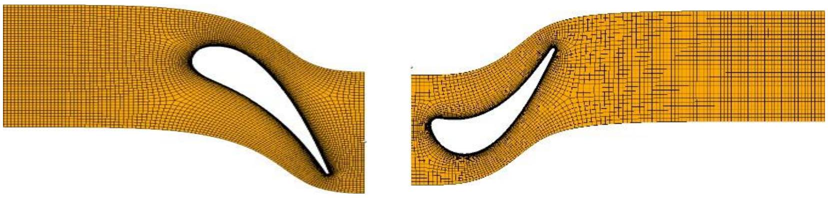

(e): 2D stator 3x mesh **(f): 2D Rotor 3x Mesh**

Figure 3-6: 2D Gas turbine blade model mesh factor between 0.5, 2, and 3 Grid independent studies

Table 3-3:2D gas turbine blade Mixing plane 0.5x,2x, and 3x grid independence studies.

S.L no	Parameters for NGV (stator)	Mesh sizes	Parameters for rotor	Mesh sizes
01	Number of elements	9082	Number of elements	6414
02	0.5x	13623	0.5x	9621
03	2x	18164	2x	12828
04	3x	27246	3x	19242

Table 3.3 shows various meshes with scaling factors of 0.5x, 2x, and 3x for mesh independence study with meshes shown in Fig 3.6. Both stator and rotor blades have slightly increased elements based on the refinements used.

3.3 Set-up of 2D simulation work

Table 3-4: Set up of 2D gas turbine blade Simulation work

Input	Selections
General	Pressure-based solver
Materials – Air – Density – Other inputs	Ideal Gas Law – Constant
Momentum and Thermal Bc's	**Stator inlet** **Pressure inlet stator** Reference frame – Absolute Guage Total pressure (pa)- 461500 Direction Specification Method – Normal to direction. Total Temperature (K) - 444.15 **Pressure outlet Rotor.** Backflow reference frame –Absolute Guage pressure (pa) – 143100 Backflow pressure specifications – Total pressure. Backflow Total Temperature (k)-300. Wall top –stator and rotor – Translations Momentum – wall motion – Stationary.
Mixing plane model	**Stator outlet: rotor inlet**
Solution method	**Scheme** Coupled **Gradient** Green Gauss node based all 2nd orders Upwind
Monitors – Residuals	**1e-6 for energy 1e-5 for rest**

The set-up of the stator and rotor blade computation domain is shown in Fig 3.3, and the velocity at the mixing plane between the stator and rotor blade shows the flow crosses the mixing planes. Due to recent update of the Ansys Fluent pressure-based solver, it can solve any complex flows at higher Mach numbers so this solver was used, with the mixing plane. Density-based solvers can be used at higher Mach numbers such as 2-3.

Meanwhile, the momentum and thermal boundary conditions play a major role in the solutions which is known past experimental published work. The pressure was set up, such that the total pressure inlet is 461500 Pa, and the rotor is outlet pressure is 143100 Pa, and the periodic boundaries are 300 K. However the bottom and top walls are stationary (stator), while the rotor is motion which is modeled with a translating wall. Improve the mixing plane interface stability but does not enforce conversion is an continuously checked after all each simulation.

In this 2D simulation, the coupled method is used and the Green Gauss node based gradient scheme is used with all 2nd order upwind discretisation schemes for calculating flow variables. If the iterations are more, it can lead to fluctuations of convergence in [166] because of the reduced number of iterations for simultaneously solving the pressure and momentum equations as mentioned in Table 3.4.

3.4 Quantitative results

To generate 2D validation results, the experimental data is manipulated for this investigation acquired from the three-dimensional geometry. Equivalent two- dimensional simulations are performed at the mid-span of the high-pressure turbine blades. This primary 2D analysis is performed as a validation step to check CFD simulation accuracy.

It allows for assessing pressure distributions and heat transfer for different combinations of turbulence models and mesh density, aligning with experimental observations. However, these outcomes and comprehensions implied from the 2D simulation analysis will form the basis for thorough 3D simulation studies, later in this chapter.

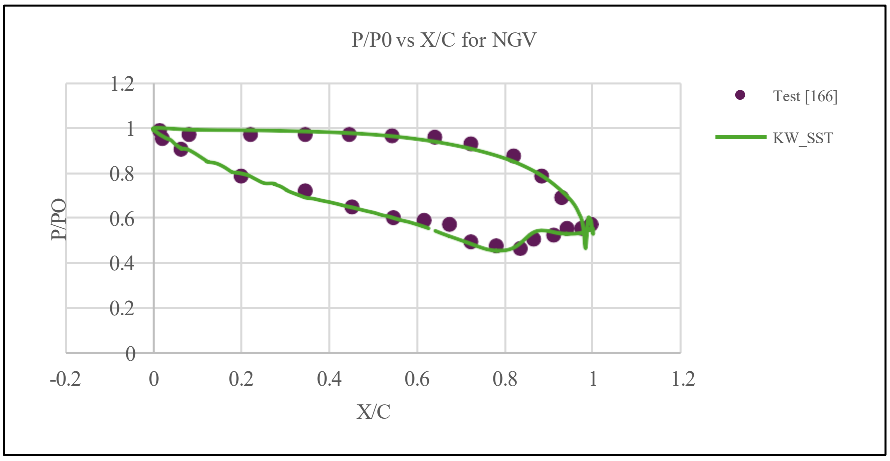

Figure 3-7: 2D gas turbine blade stator pressure distribution

Figure 3.17 presents a comparison of the pressure ratio (P/P0) along the normalised chord length (x/c) of a stator between calculations of simulation and experimental data. The green line corresponds to the simulation results, where the orange dots correspond to the experimental data points. The results exhibiting a pressure decrease down the chord with occasional variations at the trailing edge, as shown in Fig 3.7. Disparities exist between the simulation and empirical data, notably in the mid to trailing-edge areas and the experimental data points from the leading edge going downstream, and near the trailing edge on the suction side of the rotor blade. Potential causes of these differences may include oversimplifications in the simulation and experimental measurement inaccuracies.

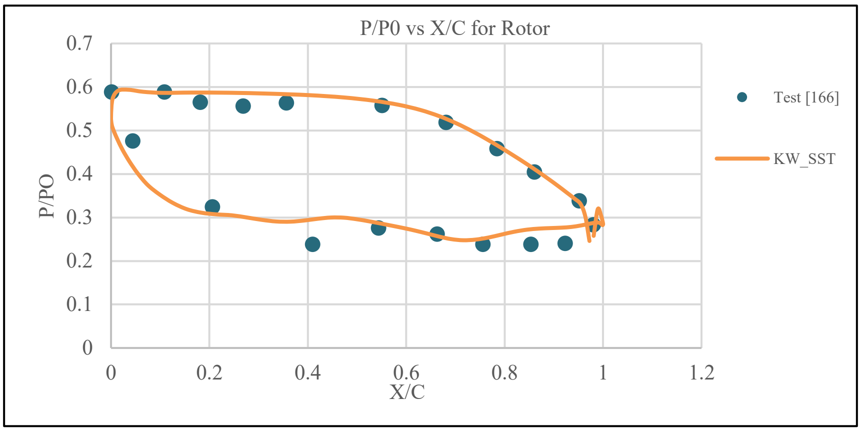

Figure 3-8: 2D gas turbine blade rotor pressure distribution

The comparison of the rotor blade between actual data as represented in orange dots and simulation blue line and these simulation studies the overall pressure distribution pattern throughout the rotor blade. However, significant differences are observed compared to the actual data, particularly in the area from the mid-chord to the trailing edge. Both the experimental data and the simulation results indicate a decrease in pressure from the leading edge to the trailing edge. However, the simulation analysis predicts a significant drop in the rotor blade.

3.4.1 Grid independence studies

In this simulation, the baseline k -ω selected turbulence model was used, which requires $y^+=1$ for the grid independence study. The grid independence studies for the pressure ratio (P/P0) along the chord length (x/c) of a stator are depicted in Fig 3.9. The study compared data obtained from four distinct mesh resolutions. Mesh GI 1x is represented by a blue line stator GI 0.5x represented an orange line, mesh GI 2x, and stator GI 3x represented a purple line. However, the close and overlap of these line confirms consistency.

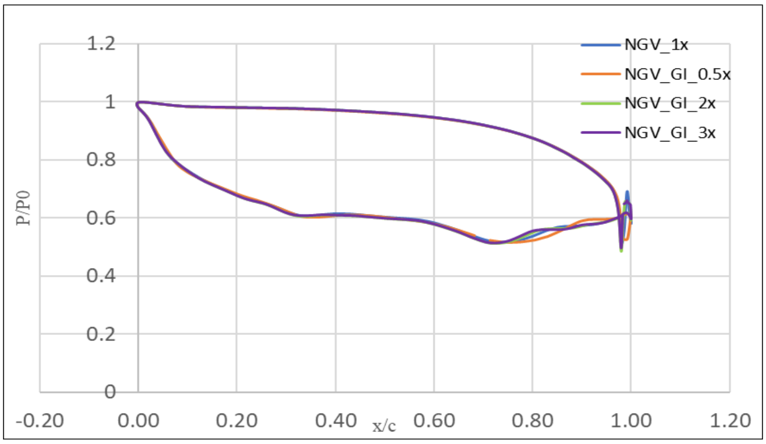

Figure 3-9: 2D gas turbine blade Stator (NGV) Grid independence studies

However, the proximity of these lines indicates the performance features, especially with pressure distribution and a grid independence study of a stator. The study compared data obtained from four distinct mesh resolutions. Stator GI 1x represented a blue line Stator GI 0.5x represented an orange line stator GI 2x, and stator GI 3x represented a green and purple line. However, the proximity of these lines indicates the performance features, especially with pressure distribution.

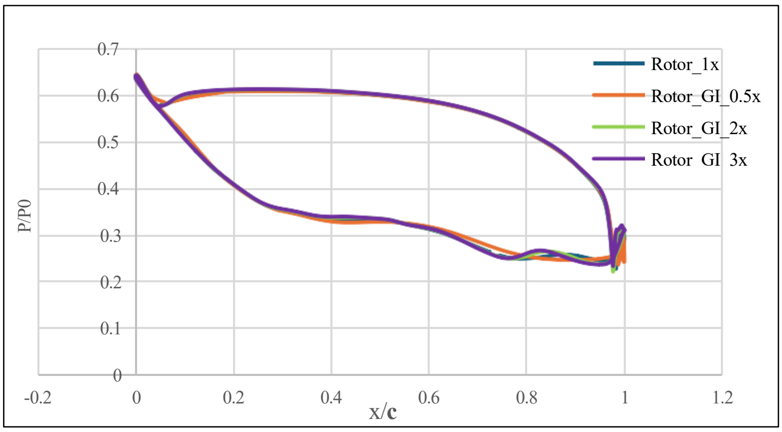

Figure 3-10: 2D gas turbine blade rotor Grid independence studies

Fig 3.10 shows the pressure distribution around the rotor for different meshes in the mesh independence study, the pressure ratio begins at the leading edge (x/c = 0). It decreases progressively throughout the blade, peaking around the mid-chord and then increasing near the trailing edge.

Minor variances are apparent, particularly around the leading and trailing edges, but these differences are generally tiny. This shows that the finer meshes between the rotor_GI_2x and Rotor_GI_3x provide similar results.

3.4.2 Turbulence models for 2D mixing plane

Fig 3.11 shows the two-coloured lines are the NGV_k -ε_30 and NGV_ RNG_30 turbulence models, which $Y^+ = 30$. These two lines follow remarkably similar paths, representing that the overall pressure distribution along the vane is consistent across these two turbulence model type. Two lines derive from a high-pressure ratio at the leading edge. Moreover, the pressure gradually reduces as the flow progresses down the vane, reaching its lowest point adjacent to the mid-chord. In the vicinity of the trailing edge (x/c) at 1, some variations in pressure manifest between both turbulence models.

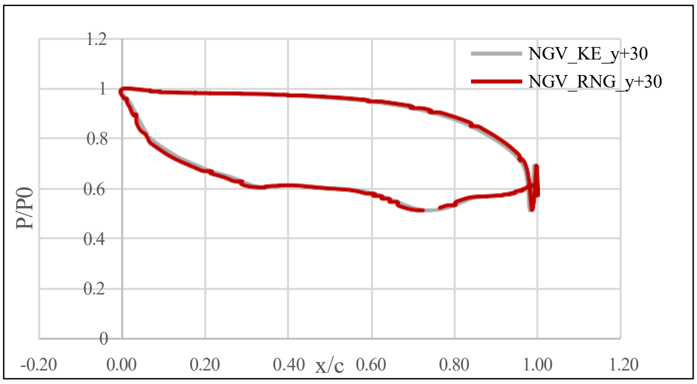

Figure 3-11: 2D gas turbine blade NGV _k - ε_y+30, and NGV_RNG_y+30 Turbulence models

The pressure ratio (P/P0) of a rotor blade under two distinct situations is seen in Fig 3.12, and two colours indicate the 2D gas turbine blade mixing planes, *k-ε* y+30 and RNG y+30. In these rotor *k-ε* y+30 and stator RNG y+30 turbulence models, these line's basic form represents that the pressure distribution along the blade is consistent under both scenarios.

Both the rotor *k-ε* y+30 and stator RNG y+30 turbulence model scenarios begin with a high-pressure ratio at the leading edge (x/c) at 0, gradually falling as the flow advances along the blade, and the pressure ratio is lowest near mid-chord (x/c) is between 0.5 to 0.7, showing flow separation.

A variation in both lines close to the trailing edge (x/c) at 1 represents intricate pressure separation

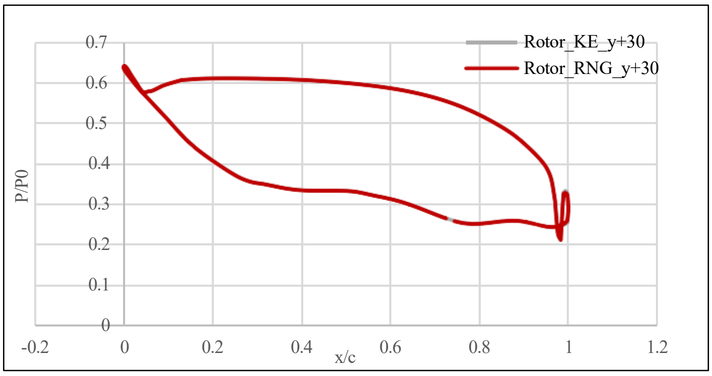

Figure 3-12: 2D gas turbine blade rotor _*k-ε*_y+30, and NGV_RNG_y+30 Turbulence models

3.4.3 Grid independence study with different types of turbulent models results

Fig 3.13 shows the 2D pressure distributions; specifically, *k-ω*, baseline y $^{+}$= 1 and further other turbulence models are *k-ε,* and RNG for all simulation scenarios. These simulation results indicate a high-pressure ratio at the leading edge corresponding to the high inlet pressure, and the pressure ratio consistently declines as the flow progresses downstream on the vane surface, ultimately reaching its lowest point around the mid-chord x/c at locations between 0.5 and 0.7. A pressure distribution near the trailing edge (x/c) at 1 is a common occurrence resulting from flow separation. However, NGV_GI 0.5x, *k- ω,* has shown to be suitable for all this pressure distribution.

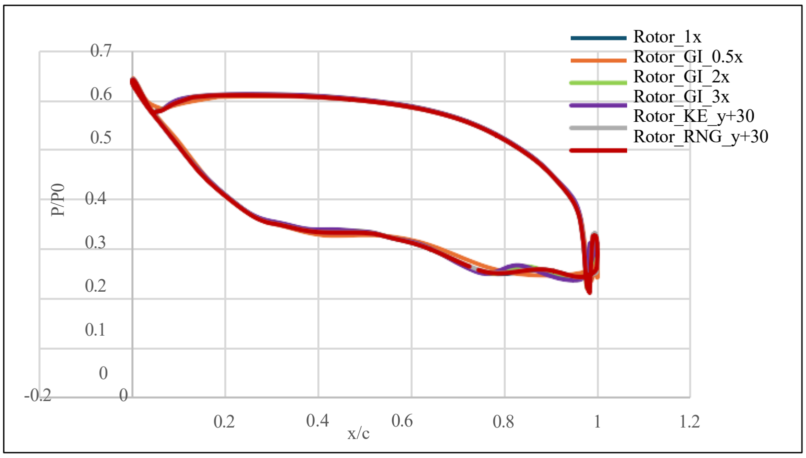

Figure 3-13: 2D mixing plane stator (NGV) Grid independence studies with *k- ω, k-ε*_y+30, and NGV_RNG_y+30 Turbulence models

A pressure ratio reaches its maximum value at the leading edge, indicating the presence of a high intake pressure. The pressure of the flow reduces as it progresses down the rotor blade, ultimately reaching its minimum value over the mid-chord (x/c) ranging from 0.5 to 0.7.

A slight pressure fluctuation or increase is observed at the trailing edge (x/c) at 1, trailing edge effects of the grid independence studies, and different turbulent modules, as shown in Fig 3.14. However, NGV_GI 0.5x, *k*- ω has shown to be suitable for all this rotor pressure distribution. All these 2D gas turbine blade mixing plane simulations were validated with experimental data.

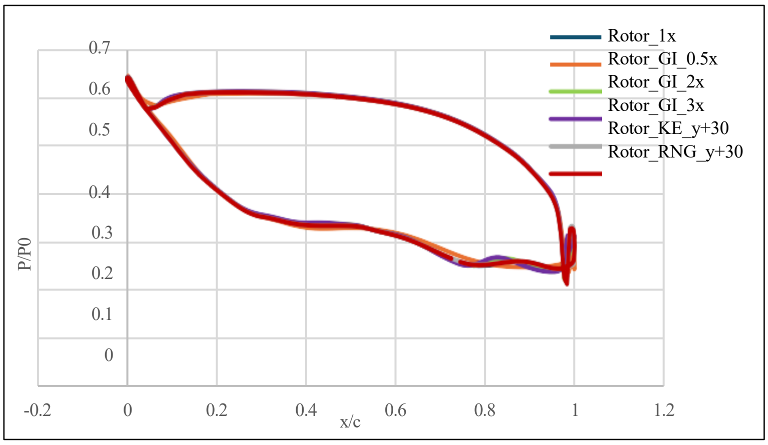

Figure 3-14: 2D MT-1 mixing plane rotor Grid independence studies with *k*-ω, *k*-ε_ $y^+ = 30$ and NGV_RNG_ $y^+ = 30$ Turbulence models

3.5 Qualitative results for Baseline *k*-ω and *k*-ε $y^+ = 30$ flow visualisations

The relative velocity magnitude contour of the 2D gas turbine blade, shown in Fig 3.15 indicates the complete mixing plane of the stator and rotor blade. This flow is shown around the stator and rotor blades. The velocity is low in the near stator area, indicated by the blue region, and the mixing plane regions on both blades, green and yellow, represent moderate velocities, with the red region is near the rotor blade, as shown in Fig 3.15 (a). However, the velocity distribution in the stationary frame is analysed within a two-dimensional 2D gas turbine blade mixing plane. Nevertheless, the velocity scale spans from 0 m/s, represented as blue, to 468.91 m/s, represented as red, and the flow begins at a modest velocity, as seen in blue, coloured green to yellow, as shown in Fig 3.15 (b). It ultimately reaches its maximum velocity near the narrow throat and directly downstream; however, red and orange spots represent the regions with the maximum velocity.

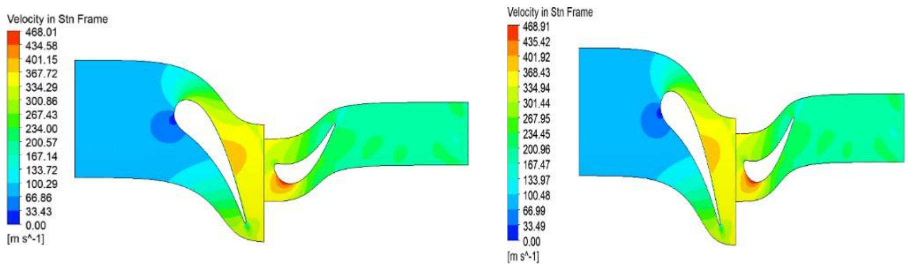

(a)

(b)

Figure 3-15: Contour velocity relative magnitude through the stator and rotor blade

Fig 3.16 (a) depicts the 2D gas turbine blade mixing plane and a different pressure range in the frame. The total pressure ranges from 121.26 kPa (blue) to 557.63 kPa (red). However, high-pressure zones vary from yellow which is the inlet and outlet of the stator blade to a red colour which is located near the inlet of the rotor blade and are situated mainly upstream of the contraction. In contrast, the low-pressure zones, which range from green to blue, downstream of the rotor blade.

Total pressure distribution in a stationary frame within a 2D mixing plane. The pressure is expressed in kilopascals (kPa), with the colour scale ranging from 119.96 kPa, exhibited in blue, to 558.35 kPa, shown red, as illustrated in Fig 3.16 (b).

However, the yellow zone represents areas of higher pressure, which progressively transitions to lower pressure, as depicted by the blue region. A notable pressure decreases over the flow channel, notably around the narrow section.

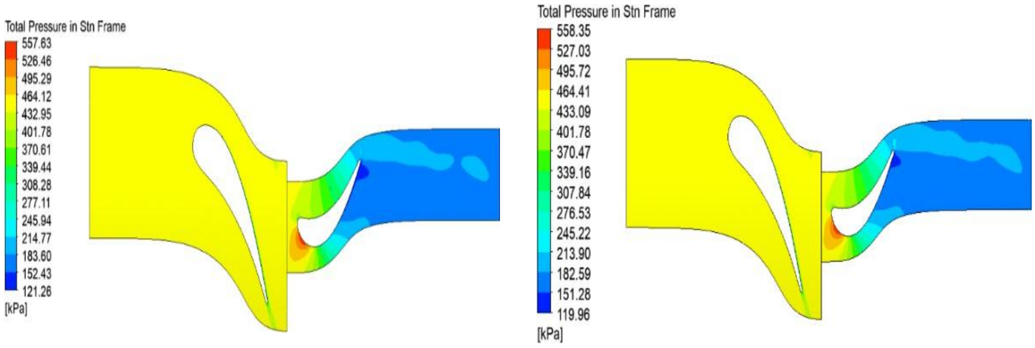

(a) (b)

Figure 3-16: Contour pressure in frame through the stator and rotor blade

3.5.1 Contour velocity relative Mach number

Fig 3.17 shows the distribution of Mach number in the flow field. The Mach number, the ratio of the flow speed, is depicted on the contour map using a variety of colours. The red (Mach 1.24) denotes the maximum Mach number seen in the simulation, indicating the presence of a supersonic flow field. Blue (Mach 0.00) represents the lowest Mach number, and Green to Yellow Indicates Mach numbers between intermediate values.

However, contours illustrate in Fig 3.17 (a) the variation in Mach number when the flow traverses several portions of a 2D gas turbine blade Mixing, perhaps a converging-diverging nozzle.

Depicted in Fig 3.17 (b) is the distribution of Mach numbers in the 2D Mixing plane. The Mach number scale spans from 0 to 1.24, representing different flow speeds. Nevertheless, the flow initiates at modest subsonic velocities as blue areas and surges through the narrowed channel, with the maximum Mach values indicated in red.

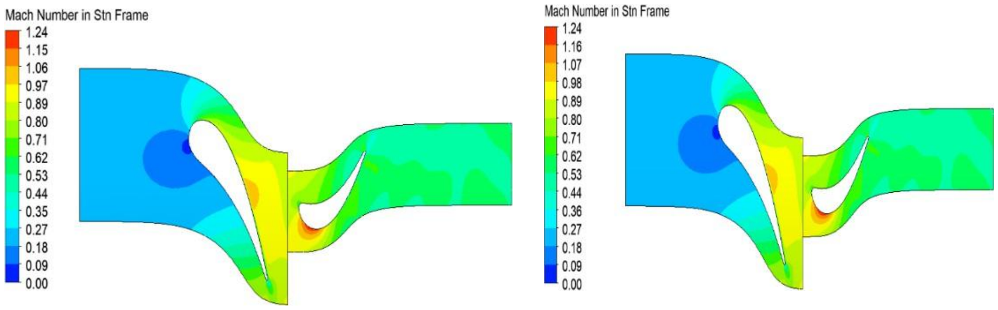

(a) (b)

Figure 3-17: Contour Mach number relative through the stator and rotor blade

3.6 3D MT-1 turbine blade. Geometry module and numerical methods

3.6.1 Geometrical models

The gas turbine blade geometry was provided by Rolls–Royce, which consists of both the stator (NGV) and rotor blades, each with their own specific domain. Although the domain is primarily separated into many sections, each portion has been assembled separately. The turbine blades are detached from the domain. In the case of the blade, Solid Works software changed the complete domain, as shown in Fig 3.18.

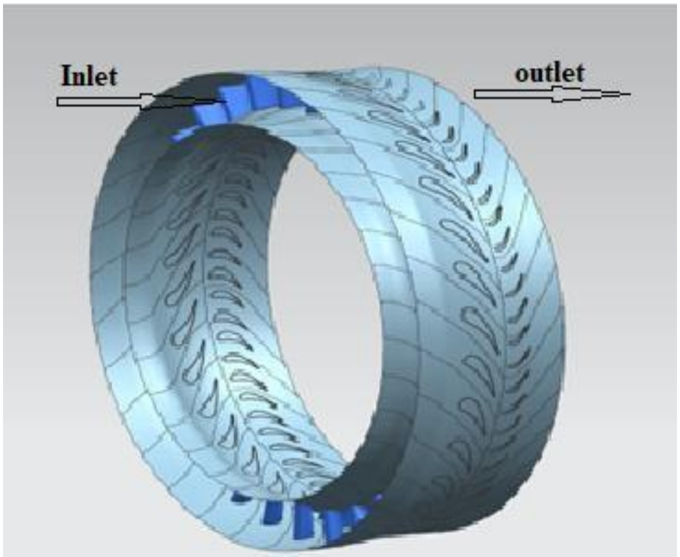

Figure 3-18: Rolls-Royce derby 3D Blade full set

Based on the provided geometry, several components need to be assembled. However, there was a problem with the skewness of this model throughout the meshing process. The rational for changing the whole flow domain of the stator and rotor blades is necessary. All the assembled pieces have been consolidated into a single flow domain.

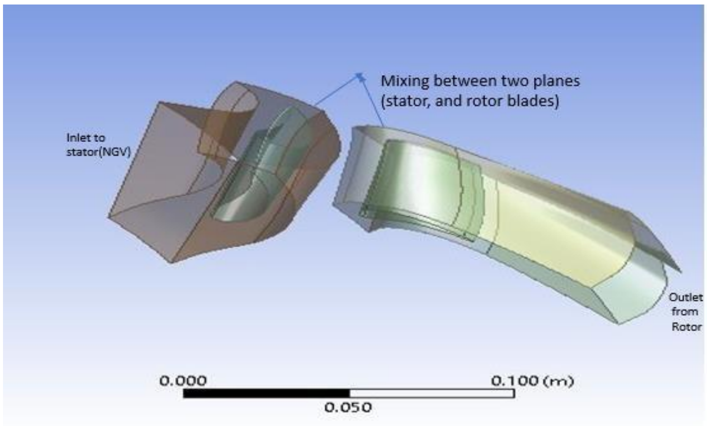

Figure 3-19: Rolls – Royce derby 3D blade geo

3.6.2 3D turbine blade geometry

The complete set of 3D blades involves the same size of each stator and rotor flow domain, as shown in Fig 3.19. However, each size of the periodic flow angle (above the blade) is 11.24^0 for a stator and 34.5^0 for a rotor, as shown in Fig 3.20 (a). Further Fig 3.20 (b) shows the front side of the single stator blade without hub, pitch or periodic boundaries highlighting the top, bottom, and principal dimensions.

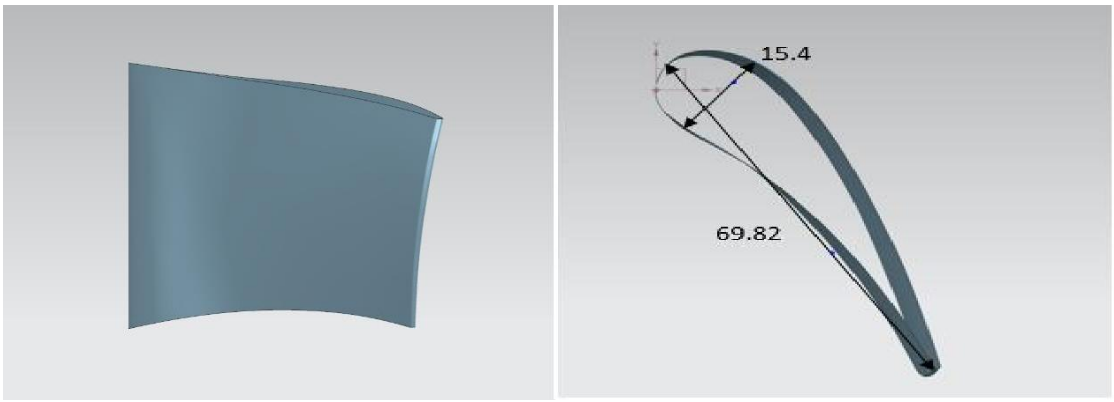

(a) (b)

Figure 3-20: Gas turbine stator blade geometry: (a) front view (b) top view.

The chord length from the leading edge to the trailing edge of the blade measures 69.82 mm. The leading edge, which refers to the trailing edge on both the top and bottom sides of the blade, measures 15.4 mm. There are two primary components for the top view of the stator blade angles are the leading and trailing edge angles, as shown in Fig 3.21. However, the leading edge (LE) angle is 42 degrees; it can be reflect either the angle of incidence, with this between a reference axis and the tangent to the curve at this point, and the 67° angle at the Trailing Edge (TE) indicates the curvature's behavior and its change in direction.

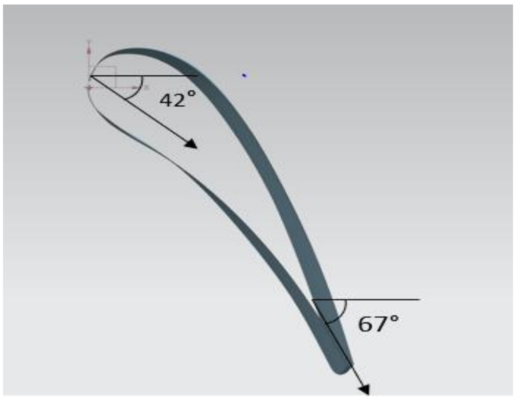

Figure 3-21: 3D gas turbine blade op views leading edge (LE) and Trailing edge (TE) with angle

Table 3.5 shows the detailed specifications for an outline of the blade parameters, highlighting the stator and rotor blades, key performance and geometric-related aspects.

Table 3-5: 3D gas turbine blade stator (NGV) specifications

Parameters	Values
Heigh/Span	39.5 [mm]
Chord	69.82 [mm]
Thickness at hub	14.4 [mm]
Thickness at middle	15.4 [mm]
Thickness at shroud	15.7 [mm]
Blade angle inlet	42 degrees
Blade angle outlet	67 degrees

3.6.3 3D gas turbine blade rotor blade geometry

The shapes of 3D gas turbine rotor blades are significance design factors in turbines, compressors, and fans, and comprehensive analysis of these rotor blades' design substantially influences the performance and efficiency of this industrial equipment as shown in Fig 3.22 (a, and b).

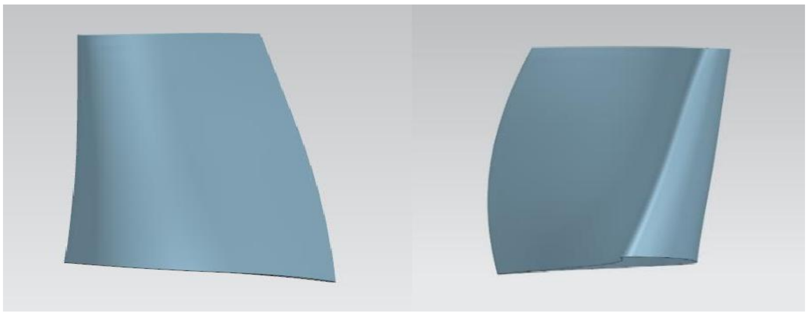
(a) (b)

Figure 3-22: 3D gas turbine blade Top and front view

Fig 3.23 depicts a three-dimensional representation of a rotor blade, emphasising two specific measurements: a length of 37.5 mm and a thickness of 4.5 mm.

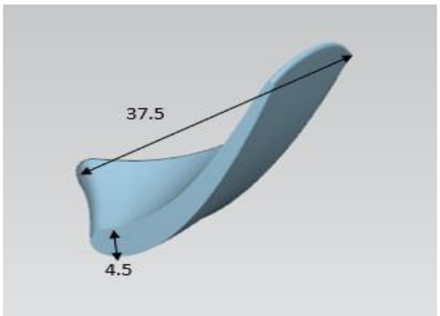

Figure 3-23: 3D gas turbine rotor blade top views

However, 37.5 mm, and 4.5 mm blade lengths are critical factors in determining its capacity to interact with a specific volume of fluid, whether it be air or gas, and 4.5 mm refers to the blade's thickness at a particular place, at the bottom or along its length. The variation in thickness at different locations along the blade is crucial for maintaining the blade's structural strength. Having adequate blade thickness is needed to withstand the operating strains and centrifugal forces while avoiding excessive thicknessed that would damage aerodynamic performance.

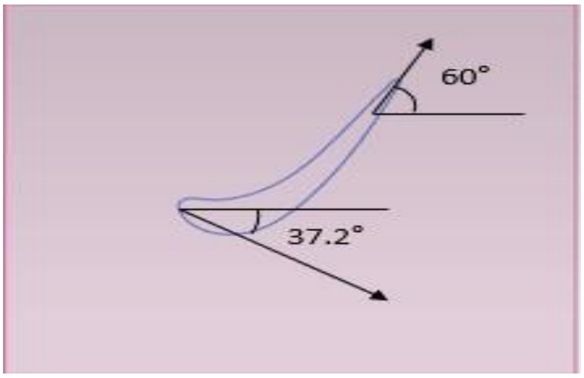

Figure 3-24: 3D gas turbine rotor blade top angle views

Fig 3.24 shows a curving trajectory and two angle measurements along perpendicular axes, such as the Leading edge (LE) and Trailing edge (TE). 60° and 37.2° indicate the path's initial angle from the Leading edge. It appears around the Trailing edge's end before the route descends.

Table 3-6: 3D gas turbine rotor blade geometry specification

Parameters	Value
Height/span	39.04 [mm]
Chord	37.5 [mm]
Thickness at hub	10.1[mm]
Thickness at Middle	7 [mm]
Thickness at Shroud	4.5 [mm]
Blade Angle inlet	37.2°
Blade Angle outlet	60°

The primary thicknesses of the hub, middle, and shroud are presented in Table 3.6, which is located above the 3D rotor, and also includes the specifications of the rotor blade, which were mentioned previously.

3.6.4 Geometry model and numerical methods

3.6.4.1 Geometry models

The meridional section stage of the stator (NGV) and rotor blade with the cylindrical-conical of the rotor hub and shroud, as shown in Fig 3.25. There are flow paths near the trailing edge of the blades. Moreover, the number of stator and rotor blades are 32 and 60, respectively. The hub diameter of the NGV and rotor blade is 258 mm the geometric turn angle is 70^0 for the stator, and the rotor is 107^0.

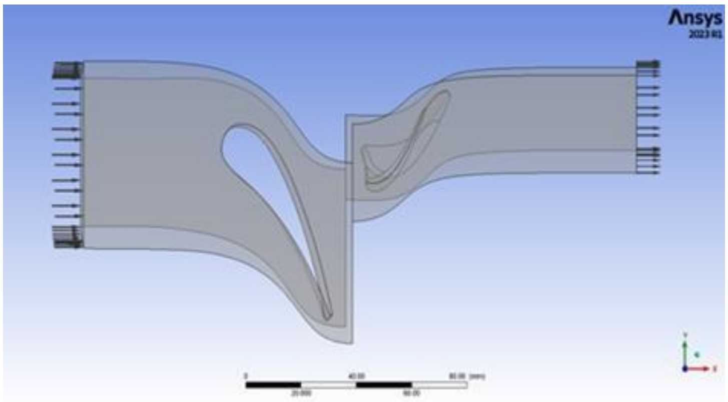

Figure 3-25: Meridional flow path of turbine stage, and stator and rotor blades in Ansys design modeler.

The rotor tip clearance is 0.56 mm; more details can be found in [166], two planes are selected downstream of the stator, and the rotor is named. A schematic picture that depicts the side view of a rotor blade assembly enclosed in a casing as shown in Fig 3.26.

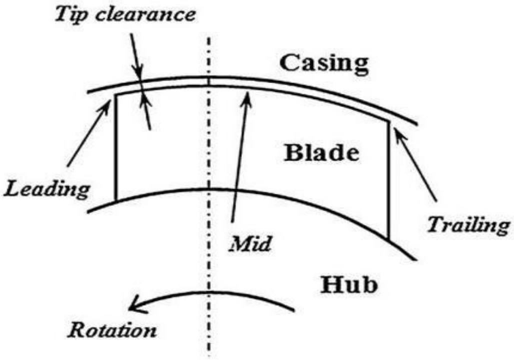

Figure 3-26: Conceptional views of tips leakage [167]

The diagram emphasises the essential components and factors that are significant for the design and functioning of these blades, however, there is a narrow space between the blade's edge and the protective covering. Optimal tip clearance is essential for minimising fluid loss over the blade tips and maintaining effective operation, as shown in Fig 3.26 [167].

3.6.5 3D MT-1 blade Mesh design

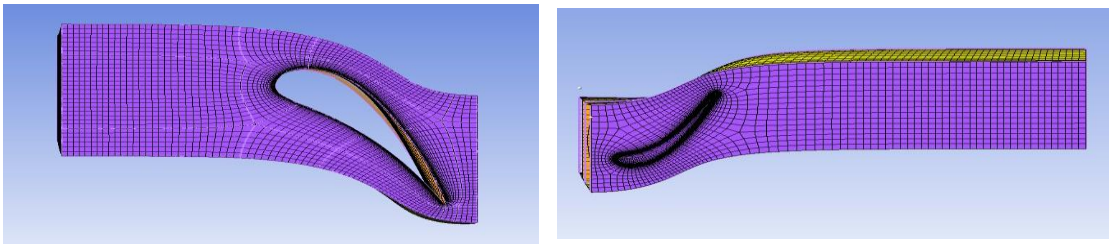
(a) NGV baseline (b) Rotor baseline

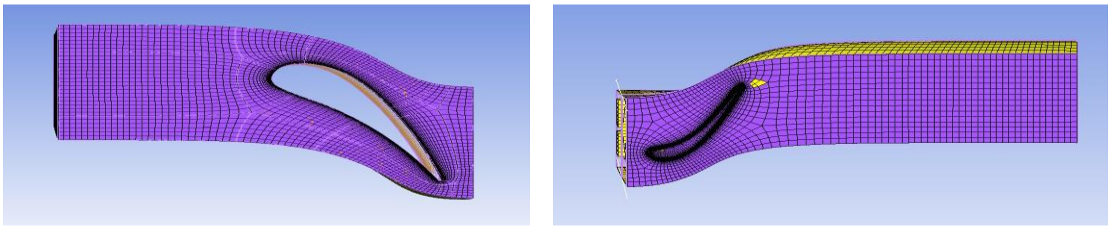
(c) NGV Mesh 0.5x (d) Rotor Mesh 0.5x

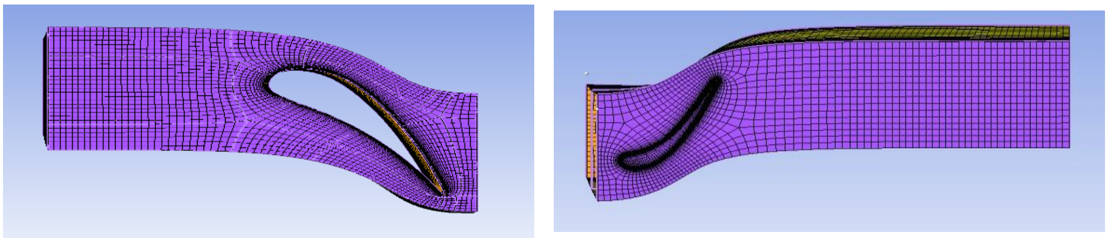
(e) Mesh 2x (f) Rotor Mesh 2x

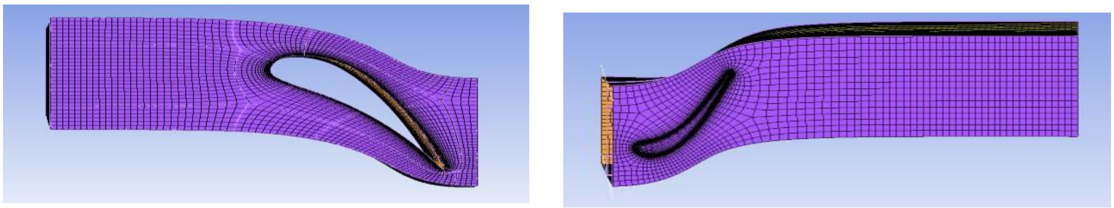
(g) NGV Mesh 3x (h) Rotor Mesh 3x

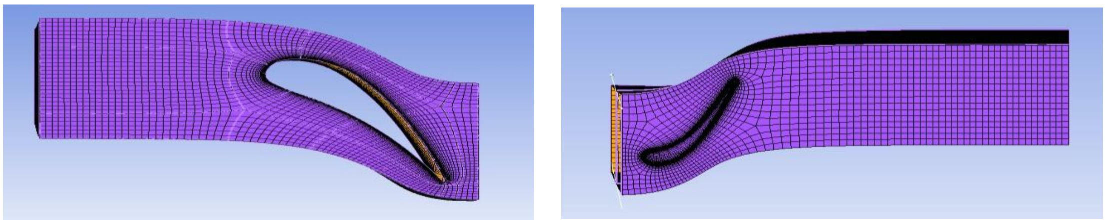
(i) NGV Mesh 4x (j) Rotor Mesh 4x

Figure 3-27: 3D mixing plane Grid independence studies stator and rotor blades

Different 3D mesh resolutions are shown in Fig 3.27. Four types of mesh, such as 0.5x, 2x, 3x, and 4x. In this study, stator and rotor blades are used for these meshes. The Figs a to j are the stator mesh with 0.5x, 2x, 3x, and 4x, meanwhile Figs b to j are the rotor mesh with the 0.5x, 2x, 3x, and 4x.

3.6.6 Set-up of simulation work

Table 3-7 Set of gas turbine blade simulations

Input	Selections
General	Pressure-based solver
Materials – Air – Density – Other inputs	Ideal Gas Law – Constant
Momentum and Thermal Bc's –	**Stator inlet** **Pressure inlet stator** Reference frame – Absolute Guage Total pressure (Pa)- 461500 Direction Specification Method – Normal to direction. Total Temperature (K) - 444. **Pressure outlet Rotor** Backflow reference frame –Absolute Guage pressure (Pa) – 143100 Backflow pressure specifications – Total pressure. Backflow Total Temperature (K)-300. Wall top –stator and rotor – Translations Momenums – wall motion – Stationary.
Mixing plane model	**Stator outlet: rotor inlet**
Solution method	**Scheme** Coupled **Gradient** Green Gauss node based all 2nd orders Upwind
Monitors – Residuals	**1e-6 for energy 1e-5 for rest**

The pressure-based solver is used to the consistent with due 2D work. The mixing plane general conditions are pressure-based solver due the recent updates from the pressure-based solver, it can solve any complex higher Mach number problems. So, this mixing plane simulation procedure solution was used. However, density-based solvers can use higher Mach numbers such as 2-3. However, the Material air- density other output hence, this compressible flow T and ρ are coupled conditions. Meanwhile momentum and thermal Bc's the boundary conditions play an essential role in every simulation work, in this simulation also, in mixing plane simulation used, the boundary condition is based on past research, which was published work. Boundary conditions are and set-up is same for 2D and 3D simulation.

3.7 Qualitative flow visualisation results for 3D MT- 1 Mixing plane, 9500 RPMs

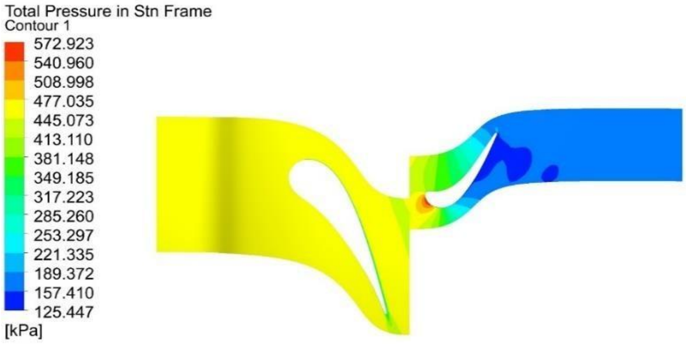

Figure 3-28: 3D gas turbine rotor blade total pressure in Stn Frame

The above Fig 3.28 indicates the total pressure distribution in a stator and rotor blade mixing plane. The contour colour map shows the pressure values in kilopascal (kPa), which range from around 124.5 kPa to 572.9 kPa. The yellow and red colour indicates high pressure, and lower pressure regions denoted by are blue and green.

Moreover, the inlet flow region starts from the stator and passes to the second blade, the rotor blade.The pressure drops in the section mixing plane between the stator and rotor blade, which is rotating at 9500 rpm. The total temperature distribution in a 3D high-pressure gas turbine blade mixing plane stator and rotor blades temperature quantities is shown in kelvin (K), and this ranges between 326.1K, as indicated in blue to 477.1K, as shown in red coloured. Higher temperatures are the yellow and red coloured as shown in Fig 3.29.

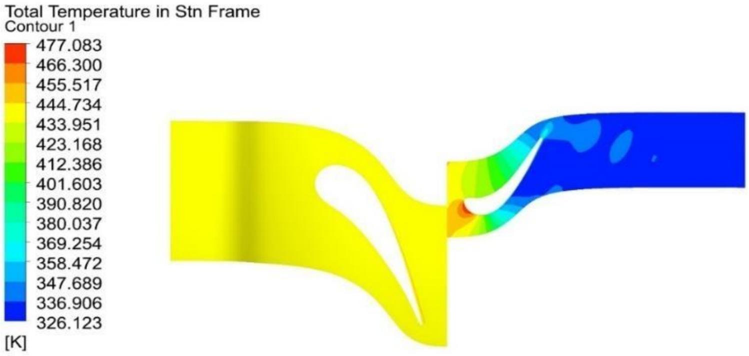

Figure 3-29: 3D gas turbine rotor blade total Temperature in Stn Frame

The 3D high-pressure gas turbine blade mixing plane Mach number distribution is shown in Fig 3.30, and Mach number characteristics are shown in the colour, which ranges from 0, which is coloured dark blue, to red coloured, which is 1.405. However, the higher Mach number increases from coloured red, its appearance surrounding the rotor blade, and the flow decelerates downstream, indicating the lower Mach number area as coloured green to blue.

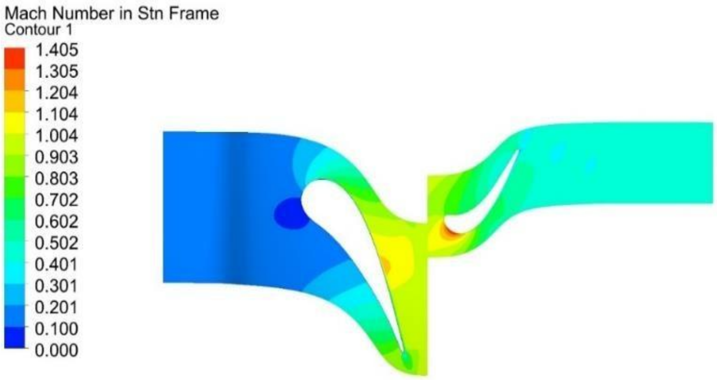

Figure 3-30: 3D gas turbine rotor blade Mach Number in Stn Frame

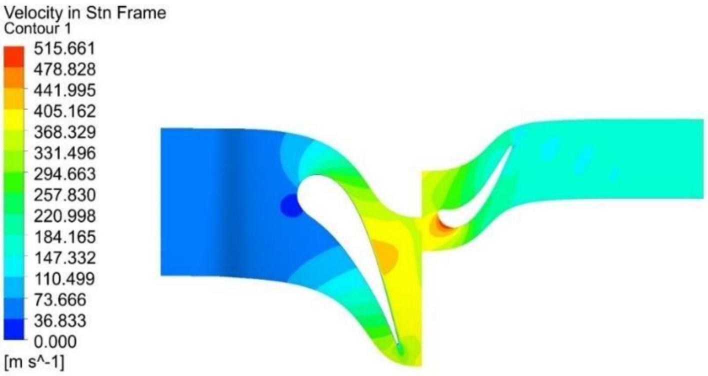

Figure 3-31: 3D gas turbine rotor blade Velocity in Stationary Frame

A 3D high-pressure gas turbine blade mixing plane velocity distribution, in m/s as shown in Fig 3.31. The colour map specifies the velocity magnitude, which varies from 0.00 to 515.661. However, the velocity zone from nearer to the red and yellow is affected near the condition, which aligns with the stator inlet condition. Furthermore, the velocity is decreasing, and this is indicated as the blue and green coloured regions, showing for downstream expansion.

3.7.1 3D MT- 1 Mixing plane for 10000 RPM

Fig 3.32 shows results at 10000 rpm, for total pressure distribution in the flow domain. This ranges between 127.1 kPa to 573.1kPa. As the inlet flow accelerates through the stator and rotor there is a significant pressure drop downstream of both blades, which is represented as blue regions. Through the high- pressure zone is as defined with yellow and red colours.

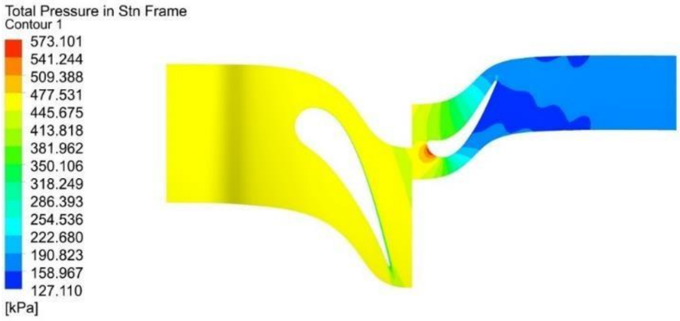

Figure 3-32: 3D gas turbine rotor blade total pressure in Stn Frame

The total pressure distribution varies, from 69.8 kPa to 466 kPa. This flow visualisation illustrates that high-pressure areas have red and orange hues. In contrast, low-pressure areas such as blue and cyan surround the rotor blades, which is presented in Fig 3.33.

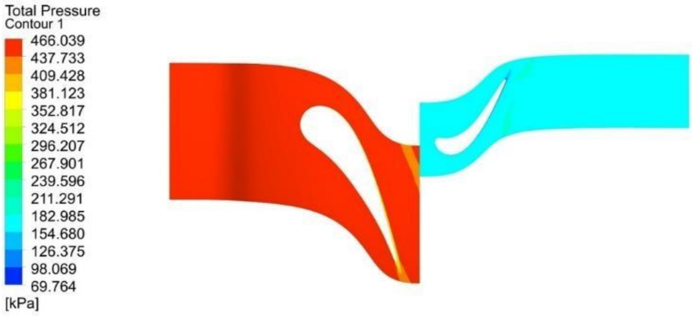

Figure 3-33: 3D gas turbine rotor blade total pressure

Fig 3.34 represents the static pressure distribution, which has values of 106.935 (kPa) to 461.455 (kPa). The red colour represents the static pressure as higher upstream, and the flow passed from the stator to the rotor blade during the process; the pressure is decreased in the given colours, which were green to blue regions.

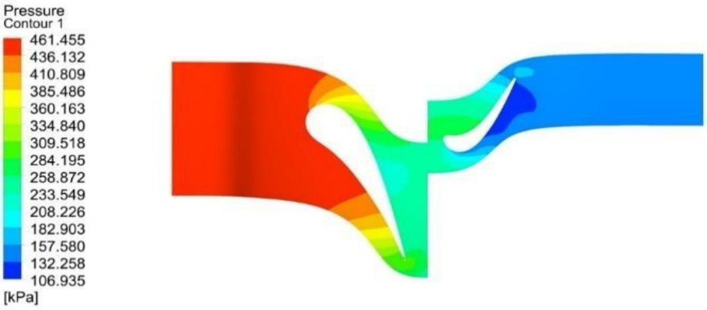

Figure 3-34: 3D gas turbine rotor blade static pressure

The total temperature distributions as shown in Fig 3.35, with a temperature range between 324.7K and 476.750K, which was coloured as red and blue. This stator and rotor blade flow patterns and the temperature is raised upstream, which is yellow to red and reduces as the flow accelerates through the stator and downstream, which is shown in green to blue areas.

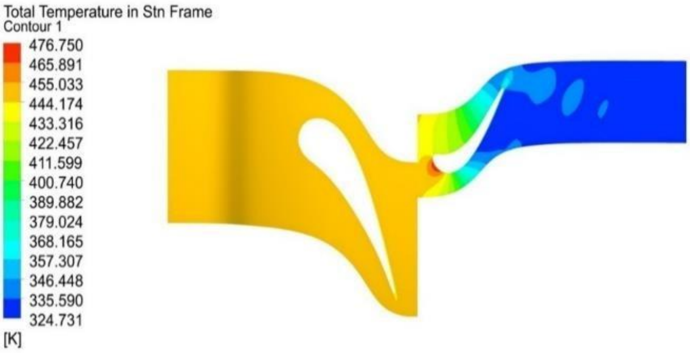

Figure 3-35: 3D gas turbine rotor blade total Temperature in Stn Frame

Fig 3.36 illustrates the total temperature distribution of a 3D high-pressure gas turbine blade mixing plane. This is indicated as the value of temperature is Kelvin, which is presented as K, and the temperature distribution ranges from 444.407 K to 302.492 K. However, the inlet temperature increases from the stator blade, which gradually drops from the rotor blades inlet.

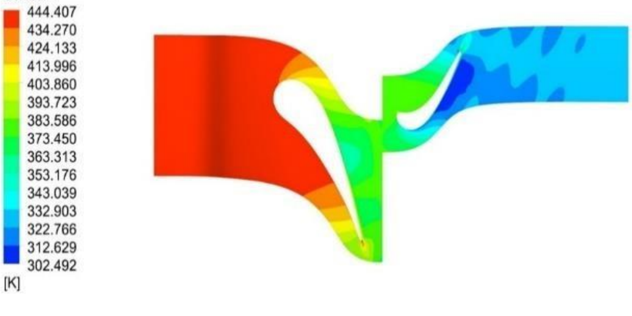

Figure 3-36: 3D gas turbine rotor blade static temperature

The absolute Mach number distribution of the 3D mixing plane as shown in Fig 3.37. This has a values range between a 0.000 to 1.356, which is shown as dark blue and red. This is near the stator (NGV) blade, and Mach number is increasing from stator to rotor blades. However, this Mach number increases near the stator outlet and rotor blades, as shown in red areas.

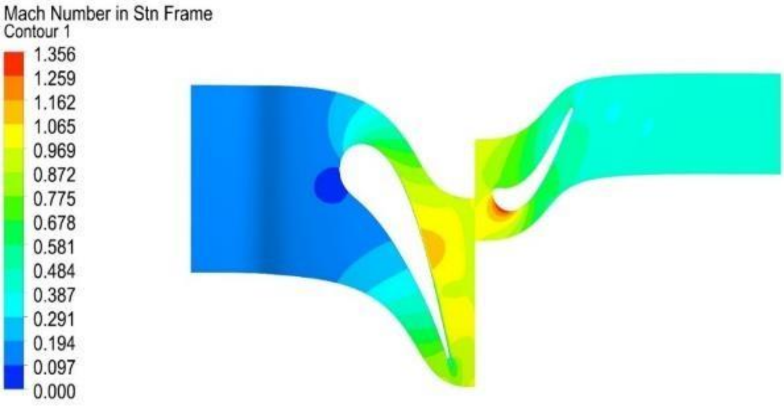

Figure 3-37: 3D gas turbine rotor blade Mach Number in Stn Frame

Fig 3.38 shows the velocity in the Stationary Frame contour; this value ranges between 0 m/s to 503 m/s, representing different colures varying the velocity within the flow 3D mixing plane of the stator and rotor blade. However, the flow decreases on the next stator blade.

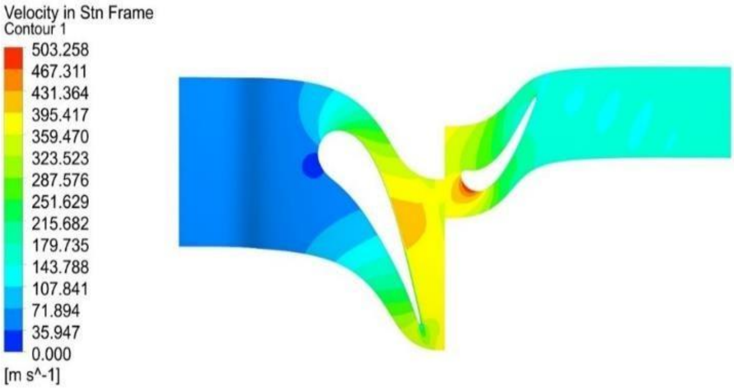

Figure 3-38: 3D gas turbine rotor blade Velocity in stn Frame

3.7.2 3D MT- 1 Mixing plane, for 10500 RPM

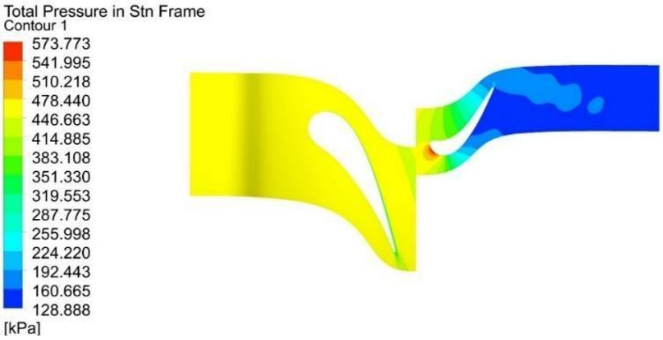

Figure 3-39: 3D gas turbine rotor blade total Temperature in stn Frame

Fig 3.39 shows the total pressure distribution in Stationary Frame, a value of the contour range between 128.888 kPa, which is indicated by the dark blue coloured, and the high pressure, which is 573.773 kPa on complete red coloured; this varies through the domain.

The total pressure, ranges from high pressure 466.060 kPa, represented in red colours, to low pressure of 66.791 kPa, indicated by blue. This pressure distribution highlights a zone with significant pressure variation connecting the two blades of this mixing plane, as shown in Fig 3.40.

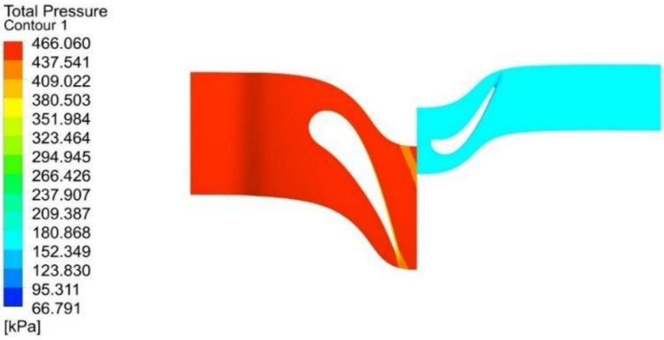

Figure 3-40: 3D gas turbine rotor blade total pressure

Figure 3-41: 3D gas turbine rotor blade static pressure

The higher pressure indicates orange and red zones; following these blue and cyan regions are lower pressure. The total static pressure contour specifies pressure values varying from high pressure at 461.471 kPa in red to the low 107.311 kPa in blue as shown in Fig 3.41.

Nonetheless, this passage from red to blue presents the gradual pressure drop across the 3D mixing plane, with the apparent states of different pressures interacting. Furthermore, the green and yellow regions, indicating mid-range pressure values, are placed between the higher-pressure region on the red/orange and the lower pressure section on the blue.

Fig 3.42 illustrates a contour plot of total temperature in a stationary frame from the simulation results. This temperature is denoted in Kelvin (K), with a gradient reaching from red, indicating a higher temperature of around 476 K, to blue, showing a lower temperature of nearly 323 K.

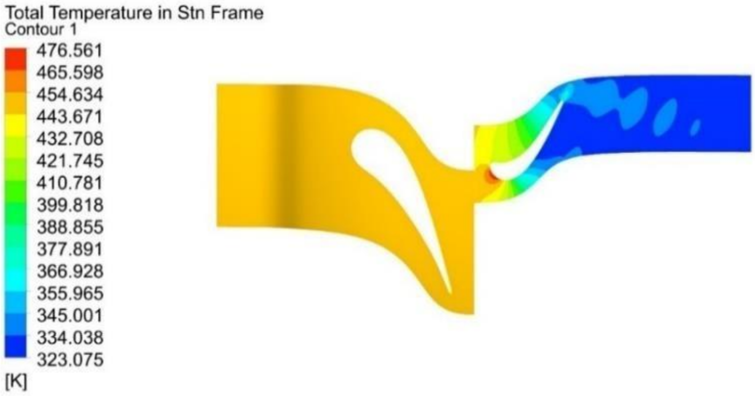

Figure 3-42: 3D gas turbine rotor blade total Temperature in Stn Frame

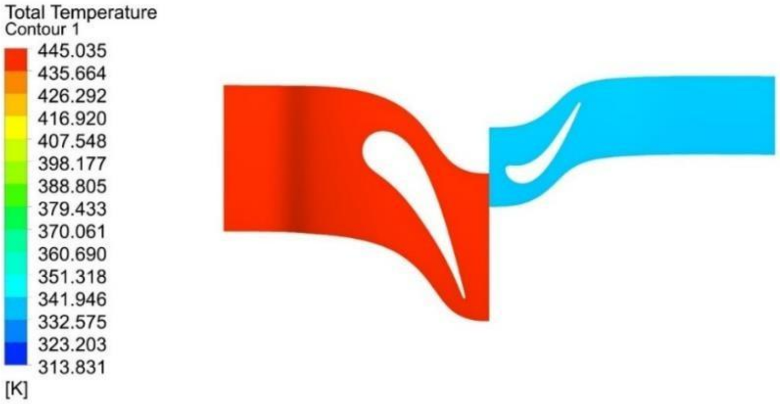

Figure 3-43: 3D gas turbine rotor blade total Temperature

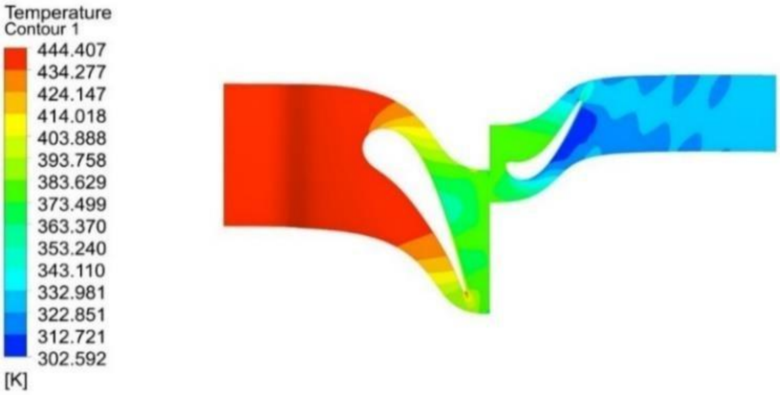

Figure 3-44: 3D gas turbine rotor blade static temperature

Moreover, the total temperature and static temperature distribution of the 3D gas turbine blade mixing plane is as donated as Kelvin (K), which is the range between 313.831 K to 445.035 K and 302.592 K to 444.407 K, which is shown Fig 3.43, and Fig 3.44.

3.8 Quantitative Results

Fig 3.45 (a) shows the Mach number near the axial distance in a nozzle guide vane (NGV) test. However, this plot contains various simulation models such as k-ε_y+30, k-ω_sst_y+1, SA_y+1, and y +2 evaluated alongside test data, characterised as orange points. The Mach number distribution looks to be plotted for two RPMs with rotation velocity cases, such as 10000 and 10500. However, the primary line with rotational velocity is 9500. There is a comparison between these three speeds, such as baseline, which is 9500, 10000, and 10500. Moreover, there is not much difference between using these RPMs and using grid independence studies, as mentioned in Fig 3.45 (b).

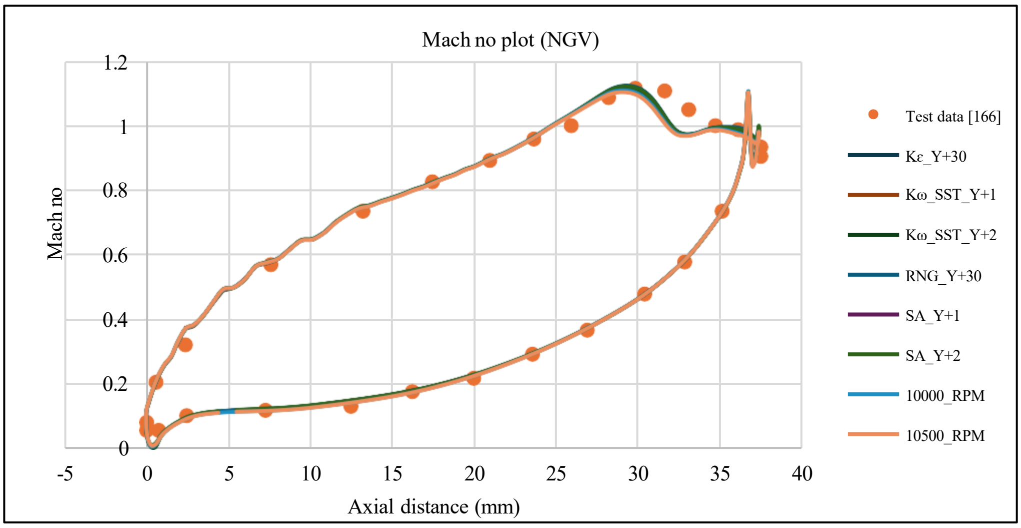

(a)

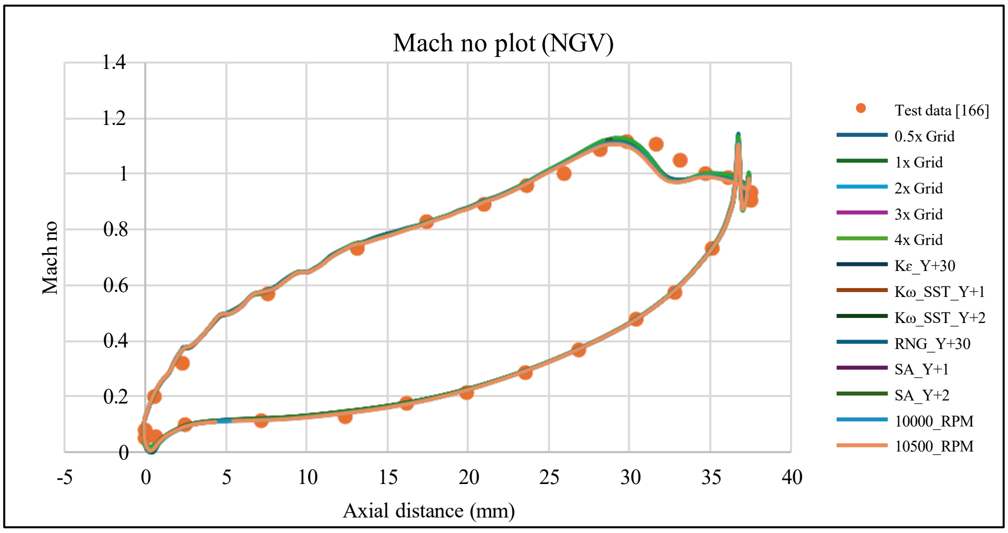

(b)

Figure 3-45: Stator Mach number distribution: (a) and (b) are used different RPMs and turbulence models with GI.

The Rotor Mach number plot on the 3D high pressure turbine blade shows the axial distance in mm, which includes test data, which is represented in orange. Different simulation results are presented, for different turbulent models such as *k-ε*_y^+ =30, *k-ω*_sst_y^+ =1, *k-ω*_sst_y^+ = 2 RNG_y^+ =30, SA_y^+ =1, SA_y^+ =2 thes all are used the further rest of the RPMs such as 10000_RPM (rotational speed of 10,000 RPM), and 10500_RPM (rotational speed of 10,500 RPM) which is shown in Fig 3.46 (a). Furthermore, Grid independence studies have been shown in Fig 3.46 (b). The Mach number rises gradually in the axial distance, and there is a tiny decrease towards the Trailing egde.

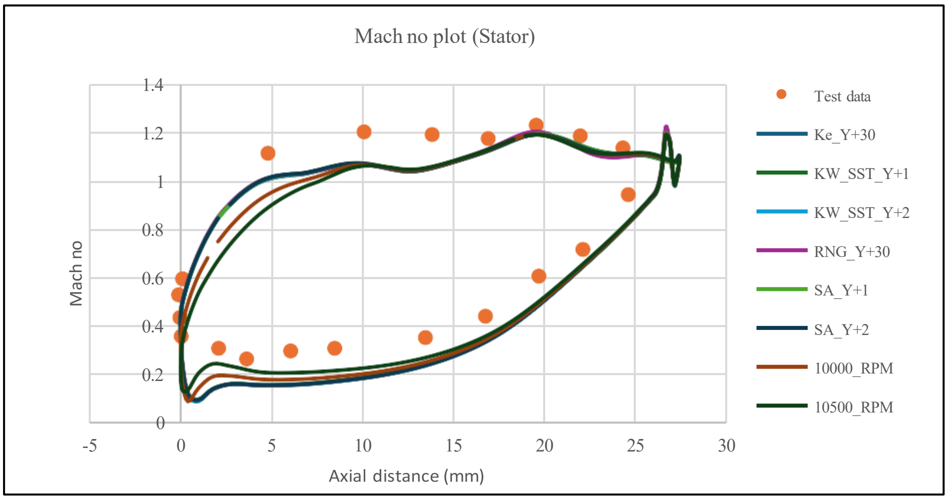

(a)

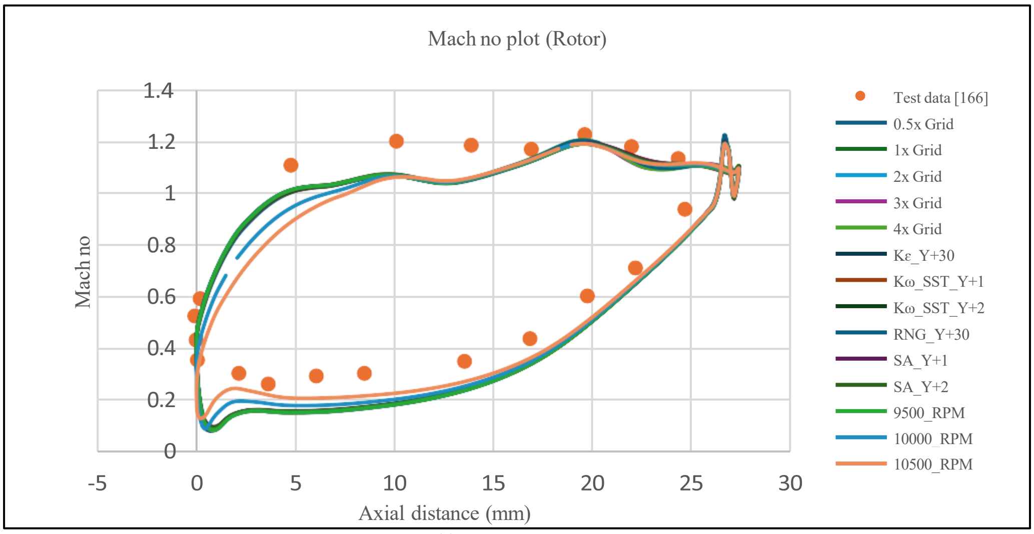

(b)

Figure 3-46: Rotor Mach number distribution: (a) and (b) are used different RPMs and turbulence models with GI.

The Difference of Nusselt number (Nu) down the surface distance at 50% span of the Nozzle Guide Vane (NGV). Furthermore, k-ε_$y^+ = 30$ shows a substantially higher surface distance of 0 mm than the other turbulent models. However, the k-ω_sst_ $y^+ = 1$ and k-ω_sst_ $y^+ = 2$ specify more uniform values closely similar the rest of the data in a particular region; moreover, the rest of the turbulent models, such as RNG_ $y^+ = 30$, SA_ $y^+ = 1$, SA_ $y^+ = 2$, with 10000, and 10500 RPM shows closer to the experimental data as shown Fig 3.47 (a) all through the different types of grid independence studies such as 0.5x,1x, 2x,3x, and 4x, which is shown in Fig 3.47 (b).

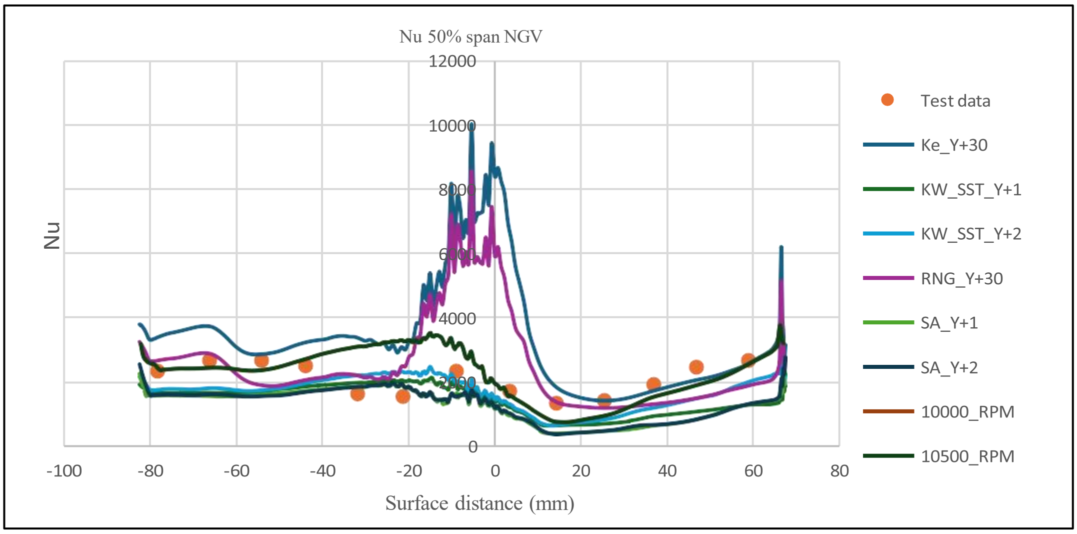

(a)

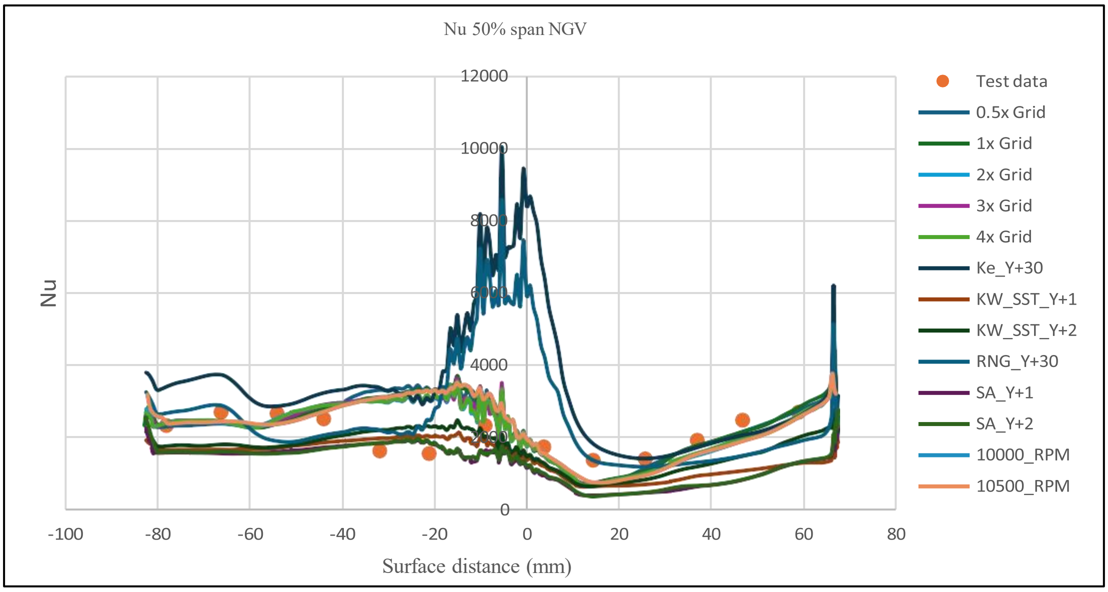

(b)

Figure 3-47: Stator Nusselt number distribution: (a) and (b) used different RPMs turbulence model and GI

The Nusselt number (Nu) distribution of the 3D high-pressure gas turbine blade at 50% rotor blade span. Which is used to compare with different turbulent models such as k-ε_ y^+=30, k-ω_sst_ y^+=1, k-ω_SST_ y^+= 2 , RNG_ y^+=30, SA_ y^+=1 and SA_ y^+=2 with using the 10000, and 10500 RPM all these simulations validated with experimental test data as shown in Fig 3.48 (a). Furthermore, grid independence studies were used this rotor Nusselt number distribution such as 0.5x,1x, 2x,3x, and 4x, which is including different type of turbulence models as shown in Fig 3.48 (b).

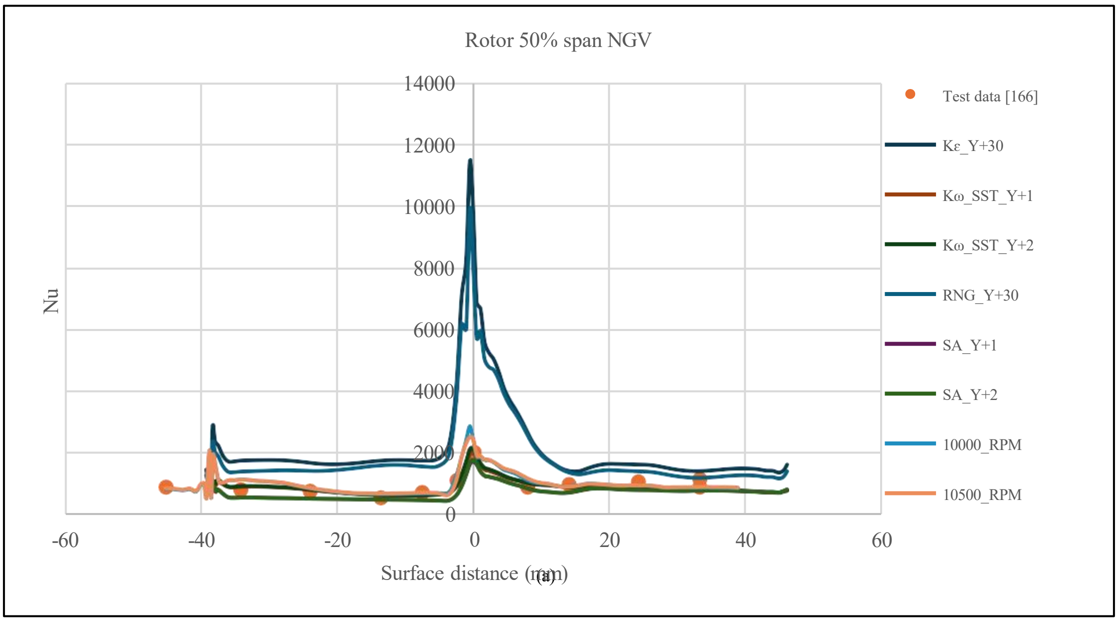

(a)

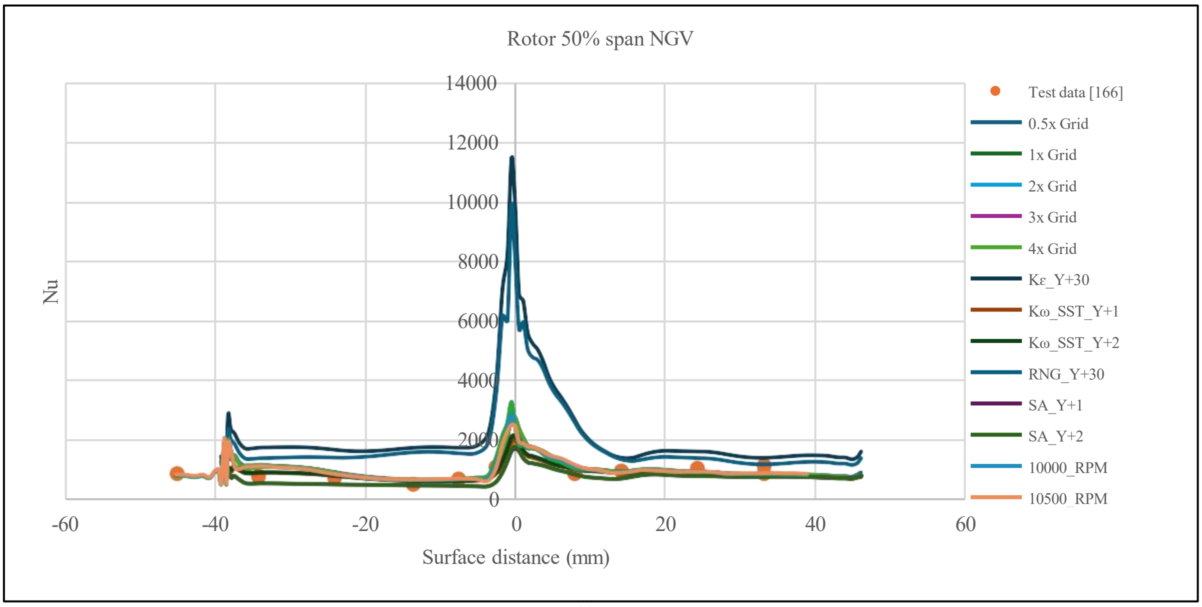

(b)

Figure 3-48: Rotor Nusselt number distribution: (a) and (b) used different RPMs turbulence model and GI

Fig 3.49 (a and b) shows a comparison of normalised pressure (P/Po) versus normalised chord length (x/c) for a Nozzle Guide Vane (NGV). It involves test data, which is signified by dots, and several computational grids, such as grid independence studies, were used this pressure distribution, such as 0.5x,1x, 2x,3x, and 4x.

Which is used to compare with different turbulent models such as k-ε_ $y^+ = 30$, k-ω_sst_ $y^+=1$, k-ω_SST_ $y^+=2$, RNG_ $y^+=30$, SA_ $y^+=1$ and SA_ $y^+=2$ with using the 10000, and 10500 RPM all these simulations validated with experimental test data.

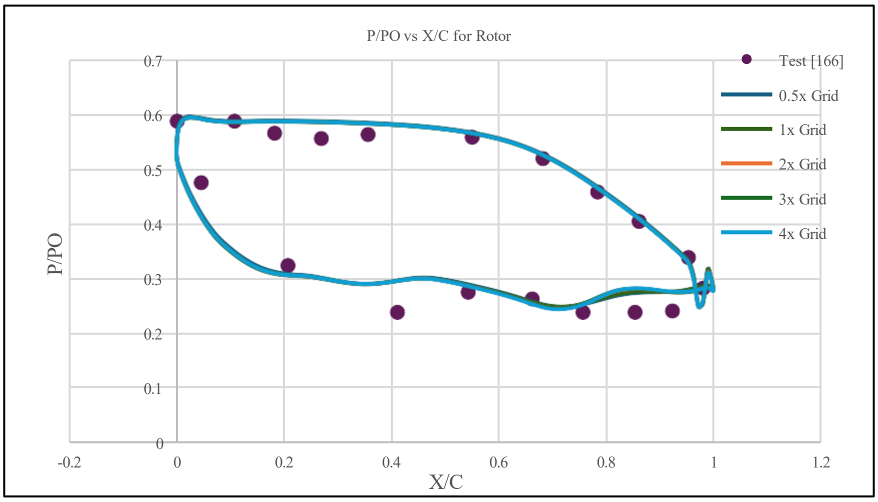

(a)

Additionally, Fig 3.49 (c) illustrates the pressure coefficient (P/P0) with the chordwise position (x/c) for a rotor, comparing various turbulence modules and grid independence studies. However, Fig 3.49 (d) shows that variation of the turbulence models for rotor blade for mixing plane.

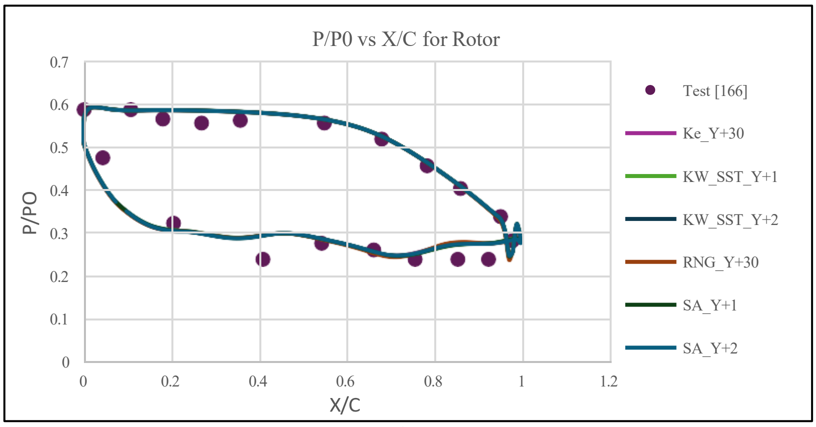

(b)

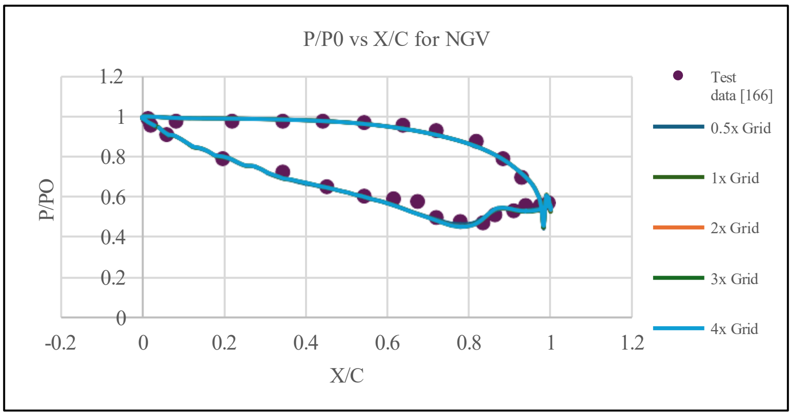

(c)

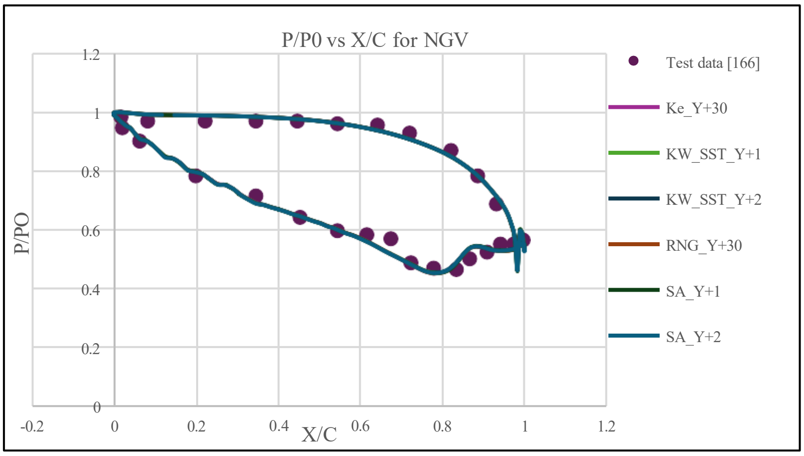

(d)

Figure 3-49: Pressure distribution: (a) stator with grid independence studies, (b) stator with turbulence model, (b) rotor with grid independence studies, and (d) rotor with turbulence models with GI.

3.9 Discussion for flow–induced mixing plane analysis

3.9.1 Grid independent studies with Different types of rotational speed

The different span locations by using the CFD methodology to predict the pressure distribution and heat transfer around rotor and stator. The research was conducted using a CFD methodology that was initially developed for the mixing plane to utilise different types of span locations. In this work there are different turbulence models such as *k-ω, k-ε,* RNG and SA for different rotational speed (10,000 and 10500). Different meshes were also used as part of a grid independence study with key results shown in Table 3.8.

Table 3-8: 3D High-pressure gas turbine blade Grid independence studies with RPMs

Grid	No of Elements in stator	No of Elements in rotor	Mass flow [kg s^-1].	Expansion ratio	Efficiency
0.5x	85608	106996	17.2685	2. 837	0.875
Baseline(1x)	166460	200990	17.2165	2.838	0.8755
2x	332920	409070	17.23	2.832	0.8764
3x	499380	614170	17.2285	2.832	0.8764
4x	665840	806220	17.234	2.832	0.8764

Mesh sizes included the baseline and scaled ones with scaling factors of 0.5x, baseline 1x, 2x, 3x, and 4x. Data in Table 3.8 the number of elements in the stator and rotor, along with the efficiency, mass flow, and expansion ratio. The mesh independence study has finer a mesh from 0.5x to and all cases; the number of nodes and elements increases; however small variations in the mass flow in each grid independence studies is reported in [168]. Meanwhile, the expansion is in the same direction, and there is a slight difference in the expansion ratio connecting each cell. Furthermore, efficiency increases somewhat with a finer grid but seems constant surrounding the 2x grid, with the same minor changes afterwards.

In this 3D mixing plane mesh independence study, the 1x baseline mesh gives us a reliable balance of accuracy, and as the efficiency difference, mass flow, and expansion ratio after all 2x are very small in [169].

3.9.2 3D High-pressure gas turbine blade turbulence models with RPMs

Simulation results for numerous turbulence models, with two rotational speed is included in Table 3.9.

Table 3-9: 3D High-pressure gas turbine blade turbulence models with RPMs

Turbulence model	No of Elements in the stator	No of Elements in the rotor	Mass flow [kg s^-1].	Expansion ratio	Efficiency
k-ε_y+30	135100	121862	17.2355	2. 8327	0.87510
k-ω_sst_y+1	226080	270830	17.215	2. 8359	0. 87591
k-ω _sst_y+2	193340	246158	17.2275	2. 8349	0. 87587
k-ω _ y +1	226080	270830	17.1815	2. 8378	0. 87558
k-ω _ y +2	193340	246158	17.1915	2. 8369	0. 87539
RNG_y+30	135100	121862	17.2675	2. 8302	0. 87603
SA_ y +1	226080	270830	17.2435	2. 8318	0. 87735
SA_ y +2	193340	246158	17.256	2. 8314	0. 87748

The comparison and wall treatment between each turbulence model (such as *k-ε*, *k-ω*, RNG, and SA (Spalart-Allmaras), and wall treatment (y^+), were calculated in [170]. However, the efficiency was evaluated from these turbulence modules, *k-ω*_sst_y^+ =1 and *k-ω*_sst_y^+ =2, which showed efficiencies of 0.87591 and 0.87587, respectively. The *k-ε*_y^+ = 30 module, following this, showed an estimated efficiency of 0.87510. Furthermore, SA (Spalart-Allmaras) models perform well, specifically for y^+ values of 1 and 2. SA_y^+ =1 and SA_y^+ = 2 have efficiencies of 0.87735 and 0.87748, respectively, locating them among the top-performance models in this investigation.

The efficiencies range from 0.8684 to 0.87748, and SA_ y^+ = 2 and SA_ y^+ = 1 models have matching efficiencies ratings, whereas *k-ω* differences perform well at about 0.875.

Table 3-10: 3D High pressure gas turbine blade different RPMs

RPMs	No of Elements in the stator	No of Elements in the rotor	Mass flow [kg s^-1].	Expansion ratio	Efficiency
10000_RPM	166460	200990	17.231	2.842	0.8684
10500_RPM	166460	200990	17.215	2.846	0.8728
Baseline RPM k-ω_sst_y+1	226080	270830	17.215	2. 8359	0. 87591

The 10,000 RPM rotational speed results have a lower efficiency than the 0.8684, and at 10,500 RPM, efficiency increases to 0.8728, showing that raising RPM improves performance but not as significantly as specific turbulence models: furthermore, increasing stator and rotor element count in models, such as the *k-ω*_sst_ y^+ = 1 results in enhanced efficiency. The baseline RPM and turbulence model were considered, and efficiency is increased as shown in table 3.10.

3.10 Flow physics and numerical limitations

This chapter investigated the MT-1 blade, and the 2D and 3D mixing-plane simulations have been validated against experimental data. This simulation analysis focuses on the interaction between the stator and rotor blade.

The pressure distribution along the blade surface reveals the key to aerodynamic performance. A strong pressure peak is observed near the leading edge of the blades due to the stagnation of the incoming flow with the fluid accelerating over the suction surface of the leading edge, as shown in Fig 3.49. The downstream pressure gradient develops, such that the static pressure reduces and the local velocity increases. This decelerating flow leads to pressure recovery. The accuracy of this pressure recovery is highly sensitive to near-wall mesh resolutions. The coarse mesh simulation underpredicted these pressure drops because they are insufficient to resolve the velocity gradients at the boundary layer interfaces. This was less of an issue for finer meshes which were used for the main analysis.

Secondary flow structures arise from the interaction between the flow domain and the rotor blade's rotation during operation. Both the k-ω and Spalart Allmaras models capture these effects more accurately than other turbulence models, as shown in the Table 3.9. Meanwhile heat transfer is enhanced near the leading edge of both blade regions due the mixing between the two blades which helps increase the wall temperatures gradually. However the downstream blades development of boundary layers on the downstream blade reduce the heat transfer because of the associated in convection due to the velocity decrease shown in Fig 3.8.

Mesh independence studies confirm that the finer meshes the improved representation of the boundary layer around both blades, leading to more reliable predictions of pressure distributions. Overall, the k-ω model gives the most consistent agreement with experimental data.

Chapter 4: Validation of the Experimental Comparison for internal single stage swirl cooling chambers

4.1 Introduction

This chapter is the second major step in the methodology and it concerns the thermal performance inside a typical swirl cooling chamber. This gives confidence that the heat transfer predicted by the CFD method for internal flow, matches well with experimental values it concerns the pressure drops and heat transfer behaviour is investigated for a single- stage swirl cooling chamber with five internal nozzles. Each nozzle has a different size and shape which are tested using CFD simulations and validated with results from literature. The results in this chapter show how accurate the simulation specifically is for predicting thermal behaviour for a relevant test case for internal swirl cooling.

4.1.1 The geometry of the experimental swirl cooling configuration

The physical layout of the internal swirl cooling chambers 3D experimental single-stage swirl cooling gas turbine leading edge is illustrated in Fig 4.1 below. This is a five-nozzle swirl cooling system with a single channel, measuring 100 mm in length.

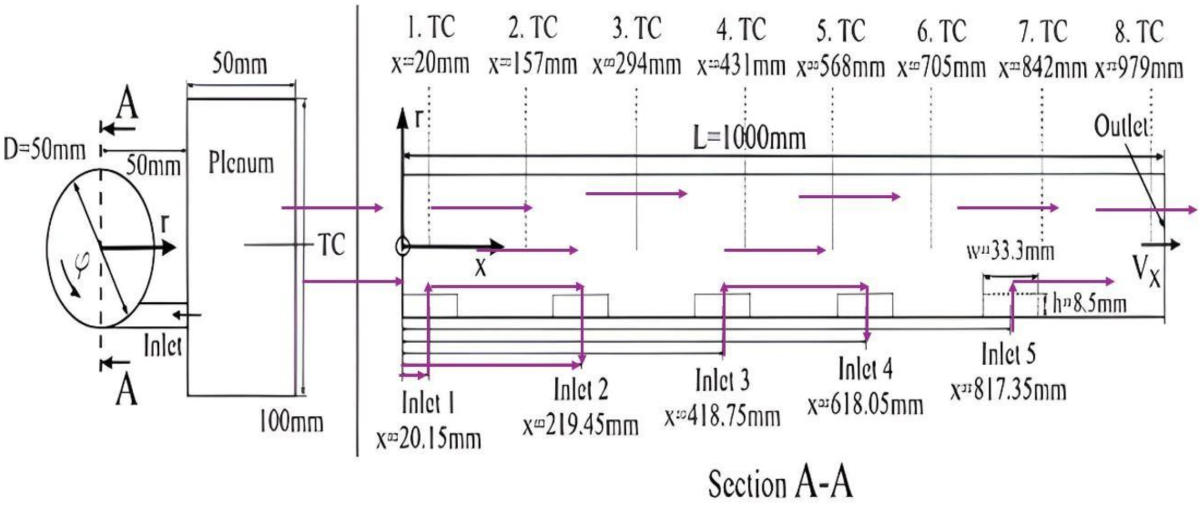

Figure 4-1: 3D EXP swirl cooling gas turbine blade leading edge [171]

The length, L of the swirl cooling chambers, specifically a circular duct, serves as the inlet (left side) of the cooling mechanism. Air enters the inlet and outlet in the X and V_x direction, and ***r***, ϕ are known as radial and angular coordinates; this is used to characterise the swirl cooling within the duct. Both axial and longitudinal views, dimensional of plenum are as shown in Table 4.1whcih is related to section sections A- A in Fig 4.1.

Table 4-1: Specification of the 3D experimental swirl cooling gas turbine blade leading edge

Parts	Size
Tube Diameter	50 [mm]
Tube length	1000 [mm]
Plenum Length	100 [mm]
Plenum width	50 [mm]
Inlet jet Tube Width	33.3 [mm]
Inlet jet Tube Height	8.5 [mm]
Tube plenum	50 [mm]

This geometry complete from the specifications, shown in Table 4.1 are illustrated in Fig 4.2, which is includes inlet jet.

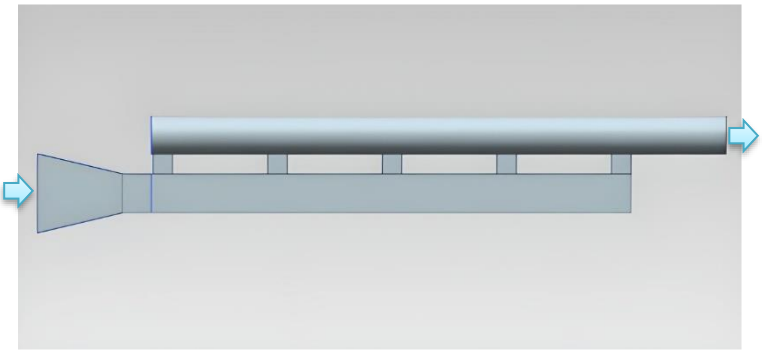

(a) .

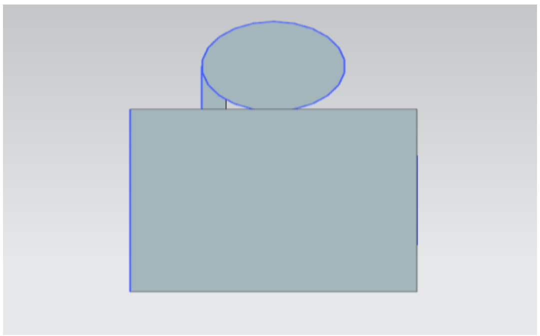

(b)

Figure 4-2: Geometry specifications of the swirl cooling specifications

Simulations are mainly focused on the pressure drop and heat transfer in this internal cooling passage. However, jet sections are almost flow is stable between the jet along the axial direction after the heat transfer on the swirl tube, and it will contain swirl with constant swirl intensity; furthermore, the multi-convergent swirl cooling channels to resist the cross-section flow, which is preventing heat transfer rate upstream and downstream of the swirl cooling tube.

Compared to a baseline swirl tube, the average Nusselt number increased for the full range of Reynolds numbers in the experimental studies as shown in the Table 4.2.

Table 4-2: Validation studies: Reynolds number and Nusselt number increasing

Reynolds Number	Nusselt Number Increase (%)
10,000	11.8
20,000	15.5
30,000	19.4
40,000	23.3

These experimental observations provide additional insights into the turbulent flow structure in the swirl channels to help guide the three-dimensional computations. In the swirl cooling channels, the flow will pass through the plenum, which has adiabatic walls which means there is no heat transfer across them. Aim enters the chamber through, velocity inlet and a pressure outlet the plenum and swirl tube of constant diameter, which has an isothermal wall. Five tangential slots or nozzles allow air to flow from inlet, and they induce swirling motion inside the swirl tube, see Fig 4.3.

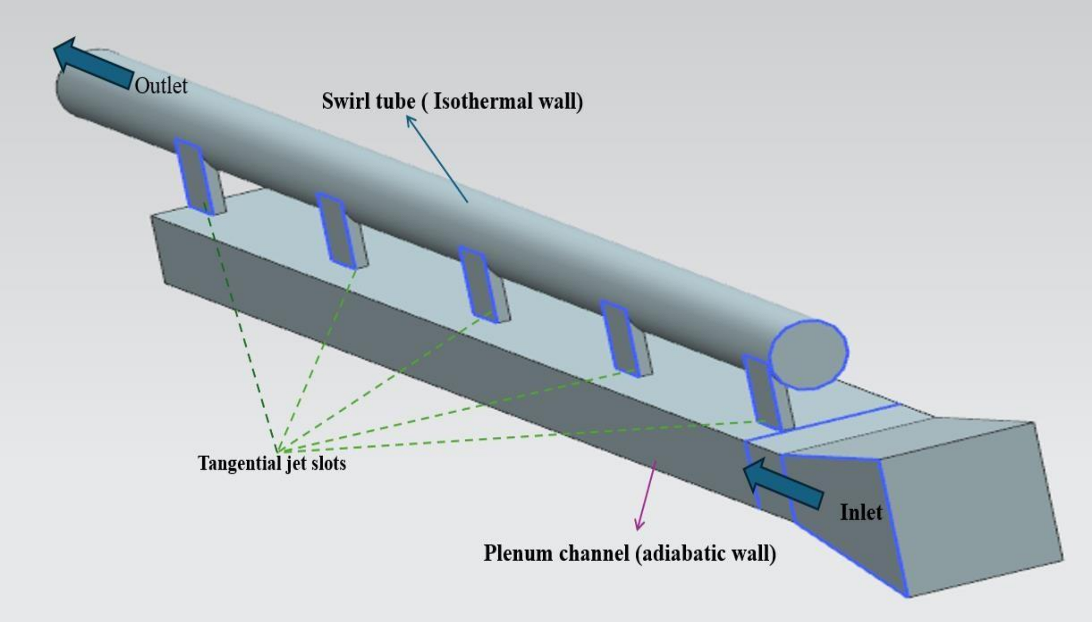

Figure 4-3: Geometry specification of the single stage swirl cooling

The air enters the inlet of the plenum and is injected through the tangential swirl cooling tube, and due to the isothermal wall conditions, the swirl flow enhances the heat transfer under the rotating swirl conditions.

4.1.2 Mesh Design for experimental cooling.

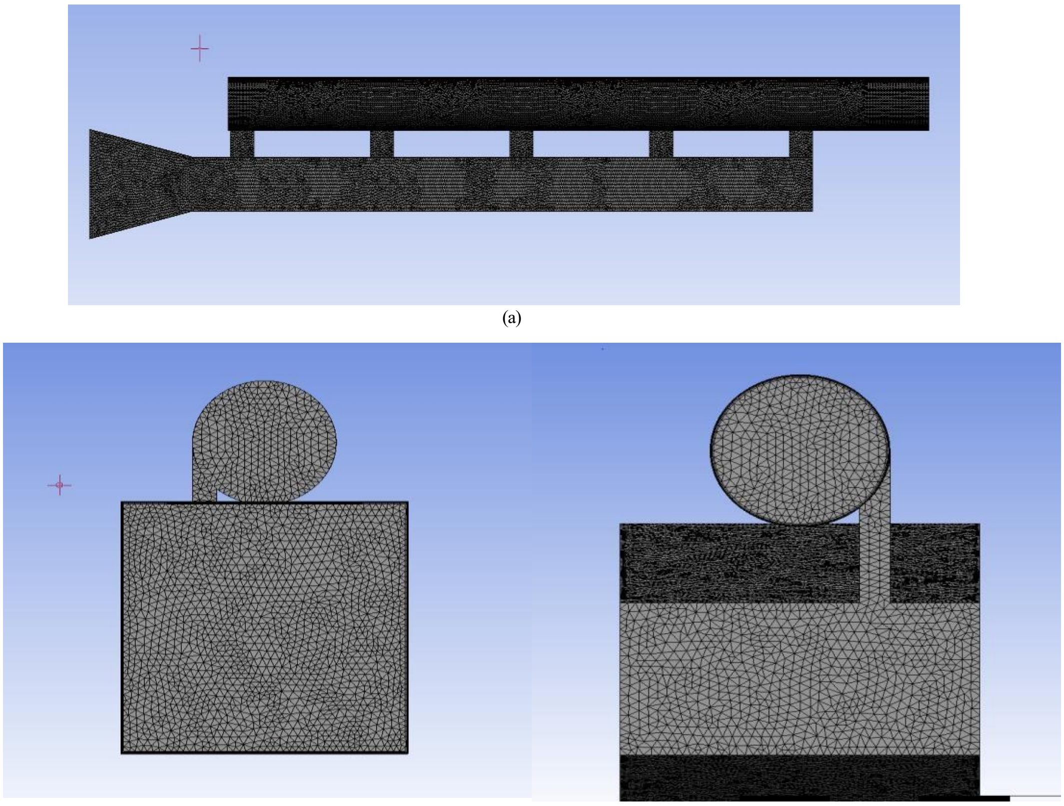

(a)

(b)

(c)

Figure 4-4: Swirl cooling mesh: (a): full duct mesh, (b) Inlet duct mesh, and (c) cross-sectional mesh duct.

Table 4-3: Mesh specifications

	Mesh Statistics	
0.5X	Nodes	346400
	Elements	1045393
1X	Nodes	690345
	Elements	2136216
1.5X	Nodes	952973
	Elements	2988908
2X	Nodes	1315811
	Elements	4163957

Fig 4.4 illustrates that the mesh generation for this swirl cooling CFD model was performed using ANSYS Fluent, and an unstructured tetrahedral high-quality mesh was used to fill the domain with cells. The global element size was set to 2 mm, giving 1.05 million elements within the computational flow domain. Near the wall, the mesh consists of 10 inflation layers with a growth ratio of 1.1. Near the wall, smooth layers are present. In this region, the thickness of the first layer to the non-dimensional wall distance y is around 1 to 1.5, and the overall mesh specification are presented in the Table 4.3.

4.1.3 Numerical set-up

In these numerical studies, the heat transfer distribution was validated against experimental data. Within the domain, the coefficient of heat transfer was calculated using flow and heat transfer simulations. Computations were conducted using a, coupled CFD solver and the energy equations to simulate these fluid flows and temperature distributions. From the simulation results, the swirl cooling walls' local heat flux (q'') are calculated. The convective heat transfer is determined by:

$$Nu = \frac{h_{cc}D}{k} \tag{4.1}$$

Were h_{cc} is the convective heat transfer coefficient, D is the characteristic diameter, and k is the thermal conductivity. The convective heat transfer for this single stage swirl cooling set -up as mentioned in Eq 2.4.

The alternative to expanding the local diameter of the swirl tube, the constant tube diameter (50 mm) near the inlet jet is described as the characteristic diameter in the description of the Nusselt number. Alternatively, the description of the Nusselt numbers of the two swirl tubes is established on the constant hydraulic diameter, which improves the comparison of the heat transfer occurrence between the two swirl tubes. According to the processed averaged results, the differentiation in the Nusselt numbers based on the continuous tube diameter and the local tube diameter is less than 5.0%.

Furthermore, the relationship between temperatures higher than the reference temperature can be observed as researched by Sua et al. [11] and Van et al. [19]. In the swirling flow classification with multiple tangential inlet jets, the temperature distribution in the tube is very complex. In this numerical validation, according to the inlet jet temperature, T_{in} was specific as a suitable reference temperature to establish the heat transfer performance is measured by using the Nusselt number *Nu.* It specified actual inlet jet flow to thermal surroundings, and then the heated air is delivered to each injection slot throughout the plenum, where the plenum's hot and cooling air mix and hot air-wall heat exchange is produce a downstream

The temperature of the jet flow is diminishing, and according to its convergent structure, the swirl tube may be categorised into five portions, with the reference temperature for each segment being the temperature at the upstream jet inlet.

To investigate the flow structure and heat transfer details of steady-state studies, a three-dimensional numerical simulation was conducted for a two-swirl cooling tube. Fig 4.3 shows a schematic of the numerical simulation model and its boundary conditions, which are same to those in the experiments.

The front and rear surfaces chambers are divided on the swirl cooling, which is set to an isothermal wall. The experimental data of the front surface chambers are chosen to compare with the simulation results. All wall surfaces are treated as no-slip boundaries. Suitable for low Mach number flows (Ma < 0.3), the flow is implicitly assumed to be incompressible, and the fluid properties are considered temperature-dependent in the computations.

This two-swirl cooling tube numerical simulation was conducted using the ANSYS Fluent 2022 in [171]. The SST *k-ω* turbulence model was preferred due to its good performance in predicting heat transfer in complex swirl cooling flow regions as reported in [172].

In this study the commercial grid generation software Fluent Meshing 2022 has been implemented to generate an unstructured mesh for all the validation cases. Fig 4.2 shows the detailed mesh information for all multi-convergent swirl tubes. The thickness of the first layer is 0.010 mm, and the mesh is concentrated near the wall flow region. This value corresponds to the first l cell and meets the requirements of the SST *k-ω* turbulence model.

Meanwhile, grid independence studies were done for the swirling flow heat transfer simulation with mesh elements approximately ranging between from 2.0 million to 10.0 million. A shown in Table 4.3 the spanwise averaged Nusselt number is presented for different grids sizes. For the 4.5 million cell mesh and the simulation averaged to a suitable value of the globally averaged Nusselt number which is less than 1.0% details are in shown in Table 4.4.

Table 4-4: Validation studies: Mesh size and Global Averaged Nusselt number

Mesh size (Million Elements)	Global Averaged Nusselt number
2.0	113.8
3.5	114.1
4.5	117.0
7.0	117.4
10.0	117.7

To further estimate the consistency of the CFD simulation, the widely- recognised grid convergence index (GCI) method [171] was chosen to calculate the discretisation error.

Table 4.5 indicates the GCI calculation resultsfor the spanwise averaged Nusselt for Re= 40.000. Significant variations are present in the system after the inlet jets; nonetheless, the mean GCI value of the globally averaged Nusselt numbers is below 1.0%, indicating that the computational mesh, comprising over 10 million elements, has a minimal impact on the predictive outcomes. After thoroughly evaluating the computational expenses and grid verification outcomes, the mesh system, comprising approximately 4.5 million elements, was selected for all calculations.

Table 4-5: Validation studies: local GCI statistic for Span-wise – Averaged Nusselt Number (Re = 40,000)

Regions	Max GCI (%)	Min GCI (%)
Inlet Jet Region	3.5	0.7
First Swirl Chamber	2.3	0.7
Middle Swirl Region	1.7	0.5
Downstream Cooling Section	1.3	0.2
Entire Computational Domain	3.4	0.3

The numerical simulations of the multi-convergent swirl tube utilise the SST *k*- *ω* turbulence model and compared with the Standard *k*-*ω* turbulence model, the Realisable *k*-*ε* turbulence model, and the RNG *k*-*ε* turbulence model with enhanced wall treatment in [100].

All simulations were conducted under identical mesh and boundary conditions and were compared with experimental data. Evaluating heat transfer and pressure loss findings, the SST *k*-*ω* turbulence model offers superior accuracy in forecasting the performance of the swirl cooling system, the complete set-up of the simulation as shown in Table 4.6.

4.2 Set up of the experimental single-stage swirl cooling

Table 4-6: Set up of the experimental single-stage swirl cooling

Input	**Selections**
General	Pressure-based solver Density-based solver usually used for very high mech No (M=2-3) However, nowadays, this pressure-based solver uses complex problems
Materials – Air – Density – Other inputs	Ideal Gas Law – Constant The flow is travelling at M > 0.3, hence is compressible (T and ρ are coupled).
Momentum and Thermal BC's –	**Cooling passage inlet** Reference frame – Absolute Mass flow rate (kg/s)- 0.028 Direction Specification Method – Normal to direction. Total Temperature (K) – 288.15K. **Pressure outlet.** Outlet pressure (bar) – 1 bar **Wall conditions** Tube wall temperature (K) – 323.15 As given in the literature To measure the heat transfer rate and thereby Nusselt number at the cooling passage walls.
Solution method	**Advection Scheme** High Resolution. 1^{st} order Reduce no. of iterations by solving pressure and momentum equations simultaneously. Better for structured mesh For stability, 1^{st} order for 300 iterations, then switched to 2^{nd} order for accuracy
Monitors – Residuals	**1e-6 for all parameters**

The main general setting is that the pressure-based solver is ideal for effectively solving complex problems, and this is in comparison with the density-based solver, can use a very high Mach number (M=2-3), and a pressure-based solver is suitable for this current application for the compressible flow (M > 0.3). This setup uses material properties as air, and the density is modelled as an ideal gas. The, the flow is compressible, with a Mach number constrained to 0.3, and the Ideal Gas Law accounts for changes density and temperature, which are linked of thermodynamically. However, inlet is justified because the absolute reference confirms that the flow properties are specified relative to a fixed coordinate procedure, simplifying the explanation of results. The solution methodology involved first using 1st order discretisation to help with stability, then switching to 2nd order to reach convergence with higher accuracy. Residuals are were required to achieve satisfactory convergence.

4.3 Quantitative Results

Fig 4.5 indicates the Nusselt number (Nu), and axial distance for different turbulence models, which displays the five sets of data and compares experimental data which used thermocouples. The horizontals axis X/D, represents the axial distance to diameter ratio (refer to Figure 4.1) of the experimental swirl cooling duct. on the vertical axis is the averaged *Nu*, representing the heat transfer and convective heat transfer in the duct, which increases the point-to-point values.

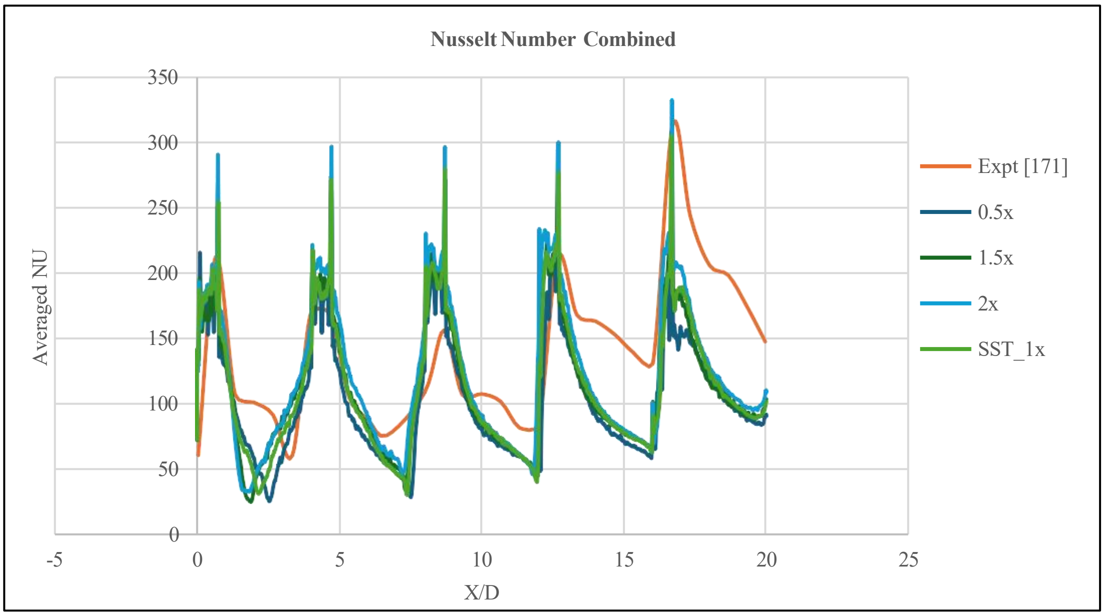

Figure 4-5: Nusselt number comparison with grid independence study

The SST k -*ω* model and experimental Nusselt number are in good agreement, mainly at the heat transfer peaks, showing good predictions for the turbulent intensity to heat transfer. However, the 1x to 1.5x turbulence is best matched with the experimental data. The 0.5x and 2x turbulence results shows some noise and overlap with experimental data.

Fig 4.6 indicates the Nusselt number (Nu), and axial distance for different turbulence models, which displays the five sets of data points and uses the thermocouples for the experimental set with other turbulence models. The (horizontal axis) X/D represents the axial distance diameter (refer Fig 4.1) of the experimental swirl cooling duct. The vertical axis is the averaged *Nu*, representing the heat transfer and convective heat transfer in the duct, which increases the point-to-point values. The comparison between experimental data and the results from three turbulence models. An orange-coloured data in the experimental measurement of the Nusselt number, which is compared with other turbulence modules, further shows a good match to that the experimental data showing the capacity of the SST k -*ω* treatment.

The heat transfer the peak for the k-ε and RNG k-ε models exhibited flatter distributions, whereas the SST k -ω demonstrated good performance in near-wall flow separation in section 4.4.

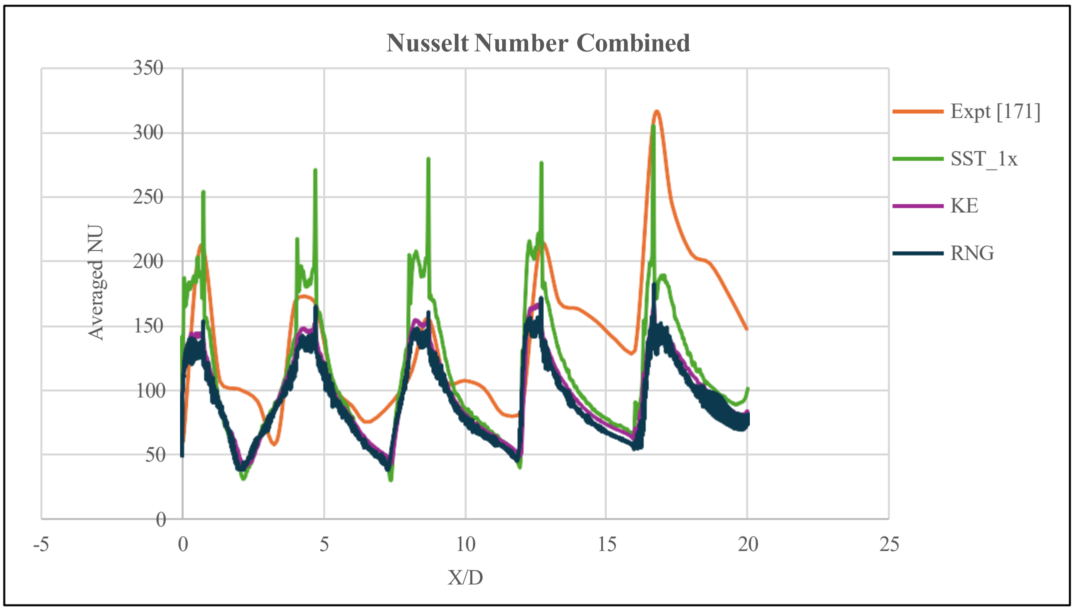

Figure 4-6: Nusselt number with different turbulence models

Fig 4.7 shows the prediction for the pressure drop across the all-gird cases of the SST k -ω with experimental data. The 1x and 1.5x cases have closest matches with experimental data, with a minor unprediction for X/D =0 to slighter over predictions at X/D =20 all cases of the SST k- ω.

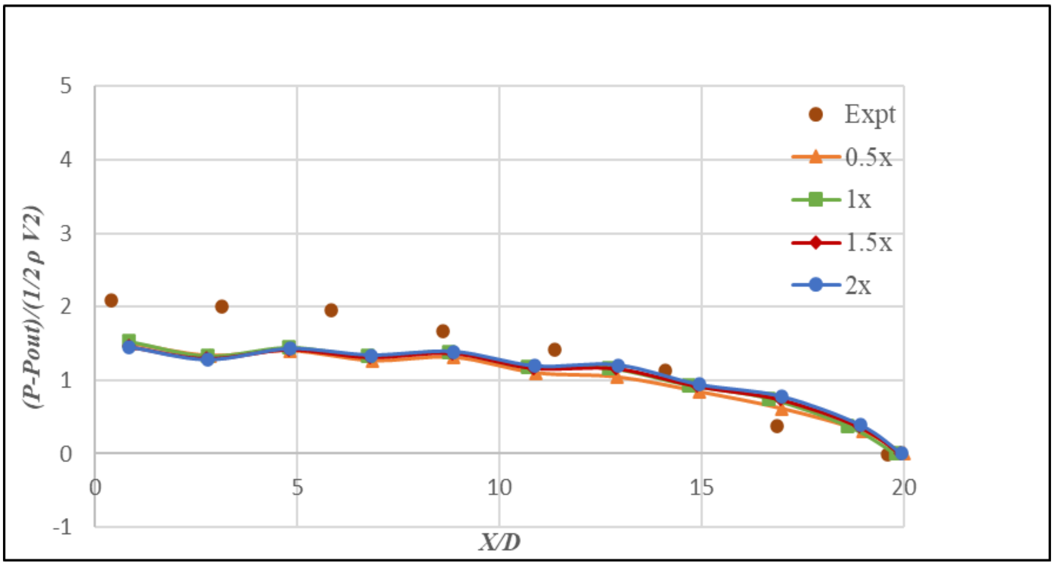

Figure 4-7: pressure drop for grid independence study

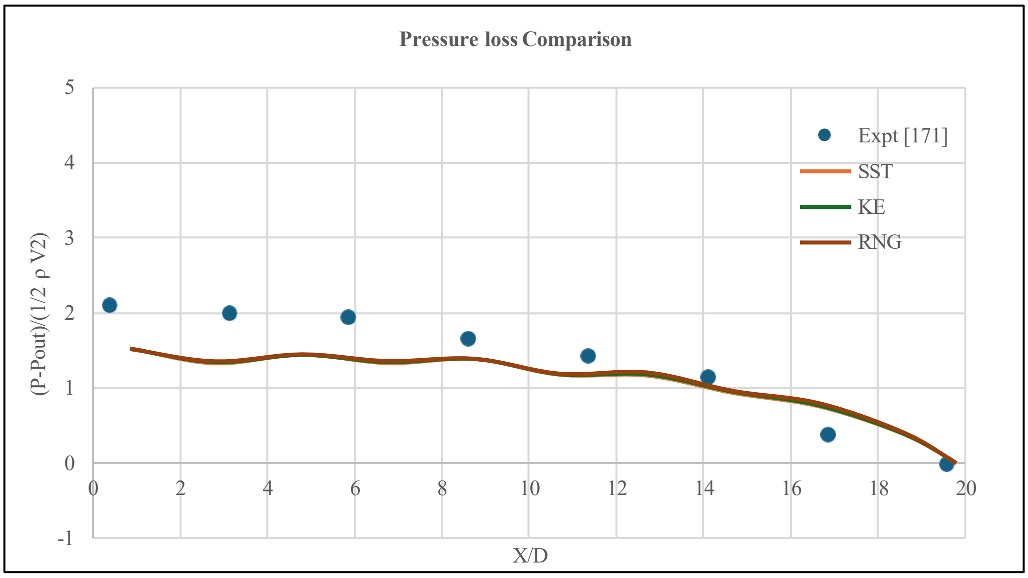

Figure 4-8: Pressure drop for different turbulence models

Fig 4.8 shows the pressure loss for different turbulence models by pressure loss, comparing the pressure loss direction, whereas X is the distance along with the flow direction. The "(P - Pout)/ (1/2 ρ v²)" is the pressure drop coefficient which is improved for simulation in the vertical direction. The experimental data in the blue coloured is the showing in the pressure loss, which is followed by SST, *k-ε,* and RNG as coloured by orange, grey, and brown. The experimental data shows in a constant pressure loss from X/D is a 10, which decreases significantly as X/D gradually decreases. Furthermore, the SST model with experimental data is close; however, it undervalues the pressure loss, particularly at the initial stage (X/D at 5). It aligns better with the experimental data as X/D gradually increases.

4.4 Qualitative results - Flow visualisation.

The velocity streamlines and vector plots for a swirl cooling design in the gas turbine blade leading edge are shown in Fig 4.9. The top view streamline plot shows the velocity distribution along the cooling passage. Which highlight areas of the high (red/ orange) and low velocity (blue regions). The swirl cooling motion of the flow is apparent, signifying improved cooling due to enhanced mixing and heat transfer. Side view vector plots are also shown in Fig 4.9 and they show a detailed swirl pattern in a cross-section view, with flow circulating within the cooling channels. The swirl cooling structure increases the turbulence, which improves the heat transfer coefficients on the cooling channels' walls.

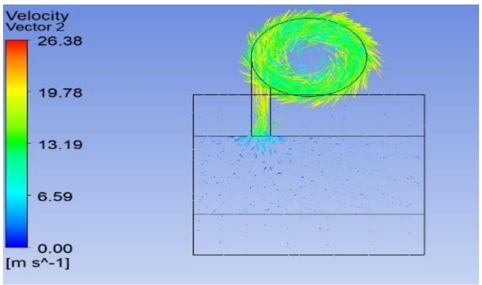

(a)

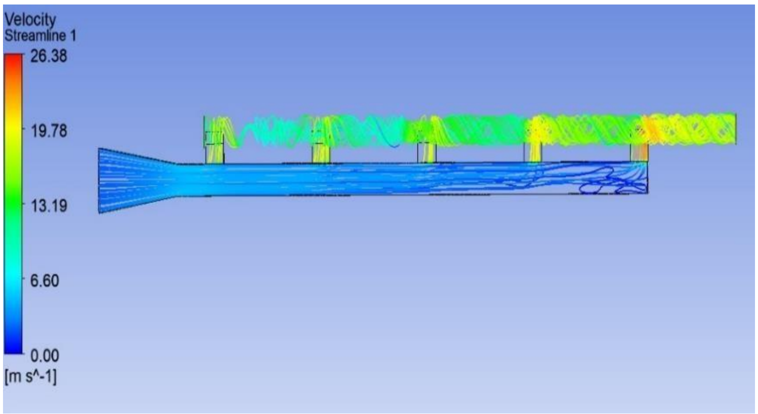

(b)

Figure 4-9: 3D swirl cooling results (a) The top view (streamline plot), (b): Bottom views (Vector plots)

The pressure distribution of the swirl cooling is shown in Fig 4.10, with pressure values ranging from 99,879.99 Pa (blue) to 100,300.94 Pa (red), in Pascal (Pa). The red colour indicates the high pressure, and the low pressure is shown as the blue colour. The variation of the colour along the swirl cooling channels means there are low and high-pressure distributions within the channels. The high-pressure is at the top of the channel regions, and the low-pressure distribution is at the bottom of the channels. The pressure increased gradually from green to red.

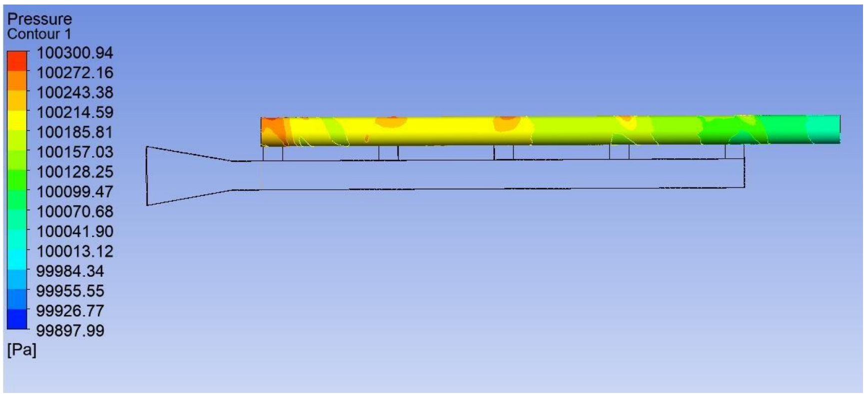

Figure 4-10: Pressure distribution of the cooling channels

Fig 4.11 shows the temperature distribution of the swirl cooling channels in the ranges of 289.03 K, represented in blue, to 313.70 K, which is in red. This high temperature represents the red region, and the blue region represents the low-temperature distribution, with the temperature distribution varying from green to red. The five nozzles produce cooler wall temperature on the channels wall locations, which indicates peak in local convective heat transfer. Meanwhile, the hotter regions are present in the nozzle locations which is reflect in the heat transfer value.

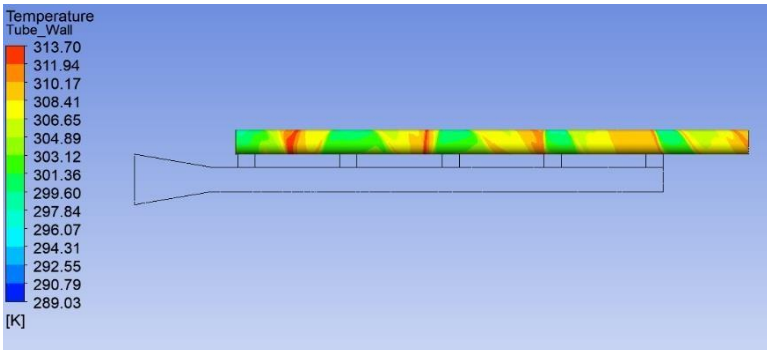

Figure 4-11: Temperature distribution of the cooling channels

4.5 Discussion for experimental validation of swirl cooling for the gas turbine blade leading edge.

The comparison between the experimental and CFD results is shown in Fig 4.12. However, Fig 4.12(a) shows the number of internal tubes Nusselt numbers with normalised axial length (z/D). The angular range is between 0^0 to 180^0 this is half of the circumference, and the localised enhancement zone is highlighted with the effect of the swirl cooling tube as mentioned in [173]. The colours show from blue (the low Nusselt number) to red (the high Nusselt number), indicating non – uniform heat transfer swirl cooling flow.

The numerical studies are shown in Fig 4.12 (b), followed by the experimental studies. The side of the flow pattern views its peak and valley (red/yellow and blue/ green). These experimental and numerical figures are spatially aligned; meanwhile, the swirl effect between the angled/ high -Nu area are high, the experimental Nusselt number is range from the 0-300,with the CFD Nusselt number range from the 0-200 (which is under certain conditions), however the CFD results are slightly unpredictable.

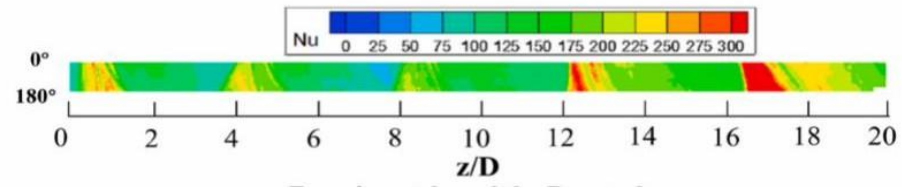

(a)

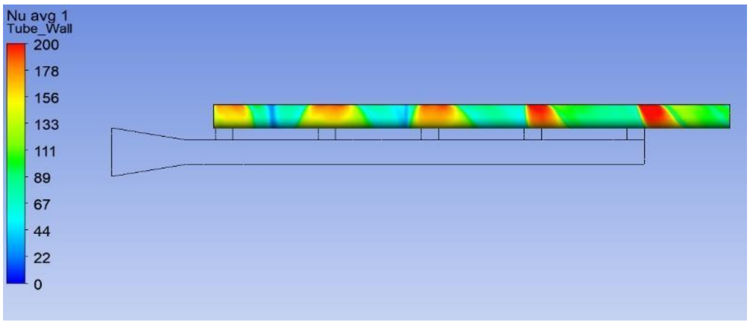

(b)

Figure 4-12: Nusselt number comparison of single stage cooling :(a) Exp, and (b) CFD

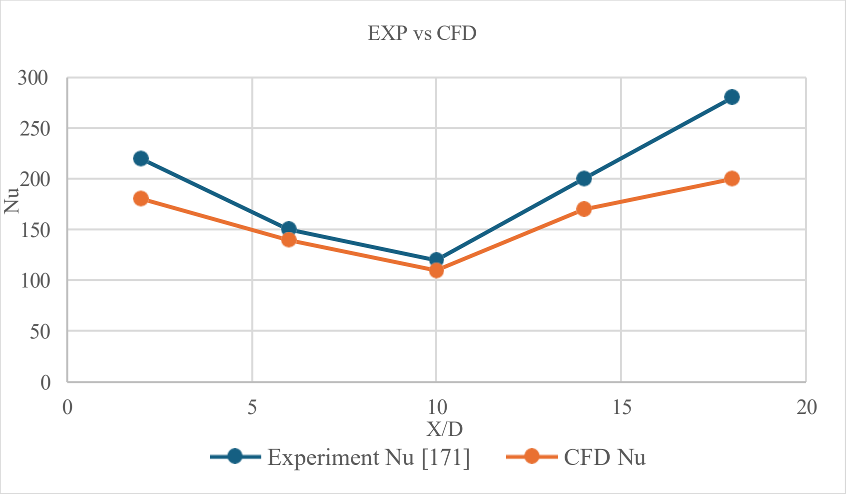

Figure 4-13: Comparison between Experimental [171] and CFD comparisons

Based on the above qualitative results (referring Fig 4.12), the CFD and experimental validation were presented are summarised shown in Fig. 4.13. This shows very good agreement between CFD and experimental.

This pressure drop is a comparison between the experimental and CFD results, is shown in Table 4.7. In this simulation, it is considered that the SST is best for all turbulence models because there are no changes to the values. In Table 4.7 shows the pressure comparison based on the cooling chamber nozzle (X/D) variation of the experimental in [171] and simulation. The experimental data start with high variation at the initial point from 2.15 but it is decreasing gradually.

Table 4-7: Pressure drop comparison for Experimental [171] and SST

X/D	Expt[171]	SST
0	2.15	1.55
5	2.01	1.27
10	1.65	0.87
15	0.94	0.1

4.6 Flow physics and experimental limitations

This second methodology chapter presented a study and validation of single-stage swirl cooling chambers to compare CFD with experimental data. The single-stage swirl cooling channels impact pressure drop and heat transfer within fluid, and various turbulence models have been used such as standard uch as the standard k–ε**,** RNG k–ε**,** and SST k–ω models.

The cooling flow is governed by the interaction between the coolant chamber and the vortex chamber; however, the coolant chamber has five nozzles that squeeze the fluid through each section, as shown in Fig 4.3. Convective heat transfer and boundary-layer control is governed by the flow through the nozzles in each section; each nozzle jet is impinged into the cross-sectional flow in the vortex chambers, which collapse the hydrodynamic and thermal boundary layers. This nozzle produces high wall shear stress and intense turbulence, which increases near-wall momentum and thermal transport, generating a local maximum Nusselt number in each nozzle. After the fluid passes through the inlet nozzle (impingement), the flow reseparates, and the boundary layer redevelops downstream of the nozzle until the next nozzle interaction, as shown in Fig 4.9. In addition, the jet–crossflow interaction generates streamwise vortices and shear layers that mix and transport high-momentum fluid into the vortex chamber, thereby removing heated fluid from the chamber surface. These cooling processes explain how the sustained convective cooling behaviour occurs in both chambers and explain the periodic variation of the heat transfer along each nozzle passage.

A accurate numerical prediction of cooling requires sufficient mesh resolution to capture the viscous layers and sublayers, given the strong shear layers generated at each nozzle. If the near wall mesh is coarse, numerical diffusion smooths velocity and temperature gradients, meanwhile turbulence modelling impacts vortex formation and turbulent heat transfer, especially in chamber regions with recirculation. This is a main limitation in turbulence closure, and grid resolutions can influence the magnitude of predicted peak on the heat transfer, although the simulation presented in this chapter properly captures each nozzle's cooling behavior.

Chapter 5: Internal Swirl cooling chambers of a high- pressure turbine blade

5.1 Introduction

This chapter combines the methods from Chapters 3 and 4 to enable simulation of the flow around the turbine blade, the cooling through it and the heat transfer through the solid region of the blade. Internal swirl cooling is applied and embedded in the MT-1 turbine blade to help cool the leading region. Numerical simulations of single, two, and three-stage swirl cooling chambers edge are explored using a conjugate heat transfer method. The single-stage chamber is taken as the baseline geometry with further modifications for two and three-stage swirl cooling designs. The results focus on the pressure drop, heat transfer and thermal performance of the swirl cooling chamber. It is found well correspond to past experimental literature.

5.2 Swirl cooling chambers geometries

5.2.1 Single stage cooling chamber

A single-stage swirl cooling chamber was created to fit inside the MT-1 stator (NGV) blade provides internal cooling. The cylindrical section of the upper part is called the vortex chamber, the rectangular section is called the coolant chamber, the rectangular nozzles are inter-connected between both chambers (vortex and coolant). The location of this swirl cooling is to alleviate thermal load at leading edge as shown in Fig 5.1.

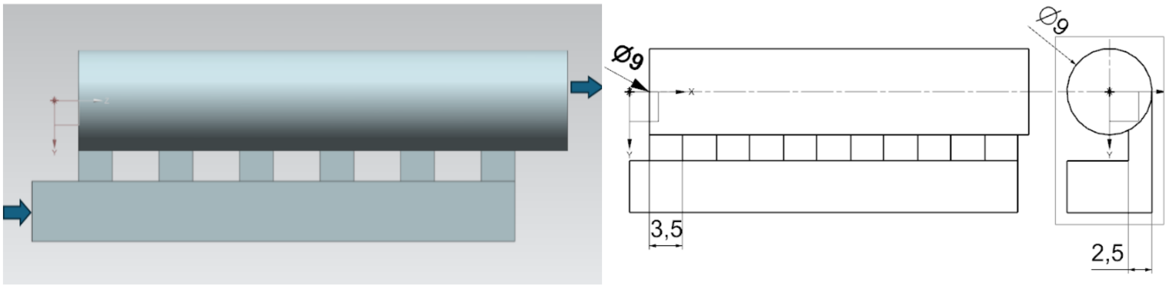

(a) (b)

Figure 5-1: Schematic diagram of single-stage swirl cooling chambers, and geometry sketch

In this system, six tangential nozzles are interconnected to the single stage swirl cooling chamber. The fluid enters the coolant chambers, through a rectangular section as shown in Fig 5.1 (b). The geometry is accompanied by the single stage swirl cooling chamber dimensions listed in Table 5.1.

Table 5-1: Single-stage swirl cooling chambers geometry specifications

Parts	Size
Tube diameter	9 [mm]
Tube length	43.375 [mm]
Plenum length	40.825 [mm]
Plenum width	9 [mm]

5.2.2 Two stage swirl cooling chambers

The fluid passes through each nozzle to first chamber then through a passage to the second chamber which is placed downstream. The two-stage cooling layout has two partitions, as shown in Fig 5.2. The upstream round tube is also a vortex chamber, and the two stage swirl cooling specifications listed in Table 5.2.

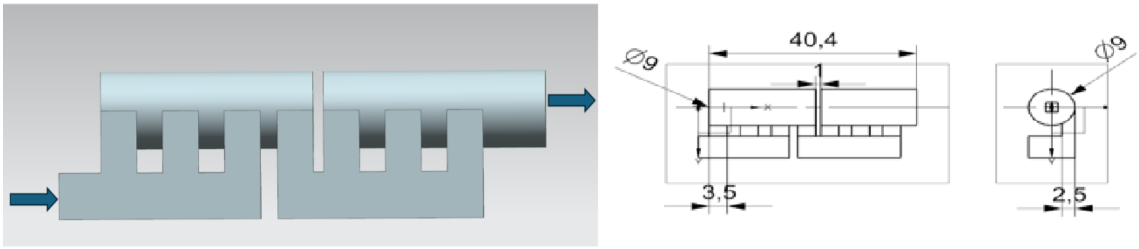

(c)

(b)

Figure 5-2: Schematic diagram of a two-stage swirl cooling chamber

Table 5-2: Two stage cooling chamber specifications

Parts	Sizes
Inlet Jet tube Width	2.5 [mm]
Inlet Jet tube Length	3.5 [mm]
Inlet jet Tube length	3 [mm]

5.2.3 Three stage cooling chambers

Fig 5.3 shows a further iteration for the swirl cooling strategy, a three – stage cooling chamber is proposed, and the rectangular tube is also divided into three partitions, which are broken down into middle of the inlet and outlet. Injections nozzles are connected between these sections as shown in Fig 5.3 (e). The intel tube width and length of the diagram specification as shown in Fig 5.3 (f).

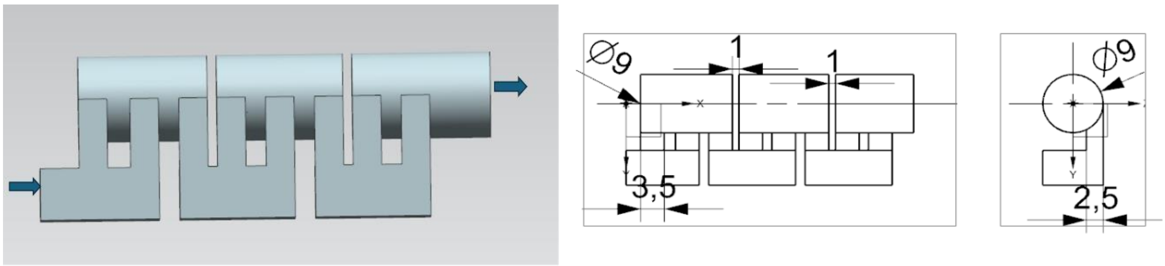

(e)

(f)

Figure 5-3: Schematic diagram of a three-stage swirl cooling chamber and specifications diagrams

The three-stage cooling chamber is carefully considered with a proper blade chord and field setup, as specified in Table 5.3.

Table 5-3: Three-stage swirl cooling chambers geometry specifications

Parts	Sizes
Inlet Jet tube Width	2.5 [mm]
Inlet Jet tube Length	3.5 [mm]

5.3 Mesh design for swirl cooling chambers

For the swirl cooling channels, an unstructured mesh with triangular elements in cross section were used. Figs 5.4, 5.5 and 5.6 (a) show the cross-section of the mesh design, which includes the cooling chamber and the vortex chamber. The inflation layer is positioned around wall, resulting in higher refinement and uniformity with a more regular element size for good quality. The mesh is unstructured tetrahedral in some regions and others contain high density hexahedral cells, near the blade cooling channels, and outer walls.

These swirl cooling flow paths help enhance internal convective heat transfer. There are two sections in this swirl cooling geometry the first one is the inlet section, followed by the outlet section. There are six nozzles for the single stage, seven for two stages and eight for three stages as shown in Figs 5.4, 5.5 and 5.6 (b). The nozzles linked the vortex chamber to the cooling chamber.

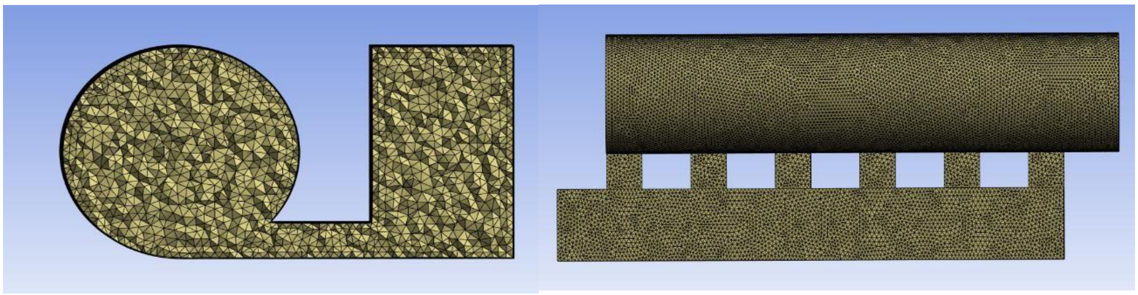

(a) (b)

Figure 5-4: Single stage cooling chamber cross sectional and surface mesh

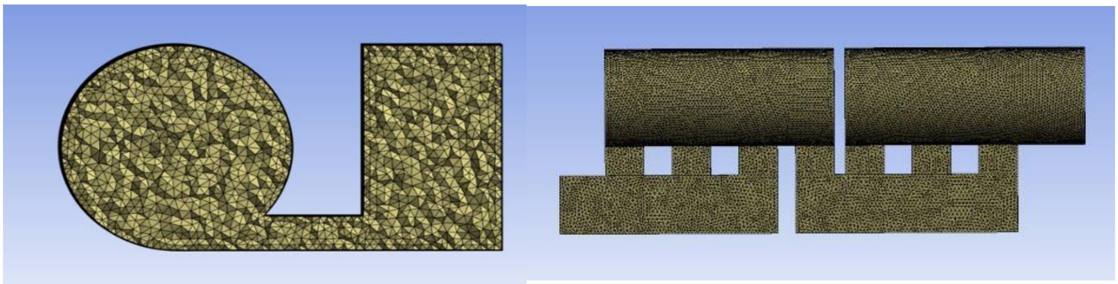
(c) (b)

Figure 5-5: Two stage cooling chamber cross sectional and surface mesh

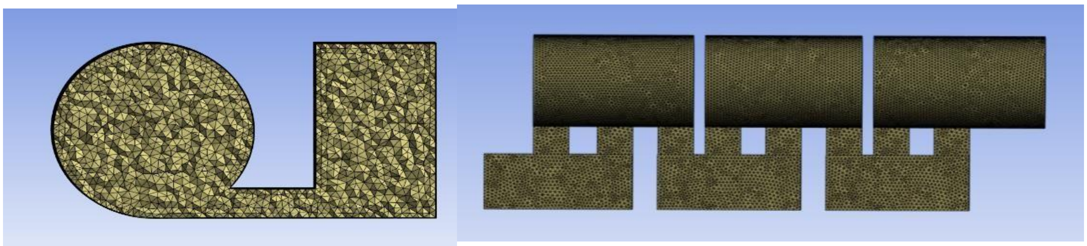
(e) (f)

Figure 5-6: Three -stage cooling chambers cross sectional and surface mesh

The in the solid region of 3D MT-1 blades Nozzle Guide Vane is unstructured, as indicated by the irregular pattern of elements. This was composed of tetrahedral elements, which commonly used for this type of complex turbo machinery-related problems, as shown in Fig 5.7(a). Furthermore, the cross-sectional external fluid on the NGV blade for the mesh is triangular and unstructured. However, some parts of the Triangular mesh are compressed in near wall regions to capture flow separation.

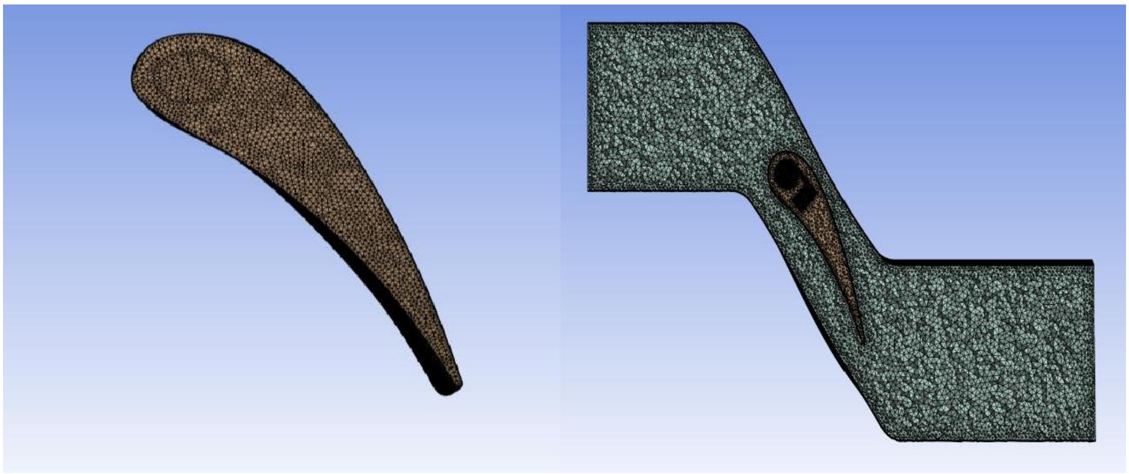
(a) (b)

Figure 5-7: blade flow domain and cross-sectional mesh

Fig 5.8 shows that single stage cooling is inset near the leading edge of this blade. There is an outlet of the single stage cooling chamber near the leading edge of the blade, and inflation layers near the wall of the blade itself.

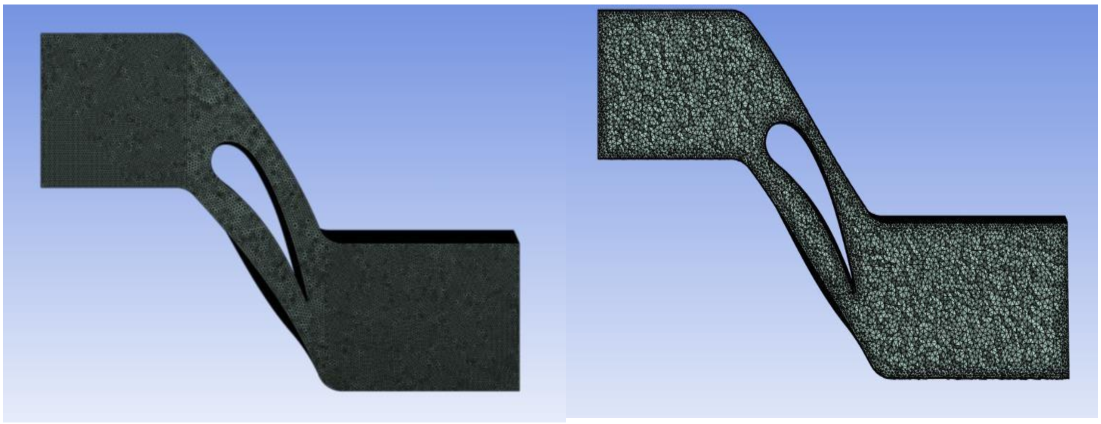

(a) (b)

Figure 5-8: NGV full blade and cross-sectional blade

Fig 5.9 shows unstructured rectangular mesh elements in the blade and through the interconnected cooling chamber. Inflation layer are used in the vortex and coolant chamber which is single has either single two or three stage cooling chambers, depending on the geometry. Fig 5.9 (a, b and c) shows all three design with the swirl cooling chambers, this shown as a horizontal view between the vortex cooling and coolant chamber six continuously nozzle is attached with same size, and unstructured mesh has been used in the swirl cooling chambers, and single stage swirl cooling chamber without nozzle unstructured mesh the mesh specification is as shown in the Table 5.4.

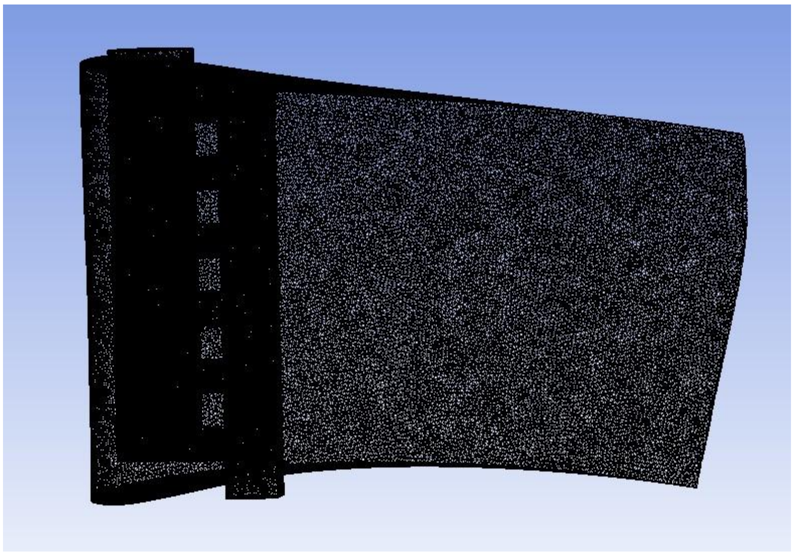

(a)

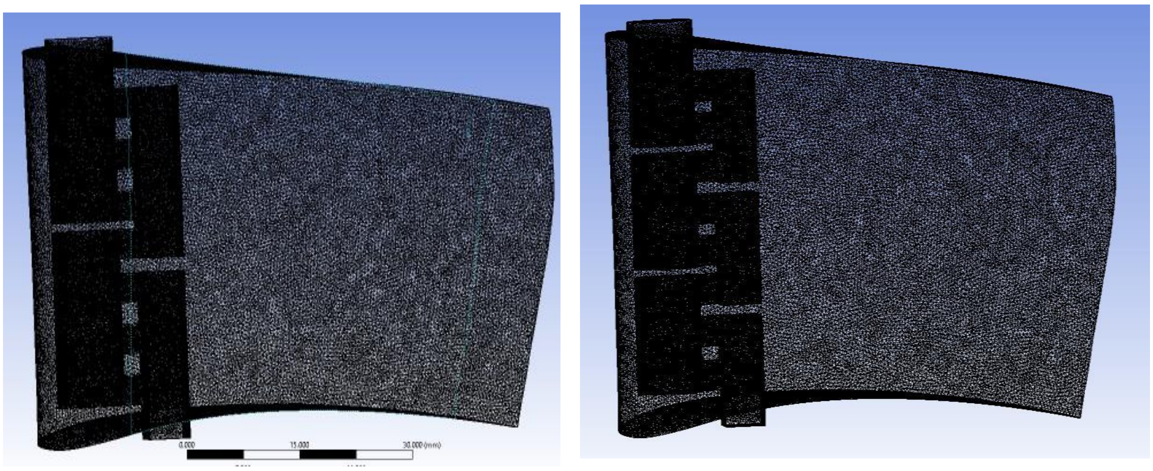

(b) (c)

Figure 5-9: Swirl cooling mesh: cross-sectional blade with inside cooling chamber flows

Table 5-4: Single-stage swirl cooling mesh specifications

Geometry/ Model of the mesh specification	Nodes	Elements
Blade Mesh	628,455	325,789
Single-Stage Swirl Cooling Chambers	333,586	1,203,284
Flow Domain	421,110	1,524,834

5.4 Numerical set up

The total pressure loss characteristics of fluid friction are defined as follows using the total pressure loss:

$$C_{P_t} = \frac{P_{t,in}-P_t}{P_{t,in}} \tag{5.1}$$

where, *Pt* is Prandtl number of the averaged total pressure in the vortex chambers in the coolant inlet. Thermal performance of the swirl cooling chamber is the between the total pressure and heat transfer in the three stage cooling configurations, and the cooling thermal performance efficiency (η) is defined as:

$$\eta c = \frac{Nu/Nu_0}{(f/f_0)^{\frac{1}{3}}} \tag{5.2}$$

$$f = \frac{P_{t,in}-P_{t.out}}{4\frac{H}{D}\left(\frac{1}{2}\rho_{in}u_{in}^2\right)} \tag{5.3}$$

$$f_0 = (0.790\ln \mathrm{Re}_D - 1.64)^{-2} \tag{5.4}$$

For the cooling temperature ratio calculation using by [75]

$$\mathrm{TR} = \frac{\mathrm{NGVT_{01}}}{\mathrm{Coolant\ T_{01}}} \tag{5.5}$$

Thermal performance is carried out for N=1, 2, and 3 with round bend sections to rectangular sections, at different Reynolds numbers (ReD) = 20,000. The two- and three-stage swirl cooling configurations with changed rectangular to round bends can provide better heat transfer improvement.

The thermal performance (η) decreases with each stage (N), from 1.10 to 0.90 for the pressure loss. Meanwhile, at (Re_D) = 30,000 and 40,000, the results vary compressed to Re_D = 20,000. As the number of stages increases thermal performance improves. This is the reason, based on thermal performance, that the Reynolds numbers (Re) at 30,000 and 40,000 result in an improvement of Nu/Nu0, which is obtained by increasing N and exceeds the cost (f/f0) by 1/3.

The frictional losses increase after modification; as a result, the three-stage configurations afford a higher thermal performance at all Reynolds numbers (Re).

5.4.1 Simulation set-up

Table 5-5: shows the MT-1 swirl cooling chamber set up

Input	Selections
General	Pressure-based solver
Materials – Air – Density – Other inputs	Ideal Gas Law – Constant
Momentum and Thermal Bc's –	**Stator inlet** **Pressure inlet stator** Reference frame – Absolute Guage Total pressure (pa)- 461500 Direction Specification Method – Normal to direction. Total Temperature (K) - 444.4 **Pressure outlet Rotor** Backflow reference frame –Absolute Guage pressure (pa) – 249.769 Backflow pressure specifications – Total pressure. Backflow Total Temperature (k)-300. Wall top –stator – Translations Wall motion – Stationery. **Cooling passage conditions** Coolant pressure (P_1) - 1080 kPa Coolant temperature (T_1) [K] - 296.2
Solution method	**Scheme** Coupled **Gradient** Green Gauss node based all 2nd orders Upwind
Monitors – Residuals	**1e-6 for energy 1e-5 for rest**

A steady state pressure-based CFD solver is used for all computations. So, this swirl cooling simulation procedure solution was used. For cooling as mentioned in [75] the conditions are calculated carefully as described in Eq 5.2. Furthermore, simulation settings for discretisation, gradient and pressure-velocity coupling schemes match what was used in the previous chapter.

5.5 Quantitative Results for Cooling Chambers

Fig 5.10 shows swirl cooling chambers data using of the average Nusselt number. This plot clearly shows the positive linear correlation between the Nusselt (Nu) and Reynolds (Re) numbers. Higher Reynolds number mean enhanced convective heat transfer as shown in Fig (a) for a single stage cooling chamber.

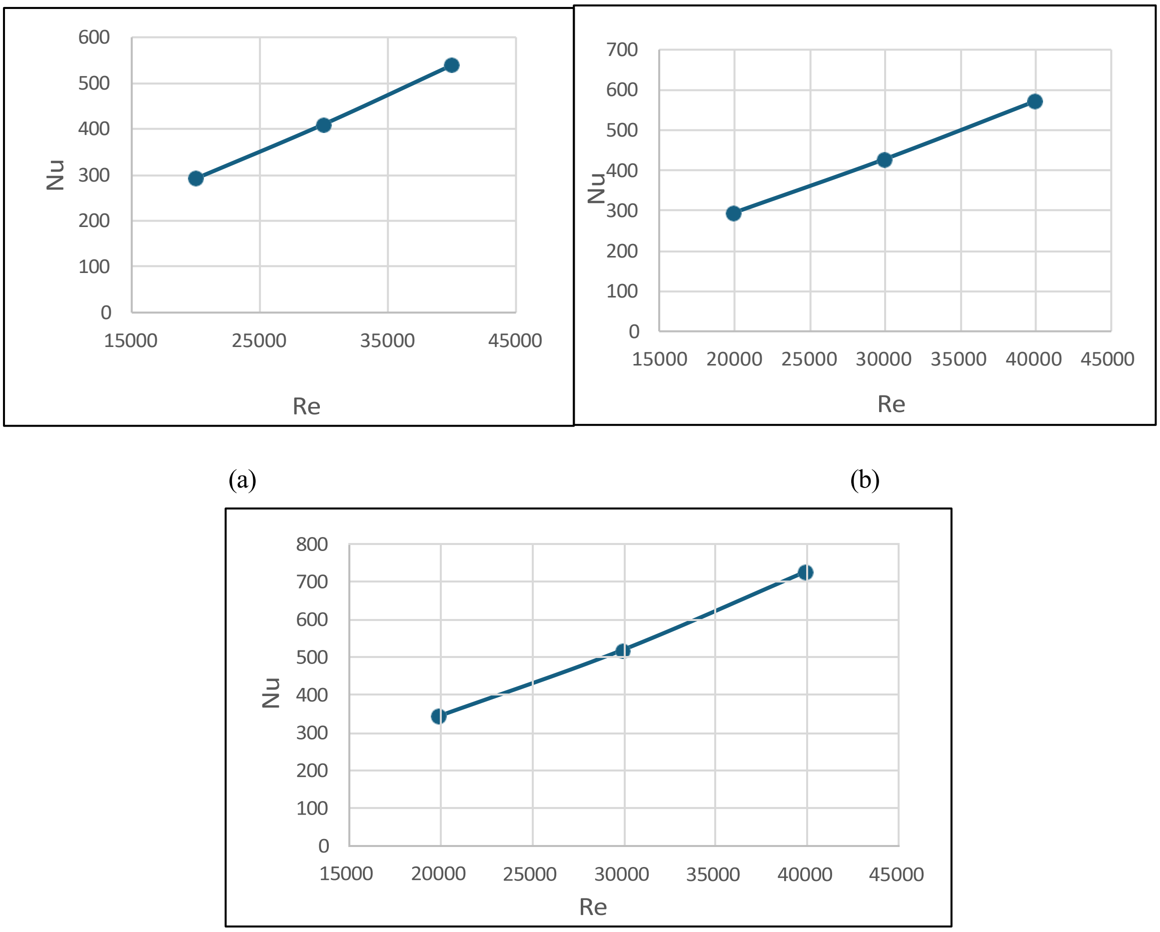

(a) (b)

(c)

Figure 5-10: Comparison of Average Nusselt number for swirl cooling chambers: (a) single stage, (b) two - stage, and (c) three- stage

Fig 5.10 (b) shows the two-stage swirl cooling correlation between Reynolds and global Nusselt number (Nu). Note that, a higher Nusselt number indicates better cooling performance by enhancing convective heat transfer efficiency.Three different Reynolds numbers were considered, and it is clear that an increasing the Reynolds number leads to better and stronger heat transfer, and a relation between the Reynolds and Nusselt numbers.

Fig 5.10 (c) shows data for three-stage swirl cooling chambers with Reynolds ranges from 15000 to 45000, and Nusselt number ranges from 0 to 800. As the Reynolds number increases, the global Nusselt number also increases, indicating a positive correlation between them. Conventional heat transfer is measured by the Nusselt number, which clearly increases with the Reynolds number.

The Reynolds number distribution varies with the Nusselt number, which has approximate points at 20,000, 30,000, and 40,000, corresponding to Reynolds numbers of 350, 520, and 725.

The performance of single, two and three-stage swirl cooling designs, a multistage chambers has a much higher Nusselt number distribution, mainly across all Reynolds numbers. The multi-stage (Two and three- stage) Nusselt-number data is the highest Nusselt number, and three-stage cooling is a much higher Nusselt number distribution, as shown in Fig 5.10.

In this study, cooling thermal efficiency and pressure drop has been investigated and these how performance parameters correlate between the heat transfer and the pressure drop penalty. The efficiency is determined as ratio of the normalized heat transfer and pressure drop as mentioned in the Equation 5.1, and 5.2.

Next, the pressure distribution of the swirl cooling chambers as a function of Reynolds number is shown in Fig 5.11. The X-axis shows the Reynolds number increases are an indication of increases in the flow rate through the chamber. Meanwhile the Y-axis shows the normalised pressure loss which is an indicator of the total pressure loss driven by the coolant. However, the Reynolds number 20.000, 30.000, and 40,000 the pressure will be increasing gradually based on the Reynolds number as shown in the Fig 5.11 (a).

Fig 5.11 (b) shows results for the two - stage design where the pressure loss increases gradually from 0.05 (5%), to 0.11(11%), and 0.22 (22%), with increasing Reynolds number. A low 20,000 Reynolds number gives the minimum pressure loss, giving by less heat transfer. The midium Reynolds number of 30,000 gives moderate with pressure loss better thermal performance, and the high Reynolds number 40,000 gives reasonable heat transfer with a high pressure drop.

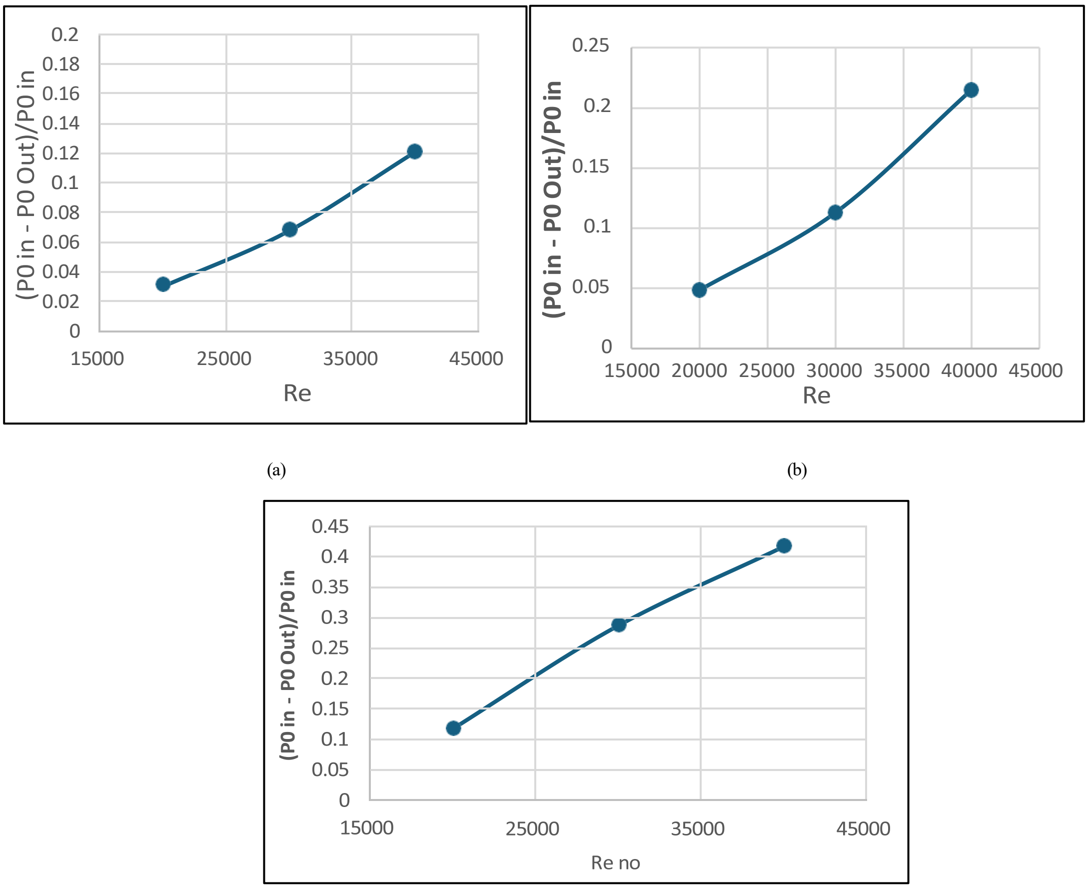

(a) (b)

(c)

Figure 5-11: Pressure drops comparison for swirl cooling chambers: (a) single stage, (b) two stages, and (c) three-stage

Fig 5.11 (c) shown results for the three stage swirls cooling design. As the Reynolds number increases, the global Nusselt number also increases. The Reynolds number distribution varies with the Nusselt number, which has approximate points at 20,000, 30,000, and 40,000, corresponding to Reynolds numbers of 350, 520, and 725. The pressure distribution of these single, two-stage, and three- stage swirl cooling chambers shows a gradual increase in pressure drop across the Reynolds numbers tested. The pressure drop gradually increases from single to three stages; however, in the three-stage swirl cooling chamber has a greater pressure drop, as shown in Fig 5.11.

5.6 Qualitative results swirl cooling chambers flow visualisations.

Fig 5.12 (a) shows streamline of the velocity magnitude of the single stage swirl cooling blade, which is this range between 13.6 to 458.8 m/s. The flow pattern is shown inside the internal cooling swirl chamber, which is influenced by thermal gradient increasing along the inside of the cooling blade. The turbulence intensity influences heat transfer which is convective thermal activity on the inside the blade surface. The more uniform cooling effect should increase, blade durability .

Fig 5.12 (b) shows single stage velocity streamline in the slower range as it approaches the blade (shown with blue colors) before it then accelerates significantly as it passes the blade which is expected for turbomachinery. In Fig 5.12 (c) the velocity streamlines are presented for the two-stage chamber. It can be seen that the region near the inlet has the highest velocity which is shown by orange/ red streamlines. Meanwhile, velocity decreases in the downstream section as indicated by the yellow and green colors. The flow in the cooling channel as shown in Fig 5.12 (d) and it can be seen that each cooling chamber has a clear vortex pattern. The highest velocity magnitude is 81 m/s and there is strong rotational flow evident. Fig 5.12 (e) shows streamlines through the domain for the three-stage chamber high speed of the flow occurs in the same location as foe the others two designs. Fig 5.12 (f) shows the flow inside the three-stage swirl cooling chamber where the velocity ranges from 1.27 m/s to 89.88 m/s, which is represented by the blue and red colours. The initial stage (first stage) of flow enters through the first two nozzles, where it flows from into the top of the chamber. The second stage (middle stage) has a more complex flow, including recirculation, and the outlet of the two nozzles. The flow is visible at a lower velocity, which shown in the cyan/light blue colours.

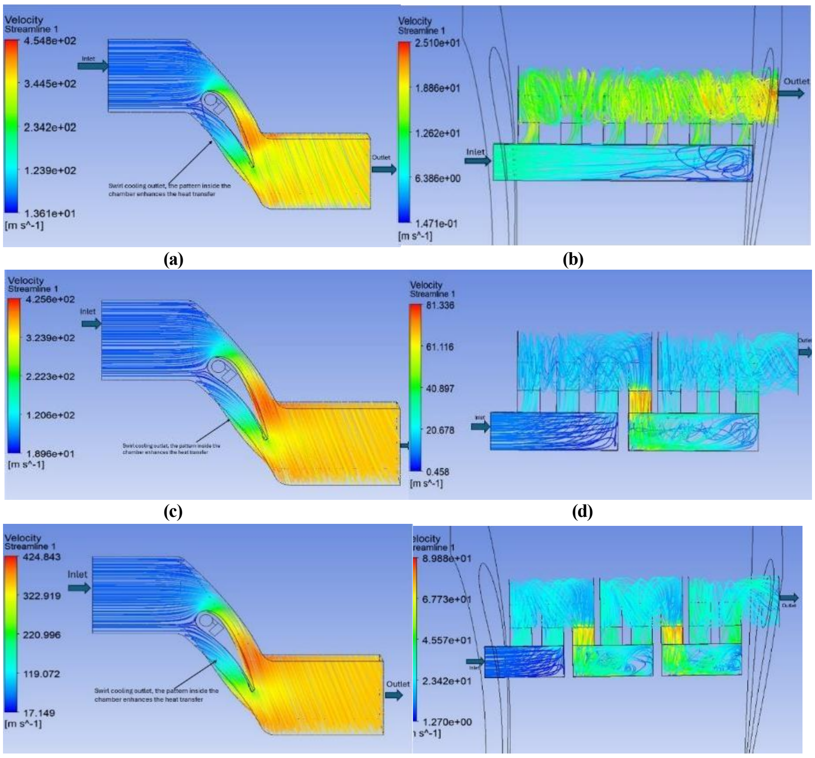

(a) (b)

(c) (d)

(e) (f)

Figure 5-12: Swirl cooling chambers: (a) single stage velocity streamline blade (b) single stage velocity streamline chambers, (c) two stage velocity streamline blade, (d) two - stage velocity streamline chamber, (e) three – stage Single stage velocity streamline blade, and (d) three – stage velocity streamline chamber.

Fig 5.13(a) shows the temperature distribution of the single stage swirl cooling channel within the turbine blade. The minimum temperature is 296.09 K which relates to the cooling inlet flow (donated as blue), and the maximum temperature is 444.38 K which occurs in the mainstream, (red coloured). The effect of the swirl cooling chamber is to noticeably reduce the temperature of the external flow downstream of the blade, by about 80K, compared to the incoming free-stream flow. Fig 5.13(b) shows the two-stage swirl cooling temperature distribution, which ranges from 304.67 K to 444.37 K. The air enters the two paths of distinct cooling, which are coloured blue and light blue which is the external flow. Meanwhile, the temperature falls gradually from the inlet to the outlet, however there few difference in single and two stage temperature waked in downstream wake of the. The temperature distribution in the three stage swirl cooling channels, as shown in Fig 5.13(c) and it has a maximum and minimum temperature range of 444.38 K to 314.04 K, represented by dark red and blue colours, respectively. The mid-range is characterised by smooth transitions. The colours in the red/orange range represent higher temperatures, while those in the green/cyan/blue range represent lower temperatures. The swirl tube inside the blade ranges from 314 to 330 K, and the mixing regions have uniform cooling down to 370 K, which is represented by the green colour.

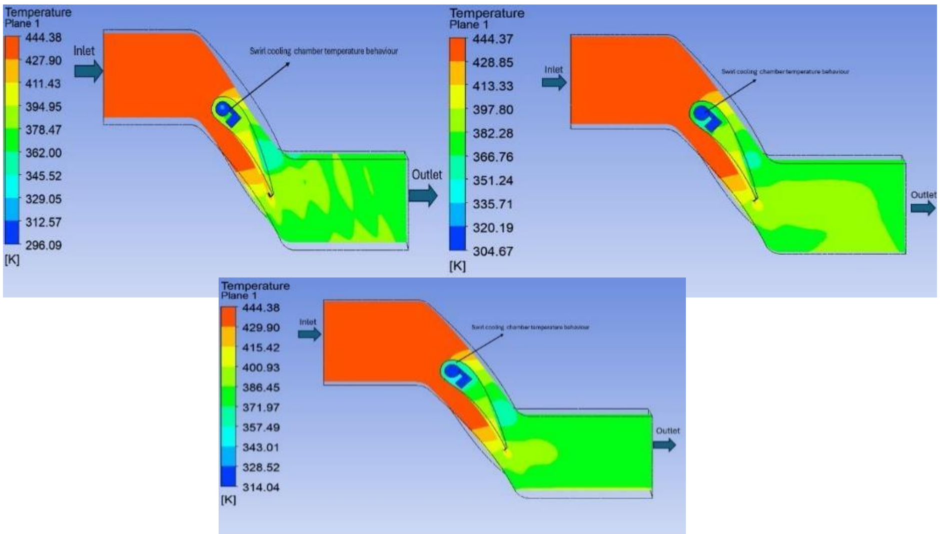

(c)

Figure 5-13: Temperature distribution for the swirl cooling chambers: (a) single -stage, (b) two -stage, and (c) three- stage.

Fig 5.14(a) shows that the single-stage swirl cooling channels' average Nusselt number distributions range between 0 and 180. The colours, from green to yellow, indicate moderate heat transfer, which ranges between 80 and 130. Furthermore, the colour ranges from cyan to green corresponds to a Nusselt number between 60 and 100, which exhibits fluctuating patterns inducing swirl cooling flow inside the chambers. The orange to red colours indicates high heat transfer, which falls within the range of 140-180.

The average Nusselt number distribution inside coolant tube is as shown in Fig 5.14 (b), with an Nusselt number variations from 50 to 150 which is on the surface of the coolant tube side wall. The red and orange zones (Nu = 138 to 150) represent the highest heat transfer near the swirl cooling zones. Yellow and green zones (Nu = 100 to 130) indicate flow attachment zones. There is lower heat transfer further down the scale (blue colours).

However, the cooling effectiveness is elongated with the tube wall, and the thermal characteristics are non-uniform. The Nusselt number distribution of the three-stage swirl cooling chamber ranges between 50 and 150, coloured blue and red. The highest Nusselt number, 150, corresponds to the red/orange colours and a moderate Nusselt number, range of between 105.56 and 138.89. The low Nusselt number distribution, range from 50.00 to 94.44, and it is coloured green and blue, as shown in Fig 5.14(c).

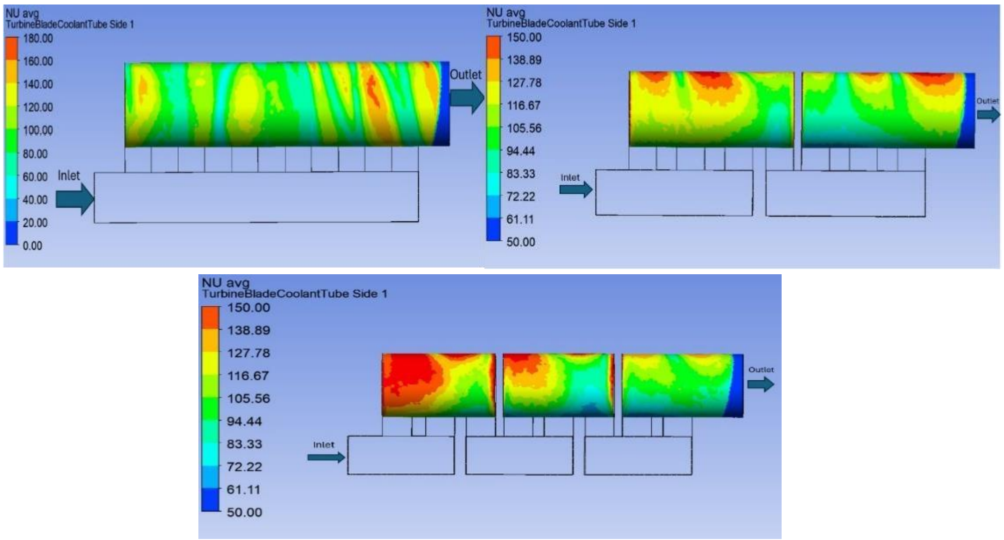

(c)

Figure 5-14: Nusselt Number (Nu) distribution for the swirl cooling chambers: (a) single -stage, (b) two - stage, and (c) three- stage

5.7 Results and discussion for all swirl cooling chambers

Fig 5.15 shows a comparison between the N-1, N-2, and N-3 design. Adding further channels (such as N-4, N-5, etc.) is extremely challenging due to the very constrained physical size of the MT-1. The plots shown in Fig 5015 presents the Re vs Nu for all three stage designs (single, two and three stage) which ranges from 0 to 800. The N-1, which is represented by the light blue line, is the lowest. The Nusselt number comparison shows that the Nu increases at N-1 compared to other channels, and N-2 is moderately enhanced which is around 20 % as compared to N-1, while N-3 exhibits the most enhanced heat transfer which is around 55% compared with N-1.

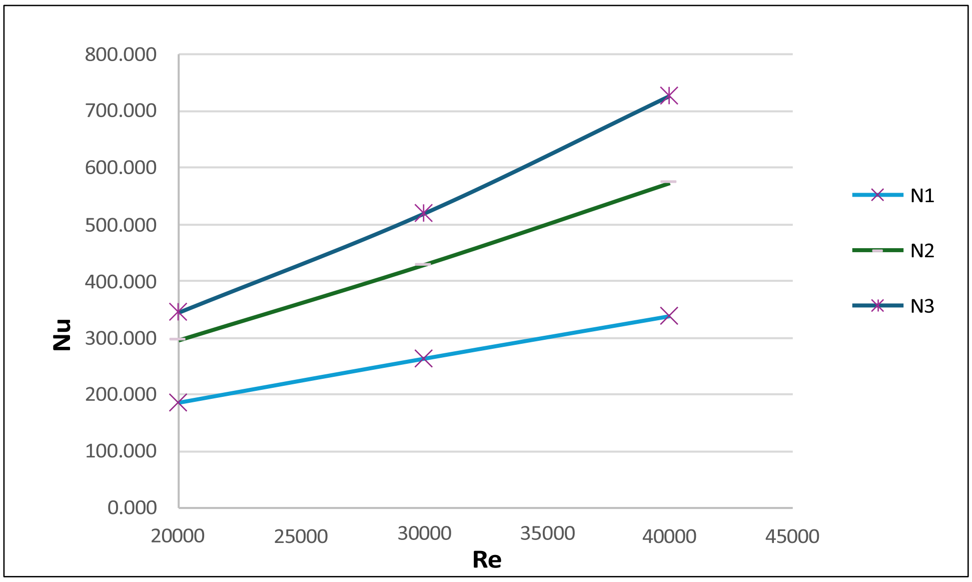

Figure 5-15: Comparison of average Nusselt number for MT-1 blade swirl cooling chambers

The comparison between the total pressure loss comparison, is shown in Fig 5.16 a relation between the Reynolds number (Re) vs normalised pressure loss ($P0_{in}$_$P0_{out}$/ $P0_{in}$) for these three cases N-1, N-2, and N-3. The N-1 blue line shows that the lowest pressure loss across all Reynolds number tested; the curve line remains nearly close to the leading ledge (zero line), indicating that it minimises losses with highly efficient flow.

The N-1 shows that the medium pressure loss with raises the Reynolds number, in this moderate pressure losses with higher flow rate and N-3 yellow line indicates the high-pressure losses with relatively higher Reynolds numbers, these losses significantly more pressure losses then N-1, and N-2, and indicate the more pressure losses due to the number of stages increasing with higher flow rates.

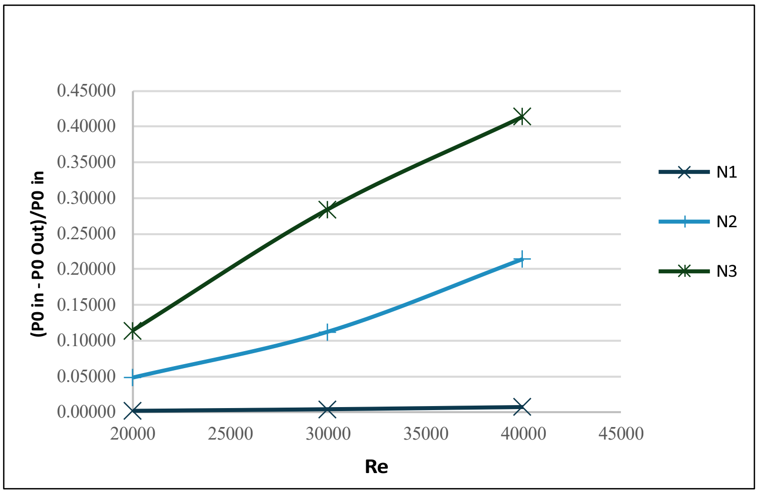

Figure 5-16: Comparison of pressure drop for MT-1 blade swirl cooling chambers

Figure 5.17 shows a comparison of cooling performance between the work in this thesis and different past studies. These single, two and three stage cooling simulation configuration concepts, are compared with Yao et al. [75].

Further this investigation validated by Rao et al. [173], studied the used single stage with fixe nozzle designs. Following this comparison, further investigations were validated with the single-stage experimental method of Fan et al. [174] and Nuo et al. [175].

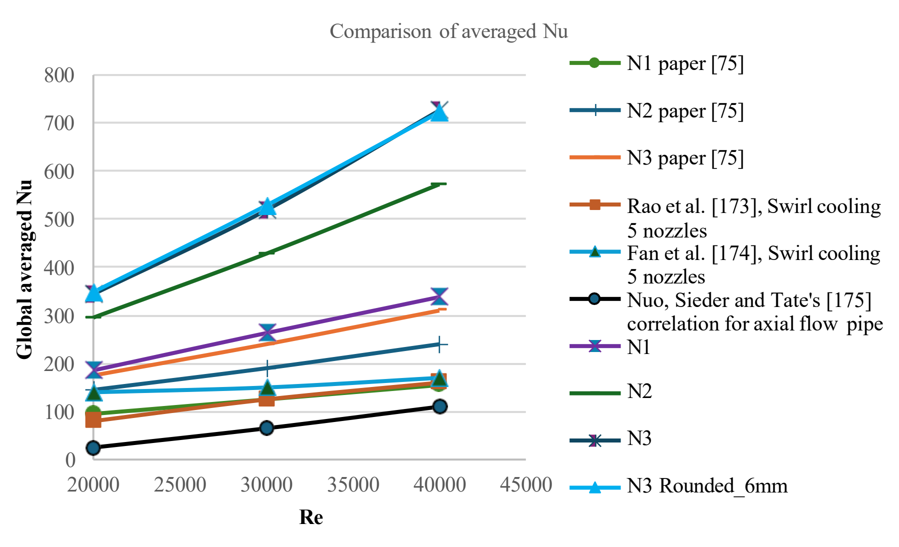

Figure 5-17: Nusselt number comparison of simulation and experiment

The SST $k-\omega$ was commonly used for all three cases to validate with the experimental methods such as Fan et al. [159] resulting in a higher heat transfer rate. The three-stage swirl cooling (N3) involves three stages, each with eight nozzles.

The flow passes through each nozzle and stage, enhancing flow mixing and steepening the temperature gradient in each nozzle and chamber.

This will effectively increase the surface area and thus thermal behaviour. These consistently outperform all other cases, exhibiting best heat transfer behaviour. Single- and two-stage cooling (N1-N3) outperforms both swirl cooling studies with correlations, confirming their superior performance.

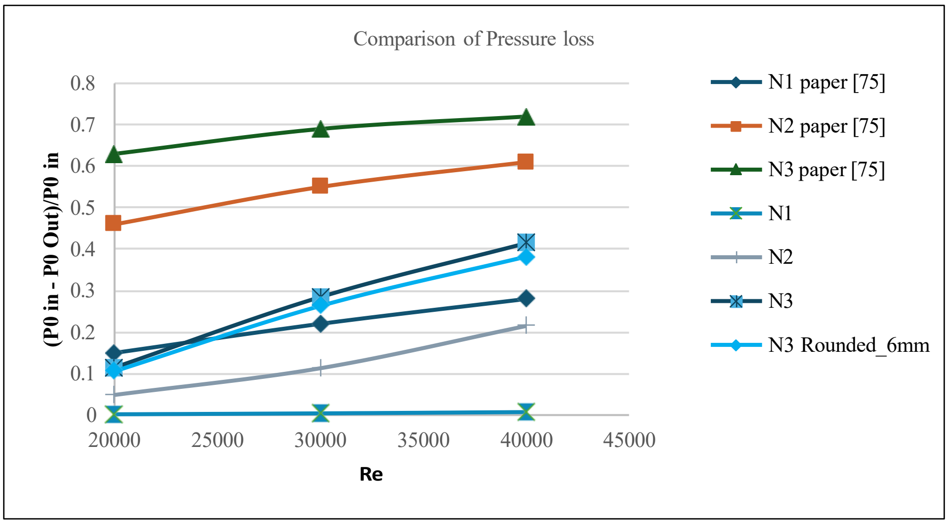

Figure 5-18: pressure drop comparison simulation and experimental

The compression of the pressure loss as shown in Fig 5.18. The x-axis represents the Reynolds number (Re), which ranges from 20,000 to 40,000. Yao et al.,[75] present single-stage cooling (N-1) which shows the medium pressure drop rising with Reynolds number (Re) ranging from 0.15 to 0.28.

The simulation for single, two and three stage swirl cooling design (N-1, N-2, and N-3) are validated through comparison between to the work of Rao et al. [75], and these numerical simulation have higher pressure drop in the single stage (N-1), and lowest and moderate cooling are in the single and two stage (N-1, and N-2) cooling chambers. Meanwhile, the Re increases with the pressure drop, which also increases in parallel due to the higher frictional rate, resulting in higher pressure losses. The N-3 studies exhibit higher pressure losses than the N-1ones. Meanwhile, the simulation three-stage swirl cooling chamber (N-3) has the most pressure loss.

5.8 Discussion for CFD analysis of the MT-1 blade swirl cooling chambers

The Fig 5.19 represents the surface average temperature on the leading edge with three stages of Reynolds numbers (20k, 30k, and 40k) for four configurations such as single, two, and three stage without round and with 6 mm round (N1, N2, N3, and N3 with round 6 mm).

The Reynolds number increases, resulting in a decrease in the average temperature of a single stage (N-1), which is the highest surface temperature; two stages (N-2) have a slightly lower temperature than the single stage (N-1) [176].

Three-stage cooling (N-3) reduces the temperature further than single-stage (N-1) and two- stage (N-2) cooling, and three-stage cooling (N-3) with a 6 mm round shape achieves the lowest temperature distribution with good cooling performance. The modification for a 6 mm round shape (N3 Round 6 mm) offers the best cooling and thermal performance at the leading edge.

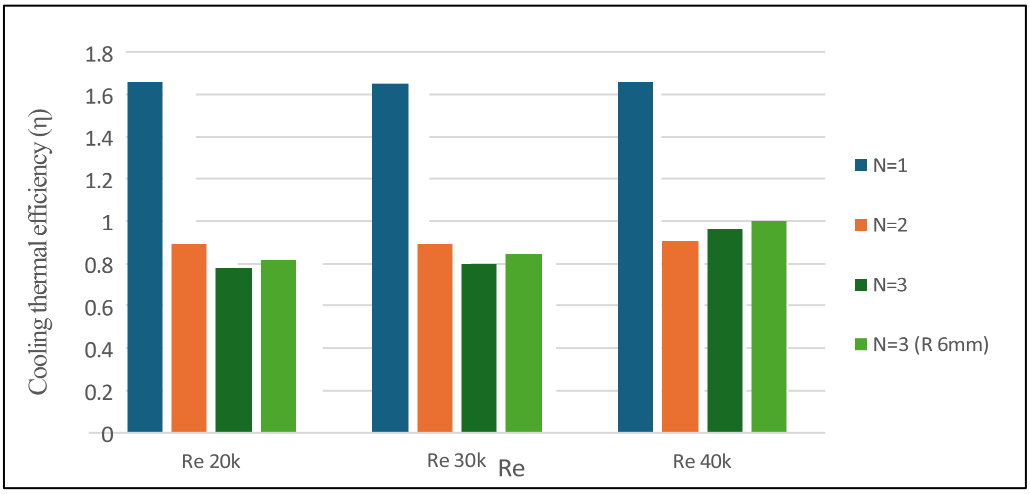

Figure 5-19: Comparison of the thermal performance for swirl cooling channels

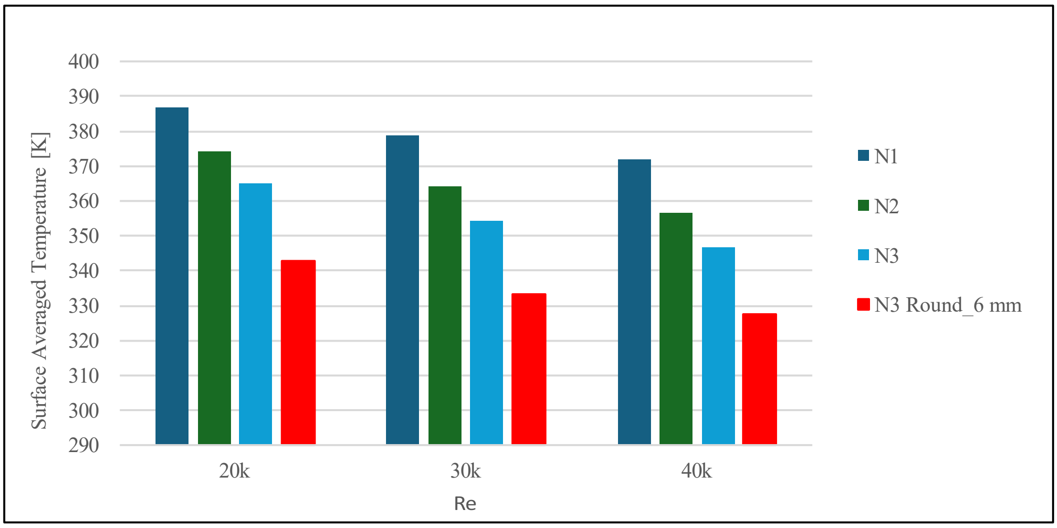

Figure 5-20: Average temperature distribution on the leading

The thermal performance (η) of the leading edge across the Reyolds number (Re) in shown in Fig 5.20. Here four swirl cooling configuration are shown including single (N-1), two (N-2), three (N-3) and three stage with round (N-3) with 6mm round, and Reynolds number 20k, 30k, and 40k are across the four configurations.

The single N-1 consistently has the highest efficiency values, nearly 1.65, which is the highest and strongest thermal performance, and the two-stage (N-2) maintains nearly 0.9, which is the moderate performance.

Furthermore three (N-3) stage 0.78 at Reynolds number (Re) 20k and improve to 1.0 at Reynolds number (Re) 40k, indicating the thermal efficiency is improved and three stage round (N-3 with 6 mm) will starts 0.82 with 20k which is increase the 1.0 at 40k, which is indicating the thermal efficiency gradually enhancing with this 6 mm modified design.

Due to the highest efficiency at N=1 flow is the least constrained and more elements of the N=2,3 with their increasing turbulence, flow separation and pressure losses and less efficiency. For the three stage (N 3) 6mm rounded which is flow separation were reduced, this makes cause the improves the pressure loses and efficiencies in particularly at higher Reynolds number as shown in Fig 5.20.

5.9 Flow physics and modelling limitations

In this chapter, the observed reduction in pressure drop is attributed to increasing the number of cooling stages in the primary chambers and to the redistribution of momentum, with flow acceleration reduced in each cooling chamber section. However, the multi-stage configurations promote a more uniform velocity profile with reduced flow separation at the turbine blade leading edge, thereby improving hydraulic performance. The cooling efficiency trends are influenced by balancing the pressure loss and increasing the turbulence intensity. Meanwhile, the single-stage configuration exhibits higher local heat transfer; multi-stage arrangements provide improved overall thermal performance by enhanced mixing over a longer flow path. The simulations assume constant fluid properties and neglect potential temperature-reliant viscosity effects at higher operating temperatures. Additionally, the steady-state method does not capture swirl flow, which may impact local heat transfer under real engine conditions.

The cooling flow divides the passage into different regions, each dominated by distinct physical mechanisms that control heat transfer and pressure drop. In the inlet regions of the cooling chamber, the flow enters, increasing the Reynolds number. As a result, the inlet regions of each chamber, such as single-, two-, and three-stage chambers, exhibit a rise in wall stress, and the thermal boundary layer becomes more susceptible to disruption from each nozzle. However, in the two- and three-stage nozzle regions, the boundary layers are weakly cooled due to the increased number of stages, and mixing of each physical parameter remains limited.

Chapter 6: Best design analysis of the internal swirl cooling chambers

6.1 Introduction

This is the final results chapter which builds on the conjugate heat transfer from chapter 6. Changes in the shape of the cooling chambers are explored to investigate whether a improved design can be found. However, a three-stage cooling chamber is taken forward in this chapter for further analysis. A parametric study is conducted to investigate the effect of chamber corner radius on the fluid dynamics and thermal performance. A range of turbine operating temperatures are considered to try and find an effective design which works in different scenarios.

6.2 Three stage swirl chambers round shapes

The three-stage swirl cooling configuration CAD geometry, as shown in Fig 6.1(a), corresponds to the technical drawing shown in Table 6.1. A series of channels with R 6 mm (referred to as R6) rounded semicircles, and a 1mm gap between each stage. However, the design features include three 1mm-spaced semicircular slots with their narrow chambers, rounded fillets (R = 0.5 mm), including the nozzles, with radii (R = 6 mm). The spaced chambers are 12.9 mm apart from centre to centre, as shown in Fig 6.1 (b) and specification of the blade as shown in Table 6.1.

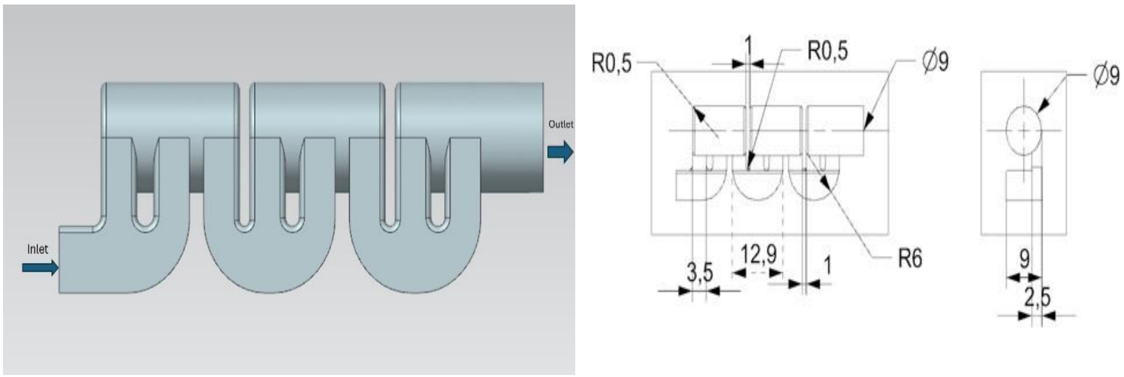

(a)

(b)

Figure 6-1: Geometry: (a) the 6 mm round shape chamber, (b) specification for the three-stage swirl cooling chamber

Table 6-1: Geometry specification for the three-stage swirl cooling 6 mm round shape

Feature	Dimension/ Value
Hole diameter (Ø)	Ø9 mm
Semicircle radius	R6mm
Corner radius	R0.5mm
Wall thickness between features	1mm
Horizontal distance between semicircle centres	12.9 mm
Horizontal distance from edge to first semicircle centre	3.5 mm
Section width (Right view)	9 mm
Offset of section from edge (Right view)	2.5 mm

The three-stage 4mm round chamber CAD model as shown in Fig 6.2 (c). In this geometry, there are six nozzles attached to cooling channels and vortex chamber. These nozzles have three stages (also known as multi-stage), and a 1 mm gap between each nozzle on the vortex and coolant chambers. The drawing of the swirl cooling in Fig 6.2 (d), which consists of the parameters as shown in Table 6.2.

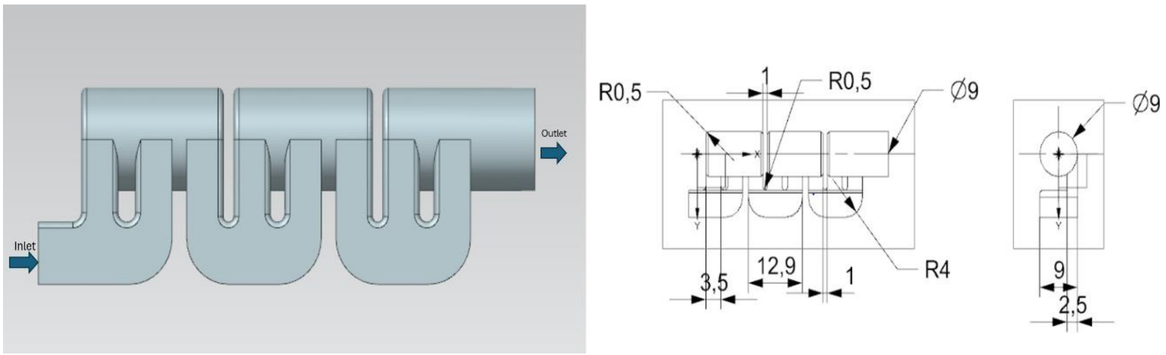

(c) (d)

Figure 6-2 Geometry: (c) swirl cooling 4 mm round shape chamber, (d) specification for the three-stage swirl cooling chamber.

Table 6-2: Three-stage swirl cooling 4mm round shape chamber parameters

Feature	Dimension
Slots bottom radius	R4
Wall thickness between slots	1mm
Vertical offsets	2.5 mm

The 2 mm round CAD swirl cooling chamber, as shown in Fig 6.3 (a) features a semicircular nozzle connected to both cooling chambers. The coolant chamber, located between the slots, contains the regions that maximise the flow. A drawing for these swirl cooling chambers, with complete parameters as shown in Fig 6.3 (b) and the parameters are listed in Table 6.3.

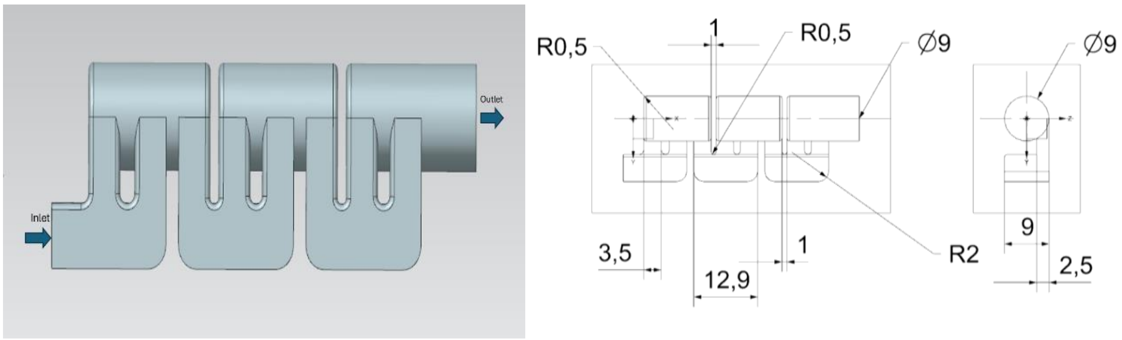

(e) (f)

Figure 6-3: Geometry: (a) swirl cooling 2 mm round shape chamber, (b) specification for the three-stage swirl cooling chamber

Table 6-3: Swirl cooling chamber 2mm round parameter specifications

Feature	Dimension
Top corner radius	R0.5
Hole diameter	Ø9
Slot bottom radius	R2
Slot spacing	12.9 mm
Left edge to first slots	3.5 mm
Wall thickens between slots	1 mm
Vertical slots dimension	9 mm
Vertical offset	2.5 mm

6.2 Mesh Design for three stage swirl cooling chambers

Fig 6.4 (a) shows cross-sectional view of the three-stage 6 mm swirl cooling chambers mesh, the vortex chamber, and the coolant chamber, with attached nozzles. This mesh is composed of quadrilateral and triangular elements, and Fig 6.4 (b) shows the cross-sectional swirl cooling chamber, consisting mainly of triangular elements. These meshes are well-sized to capture the curved semicircular geometry. However, the higher mesh density is at the curved semicircle edge. The mesh statistics are shown in Table 6.4.

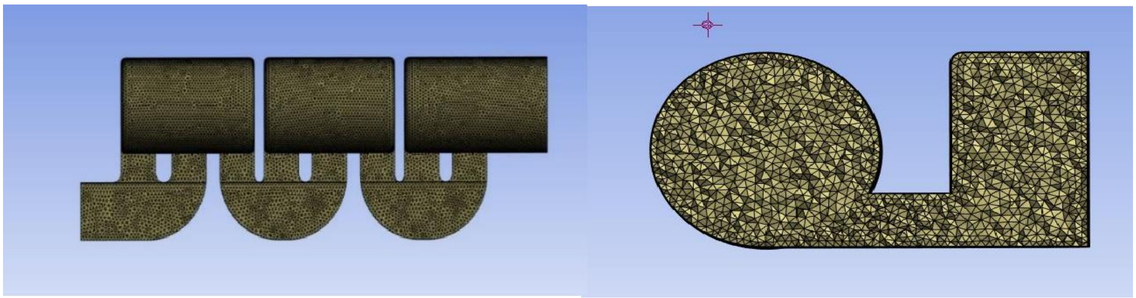

(a) (b)

Figure 6-4: Mesh design: (a) the swirl cooling channels, (b) Cross-section mesh for swirl cooling channels

Table 6-4: Mesh statistics for the 6 mm round swirl cooling chambers

Mesh Statistics	
Nodes	297653
Elements	1051642
Skewness	0.75
Number of layers	5
Total thickness	0.05 [mm]
Element size	03 [mm]
Maximum Element size	0.4 [mm]

The swirl cooling chamber, featuring a 4 mm mesh semicircular design for vortex generation and a coolant chamber, is connected to nozzles as well as a circular block and a triangular mesh with an inflation layer around the cooling chambers, as shown in Fig 6.5 (a). Further Fig 6.5(b) shows the cross-sectional mesh for the coolant and vortex chambers with attached six three-stage 4 mm nozzle round shapes. A quadrilateral mesh is used throughout the swirl cooling chamber.

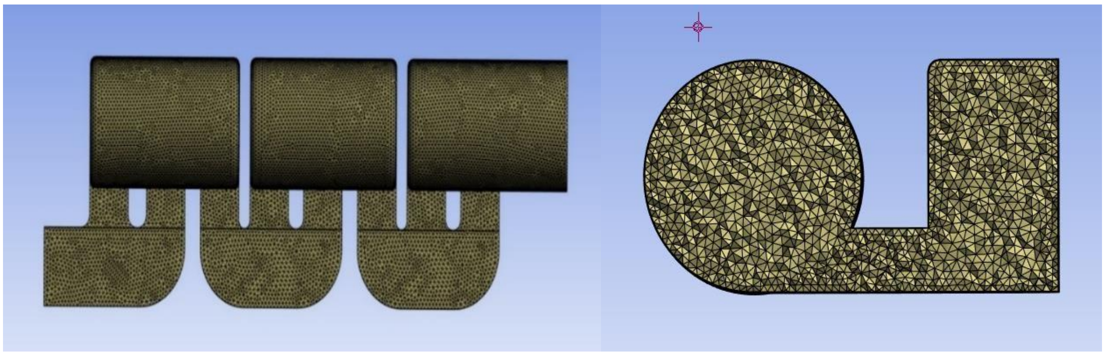
(a) (b)

Figure 6-5: Mesh design: (a) the swirl cooling channels, (b) Cross-section mesh for swirl cooling channels

These three-stage swirl cooling chambers, with a 4mm round shape, have mesh statistics as shown in Table 6.5.

Table 6-5: Mesh statistics for the 4 mm round swirl cooling chambers

Mesh Statistics	
Nodes	339139
Elements	1184679
Skewness	0.80
Number of layers	5
Total thickness	0.05 [mm]
Average Quality	0.59107
Element size	03 [mm]
Maximum Element size	0.4 [mm]

The cross-sectional chamber for the mesh, as shown in Fig 6.6 (a) consists of the unstructured triangular mesh covering the entire domain, with inflation layers attached near the edge of the vortex and coolant chambers. The mesh is completely unstructured and triangular, with higher density near the round shape of the nozzles. Furthermore, Fig 6.6 (b) shows the vortex and coolant chambers without nozzles, which are unstructured with a triangular mesh statistic as shown in Table 6.6.

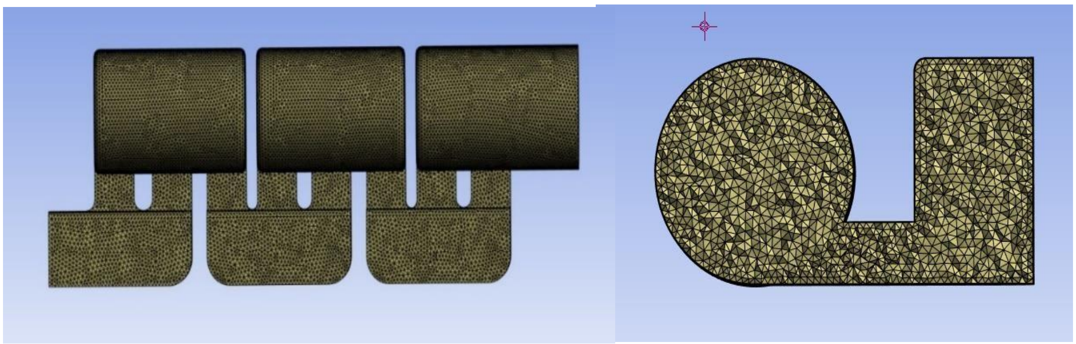

(a) (b)

Figure 6-6: Mesh design: (a) the swirl cooling channels, (b) Cross-section mesh for swirl cooling channels

Table 6-6: mesh statistics for the 2 mm round swirl cooling chambers

Mesh statistics	
Nodes	345084
Elements	1207508
Skewness	0.75
Number of layers	5
Total thickness	0.05 [mm]
Element size	03 [mm]
Maximum Element size	0.4 [mm]

6.3 Quantitative results flow visualisations

The computational simulation model applied in this study is based on the stages work plan as mentioned in on chapter 5. This definition of the computational domain, mesh generation and discretizational geometries for these swirl cooling chambers as well as the materials properties are allocated based on method Table 5.6. The three- stage swirl cooling features a 6 mm round streamline flow pattern, as shown in Fig 6.7.

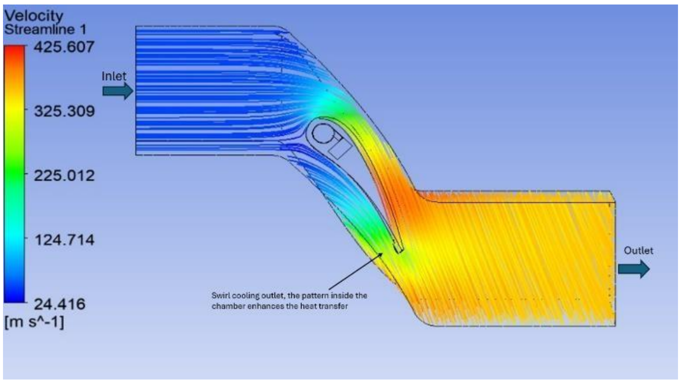

Figure 6-7: Velocity streamline of the flow domain for 6 mm round shape

The flow through the cooling channels and the velocity ranges from low speed to high as speed indicated in red which is where the flow is compressible flow. As flow enters the domain of the blade, Fig 6.8, swirl cooling chamber velocity streamlines indicates a maximum velocity up to 90 m/s. The streamlines display a complex recirculation pattern inside the tube slots. A flow enters each semicircular chamber, it is observed that a high pressure drops coincides with these streamline.

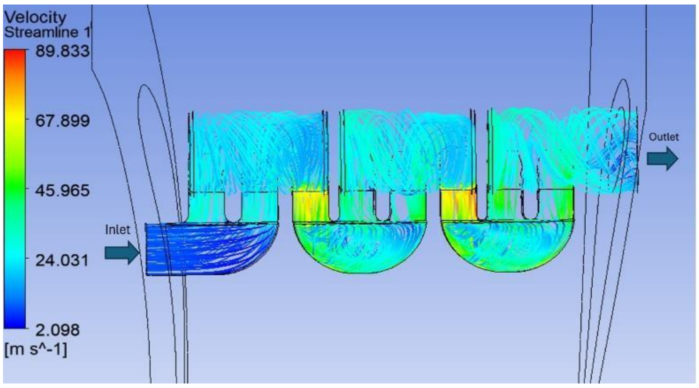

Figure 6-8: Velocity streamline for the swirl cooling chamber for 6 mm round shape

The velocity streamline inside the 4 mm round three – stage swirl cooling chamber is shown in Fig 6.9. Here the inlet velocity has been very high, peaking around channels, which is shown in red colour. The streamlines accelerate as they pass through the narrowing, and the flow enters with a moderate velocity of 24 m/s, which is indicated by the blue colour. Meanwhile, the green/yellow zones are the obstructions within the separation of the flow domain.

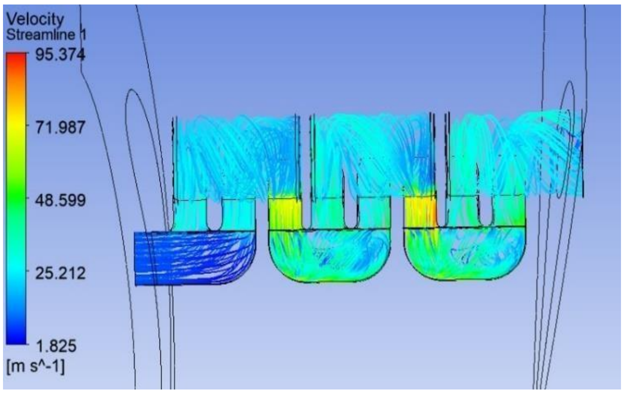

Figure 6-9: Velocity streamline of the flow domain for 4 mm round shape

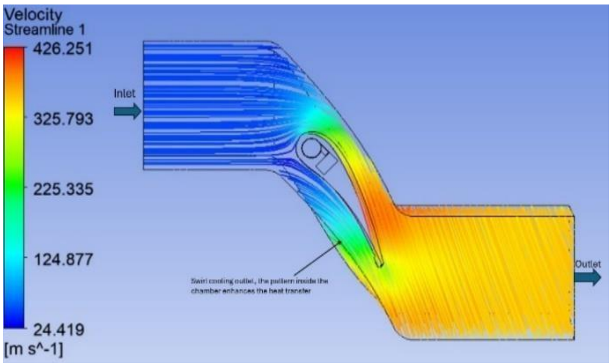

Figure 6-10: Velocity streamline for the swirl cooling chamber for 4 mm round shape

Fig 6.10 is an indicates that the flow enters from the top, passes through four semicircular vortex chambers, and then reaches the coolant chambers. The maximum velocity is around 95 m/s, which is indicated by the red region near the coolant chamber slots. Meanwhile, inside the slots, the flow slows down to 2 m/s, which is blue coloured.

The velocity streamline for the 2 mm round size swirl cooling domain, as shown in Fig 6.11. The streamline shows the flow pattern for the flow entering domains. This domain, the velocity is increase with red and yellow, as well as the fluid passing through smooth and dense areas, also known as laminar and turbulent streamlines.

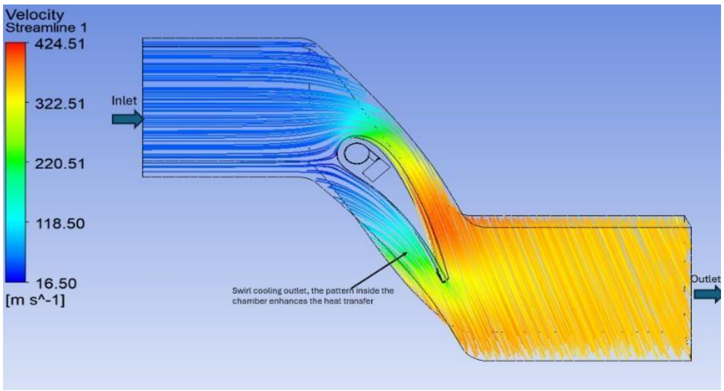

Figure 6-11: Velocity streamline for 2 mm round flow domain

Another internal velocity stream for cooling chambers, as shown in Fig 6.12, and it has a velocity range between 1.28 m/s and 99.23 m/s, which is coloured blue and red. A strong recirculation pattern in the internal chambers and high velocities are indicated by the yellow/blue streamline visible for narrow paths in these chambers. Some of the streamlines are separated over the vortex formations.

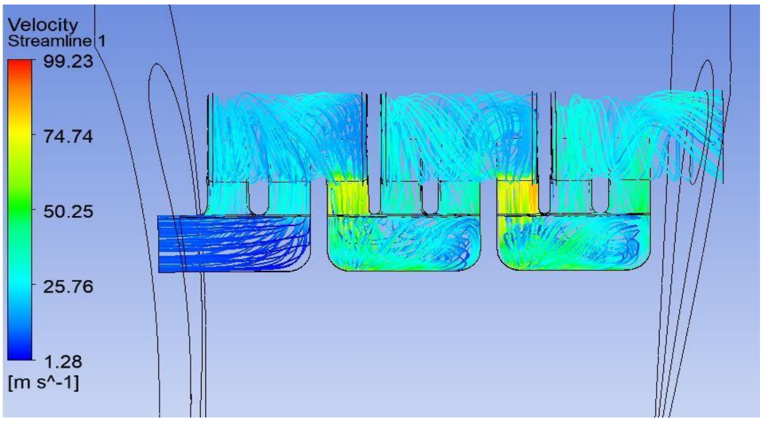

Figure 6-12: Velocity streamline for 2 mm round cooling chambers

6.4 Quantitative Results for the all-around shape of cooling channels

Fig 6.13 shows the pressure loss (P0in - P0out)/P0i of the swirl cooling gas turbine blade leading edge versus Reynolds number (ReD), with each of the different cooling chamber configurations such as N = 1, N = 2, and N = 3 by using these Eq 6.1.

$$\Delta P_{\text{rel}} = \frac{P_{0\text{in}} - P_{0\text{out}}}{P_{0i}} \tag{6.1}$$

where, ΔP_{rel} is the total relative pressure, P_{0in} is the total inlet pressure of the swirl chamber channels, P_t is the total average pressure in intel vortex cooling chambers, and P_{0out} is the total outlet pressure. There is a comparison to the result by Rao et al. [75] with the present investigation simulation variations, such as N=3 with rounded values of 2 mm, 4 mm, and 6 mm. All pressure losses increase with the Reynolds number. Fig 6.13 shows that the papers N=1, N=2, and N=3 have a higher ratio of pressure loss with simulation values.

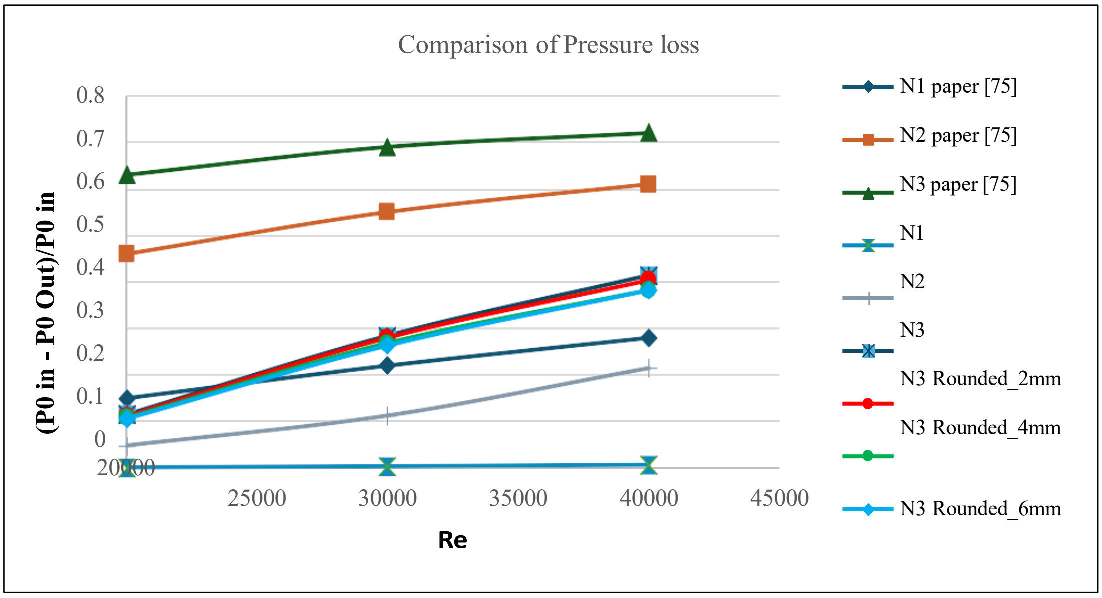

Figure 6-13: Pressure losses comparison of the swirl cooling chambers

However, there is a difference between the rounded N=3 simulation data and the standard non rounded designs. The effect of N=3 with all-rounding is significantly reduced, particularly with the 4 mm N=3 rounded, which exhibits the lowest pressure losses, resulting in smoother and more efficient flow as shown in Table 6.7.

Table 6-7: Pressure drop comparison: cooling chamber round and without round shape

Re	N1	N2	N3	N3- Rounded_2mm	N3 -Rounded_4mm	N3 -Rounded_6mm
20000	0	0.06	0.12	0.116	0.13	0.107
30000	0.00056	0.13	0.286	0.287	0.275	0.264
40000	0.0011	0.23	0.410	0.402	0.397	0.37

As shown in Fig 6.14, the pressure losses for the turbine blade leading edge are in proportion to the averaged Nusselt number distributions, which show that the Reynolds number increases as the Nusselt number also increases. The rounded N=3, 6 mm, 4 mm, and 2 mm are the highest Nusselt numbers (Nu) values, which indicate that the convective heat transfer performance is superior. However, the high Nusselt numbers were maintained in these all-rounded swirl cooling designs across all values of Reynolds number (700+ at Re 40,000). Meanwhile, the N3, N2, and N3 designs show moderate Nusselt numbers are present; however, N=3 is leading these designs.

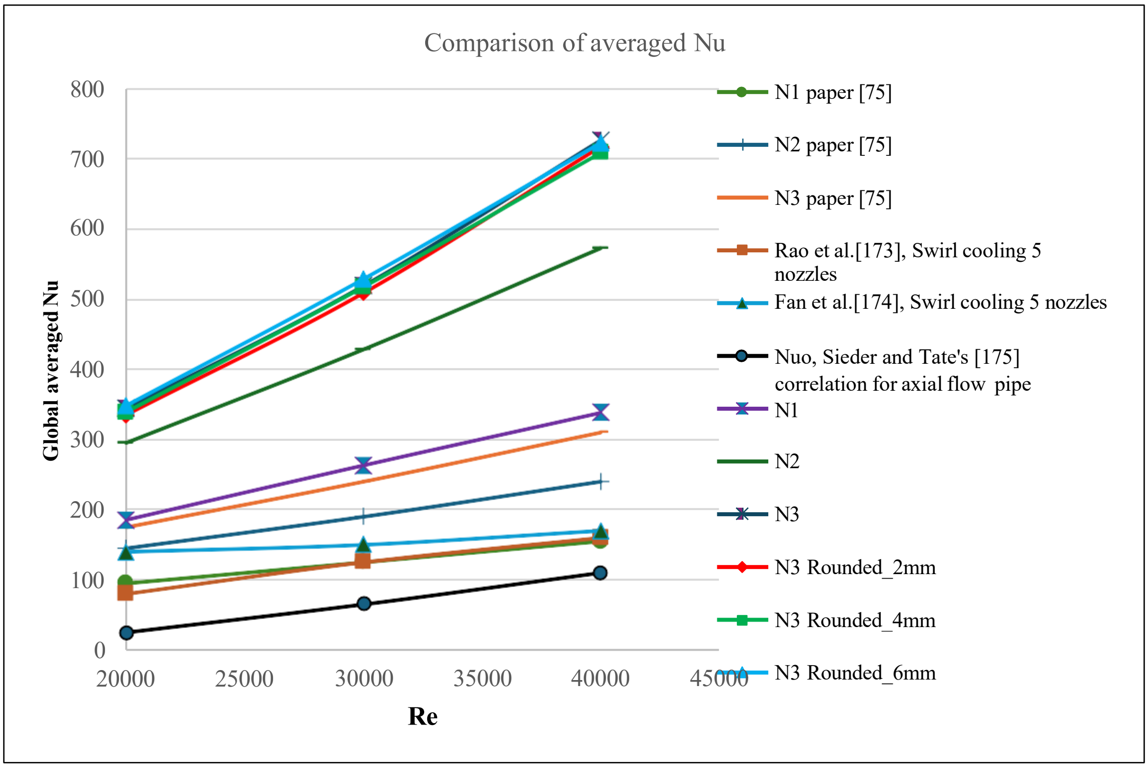

Figure 6-14: Global average Nusselt number for swirl cooling chambers

The N= 3 with 4 mm rounded are superior in terms of heat transfer with low pressure loss (Fig 6.13). At the all Reynolds numbers such as 20,000, 30,000, and 40,000 the N=3 4 mm the is the highest Nu numbers, however the 2 mm and 6 mm are limited increasing. The convective performance is better and increasing for the 4 mm design these Nu gain and correlation with the CFD temperature regions, which is showing decreases the temperature with Δ_p has been measured. In this region, as 4 mm around has improved the flow and optimal heat transfer comparison with other investigations as shown in Table 6.8. These global Nusselt numbers are validated with experimental studies of the swirl cooling with five nozzles by Rao et al. [173], further Fan et al. [174] for helical merge single stage tube with five nozzles and as researched the single cooling chamber axial flow inside the vortex chamber Nuo et al.[175].

Table 6-8: Nusselt number comparison; different types of the Reynolds number with N-3 -2mm,4mm and 6 mm round shapes

Re	N1	N2	N3	N3_Rounded_2mm	N3_Rounded_4mm	N3_Rounded_6mm
20000	180000	300000	346000	330000	340000	350000
30000	270000	420000	530000	520000	450000	540000
40000	340000	580000	700000	720000	580000	720000

6.5 Three-stage swirl cooling best design for Nusselt number

Table 6-9: Three-stage swirl cooling chambers: 2 mm, 4 mm, and 6 mm round shape details studies

Reynolds number 20k			
	2mm	4mm	6mm
280 [K]	333.32	335.81	345.74
296.2 [K]	335.31	339.37	348.52
310 [K]	337.04	339.91	351.07
Reynolds number 30k			
280 [K]	504.18	512.94	524.34
296.2 [K]	508.83	517.40	528.71
310 [K]	515.51	521.54	534.07
Reynolds number 40k			
280 [K]	693.99	701.17	712.31
296.2 [K]	697.78	708.51	722.75
310 [K]	707.52	716.80	726.93

Table 6.9 shows the analysis of the heat transfer data for various Reynolds numbers (20,000, 30,000, and 40,000), and the temperature (280K, 296K, and 310K) with the three-stage swirl cooling chamber nozzles, the diameters are 2 mm, 4 mm and 6 mm. The effect of the Reynolds number from 20,000 to 40,000, shows that simulation results increase the amount of heat transfer performance, across the 2 mm, 4 mm and 6 mm round shapes and temperature for these three-stage swirl cooling chambers. However, the high Reynolds number will cause a higher turbulent flow; further, this turbulence enhances the fluid's behaviour later in each turbulent region, which reduces the boundary layer of each model and, as a result, improves the convective heat transfer. For example 280K with the 2 mm diameter, these values increase from 333.32 to 504.18 to 693.99 for respective Reynolds number of 20,000, 30,000, and 40,000. In this case, further designs of 4 mm and 6 mm will affect the Reynolds number and temperature.

At 280K and 310K temperatures, this leads to a constant and moderate increase in the heat transfer at 20,000, 30,000 and 40,000 Reynolds numbers (Re) with three-stage swirl cooling round shape diameters. In case, at Re = 30k and 6 mm diameter, the values increase from 524.34 at 280 K to 528.71 at 296.2 K, then to 534.07 at 310 K, which is a gradual increase of ~ 3% to 4% across the cooling range. However, the heat transfer effect of 2 mm, 4 mm, and 6 mm radii gives some improvements, but 4mm to 6mm produces a somewhat slight incremental advantage. At Re 40k, for all cases with a temperature of 310K, the cost for 2 mm is 707.52. 4 mm is 716.80.

6.6 MT-1 swirls cooling focused on the best design

The N=1,2,3 with 6mm round size was taken from chapter 5 to continue for further investigation; however, Figs 6.15 show that N-1 gradually increases and has a higher temperature at all Reynolds numbers. Meanwhile, the N=3 geometries have a larger edge round shape, with the 4 mm and 6 mm design showing the lowest averaged temperatures. As the Reynolds number decreases, the surface temperature indicates higher heat transfer. The round shape significantly reduces the average temperature, particularly at higher Reynolds numbers as shown in Fig 6.15.

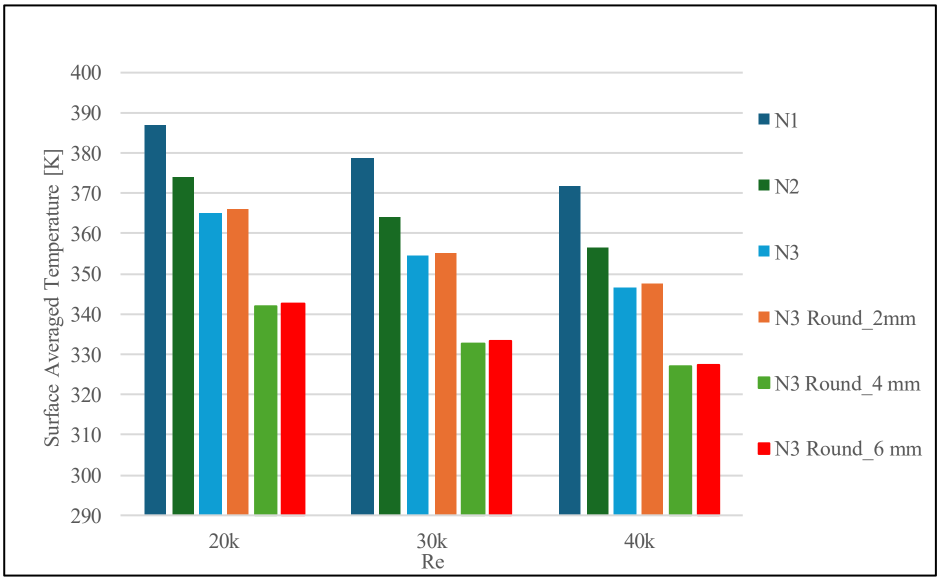

Figure 6-15: Swirl cooling chamber: averaged temperature on the leading edge with different Reynolds numbers

Fig 6.16 shows that the thermal performance of the swirl cooling gas turbine blade leading edge is higher at N = 1, across the 20,000, 30,000, and 40,000 Reynolds numbers. However, N=2 and N=3 has the lowest thermal performance. N=3 with a round 6 mm is the best thermal performance improvement region.

A higher Reynolds number (40k), it reaches and the thermal performance increases with the Reynolds numbers for all given model configurations, particularly N=3 with rounded shapes, which improve the thermal performance.

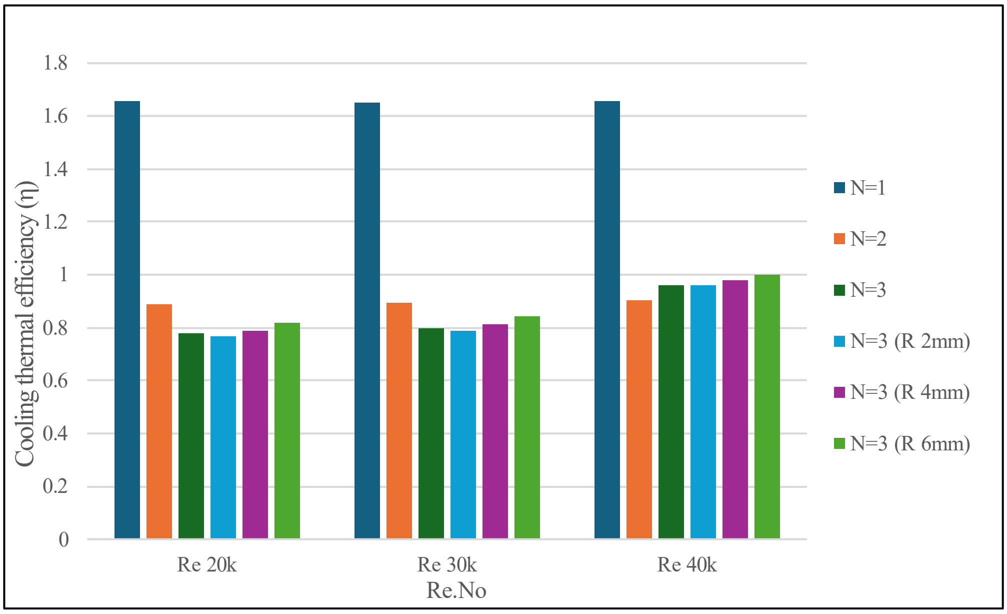

Figure 6-16: Thermal performance for swirl cooling chambers

Fig. 6.16 indicates that the N = 3 R 4 mm configuration provides better thermal cooling performance than the N = 3 R 6 mm and N=3 R 2 mm configurations. However, these improvements are based on changes to the flow structure in swirl cooling chambers, and N=3 R 2 mm is the swirl intensity at this N= R 2 mm, which is excessively high. Which is affected by increasing turbulence, but this also results in very low heat transfer and higher-pressure losses. Further, N=3 R 6mm are low and weak swirl intensities, indicating insufficient mixing in the swirl flow. In contrast, N=3 R 4mm has a higher swirl intensity, which enhances both swirl strength and flow stability; in this N=3 R 4mm rounding offers the optimum equilibrium between pressure drop and heat transfer reinforcement. This does not represent maximal thermal efficiency, but rather a relative index that improves cooling performance within the examined parameter range. In this study, cooling thermal efficiency (η) is characterised as a relative performance parameter that associates heat transfer reinforcement with the corresponding pressure drop penalty. This efficiency is determined as the ratio of normalised heat transfer performance to normalised pressure drop. This efficiency indicator provides a qualitative assessment of the relationship between pressure drop and heat transfer. These elevated values indicate setups that enhance convection heat transfer without a commensurate rise in pressure drop. The metric is used exclusively for the comparative evaluation of the configuration examined, as shown in Eqs 5.1 and 5.2. and Figures 5.19 and 6.16.

6.7 Design interpretation and limitations

In this chapter, the parametric studies for a three-stage cooling chamber were studied, with each nozzle's size (radius) changing. The flow behaviour inside the multistage cooling chamber is dominated by curvature-induced secondary motion and nozzle cross-section flow interaction, which control both heat transfer and pressure distributions. The inlet bend regions generate centrifugal forces that turn the flow, driving the fluid towards the vortex chambers, which produce strong velocity gradients and local acceleration in each round-shaped region. The radii enhance mixing, leading to thicker thermal boundary layers and a higher Nusselt number in the all-around shape configuration. However, in the three-stage round-shaped cooling chambers, the flow develops recirculation zones and bends. These secondary motions continuously flow toward the vortex chambers and, during this process, remove heat from the chambers' surfaces, sustaining convective cooling. However, the velocity streamline plots show intensified swirling motion and recirculation within each chamber, which is responsible for the observed Nusselt number increase with Reynolds number. As the Reynolds number rises, turbulence intensity and secondary flow also increase together, which causes increased pressure losses.

The relative performance assessment determines that a rounded multi-stage configuration achieves lower pressure loss by reducing the rectangular edges that turn and by suppressing separation at chamber sections. However, the enhanced thermal performance observed for the N-3 rounded configurations is attributed to improved swirl stability and sustained turbulence generation, which enhance convective heat transfer while maintaining acceptable pressure losses. Design and modelling limitations of the optimisation conclusions are based on a constrained range of geometric parameters and Reynolds numbers. Meanwhile, the predictable three-stage (N-3) configurations demonstrate enhanced performance within the investigated range. However, additional investigation is required to assess scalability under full-engine operating conditions and transient loading scenarios.

Chapter 7: Conclusion

This chapter evaluates how well the research achieved, the objectives that were set at the outset. The aim of this research was to study thermal analysis of the design of internal swirl cooling configurations applied to a high-pressure turbine blade, focusing on the leading-edge region. This involved the design of a standard MT-1 and use of a blade mixing plane CFD set up. Following range of parametric studies, the performance of a novel swirl cooling design was tested through a series of structured objectives.
A review for each objective is described here:

Objective 1- Using literature, to get the important characteristics of turbine blade operation, cooling methods and approaches to modelling and simulating fluid dynamics and heat transfer.

The first objective is successfully completed. The literature review covered the understanding of basic turbine operation and blade design characteristics. Further literature contain the identified high temperature operating conditions, which is the most challenging, with necessities for more efficient cooling strategies to balancing turbine blade operation conditions. As described in the literature review, convective internal cooling such as film, impingement, and swirl cooling are widely applied in high-pressure turbine blades applications for improved thermal efficiencies, heat transfer and pressure drop. Computation modelling approaches were explored to show an understanding of thermal behavior, heat transfer, and aerodynamic concepts. Computational modelling was explored for the use of different types of turbulence models conjugate heat transfer approaches, which is allowed the detailed studies for thermal activities in certain regions.

A major finding was that steady – state RANS turbulence models are well suited to these kinds of simulations. Further insights were obtained linking concepts to the coherent framework of turbine blade operations, including new and existing cooling strategies by using well- established simulation modelling methods. Nevertheless, the contribution of these methods aligns with gaps in knowledge internal swirl cooling strategies, with fluid and thermal activities behaviour able to be accounted for. A novel area of work identified was for the evaluation of internal swirl cooling techniques by applying computational fluid dynamic CFD. This can sufficiently demonstrate the performance of internal swirl cooling behaviour, especially in the leading edge regions of turbine blade.

Objective 2 - To develop and validate a CFD modeling approach to accurately and reliably simulate the aerodynamic flow around a generic high pressure blade, the MT-1 blade design, including the effect of rotor – stator interaction, using experimental data.

This objective is successfully met. The generic MT-1 turbine blade provided a baseline design, from which to base the analysis. The aerodynamic performance was robustly tested under various operation conditions such as baseline configurations. Initially 2D simulations were made possible by taking slices of the 3D domain are the 50% span location to enable the modelling approach to be developed. Using, mixing plane between rotor and stator regions was shown to be effective for simulating the interaction between these two blades. Different types of turbulence model were explored, and grid independence was investigated. Both pressure distribution and heat transfer were investigated by using the following turbulence models RNG k-ε, SSTk-ω, Spalart–Allmaras (SA) model. This was done for a number of meshes as part of the grid independence study.

It was found that the SST k-ω model gave the best predictions of pressure and heat transfer behavior compared to other turbulence models. This also applied for cases of different rotational velocities. Accounting for all results, including pressure distributions and heat transfer behaviour the baseline SST k-ω model gave the best efficiency around 0.88. This compared well to the experimental data for efficiency pressure and heat transfer distributions from validation Chana et al. [166]. These results are described in Chapter 3.

Objective 3 - To develop a separate CFD approach to accurately model internal flow and heat transfer through a swirl cooling chamber by validating with available experimental data.

This objective is also successfully achieved. It was important to develop an accurate simulation approach for single stage swirl cooling, through validation of both pressure drop and heat transfer behavior. This involved past literature on experimental research to guide simulation work. This aspect of the work presented in this thesis underlined the importance of validation approaches to provide clear understanding of the heat transfer activities and pressure drop characteristics. A single stage cooling chamber comprising of five nozzles was identified suitable validation case, this also contained vortex and coolant chambers as shown in Chapter 4.

Rao et al. [171] provided validation date to compare the CFD modelling approach. Important aspects of the CFD method include mesh design, turbulence model selection and using appropriate solver settings to simulate this thermal and flow characteristic. Good agreement between CFD results and experimental data was presented in which provided the foundations for the novel work in Chapter 5 and 6.

Objective 4 - Combine the results from objectives (2) and (3) to simulate conjugate heat transfer within a generic high–pressure turbine blade. This will involve the design of internal swirl cooling channels, including validations in the number of cooling stages.

This objective was also successfully met. Chapter 5 set out to investigate two-stage and three-stage concept for internal swirl cooling within the generic gas turbine blade. This objective was to overcome the drawbacks of conventional internal swirl cooling with single- stage chambers and to investigate whether enhancement in heat transfer could be achieved with extra stages.

Earlier research finding have shown that single-stage swirl cooling chambers can effectively be modelled numerically in [180] [181]. These traditional cooling technologies are work but they do not fully address the need to achieve both high cooling efficiency and temperature uniformity within a turbine blade. The investigation revealed a design with only three-stages (N=3) as necessary to improve thermal performance. One three-stage design incorporated modifications through rounding in the corners of the cooling chambers with a rounding radius 6 mm. This design was compared to standard single, two and three stage (non-rounding) to determine which design yielded the best thermal effect, without a significant pressure drop. The three-stage cooling configuration (N=3) delivered the greatest benefit, achieving up to 60% of the Nusselt number and over 40 K of temperature distribution improved overall compared to the baseline single stage swirling chamber design. However, this came at a cost of greater pressure drop (i.e, losses). The application of 6 mm rounding described above improved the situation leading to of pressure drop.

Overall, It has been established that multistage swirl cooling as a concept can be applied in a systematic way to design suitable arrangements of cooling chambers. Confidence in this finding was gained from good comparison to further experimental validation as outlined in Chapter 5.

Objective 5- Investigation of the impact of parametric changes, such as critical channel radii, on the design of swirl cooling channels within the turbine blades.

This objective was successfully met. In this objective detailed research was carried out to focus on the key factors based on the swirl cooling configuration for the baseline MT-1 high pressure turbine blade with a focus on leading edge cooling. Extending the work from Chapter 5, the three stage (N =3) swirl cooling chamber design was again studied but with comparisons between the standard rectangular design and round nozzles of with rounding diameters of R = 2, 4, 6 mm. Based on this all the data the R 4mm round design is the best between each other's designs. In terms of minimising pressure drop, whilst delivering effective, heat transfer.

This performance was confirmed to occur for a range of Reynolds numbers varying between 20,000 and 40,000. Furthermore, these results compare favorably with work [75, 173, 174] because the pressure drop is less in the novel work presented in Chapter 6. Nevertheless, when the Reynolds number increases, the parallel efficiency also changes. Also considered was the effectiveness of changing the temperature distribution as boundary conditions to rest how robust the best design is. It was found that increasing the temperature gradually will result in increased heat transfer and pressure drop for all three stages with rounded nozzles. All the obtained results were compared with Comeau et al. [158] and Wang et al. [172] and were also investigated with multiple cooling configurations. In general, the work in Chapter 6 matched well with their investigation, particularly in terms of heat transfer and pressure drop.

Overall, this investigation is dominated by thermal behavior and pressure drop across a range using the Reynolds number. The research outcomes demonstrated that pressure drop and thermal performance across the Reynolds number range were reliable and consistent with previous researched by Fan et al. [174] and Rao et al. [173]. It is clear from the results that modification of three-stage designs improves performance both in terms of the pressure drop and thermal behaviors. However, the 4 mm is considered the best design operation at 296K, with a 5.3% decrease in pressure losses and an overall thermal efficiency of 2.5%, which is better than all rounded models.

As a general observation, the constant increase in inlet temperature enhances the heat transfer for rounded nozzles, resulting in better overall heat transfer distribution. These outcomes were compared with [158] and [172]. This is a novel concept of addressing overall thermal performances.

The research concludes that the different types of rounded nozzles are best for thermal efficiencies, heat transfer, and pressure drop, thereby improving cooling performance in high-pressure gas turbine engineering solutions. These three-stage configuration results outcome are significant because they indicate improved the cooling and increased robustness of thermal behaviour. These outcomes are compared with published data one multistage swirl cooling configuration by Yao et al. [75], single-stage swirl cooling with five nozzles by Rao et al. [173], further single-stage experimental studies with Fan et al. [174], and single-stage correlation with double helical numerical and experimental studies, by Nuo et al. [175].

These validated results support the conclusion that enhanced cooling occurs due to the design of swirl cooling chambers.

7.1 Future work

The first part is the 2D mixing plane, which was researched to establish a baseline for the mixing plane. The research aimed to find the basic behaviour of the pressure distribution and heat transfer in the high-pressure turbine blades. Followed by the 2D mixing plane, further carried out the 3D mixing plane which is mainly focus in the used different type of spam location with varying types of RPMs to find the pressure distribution and heat transfer behaviour by adding these pressure distribution P/P0 , in this investigation used the different type of the turbulence models and Grid independence studies were used the grid independence studies k-ω, k-ε_y+30, and NGV_RNG_y+30 turbulence models to investigate the better flow performance of the mixing plane these investigation is validates with Chana et al. [166].

Further investigated the experimental validation forsingle stage swirl cooling with this numerical single stage simulation, in this investigation used the long swirl cooling duct with nozzles attached with vortex and coolant chamber was used to find the pressure drop and heat transfer of thissingle-stage ductswirl cooling channels.

In this work, several further work opportunities, such as changing the grids, may be possible to affect this validation. The second area of research in this current research were carried out entirely high-pressure gas turbine blade internal swirl cooling chambers, in this investigation design the different type such as single, two and three stage swirl cooling chambers based on the gas turbine blade specifications, in this mainly investigated the pressure drop, heat transfer, thermal performance of the of the each cooling chambers which is in the Chapter 5.

To continue the cooling chamber best design. In this design, took the three-stage cooling chamber, where changed the round shapes to 2 mm, 4 mm, and 6 mm as mentioned in chapter 6. Following these round shape to find the best design to find the pressure drop, heat transfer and thermal performance of this model. Further changed the boundary conditions for each design and found the pressure drop and heat transfer with thermal behaviours. In the swirl cooling chamber, there are more research opportunities, such as merging swirl cooling and impingement cooling, which can affect the pressure drop and thermal activitie

Reference

[1] S. Byworth, “Design and development of high temperature turbines,” *Roll. Mag.*, vol. 44, 1986.

[2] G. Garratt and D. E. Gee, “Paper 5: The Application of Some Analytical Techniques to the Study of Turbocharging the Automotive Diesel Engine,” *Proc. Inst. Mech. Eng. Conf. Proc.*, vol. 180, no. 14, pp. 62–74, 1965, doi: 10.1243/pime_conf_1965_180_386_02.

[3] G. Xiao *et al.*, “Recuperators for micro gas turbines: A review,” *Appl. Energy*, vol. 197, pp. 83–99, 2017, doi: 10.1016/j.apenergy.2017.03.095.

[4] J. P. Stalder, “Gas turbine compressor washing state of the art - Field experiences,” *Proc. ASME Turbo Expo*, vol. 4, 1998, doi: 10.1115/98-GT-420.

[5] J. H. Horlock, D. T. Watson, and T. V. Jones, “Limitations of gas turbine performance imposed by large turbine cooling flows,” *J. Eng. Gas Turbines Power*, vol. 123, no. 3, pp. 487–494, 2001, doi: 10.1115/1.1373398.

[6] L. M. Wright, M. F. Malak, D. C. Crites, M. C. Morris, V. Yelavkar, and R. Bilwani, “Review of platform cooling technology for high pressure turbine blades,” *Proc. ASME Turbo Expo*, vol. 5B, pp. 1–12, 2014, doi: 10.1115/GT2014-26373.

[7] G. A. Halls, “Air Cooling of Turbine Blades and Vanes,” *Aircraft Engeering. Aerospace. Technology.*, vol. 39, no. 8, pp. 4–14, January 1967, doi: 10.1108/eb034284.

[8] P. Yang, W. Yue, J. Li, G. Bin, and C. Li, “Review of damage mechanism and protection of aero-engine blades based on impact properties,” *Eng. Fail. Anal.*, vol. 140, no. June, p. 106570, 2022, doi: 10.1016/j.engfailanal.2022.106570.

[9] D. Andreadis, “Scramjet Engines Enabling the Seamless Integration of Air & Space Operations,” *Prot. Coatings Turbine Bl.*, vol. 30, no. Supplement, pp. 1–28, 2002, [Online].Available: http://content.wkhealth.com/linkback/openurl?sid=WKPTLP:landingpage&an=00000446 200809001-00006.

[10] J. Pohl *et al.*, “Innovative Turbine Stator Well Design Using Design Optimisation To cite this version : HAL Id : hal-01887489 Innovative Turbine Stator Well Design Using Design Optimisation,” 2018.

[11] M. Suo, “Turbine cooling,” *Aerothermodyn. Aircr. Engine Components*, pp. 275–328, 1985.

[12] E. I. Esposito, “Jet impingement cooling configurations for gas turbine combustion,” p. 46, 2006.

[13] J. A. Parker, “High Pressure Turbine Blade Platform Cooling and Feed Architecture,” 2021.

[14] H. Salleh, A. Khalid, M. A. Hashim, W. Razzaly, S. H. Amirnordin, and M. Suardi,

"Effects of Mass Flow Rate on Combustion Characteristics and Emissions of Micro Gas Turbine," vol. 2, no. 1, pp. 1–6, 2020.

[15] S. Zhu, Y. Li, J. Yan, and C. Zhang, "Recent Advances in Cooling Technology for the Leading Edge of Gas Turbine Blades," *Energies*, vol. 18, no. 3, pp. 1–21, 2025, doi: 10.3390/en18030540.

[16] D. Dunn-Rankin, M. M. Miyasato, and T. K. Pham, "Chapter 1 - Introduction and Perspectives," in *Lean Combustion*, D. Dunn-Rankin, Ed., Burlington: Academic Press, 2008, pp. 1–18. doi: https://doi.org/10.1016/B978-012370619-5.50002-9.

[17] O. Siddiqui and I. Dincer, "Chapter 2.1 - Energy and Exergy Analyses of a Geothermal-Based Integrated System for Trigeneration," in *Exergetic, Energetic and Environmental Dimensions*, I. Dincer, C. O. Colpan, and O. Kizilkan, Eds., Academic Press, 2018, pp. 213–231. doi: https://doi.org/10.1016/B978-0-12-813734-5.00013-5.

[18] Y. A. Cengel, "Thermodynamics: an engineering approach Introduction and Basic Concepts," *vol. 8th Ed.*, pp. 1–59, 2015.

[19] H. F. Van Roon, H. F. Van Sprang, and A. H. Verdonk, "'Work' and 'Heat': on a road towards thermodynamics," *Int. J. Sci. Educ.*, vol. 16, no. 2, pp. 131–144, 1994, doi: 10.1080/0950069940160203.

[20] L. Bovo *et al.*, "Restoration of the third law in spin ice thin films," *Nat. Commun.*, vol. 5, pp. 1–8, 2014, doi: 10.1038/ncomms4439.

[21] Y. Cengel, J. Cimbala, and R. Turner, *EBOOK: Fundamentals of Thermal-Fluid Sciences (SI Units)*. McGraw Hill, 2012.

[22] F. A. Kulacki *et al.*, *Handbook of thermal science and engineering*. 2018. doi: 10.1007/978-3-319-26695-4.

[23] M. Potter and E. Scott, "Thermal sciences," *Brooks/Cole*, 2004.

[24] J. C. Cuevas and F. J. García-Vidal, "Radiative Heat Transfer," *ACS Photonics*, vol. 5, no. 10, pp. 3896–3915, 2018, doi: 10.1021/acsphotonics.8b01031.

[25] M. Raisee, A. Noursadeghi, and H. Iacovides, "Application of a non-linear k-ε model in prediction of convective heat transfer through ribbed passages," *Int. J. Numer. Methods Heat Fluid Flow*, vol. 14, no. 3, pp. 285–304, Jan. 2004, doi: 10.1108/09615530410517968.

[26] H. Kawamura, H. Abe, and Y. Matsuo, "DNS of turbulent heat transfer in channel flow with respect to Reynolds and Prandtl number effects," *Int. J. Heat Fluid Flow*, vol. 20, no. 3, pp. 196–207, 1999, doi: 10.1016/S0142-727X(99)00014-4.

[27] W. M. Kays, "Turbulent Pratidtl Number - Where Are We ? •," no. May, 1994.

[28] C. Heat, "Kays and Crawford." McGraw-Hill, 1993.

[29] J. Bredberg, S. H. Peng, and L. Davidson, "An improved k - ω turbulence model applied to recirculating flows," *Int. J. Heat Fluid Flow*, vol. 23, no. 6, pp. 731–743, 2002, doi:

10.1016/S0142-727X(02)00148-0.

[30] M. M. Gibson and B. E. Launder, “On the calculation of horizontal, turbulent, free shear flows under gravitational influence,” *ASME J. Heat Transf.*, vol. 98, pp. 81–87, 1976.

[31] Y. G. Lai and R. M. C. So, “Near-wall modeling of turbulent heat fluxes,” *Int. J. Heat Mass Transf.*, vol. 33, no. 7, pp. 1429–1440, 1990, doi: 10.1016/0017-9310(90)90040-2.

[32] J. Larsson, *Numerical simulation of turbulent flows for turbine blade heat transfer applications*. Chalmers University of Technology, 1998.

[33] H. S. Dol, K. Hanjalić, and S. Kenjereš, “A comparative assessment of the second-moment differential and algebraic models in turbulent natural convection,” *Int. J. Heat Fluid Flow*, vol. 18, no. 1, pp. 4–14, 1997, doi: 10.1016/S0142-727X(96)00149-X.

[34] B. J. Azzopardi, *Gas-liquid flows*. Begell house New York, 2006.

[35] J. F. Douglas, *Fluid mechanics*. Pearson education, 2005.

[36] I. A. Frigaard and C. Nouar, “On the usage of viscosity regularisation methods for visco-plastic fluid flow computation,” *J. Nonnewton. Fluid Mech.*, vol. 127, no. 1, pp. 1–26, 2005, doi: 10.1016/j.jnnfm.2005.01.003.

[37] D. Gebreselasie, “Mechanics and Oscillations: University Physics I”.

[38] N. W. Ryan and M. M. Johnson, “Transistion from laminar to turbulent flow in pipes,” *AIChE Journal*, vol. 5, no. 4, pp. 433–435, 1959.

[39] H. L. Dryden, “Transition from laminar to turbulent flow,” *Turbul. Flows Heat Transf.*, vol. 5, pp. 3–74, 2015.

[40] L. Jorge and L. Ferris (2012) “Heat transfer in swirl cooling blades,” university of Porto.

[41] M. Brunke and T. O. M. Gonser, “The ecological significance of exchange processes between rivers and groundwater,” *Freshw. Biol.*, vol. 37, no. 1, pp. 1–33, 1997.

[42] N. J. Balmforth, I. A. Frigaard, and G. Ovarlez, “Yielding to stress: Recent developments in viscoplastic fluid mechanics,” *Annu. Rev. Fluid Mech.*, vol. 46, pp. 121–146, 2014, doi: 10.1146/annurev-fluid-010313-141424.

[43] H. C. Ohanian and R. Ruffini, *Gravitation and spacetime*. Cambridge University Press, 2013.

[44] F. M. Approach, “Field Modeling Approach,” in *Computational. Fluid Dynamic for Fire Engineering.*, pp. 29– 133, 2009, doi: 10.1016/b978-0-7506-8589-4.00002-8.

[45] J. L. Heiman and L. Hesselink, “Visualizing Vector Field Topology in Fluid Flows,” *IEEE Comput. Graph. Appl.*, vol. 11, no. 3, pp. 36–46, 1991, doi: 10.1109/38.79452.

[46] T. Papanastasiou, G. Georgiou, and A. N. Alexandrou, *Viscous fluid flow*. CRC press, 2021.

[47] I. Sadrehaghighi, “Aerodynamic Basics,” no. April, pp. 0–237, 2002, doi: 10.13140/RG.2.2.32859.72488.

[48] B. Stanković, A. Stojanović, M. Sijerčić, S. Belošević, and S. Čantrak, “Evaluation and limitations of standard wall functions in channel and step flow configurations,” *J. Serbian Soc. Comput. Mech.*, vol. 8, no. 1, pp. 1–22, 2014, doi: 10.5937/jsscm1401001S.

[49] E. Dick, “Introduction to finite volume methods in computational fluid dynamics,” vol. M, pp. 275–301, 2009, doi: 10.1007/978-3-540-85056-4_11.

[50] J. Zhang *et al.*, “Failure analysis of local effusion corrosion in small diameter gas pipeline: Experiment and numerical,” *Eng. Fail. Anal.*, vol. 161, no. February, p. 108300, 2024, doi: 10.1016/j.engfailanal.2024.108300.

[51] M. Han, R. Ooka, and H. Kikumoto, “A wall function approach in lattice Boltzmann method: Algorithm and validation using turbulent channel flow,” *Fluid Dyn. Res.*, vol. 53, no. 4, 2021, doi: 10.1088/1873-7005/ac1782.

[52] R. A. Gomes, “On Aerothermal Effects of Film Cooling on Turbine Blades with Flow Separation,” p. 530, 2010.

[53] C. Li, G. H. Yeoh, S. C. P. Cheung, and J. Y. Tu, “Modelling horizontal gas-liquid flow using averaged bubble number density approach,” *J. Comput. Multiph. Flows*, vol. 2, no. 2, pp. 89–99, 2010, doi: 10.1260/1757-482X.2.2.89.

[54] Y. Li and P. V. Nielsen, “Commemorating 20 years of Indoor Air: CFD and ventilation research,” *Indoor Air*, vol. 21, no. 6, pp. 442–453, 2011, doi: 10.1111/j.1600-0668.2011.00723.x.

[55] J. Tu, G. H. Yeoh, C. Liu, and Y. Tao, *Computational fluid dynamics: a practical approach*. Elsevier, 2023.

[56] C. Hirsch, *Numerical computation of internal and external flows: The fundamentals of computational fluid dynamics*. Elsevier, 2007.

[57] S. Patankar, *Numerical heat transfer and fluid flow*. CRC press, 2018.

[58] J. D. Anderson and J. Wendt, *Computational fluid dynamics*, vol. 206. Springer, 1995.

[59] C. A. Gilkeson, “Analysis and optimization of ventilation and drag in small livestock trailers using computational fluid dynamics.” University of Leeds, 2009.

[60] R. Peyret, *Handbook of computational fluid mechanics*. Elsevier, 1996.

[61] E. mecánica, fluid mechanics,” vol. 1, no. April, pp. 1–6, 2008.

[62] V. D. F. Maschinenbau and E.- Energiesysteme, “The Turbulent Very Wide-Gap Taylor-Couette Flow : Experimental Investigation,” 2023, doi: 10.26127/BTUOpen- 6445.

[63] X. Li and J. Tu, “Evaluation of the eddy viscosity turbulence models for the simulation of convection–radiation coupled heat transfer in indoor environment,” *Energy Build.*,

vol. 184, pp. 8–18, 2019, doi: 10.1016/j.enbuild.2018.11.043.

[64] H. K. Versteeg and W. Malalasekera, *An introduction to computational fluid dynamics: the finite volume method*. Pearson education, 2007.

[65] C. A. Gilkeson, V. V. Toropov, H. M. Thompson, M. C. T. Wilson, N. A. Foxley, and P. H. Gaskell, “Dealing with numerical noise in CFD-based design optimisation,” *Computational fluid mechanics*, vol. 94, pp. 84–97, 2014, doi: 10.1016/j.compfluid.2014.02.004.

[66] M. Tsubokura *et al.*, “Computational visualization of unsteady flow around vehicles using high performance computing,” *Comput. Fluids*, vol. 38, no. 5, pp. 981–990, 2009, doi: 10.1016/j.compfluid.2008.01.020.

[67] Kajishima, *Computational Fluid Dynamics, Applied Computational Fluid Dynamics*, Fifth Edit., no. March 2012. Elsevier, 2012. doi: 10.1016/B978-0-12-382100-3.10010-1.

[68] B. E. LAUNDER and D. B. SPALDING, *the Numerical Computation of Turbulent Flows*, vol. 3. Pergamon Press, Ltd, 1983. doi: 10.1016/b978-0-08-030937-8.50016-7.

[69] D. Wilcox, D. C., Turbulence Modeling for CFD, Vol. 2, pp. 172–180 and C. Industries, La Canada, “H133907.” 1998.

[70] F. R. Menter, “Two-equation eddy-viscosity turbulence models for engineering applications,” *AIAA J.*, vol. 32, no. 8, pp. 1598–1605, 1994.

[71] Z. J. Chen and A. J. Przekwas, “A coupled pressure-based computational method for incompressible/compressible flows,” *J. Comput. Phys.*, vol. 229, no. 24, pp. 9150–9165, 2010, doi: 10.1016/j.jcp.2010.08.029.

[72] T. NAKAJIMA, Y. SHIKANO, and Y. YAMASHITA, “318 Prediction of Unsteady Force for Axial Turbine Buckets,” *Proc. Ibaraki Dist. Conf.*, vol. 2012.20, no. 0, pp. 91–92, 2012, doi: 10.1299/jsmeibaraki.2012.20.91.

[73] U. Force and A. T. Buckets, “駕,” 2012.

[74] C. Lockwood, P. C. Ivey, and R. G. Wells, “Experimental audit of the mixing-plane approach to turbomachinery analysis and a review of alternative multi-row techniques,” *Aeronaut. J.*, vol. 104, no. 1033, pp. 117–124, 2000, doi: DOI: 10.1017/S0001924000025306.

[75] R. Yao, H. Su, Y. Cheng, J. Wang, and J. Pu, “Numerical investigation of a novel multistage swirl cooling conception in blade leading edge of gas turbine,” *Int. J. Therm. Sci.*, vol. 172, no. PA, p. 107269, 2022, doi: 10.1016/j.ijthermalsci.2021.107269.

[76] N. Kaewchoothong, S. Gonsrang, and N. A. Cheputeh, “Flow and Heat Transfer in Ribbed Swirl Tubes with a Tangential Inlet Jet for Gas Turbine Blade Leading Edge Cooling,” *Heat Transf. Eng.*, vol. 0, no. 0, pp. 1–20, 2025, doi: 10.1080/01457632.2025.2459985.

[77] X. Fan and Y. Xue, “Numerical investigation of nozzle geometry influence on the vortex cooling in an actual gas turbine blade leading edge cooling system,” *Heat Mass Transfer,*

und Stoffue barraging, vol. 58, no. 4, pp. 575–586, 2022, doi: 10.1007/s00231-021-03131-9.

[78] F. Kreith and O. K. Sonju, “The decay of a turbulent swirl in a pipe,” *J. Fluid Mech.*, vol. 22, no. 2, pp. 257–271, 1965, doi: 10.1017/S0022112065000733.

[79] T. Sarpkaya, “Effect of the adverse pressure gradient on vortex breakdown,” *AIAA J.*, vol. 12, no. 5, pp. 602–607, 1974.

[80] A. Mager, “Incompressible, viscous, swirling flow through a nozzle,” *AIAA J.*, vol. 9, no. 4, pp. 649–655, 1971.

[81] B. Kobiela, *“Heat transfer in a cyclone cooling of a gas turbine blade” PhD thesis*. Verlag Dr. Hut, 2014.

[82] T. Arts, “Convective Heat Transfer with Film Cooling Around a Rotor Blade,” *Mod. Res. Top. Aerosp. Propuls.*, pp. 253–274, 1991, doi: 10.1007/978-1-4612-0945-4_14.

[83] M. Engineering, “HEAT TRANSFER IN TURBULENT AND FRICTION b y F R A N K K R E I T H and DAVID MARGOLIS *),” vol. 8.

[84] S. Pressure and S. I. Tube, “l :::;?: y,” vol. 15, no. 6, pp. 837–842.

[85] A. H. Nissan and V. P. Bresan, “Swirling flow in cylinders,” *AIChE J.*, vol. 7, no. 4, pp. 543–547, 1961, doi: 10.1002/aic.690070404.

[86] R. R. Parchen, “Decay of swirl in turbulent pipe flows door,” vol. 1, no. 1993, 1993, doi: 10.6100/IR389647.

[87] M. J. Reader-Harris, “The decay of swirl in a pipe,” *Int. J. Heat Fluid Flow*, vol. 15, no. 3, pp. 212–217, 1994, doi: 10.1016/0142-727X(94)90040-X.

[88] D. Version, *Turbulent pipe flow with swirl Turbulent Pipe Flow with Swirl*, vol. 1, no. 1995. 1995. doi: 10.6100/IR430720.

[89] W. Steenbergen and J. Voskamp, “The rate of decay of swirl in turbulent pipe flow,” *Flow Meas. Instrum.*, vol. 9, no. 2, pp. 67–78, 1998, doi: 10.1016/S0955-5986(98)00016-8.

[90] M. Yilmaz, Ö. Çomakli, and S. Yapici, “Enhancement of heat transfer by turbulent decaying swirl flow,” *Energy Convers. Manag.*, vol. 40, no. 13, pp. 1365–1376, 1999, doi: 10.1016/S0196-8904(99)00030-8.

[91] A. Khalatov, N. Syred, P. J. Bowen, and R. M. Al-Ajmi, “Enhanced cyclone cooling technique for high performance gas turbine blades,” in *International Heat Transfer Conference Digital Library*, Begel House Inc., 2002.

[92] A. A. Khalatov, “Swirl Flows: Fundamentals and Applications,” *Ukr. Nauk. ТЕПЛО-И МАССООБМЕННЫЕ ПРОЦЕССЫ*, 1989.

[93] A. A. Khalatov and V. K. Schukin, “Heat, Mass Transfer and Hydrodynamics of Swirl Flows in Axisymmetrical Channels,” *Mashinostroenie, Moscow, Russ.*, 1982.

[94] B. O. Kitoh, "Experimental study of turbulent swriling flow in a straight pipe," *Prog. Energy Combust. Sci.*, vol. 225, 1991.

[95] V. K. Dhir and S. Monica, " Heat Transferenhancement Using Tangental Nection," no. 19, 1992.

[96] F. Chang and V. K. Dhir, "Turbulent flow field in tangentially injected swirl flows in tubes," *Int. J. Heat Fluid Flow*, vol. 15, no. 5, pp. 346–356, 1994, doi: 10.1016/0142-727X(94)90048-5.

[97] F. Chang and V. K. Dhir, "Mechanisms of heat transfer enhancement and slow decay of swirl in tubes using tangential injection," *International Journal of Heat and Fluid Flow*, vol. 16, no. 2. 1995. doi: 10.1016/0142-727X(94)00016-6.

[98] B. Glezer, H. K. Moon, J. Kerrebrock, J. Bons, and G. Guenette, "Heat transfer in a rotating radial channel with swirling internal flow," *Proc. ASME Turbo Expo*, vol. 4, 1998, doi: 10.1115/98-GT-214.

[99] B. Glezer and T. O. Connell, "Mimi 11 11," 2019.

[100] C. R. Hedlund and P. M. Ligrani, "Local swirl chamber heat transfer and flow structure at different Reynolds numbers," *Proc. ASME Turbo Expo*, vol. 3, no. April, pp. 375–385, 1999, doi: 10.1115/99-GT-164.

[101] C. Heat, S. L. City, T. C. Design, and S. Diego, "Blade Internal Cooling," 2017.

[102] P. M. Ligrani, C. R. Hedlund, B. T. Babinchak, R. Thambu, H. K. Moon, and B. Glezer, "Flow phenomena in swirl chambers," *Exp. Fluids*, vol. 24, no. 3, pp. 254–264, 1998, doi: 10.1007/s003480050172.

[103] H.-K. Moon, T. O'Connell, and B. Glezer, "Heat transfer enhancement in a circular channel using lengthwise continuous tangential injection," in *International Heat Transfer Conference Digital Library*, Begel House Inc., 1998.

[104] R. Thambu, B. T. Babinchak, P. M. Ligrani, C. R. Hedlund, H. K. Moon, and B. Glezer, "Flow in a simple swirl chamber with and without controlled inlet forcing," *Exp. Fluids*, vol. 26, no. 4, pp. 347–357, 1999, doi: 10.1007/s003480050298.

[105] A. A. Khalatov, N. Syred, P. J. Bowen, and R. Al-Ajmi, "Quasi two-dimensional cyclone-jet cooling configuration: Evaluation of heat transfer and pressure losses," *Proc. ASME Turbo Expo*, vol. 3, pp. 1–8, 2001, doi: 10.1115/2001-GT-0182.

[106] J.-G. Nam and J.-Y. Choi, "A study for NOx discharge characteristics of diesel engines," *J. Korean Soc. Mar. Eng.*, vol. 27, no. 3, pp. p373-380, 2003.

[107] N. Winter and H.-P. Schiffer, "Effect of rotation on the cyclone cooling method mass transfer measurements," in *TURBINE-09. Proceedings of International Symposium on Heat Transfer in Gas Turbine Systems*, Begel House Inc., 2009.

[108] M. Bruschewski, C. Scherhag, H. P. Schiffer, and S. Grundmann, "Influence of channel geometry and flow variables on cyclone cooling of turbine blades," *J. Turbomach.*, vol. 138, no. 6, pp. 1–10, 2016, doi: 10.1115/1.4032363.

[109] S. Grundmann, F. Wassermann, R. Lorenz, B. Jung, and C. Tropea, "Experimental investigation of helical structures in swirling flows," *Int. J. Heat Fluid Flow*, vol. 37, pp. 51–63, 2012, doi: 10.1016/j.ijheatfluidflow.2012.05.003.

[110] S. Grundmann, "GT2012-6 9395," pp. 1–16, 2012.

[111] C. Qian *et al.*, "Innovative vortex cooling concept and its application to turbine airfoil trailing edge cooling design," in *33rd Joint Propulsion Conference and Exhibit*, 1997, p. 3013.

[112] N. W. Harvey and M. Lane, "GT2006-90352," pp. 1–16, 2006.

[113] J. P. C. W. Ling, "Development of heat transfer measurement techniques and cooling strategies for gas turbines." University of Oxford, 2005.

[114] S. V. Ekkad, G. Pamula, and S. Acharya, "Influence of Cross-Flow Induced Swirl and Impingement on Heat Transfer in an Internal Coolant Passage of a Turbine Airfoil," *ASME International mechanical engineering. Congress, and Exposition,* vol. 1999-O, no. August, pp. 227–233, 1999, doi: 10.1115/IMECE1999-0989.

[115] A. Engineering, E. Sciences, C. Biegger, G. Main, B. W. Prof, and Y. Rao, "Flow and Heat Transfer Investigations in Swirl Tubes for Gas Turbine Blade Cooling," no. February, 2017.

[116] D. R. Weske, "Experimental study of turbulent swirled flows in a cylindrical tube," *Fluid Mech. Res.*, vol. 3, no. 1, pp. 77–82, 1974.

[117] M. Salcudean, I. Gartshore, K. Zhang, and I. McLean, "An experimental study of film cooling effectiveness near the leading edge of a turbine blade," *J. Turbomach.*, vol. 116, no. 1, pp. 71–79, 1994, doi: 10.1115/1.2928280.

[118] R. Kumar and T. Conover, "Flow visualization studies of a swirling flow in a cylinder," *Exp. Therm. Fluid Sci.*, vol. 7, no. 3, pp. 254–262, 1993, doi: 10.1016/0894-1777(93)90009-8.

[119] M. Forster and B. Weigand, "Experimental and numerical investigation of jet impingement cooling onto a concave leading edge of a generic gas turbine blade," *Int. J. Therm. Sci.*, vol. 164, no. January, p. 106862, 2021, doi: 10.1016/j.ijthermalsci.2021.106862.

[120] N. Hay and P. D. West, "Heat Transfer in Free Swirling Flow in a Pipe.," *Am. Soc. Mech. Eng.*, no. 75-HT-YY, pp. 411–416, 1975.

[121] T. Akiyama and M. Ikeda, "Fundamental Study of the Fluid Mechanics of Swirling Pipe Flow with Air Suction," *Ind. Eng. Chem. Process Des. Dev.*, vol. 25, no. 4, pp. 907–913, 1986, doi: 10.1021/i200035a012.

[122] B. Glezer, H. K. Moon, J. Kerrebrock, J. Bons, and G. Guenette, *Heat transfer in a rotating radial channel with swirling internal flow*, vol. 78651. American Society of Mechanical Engineers, 1998.

[123] D. Symmetric and S. Expansion, "Technical Briefs," *Noise Vib. Worldw.*, vol. 39, no. 7,

pp. 28–32, 2008, doi: 10.1260/095745608785260648.

[124] S. Jakirlic, K. Hanjalic, and C. Tropea, “Modeling rotating and swirling turbulent flows: a perpetual challenge,” *AIAA J.*, vol. 40, no. 10, pp. 1984–1996, 2002.

[125] J. C. Chen and C. A. Lin, “WITH SECOND-MOMENT CLOSURES,” vol. 508, no. February 1998, pp. 493–508, 1999.

[126] J. Paik and F. Sotiropoulos, “Numerical Simulation of Strongly Swirling Turbulent Flows Through an Abrupt Expansion.” pp. 779–784, 2022. doi: 10.1615/tsfp6.1250.

[127] Z. Liu, J. Li, and Z. Feng, “Numerical study on the effect of jet slot height on flow and heat transfer of swirl cooling in leading edge model for gas turbine blade,” *Proc. ASME Turbo Expo*, vol. 3, 2013, doi: 10.1115/GT2013-94819.

[128] B. A. Younis, C. G. Speziale, and T. T. Clark, “A rational model for the turbulent scalar fluxes,” *Proc. R. Soc. A Math. Phys. Eng. Sci.*, vol. 461, no. 2054, pp. 575–594, 2005, doi: 10.1098/rspa.2004.1380.

[129] C. G. Speziale, “Turbulence modelling for time-dependent RANS and VLES: a review,” *AIAA Journal*, vol. 36, no. 2, pp. 173–184, 1998.

[130] K. Kusterer, G. Lin, D. Bohn, T. Sugimoto, R. Tanaka, and M. Kazari, “Heat transfer enhancement for gas turbine internal cooling by application of double swirl cooling chambers,” *Proc. ASME Turbo Expo*, vol. 3, pp. 1–11, 2013, doi: 10.1115/GT2013-94774.

[131] L. S. Caretto, R. M. Curr, and D. B. Spalding, “Two numerical methods for three-dimensional boundary layers,” *Comput. Methods Appl. Mech. Eng.*, vol. 1, no. 1, pp. 39–57, 1972, doi: 10.1016/0045-7825(72)90020-5.

[132] R. S. Bunker, “Film cooling effectiveness due to discrete holes within a transverse surface slot,” *Am. Soc. Mech. Eng. Int. Gas Turbine Institute, Turbo Expo IGTI*, vol. 3 A, pp. 129–138, 2002, doi: 10.1115/GT2002-30178.

[133] Z. Liu, Z. Feng, and L. Song, “GT2011-46125,” 2011.

[134] B. Gmbh, J. Straße, and D. Bohn, “GT2014-25851,” pp. 1–11, 2014.

[135] G. Lin *et al.*, “Numerical investigation on heat transfer in an advanced new leading edge impingement cooling configuration,” *Propulsion and Power Research*, vol. 4, no. 4. pp. 179–189, 2015. doi: 10.1016/j.jppr.2015.10.003.

[136] M. A. Leschziner and S. Hogg, “Computation of highly swirling confined flow with a Reynolds stress turbulence model,” *AIAA J.*, vol. 27, no. 1, pp. 57–63, 1989.

[137] Y. Bazilevs, M. Hsu, J. Kiendl, R. Wüchner, and K. Bletzinger, “3D Simulation of Wind Turbine Rotors at Full Scale. Part II: Fluid – Structure Interaction Modeling with Composite Blades,” *Int. J. Numer. Methods Fluids*, vol. 65, no. October 2010, pp. 236–253, 2011, doi: 10.1002/fld.

[138] O. V. Kazantseva, S. A. Piralishvili, and A. A. Fuzeeva, “Numerical simulation of

swirling flows in vortex tubes," *High Temp.*, vol. 43, no. 4, pp. 608–613, 2005, doi: 10.1007/s10740-005-0102-8.

[139] A. Gupta and R. Kumar, "Three-dimensional turbulent swirling flow in a cylinder: Experiments and computations," *Int. J. Heat Fluid Flow*, vol. 28, no. 2, pp. 249–261, 2007, doi: 10.1016/j.ijheatfluidflow.2006.04.005.

[140] G. Lin, K. Kusterer, D. Bohn, T. Sugimoto, R. Tanaka, and M. Kazari, "Impingement cooling with spent flow in the blade leading edge using double swirl chambers," in *International Heat Transfer Conference Digital Library*, Begel House Inc., 2014.

[141] H. Foroutan and S. Yavuzkurt, "A partially-averaged Navier-Stokes model for the simulation of turbulent swirling flow with vortex breakdown," *Int. J. Heat Fluid Flow*, vol. 50, pp. 402–416, 2014, doi: 10.1016/j.ijheatfluidflow.2014.10.005.

[142] G. Lin, K. Kusterer, D. Bohn, T. Sugimoto, R. Tanaka, and M. Kazari, "Investigation on heat transfer enhancement and pressure loss of double swirl chambers cooling," *Propuls. Power Res.*, vol. 2, no. 3, pp. 177–187, 2013, doi: 10.1016/j.jppr.2013.07.003.

[143] W. He, Q. Deng, G. Yang, and Z. Feng, "Effects of Turning Angle and Turning Internal Radius on Channel Impingement Cooling for a Novel Internal Cooling Structure," *J. Turbomach.*, vol. 143, no. 9, pp. 1–11, 2021, doi: 10.1115/1.4050608.

[144] X. Yang, F. Seibold, Z. Feng, and B. Weigand, "Effects of blade lean on internal swirl cooling at turbine blade leading edges," *Int. J. Heat Mass Transf.*, vol. 194, p. 123111, 2022, doi: 10.1016/j.ijheatmasstransfer.2022.123111.

[145] X. Fan, C. Du, L. Li, and S. Li, "Numerical simulation on effects of film hole geometry and mass flow on vortex cooling behavior for gas turbine blade leading edge," *Appl. Therm. Eng.*, vol. 112, pp. 472–483, 2017, doi: 10.1016/j.applthermaleng.2016.10.059.

[146] S. C. Underwood, "Aerothermodynamics of Impingement and Film Cooling in a Gas Turbine Blade Aerothermodynamics of Impingement and Film Cooling in a Gas Turbine Blade," 2008.

[147] Y. Lu, "Effect of Hole Configurations on Film Cooling From Cylindrical Inclined Holes for the Application To Gas Turbine Blades," *Transport*, no. December, 2007.

[148] F. Whittle, "The early history of the whittle jet propulsion gas turbine," *Arch. Proc. Inst. Mech. Eng. 1847-1982 (vols 1-196)*, vol. 152, no. 1945, pp. 419–435, 2006.

[149] A. C. Jones, "Design and test of a small, high pressure ratio radial turbine," *Proc. ASME Turbo Expo*, vol. 1, no. April, pp. 362–370, 1994, doi: 10.1115/94-GT-135.

[150] V. Talimi, Y. S. Muzychka, and S. Kocabiyik, "A review on numerical studies of slug flow hydrodynamics and heat transfer in microtubes and microchannels," *Int. J. Multiph. Flow*, vol. 39, pp. 88–104, 2012, doi: 10.1016/j.ijmultiphaseflow.2011.10.005.

[151] H. Fawzy, Q. Zheng, N. Ahmad, and Y. Jiang, "Optimization of a swirl with impingement compound cooling unit for a gas turbine blade leading edge," *Energies*, vol. 13, no. 1, 2020, doi: 10.3390/en13010210.

[152] J. N. Prausa, “Heat Transfer Coefficient and Adiabatic Effectiveness Measurements for an Internal Turbine Vane Cooling Feature Heat Transfer Coefficient and Adiabatic Effectiveness Measurements for an Internal Turbine Airfoil Cooling Feature,” 2004.

[153] M. Sheikholeslami, M. Gorji-Bandpy, and D. D. Ganji, “Review of heat transfer enhancement methods: Focus on passive methods using swirl flow devices,” *Renew. Sustain. Energy Rev.*, vol. 49, pp. 444–469, 2015, doi: 10.1016/j.rser.2015.04.113.

[154] C. Du, L. Li, and X. Fan, “Numerical study on vortex cooling flow and heat transfer behavior under rotating conditions,” *Int. J. Heat Mass Transf.*, vol. 105, pp. 638–647, 2017, doi: 10.1016/j.ijheatmasstransfer.2016.10.028.

[155] T. C. Maloney, “Graduate Program in Mechanical and Aerospace Engineering,” 2012.

[156] H. Fawzy, Q. Zheng, and N. Ahmad, “Effect of Slot Area Ratio and Slot Angle on Swirl Cooling in a Gas Turbine Blade Leading Edge,” *J. Aerosp. Eng.*, vol. 33, no. 5, pp. 1–13, 2020, doi: 10.1061/(asce)as.1943-5525.0001161.

[157] P. G. Aleiferis and N. Papadopoulos, “Heat and mass transfer effects in the nozzle of a fuel injector from the start of needle lift to after the end of injection in the presence of fuel dribble and air entrainment,” *Int. J. Heat Mass Transf.*, vol. 165, p. 120576, 2021, doi: 10.1016/j.ijheatmasstransfer.2020.120576.

[158] D. Comeau, “ATRAP Buffer-Gas Positron Accumulator,” no. June, 2014.

[159] X. Fan, L. Li, J. Zou, and Y. Zhou, “Cooling methods for gas turbine blade leading edge: Comparative study on impingement cooling, vortex cooling and double vortex cooling,” *Int. Commun. Heat Mass Transf.*, vol. 100, no. January, pp. 133–145, 2019, doi: 10.1016/j.icheatmasstransfer.2018.12.017.

[160] B. lun Zhang, H. ren Zhu, C. yi Yao, and C. liang Liu, “Investigation on aerothermal performance of a rib-slot scheme on the multi-cavity tip of a gas turbine blade,” *Int. J. Heat Mass Transf.*, vol. 176, p. 121408, 2021, doi: 10.1016/j.ijheatmasstransfer.2021.121408.

[161] C. Biegger, C. Sotgiu, and B. Weigand, “Numerical investigation of flow and heat transfer in a swirl tube,” *Int. J. Therm. Sci.*, vol. 96, pp. 319–330, 2015, doi: 10.1016/j.ijthermalsci.2014.12.001.

[162] B. Latini, M. Fiore, and F. Nasuti, “Modeling liquid rocket engine coolant flow and heat transfer in high roughness channels,” *Aerosp. Sci. Technol.*, vol. 126, p. 107672, 2022, doi: 10.1016/j.ast.2022.107672.

[163] R. S. Bunker, “Evolution of turbine cooling,” *Proceeding of the ASME Turbo Expo 2017: Turbo machinery technical conference and exposition*, Charlotte, pp. 1– 26, 2017, doi: 10.1115/GT2017-63205.

[164] M. Hasan, “Novel efficient wing buoyant aircraft design for enhanced aerodynamic performance.” PhD thesis, University of Sheffield, 2021.

[165] A. Nikparto and M. T. Schobeiri, “Combined numerical and experimental investigations of heat transfer of a highly loaded low-pressure turbine blade under periodic inlet flow condition,” *Proc. Inst. Mech. Eng. Part A J. Power Energy*, vol. 232, no. 7, pp. 769–

784, 2018, doi: 10.1177/0957650918758158.

[166] K. S. Chana, U. K. Singh, and T. Povey, "Turbine heat transfer and aerodynamic measurements and predictions for A 1.5 Stage configuration," *Proc. ASME Turbo Expo 2004*, vol. 3, pp. 825–832, 2004, doi: 10.1115/gt2004-53951.

[167] Z. Taha, Sugiyono, T. M. Y. S. Tuan Ya, and T. Sawada, "Numerical investigation on the performance of Wells turbine with non-uniform tip clearance for wave energy conversion," *Appl. Ocean Res.*, vol. 33, no. 4, pp. 321–331, 2011, doi: 10.1016/j.apor.2011.07.002.

[168] A. Kelly, "The Optimisation of Finite Element Meshes," 2014, [Online]. Available: https://theses.gla.ac.uk/5730/1/kelly2014phd.pdf

[169] C. Habchi, A. Ghanem, T. Lemenand, D. Della Valle, and H. Peerhossaini, "Mixing performance in Split-And-Recombine Milli-Static Mixers—A numerical analysis," *Chem. Eng. Res. Des.*, vol. 142, pp. 298–306, 2019, doi: 10.1016/j.cherd.2018.12.010.

[170] A. G. Dixon, M. Ertan Taskin, M. Nijemeisland, and H. H. Stitt, "Systematic mesh development for 3D CFD simulation of fixed beds: Single sphere study," *Comput. Chem. Eng.*, vol. 35, no. 7, pp. 1171–1185, 2011, doi: 10.1016/j.compchemeng.2010.12.006.

[171] Y. Luan, Y. Rao, and H. Yan, "Experimental and numerical study of swirl impingement cooling for turbine blade leading edge with internal ridged wall and film extraction holes," *Int. J. Heat Mass Transf.*, vol. 201, p. 123633, 2023, doi: 10.1016/j.ijheatmasstransfer.2022.123633.

[172] Y. You, F. Seibold, S. Wang, B. Weigand, and U. Gross, "URANS of turbulent flow and heat transfer in divergent swirl tubes using the k-ω SST turbulence model with curvature correction," *Int. J. Heat Mass Transf.*, vol. 159, p. 120088, 2020, doi: 10.1016/j.ijheatmasstransfer.2020.120088.

[173] Y. Rao, C. Biegger, and B. Weigand, "Heat transfer and pressure loss in swirl tubes with one and multiple tangential jets pertinent to gas turbine internal cooling," *Int. J. Heat Mass Transf.*, vol. 106, pp. 1356–1367, 2017, doi: 10.1016/j.ijheatmasstransfer.2016.10.119.

[174] S. Fries, S. Skusa, and A. Luke, "Heat transfer and pressure drop of condensation of hydrocarbons in tubes," *Heat Mass Transf. und Stoffuebertragung*, vol. 55, no. 1, pp. 33–40, 2019, doi: 10.1007/s00231-018-2318-2.

[175] H. R. Jasim, "Design and Heat Transfer Analysis of Gas Hadeel Raheem Jasim," no. April, 2023.

[176] A. J. Robinson and E. Schnitzler, "An experimental investigation of free and submerged miniature liquid jet array impingement heat transfer," *Exp. Therm. Fluid Sci.*, vol. 32, no. 1, pp. 1–13, 2007, doi: 10.1016/j.expthermflusci.2006.12.006.

[177] R. J. Perdue, "ePrints Soton Existing Theory".

[178] X. Wang *et al.*, "Numerical simulation of radial duel-stage nozzle vortex cooling at the

leading edge of a gas turbine blade,” *Appl. Therm. Eng.*, vol. 260, no. November 2024, p. 125017, 2025, doi: 10.1016/j.applthermaleng.2024.125017.

[179] B. Sunden and G. Xie, “Gas turbine blade tip heat transfer and cooling: A literature survey,” *Heat Transf. Eng.*, vol. 31, no. 7, pp. 527–554, 2010, doi: 10.1080/01457630903425320.

[180] O. Kaleem Siddiqui, “ANALYTICAL INVESTIGATION OF FLOW DISTRIBUTION IN HEAT EXCHANGER MANIFOLDS Mechanical Engineering,” 2018.

[181] T. Bai, C. Cheng, K. P. Griffin, X. Li, and L. Fu, “Study of the vortex structure in compressible wall-bounded turbulence,” *Phys. Rev. Fluids*, vol. 8, no. 12, pp. 1–36, 2023, doi: 10.1103/PhysRevFluids.8.124603.

[182] Ö. Ağra, H. Demir, S. Ataylmaz Özgür, F. Kantaş, and A. S. Dalklç, “Numerical investigation of heat transfer and pressure drop in enhanced tubes,” *Int. Commun. Heat Mass Transf.*, vol. 38, no. 10, pp. 1384–1391, 2011, doi: 10.1016/j.icheatmasstransfer.2011.07.013.

[183] S. Dutta and P. Singh, “Opportunities in jet-impingement cooling for gas-turbine engines,” *Energies*, vol. 14, no. 20, pp. 1–29, 2021, doi: 10.3390/en14206587.

[184] A. Hellsten, “Some improvements in Menter’s k-omega SST turbulence model,” in *29th AIAA, Fluid Dynamics Conference*, 1998, p. 2554.

Appendix A

Appendix A-1: Elsevier Copyright permission Licence these are mentioned at chapter

This documents constitutes the legal copyright proceeded by Elesvier for the copies of Figure 1.1 *.From Modern Gas Turbine Systems (A.M.Y. Razak, 2013) in this thesis.*

This documents constitutes the legal copyright proceeded by Elesvier for the replicas of Figure 1.2,*. On the design and structural analysis of jet engine fan blade structures Licensed Content Author Leye M. Amoo Licensed Content Date Jul 1, 2013*

This documents constitutes the legal copyright proceeded by Elesvier for the copies of Figure 1.3. *Variability in Coastal Flooding predictions due to forecast errors during Hurricane Arthur Licensed Content Author R. Cyriac,J.C. Dietrich,J.G. Fleming,B.O. Blanton,C. Kaiser,C.N. Dawson,R.A. Luettich Licensed Content Date Jul 1, 2018.*

This documents constitutes the legal copyright proceeded by Elesvier for the replicas of Figure 1.4. *Energy conservation and the principle of equivalence Licensed Content Author Mark P Haugan Licensed Content Date Mar 1, 1979.*

These Copyrights are use in the Figs 1.2,1.3,1.4.